Investigation and assessment of physico-morphological and thermomechanical responses of few sedimentary rocks

Submitted in partial fulfillment of the requirements

for the degree of

Doctor of Philosophy

of the

Indian Institute of Technology, Bombay, India

and

Monash University, Australia

by

Bankim Chandra Mahanta

Supervisors:

Prof. T N Singh (IIT Bombay)

Prof. Vikram Vishal (IIT Bombay)

Prof. P G Ranjith (Monash University)

Prof. WenHui Duan (Monash University)

The course of study for this award was developed jointly by
the Indian Institute of Technology, Bombay and Monash University, Australia
and given academic recognition by each of them.
The programme was administered by The IITB-Monash Research Academy

(2019)

Approval Sheet

The thesis entitled "*Investigation and assessment of physico-morphological and thermomechanical responses of few sedimentary rocks*" by *Bankim Chandra Mahanta* is approved for the degree of **Doctor of Philosophy**.

Prof. A Basu
External Examiner

Prof. K H Singh
Internal Examiner

Prof. T N Singh
IITB Main-supervisor

Prof. Vikram Vishal
IITB Co-supervisor

Prof. P G Ranjith
Monash Main-supervisor

Prof. WenHui Duan
Monash Co-supervisor

Prof. J. Adinarayana
Chairman

Date: 10.01.2019

Place: IITB-Monash research Academy, IIT Bombay, Mumbai, India

Declaration

I declare that this written submission represents my ideas in my own words and where others' ideas or words have been included, I have adequately cited and referenced the original sources. I also declare that I have adhered to all principles of academic honesty and integrity and have not misrepresented or fabricated or falsified any idea/data/fact/source in my submission. I understand that any violation of the above will be cause for disciplinary action by the Institute and can also evoke penal action from the sources which have thus not been properly cited or from whom proper permission has not been taken when needed.

Notice 1

Under the Copyright Act 1968, this thesis must be used only under the normal conditions of scholarly fair dealing. In particular, no results or conclusions should be extracted from it, nor should it be copied or closely paraphrased in whole or in part without the written consent of the author. Proper written acknowledgement should be made for any assistance obtained from this thesis.

Notice 2

I certify that I have made all reasonable efforts to secure copyright permissions for third-party content included in this thesis and have not knowingly added copyright content to my work without the owner's permission.

Bankim Chandra Mahanta

IITB ID: 

Monash ID: 

Abstract

At present, the consumed global energy comprises oil (36 per cent), coal (28 per cent), natural gas (24 per cent), and renewable energy (7 per cent), which includes hydro, solar, and nuclear (6 per cent) energies. After petroleum, coal is the second largest energy commodity worldwide. Coal contributes to over 30 per cent of the world's primary energy consumption; more than 40 per cent of the electricity production worldwide comes from coal consumption in thermal power plants. Since India is a developing country, rising economic growth demands additional energy sources. As a first step towards development, coal is being used as the primary source of energy because it is found in abundance and is easier to extract than any other source of energy. India ranks third in coal production, and most of its energy demands are being fulfilled by coal. However, while using these conventional sources of energy, various environmental issues need to be addressed. In such scenarios, the future trend for energy supply is moving towards various alternative or unconventional energy sources. Underground coal gasification is a technique that is used for the exploration of energy from unmineable coal seams that are either uneconomical to explore by conventional coal mining techniques or are inaccessible and lack of modern mining methods. Based on the literature review, it is quite clear that most of the thermo-mechanical characterisations of sandstone have been concentrated in the various physical and mechanical aspects. However, no microstructural observation was encountered in the literature. Therefore, in addition to the various mechanical and physical aspects of the sandstone, the microstructural responses of sandstone are one of the primary goals of the research work, which will better explain the thermal behaviour of sandstones under and after exposed to high temperatures. Jodhpur sandstone, which is used in the current study, belongs to the Jodhpur area of Rajasthan, India. The experimental investigation includes investigation of various physico-morphological and mechanical behaviour of rocks under the influence of temperatures. There is still a gap in the knowledge of the evolution of microscopic pore structures in rocks that are exposed to high temperatures. In order to close the gap in knowledge, a micro-nano-scale investigation of the structural change of sandstone has been made with the support of micro-CT techniques. The in-depth investigation includes the observation of microstructural responses, pore space evolution and pore-network models as a function of temperatures. At different temperatures and stress levels, the pore network models analysis was performed that represented the pore and throat configuration of the studied sandstone and its progressive evolution with the increased temperatures and progressive loading. All the physical changes and chemical reactions as a result of being exposure to

temperatures bring changes into the structure of the rock in the form of porosity increment, mineral transformation, minerals decomposition, and dihydroxylation, reduction in the adhesive force between the minerals, development of microcracks and their accumulation that results in macrocracks. After 400 °C, a significant reduction in the P-wave velocity of the sandstone is observed. In the temperature range 400 °C – 900 °C, the induced structural damages within the structure of the sandstone provide major contribution for the reduction of the P-wave velocity. SEM, petrographic analysis of thermally treated and rapid cooled sandstone display induction of major structural damage for 600 °C and 800 °C cases. The extent of structural damage is correlated to the thermal expansion of minerals and the formation of microcracks such as intergranular, intragranular and transgranular cracks and their network. The tested sandstone underwent major structural damage in the temperature window of 400 °C to 680 °C. It was found that the formation of new microcracks, chemical alteration of clay and carbonate minerals (kaolinite, dickite, and calcite, respectively) and the phase transition of quartz mineral at 573 °C led to these structural damages. An overall reduction in the strength of the tested samples upon heating was observed. However, a marginal increase in the UCS and the tensile strength of the sandstone was observed after 700 °C. This is possibly due to the formation of a new cementing mineral, Portlandite that may be the by-product of the dihydroxylation of dickite ($Al_2\ SI_2\ O_5\ (OH)_4$) at 680 °C and the decomposition of calcite ($CaCO_3$) at approximately 700 °C. At room temperature, the crack initiation and the crack damage stage start at around 41 per cent and 91 per cent of the failure strength, respectively. However, the crack initiation and the crack damage stage start at nearly 17 per cent and 62 per cent of the failure strength in the specimens at 700 °C, which suggests a possible reduction in the linear-elastic region and the stable crack propagation region in thermally treated specimens. Based on the cyclic loading-unloading analysis it can be concluded that for higher temperature condition Kaiser effect is insignificant as compared to the room temperature condition. In such situation, the accuracy of Kaiser effect or the stress memory effect of the sandstone can be explained in terms of Felicity ratio. Based on the results if triaxial test, it can be stated that mechanically formed shear bands revealed the higher porous nature of the inside shear band as compared to the outside shear zone. For all the combination of investigated temperatures and pressures, the inside shear bands were observed with having finer grains compared to the outside shear band. Jodhpur sandstone possessed its maximum porosity at 600 °C and, thereby, a decreasing trend up to 800 °C, which can be due to the formation of a new cementing material in between 600 °C and 800 °C. Based on the micro-CT study performed at different stress level of the peak load reveals the appearance of macrofractures at 50 per cent of the peak load. In

addition, it suggests, with increasing the load level total porosity of the sandstone gradually increases whereas, the volume of non-connected pores gradually decreases that indicates the coalescence of non-connected microfractures to form macrofractures that results in the increase of total pores of the sandstone.

Table of Contents

List of Figures ..... **xii**

List of Tables ..... **xxi**

Chapter 1 Introduction **1**

1.1 Clean energy and its importance in the current scenario 1

1.2 Application of high-temperature rock behaviours 3

1.3 Motivation 5

1.3.1 Rock mechanical aspects of UCG 5

1.3.2 Hydrogeological aspects of UCG 6

1.4 Objective and approach 7

1.5 Structure of the thesis 8

Chapter 2 Review of literature **10**

2.1 Underground Coal Gasification 10

2.1.1 Methods of UCG implementation 11

2.1.2 Development of UCG in India 13

2.2 Effect of temperature on physico-mechanical properties 16

2.2.1 Effect of temperature on mechanical properties of sandstones 17

2.2.2 Effect of temperature on physical properties of sandstones 25

2.3 Effect of temperature on the flow behaviour of sandstone 28

2.4 Knowledge gap 29

Chapter 3 Materials and general methodology **30**

3.1 Location and general geological information about sandstone 30

3.2 Mineralogical characterisation and hardness test of sandstone 31

3.2.1 Petrographic study 31

3.2.2 XRD analysis 32

3.2.2.1 Room-temperature XRD analysis 32

3.2.2.2 High-temperature XRD analysis 33

3.2.3 EDS analysis 33
3.2.4 Grain-size analysis 34
3.2.5 Nanoindentation hardness test 35
3.3 Other rock types used for comparison 36
3.3.1 Dholpur sandstone 36
3.3.2 Manoharpur sandstone 37
3.3.3 Gondwana sandstone 40
3.3.4 Jhiri shale 40
3.4 Specimen preparation, and the methodology of the heat treatment used for experimental investigation 42
Chapter 4 Experimental investigation of the physical and mechanical behaviour of sandstones with varying temperatures 46
4.1 Investigation of physico-morphological responses 46
4.1.1 Macroscopic observation 46
4.1.2 Petrographic thin-section images of the sandstone 46
4.1.3 SEM study for surface morphology 48
4.1.4 Effect of temperatures on the seismic wave velocity of sandstones 49
4.1.5 Thermal expansion of sandstones in response to varying temperatures 52
4.1.6 Mass loss of sandstone in response to varying temperatures 53
4.1.7 Thermogravimetric analysis of sandstones 54
4.2 Investigation of thermo-mechanical responses 56
4.2.1 Experimental methodology 56
4.2.1.1 Mechanical strength tests 56
4.2.1.2 Acoustic emission technique 58
4.2.1.3 DIC using ARAMIS 59
4.2.2 Results and discussion 61
4.2.2.1 Variation of mechanical strength parameters in response to temperatures 61
4.2.2.1.1 Effect of heating on stress-strain behaviour 61

4.2.2.1.2 Effect of heating on the UCS and tensile strength 68
4.2.2.1.3 Effect of heating on the elastic modulus and failure strain 70
4.2.2.1.4 Effect of temperature on damage factor and Poisson's ratio 71
4.2.2.1.5 Fracturing characteristic of thermally treated specimens by using AE.. 73
4.2.2.2 Comparison of the experimental results along with existing literature 77
Chapter 5 Experimental investigation of the effect of cyclic loading-unloading and the strain rate on sedimentary rocks 81
5.1 Effect of the loading-unloading cycle on the mechanical and AE characteristics of sandstone 81
5.1.1 Experimental investigation 81
5.1.1.1 Multiple cycles at different stress levels of the peak load 83
5.1.1.2 Incremental stress cycles based on certain percentages of the peak load... 83
5.1.1.3 Incremental stress cycles based on the acoustic characteristics 83
5.1.2 Results and discussion 83
5.1.2.1 Multiple cycles at different stress levels of the peak load 84
5.1.2.2 Incremental stress cycles based on certain percentages of the peak load... 87
5.1.2.3 Incremental stress cycles based on acoustic characteristics 89
5.1.2.4 The Kaiser effect and the Felicity effect in the failure and deformation stages of thermally treated specimens 90
5.2 Effect of strain rates on the mechanical properties of shale 91
5.2.1 Overview 91
5.2.2 Background knowledge 92
5.2.3 Experimental investigation 94
5.2.4 Results and discussion 95
5.2.4.1 Macroscopic fracture failure 97
5.2.4.2 Mesoscopic and microscopic fracture surface 97
5.2.4.3 Influence of strain rate on various mechanical strength parameters 98
5.2.4.4 Regression analysis based on the experimental results 101

5.2.4.5 Correlation between fracture toughness and brittleness index 101
5.2.4.6 A comparison of the effect of strain rate on rocks 102
Chapter 6 Experimental Investigation of Fracture Mechanical Attributes of sandstone and shale in response to varying temperatures and strain rates 104
6.1 Influence of temperature on the fracture mechanical attributes of sandstones 104
6.1.1 Overview 104
6.1.2 Preparation of CSTSCB Specimen 104
6.1.3 Determination of mode I fracture toughness using CSTSCB specimens 105
6.1.4 Experimental work 107
6.1.5 Geo-mechanical properties 107
6.1.5.1 Petrographic study 107
6.1.5.2 SEM study 108
6.1.6 Results and discussion 110
6.1.6.1 Load and load line displacement curve 110
6.1.6.2 Change in physical appearance 111
6.1.6.3 Fracture toughness vs tensile strength 114
6.1.6.4 Temperature vs fracture toughness 115
6.2 Influence of strain rate on the fracture mechanical attributes of shale 119
6.2.1 Overview 119
6.2.2 Background knowledge 120
6.2.3 Testing methodology 123
6.2.3.1 Fracture toughness determination 123
6.2.3.2 Applied energy 125
6.2.4 Experimental investigation 126
6.2.4.1 SEM study 126
6.2.5 Results and discussion 126
6.3 Influence of strain rate on the fracture toughness and tensile strength of sandstone using flattened Brazilian disc 134

6.3.1 Overview 134
6.3.2 Background knowledge 134
6.3.3 Methodology 136
6.3.3.1 Results and discussion 138
Chapter 7 Experimental investigation of the mechanical behaviour of sandstone under high-temperature and high-pressure conditions 141
7.1 Sample preparation 141
7.2 Experimental methodology 141
7.2.1 Experimental setup 141
7.3 Results and discussion 143
7.3.1 Failure characteristics of the specimens 143
7.3.2 Stress-strain behaviour at different temperatures and confinements 145
7.3.3 Effect of temperature and pressure on the mechanical strength parameters of sandstone 146
7.4 Insight into the post-failure microstructure 147
7.4.1 Methodology of micro-CT-based investigation 147
7.4.2 Results and discussion 150
7.4.2.1 Grain-size-based investigation 150
7.4.2.2 Porosity-based investigation 153
Chapter 8 Micro-CT based microstructural investigation of sandstones 154
8.1 Microstructural insight into progressive deformation of sandstone after heat treatment 154
8.1.1 Overview 154
8.1.2 Background knowledge 154
8.1.3 Specimen preparation and methodology 158
8.1.3.1 Specimen preparation 158
8.1.3.2 Methodology 159
8.1.3.3 Image acquisition 159

8.1.3.4 Image Processing 160
8.1.3.4.1 Smoothening and denoising 161
8.1.3.4.2 Sharpening 162
8.1.3.4.3 Segmentation 162
8.1.3.5 Computationally simulated rock properties 163
8.1.3.5.1 Pore-data extraction 163
8.1.3.5.2 Pore-network modelling 163
8.1.4 Results and discussion 164
8.1.4.1 Microstructural modification as a function of temperatures 165
8.1.4.2 Evolution of pore spaces as a function of temperatures 168
8.1.4.3 PNM as a function of temperatures 177
8.2 Microstructural insight into progressive deformation of sandstone at different stress levels 184
8.2.1 Sample preparation and methodology 185
8.2.2 Results and discussion 186
8.2.2.1 Evolution of pore spaces at different stress levels 186
8.2.2.2 PNM at different stress levels 188
Chapter 9 Conclusions and future work 192
9.1 Conclusions 192
9.1.1 Summary and conclusions from the physico-morphological investigation 192
9.1.2 Summary and conclusions from mechanical testing 192
9.1.2.1 Investigation in the unconfined condition 192
9.1.2.2 Investigation in the confined condition 193
9.1.3 Summary and conclusions from the cyclic loading-unloading and strain rate tests 194
9.1.4 Summary and conclusions from fracture mechanical investigations 195
9.1.4.1 With varying temperatures 195
9.1.4.2 With varying strain rates 195

9.1.5 Summary and conclusions from the microstructural investigation 196
9.2 Recommendations for future work 197
Appendix 199
Appendix 1 The theoretical background for the strain-rate effect on the rock properties 199
Appendix 2 Energy-release rate 201
Appendix 3 Number of specimens used for various mechanical testing 203
References 204
Publications out of the research work 232
Other publications during the course of the research work 234
Acknowledgement 235

List of Figures

Figure 1.1 Announced or planned UCG test sites around the world (Lawrence Livermore National Laboratory 2012)..... 2
Figure 1.2 2015 installed geothermal capacity (Bertani 2015)..... 2
Figure 2.1 Schematic of underground coal gasification 10
Figure 2.2 Schematics of the types of UCG projects: (a) LVW, (b) steeply dipping coal seams, and (c) controlled retraction injection point (CRIP) (modified after Elahi, 2016) 11
Figure 2.3 Schematic of the long-tunnel large-section two-stage method (modified after Deng (2007))..... 12
Figure 2.4 Distribution of different types of coals and lignite in India (Indian Bureau of Mines, 2018) 13
Figure 2.5 Occurrence of Gondwana coal in different states of India (Indian Bureau of Mines, 2018) 14
Figure 2.6 Occurrence of tertiary coal and lignite in different states of India (Indian Bureau of Mines, 2018) 14
Figure 2.7 Comparison of the UCS of thermally treated sandstones..... 18
Figure 2.8 Comparison of the UCS of sandstones at high temperatures 19
Figure 2.9 A comparison of the tensile strength of different thermally treated sandstones 19
Figure 2.10 A comparison of the peak strain, tensile strength, and fracture toughness of sandstones at high temperatures..... 20
Figure 2.11 A comparison of the Young's modulus of thermally treated sandstones..... 20
Figure 2.12 A comparison of peak strain and Poisson's ratio of thermally treated sandstones 21
Figure 2.13 A comparison of the fracture toughness of thermally treated sandstones..... 22
Figure 2.14 Volumetric strain under various effective pressure and temperatures (Hassanzadegan et al., 2014) 24
Figure 2.15 Porosity and crack porosity variation under different pressures at different temperatures (Hassanzadegan et al., 2014)..... 25
Figure 2.16 Aspect ratio distribution for loading (a) and unloading (b) condition at different temperatures (Hassanzadegan et al., 2014)..... 25
Figure 2.17 A comparison of mass loss and density of different thermally treated sandstones 26
Figure 2.18 Comparison of P-wave velocity and porosity of various sandstones..... 26

Figure 2.19 A comparison of linear expansion and volumetric expansion of sandstones (Sirdesai et al., 2017a) 27
Figure 2.20 Influence of temperature and pressure on the permeability of sandstone (Guo et al. 2017) 29
Figure 3.1 Geological map of the studied rock type. The image on the left shows the geological map of Rajasthan, indicating the Jodhpur area 30
Figure 3.2 Lithostratigraphic succession of the Marwar Supergroup, western Rajasthan, representing the stratigraphy of Jodhpur sandstone (Pareek, 1984; Chauhan et al., 2004) 31
Figure 3.3 Petrographic micrographs of the sandstone at room temperature 32
Figure 3.4 XRD Analysis of the studied sandstone, indicating major mineral phases in the sandstone 32
Figure 3.5 High-temperature XRD analysis of the sandstone 33
Figure 3.6 EDS Analysis of the sandstone indicating the presence of dominant elemental phases in the sandstone 34
Figure 3.7 Grain-size analysis of the sandstone 34
Figure 3.8 Load versus displacement curve of the nanoindentation analysis used for the measurement of hardness of the studied sandstone 35
Figure 3.9 Geological map of the sedimentary rocks that have been used for comparison in the current study. The map at the top left represents the geological map of Rajasthan, India and indicates the location of Dholpur sandstone (a); the map at the top right represents the geological map of Jharkhand, India, and indicates the location of Gondwana sandstone (b); the map at the bottom left represents the geological map of Madhya Pradesh, India, and indicates the location of Jhiri shale (c); the map at the bottom right represents the geological map of Odisha, India, and indicates the location of Manoharpur sandstone (d) 38
Figure 3.10 XRD analysis, indicating the presence of different mineral phases within the different rock types that are used for comparison in the study. ‘a’ represents Dholpur sandstone; ‘b’ represents Gondwana sandstone; ‘c’ represents Manoharpur sandstone; and ‘d’ represents Jhiri shale. 39
Figure 3.11 Stratigraphic cuccession of the Vindhyan Supergroup, representing the stratigraphy of Dholpur sandstone (After Bhattacharya, 1996; Valdiya, 2016) 37
Figure 3.12 Stratigraphic of the Gondwana succession in the Damodar Basin, representing the stratigraphy of Gondwana sandstone (Valdiya, 2016) 40
Figure 3.13 Micrographic thin section images of Jhiri shale, which indicate a significant presence of minerals such as quartz and goethite in the rock 41

Figure 3.14 Prepared cylindrical specimens for the UCS test that is 51 mm in diameter and 102 mm in length 42
Figure 3.15 Prepared disc specimens for the indirect tensile test that is 51 mm in diameter and 25 mm in width 43
Figure 3.16 Face grinding of the specimens prior to testing (a). The furnace used for the thermal treatment (b), along with the heating process (c) 43
Figure 3.17 Structural damages induced in Jodhpur sandstone at 950 °C and 1000 °C for both rapidly cooled and thermally treated specimens 44
Figure 3.18 Schematic diagram of the workflow that was followed in the current investigation 44
Figure 4.1 Colour change in thermally treated sandstone specimens 46
Figure 4.2 Colour change in rapid-cooled sandstone specimens 46
Figure 4.3 Petrographic thin-section images of thermally treated Jodhpur sandstone 47
Figure 4.4 Petrographic thin-section images of rapid-cooled Jodhpur sandstone 47
Figure 4.5 Petrographic thin-section magnified images of Jodhpur sandstone at TT_600 °C, TT_800 °C, and RC_800 °C 48
Figure 4.6 SEM images of the sandstone at different temperatures 49
Figure 4.7 Experimental setup used for the measurement of the P-wave velocity of the sandstone 50
Figure 4.8 Variation of P-wave velocities of Jodhpur sandstone in both thermally tretaed and rapid-cooled specimens 51
Figure 4.9 Thermal expansion of the sandstone at a high temperature and after cooling to room temperature 52
Figure 4.10 Variation of mass loss of Jodhpur sandstone after exposure to high temperatures 54
Figure 4.11 Perkin Elmer Diamond thermogravimetric/differential thermal analyser 55
Figure 4.12 Thermogravimetric Analysis of the studied sandstone 55
Figure 4.13 Prearrangement of thermally tretaed and rapid cooling specimens prior to the mechanical testing 57
Figure 4.14 Experimental setup for the measurement of UCS and tensile strength (a) for the thermally treated and rapid cooled specimens. The AE setup that is used for the measuring of acoustic events (b) and a failed specimen after the UCS test (c) 57
Figure 4.15 Experimental setup for the measurement of UCS and tensile strength at high temperature condition 58

Figure 4.16 Schematic diagram of the simple AE waveform (Eberhardt et al. 1998)..... 59
Figure 4.17 ARAMIS setup and the calibration panel used prior to the measurement (modified after Hu et al., (2015))..... 60
Figure 4.18 Processed-ARAMIS images, indicating the developed strain in thermally treated specimens (25 °C – 400 °C)..... 62
Figure 4.19 Processed-ARAMIS images, indicating the developed strain in thermally treated specimens (500 °C – 600 °C)..... 63
Figure 4.20 Processed-ARAMIS images, indicating the developed strain in rapidly cooled specimens (25 °C – 400 °C)..... 64
Figure 4.21 Processed-ARAMIS images, indicating the developed strain in rapid cooled specimens (500 °C – 900 °C)..... 65
Figure 4.22 Stress-strain curves of thermally treated specimens, at different temperatures ... 66
Figure 4.23 Stress-strain curves of rapid cooled specimens, at different temperatures..... 66
Figure 4.24 High-temperature stress-strain curves of the studied sandstone..... 67
Figure 4.25 Variation of UCS of the sandstone as a function of temperature 67
Figure 4.26 Variation of tensile strength of the sandstone as a function of temperature 69
Figure 4.27 Variation of Elastic modulus and failure strain of the sandstone for different thermally treated specimens..... 70
Figure 4.28 Variation of Elastic modulus and failure strain of the sandstone for different thermally treated and rapid cooled specimens 70
Figure 4.29 Variation of damage factor as a function of increasing temperature..... 72
Figure 4.30 Variation of Poisson's Ratio of the sandstone as a function of temperature..... 72
Figure 4.31 Correlation of AE events with the UCS and the axial strain for thermally treated specimens..... 74
Figure 4.32 Correlation of AE events with the UCS and the axial strain for rapid cooled specimens..... 75
Figure 4.33 Variation of different stress thresholds and the stress threshold ratio as a suction of temperatures..... 77
Figure 4.34 Comparisons of different mechanical properties of different sandstones along with the sandstone used in the current study. Figures 22a, 22b, 22c and 22d represent the comparison of UCS, elastic modulus, tensile strength and peak strength of various sandstones, respectively 79
Figure 5.1 Schematic of the different cyclic loading-unloading patterns follwed in the experiment..... 82

Figure 5.2 Axial stress versus time curves of Jodhpur sandstone in multiple cycles at different stress levels of the peak load 85
Figure 5.3 Normalised cumulative AE counts of Jodhpur sandstone in multiple cycles at different stress levels of the peak load 86
Figure 5.4 Axial stress versus time curves of Jodhpur sandstone in incremental stress cycles at different stress levels of the peak load 88
Figure 5.5 Normalised cumulative AE counts of Jodhpur sandstone in incremental stress cycles at different stress levels of the peak load 88
Figure 5.6 Axial stress versus time curves of Jodhpur sandstone in incremental stress cycles based on acoustic characteristics 89
Figure 5.7 Normalised cumulative AE counts of Jodhpur sandstone in incremental stress cycles based on acoustic characteristics 89
Figure 5.8 Felicity ratio for the sandstone tested with incremental stress cycles based on certain percentages of the peak load 90
Figure 5.9 Felicity ratio for the sandstone tested with incremental stress cycles based on acoustic characteristics 91
Figure 5.10 Stress-strain curve of the rock at different strain rates (a). Fractured samples after compression test at different strain rates (b). Fractured samples recovered after Brazilian tensile tests at different strain rates (c) 96
Figure 5.11 SEM micrographs of the studied rock representing the pore spaces, different types of granular fractures and the presence of clay minerals in the rock (Mahanta et al. 2017b) ... 98
Figure 5.12 Variation of UCS (a), tensile strength (b), Young's modulus, (c) and failure strain (d) with strain rates 99
Figure 5.13 Variation of mode I fracture toughness (a), mode II fracture toughness (b), brittleness index B_1 (c) and brittleness index B_2 (d) with strain rates 100
Figure 5.14 Correlation between measured fracture toughness and brittleness index of the rock 102
Figure 5.15 Comparison of uniaxial compressive strength of various rocks with strain rates 102
Figure 5.16 Comparison of tensile strength of various rocks with strain rates 103
Figure 6.1 Specimen geometry and loading configuration for the CSTSCB specimen 106
Figure 6.2 Petrographic thin section of rock types, of which, all others except for 'f' are taken under the crossed polarised light. 'a', 'b', 'c' and 'd' represent Manoharpur sandstone at

150 °C, 450 °C 550 °C and 600 °C, respectively. ‘‘j’, ‘k’, ‘l’ and ‘h’ represent Dholpur sandstone at 150 °C, 450 °C, 550 °C and 600 °C, respectively 109
Figure 6.3 SEM images of the three types of rock at different temperatures that show the development of micro-fractures within the rocks as a function of temperature increment. ‘a’ and ‘b’ represent Manoharpur sandstone; and ‘c’ and ‘d’ represent Dholpur sandstone 108
Figure 6.4 Load and displacement curves for all the rocks at various temperature where ‘a’ and ‘b’ represent Manoharpur sandstone and Dholpur sandstone, respectively 111
Figure 6.5 Weight loss in different rocks as a function of elevated temperature, compared to room temperature 111
Figure 6.6 Comparison of the change in porosity in different rocks at room temperature and after treatment at 600 °C 112
Figure 6.7 Change in physical appearance of sample specimens after thermal treatment at different temperatures 112
Figure 6.8 Fracture toughness vs tensile strength of three different rocks at ambient condition 114
Figure 6.9 Variation of fracture toughness in the rocks with elevated temperature, of which, ‘a’ represents Manoharpur sandstone and, b represents Dholpur sandstone, respectively 118
Figure 6.10 Comparison of the effect of thermal temperature on measured mode-I fracture toughness of various rocks (adapted after Al-Shayea et al., 2000; Funatsu et al., 2004; Whittaker et al., 1992) 118
Figure 6.11 Schematic diagram of the preparation of the SCB specimens 122
Figure 6.12 Loading configuration of the semicircular bending specimen 123
Figure 6.13 Normalised stress intensity factors Y_I and Y_{II} (modified after Lim et al. (1993)) 125
Figure 6.14 Schematic diagram of applied load and the displacement 126
Figure 6.15 Shale specimens of different notch angles (a: 0°, b: 15°, c: 30°, d: 40°) 126
Figure 6.16 Load versus displacements curves for different strain rates 127
Figure 6.17 Strain rate and applied load with different modes: 0° for mode I; 15° and 30° for mixed mode; and 40° for mode II 128
Figure 6.18 Variation of effective fracture toughness in response to increasing strain rates 129
Figure 6.19 Fracture toughness for different modes with different notch angles at the variable strain 131
Figure 6.20 Total energy-release rates at different strain rates 132

Figure 6.21 A comparison between the applied energy and the energy-release rates for different modes, including mode I, mixed mode (I/II) and mode II. S1, S2, S3 and S4 represent the strain rates at which those specimens were loaded 133
Figure 6.22 Schematic diagram of the FBD specimens (left) and load-displacement curve (right) 136
Figure 6.23 FBD specimens with required loading angles (a, b, c) and failed specimens (d, e) 137
Figure 6.24 A correlation between mode I fracture toughness and strain rates (left). Comparison between the tensile strength measured through complete Brazilian disc specimens and flattened Brazilian disc specimens 140
Figure 7.1 Cylindrical specimens that are 22.5 mm in diameter and 45 mm in height 141
Figure 7.2 Experimental setup indicating different components of the high-temperature and high-pressure loading system 143
Figure 7.3 Experimentally failed sandstone specimens, indicating the developed shear bands 144
Figure 7.4 Stress-strain curves of sandstone at different temperatures 144
Figure 7.5 Variation in the deviatoric stress of sandstone at different temperatures and different confinements 145
Figure 7.6 Variation in the deviatoric stress of sandstone at different confinements and different temperatures 145
Figure 7.7 Mohr–Coulumb failure envelope of the sandstone at different temperatures 146
Figure 7.8 Variation of cohesion and friction angles of the sandstone at different temperatures 147
Figure 7.9 Visible shear bands on the surface of the specimen (30 MPa, 100 °C) 148
Figure 7.10 Developed shear bands in the micro-CT images of the sandstone (30 MPa and 100 °C) 149
Figure 7.11 Greyscale micro-CT images and processed images of the inside shear zone and the outside shear zone of specimens tested at different confinements and temperatures 151
Figure 7.12 Frequency distribution of grain matrix at different confinements and temperatures 152
Figure 7.13 Comparison of the porosities inside the shear zone and outside the shear zone at different temperatures (a), difference between the porosities of the two zones (b) 153
Figure 8.1 The Xradia Versa 520 instrument used for image acquisition, and its principle (modified after Zeiss TM 2013) 160

Figure 8.2 Schematic diagram of the volume used in the current study 161
Figure 8.3 Schematic diagram illustrating the workflow used for the analysis 161
Figure 8.4 A comparison of microstructural modification in Dholpur sandstone at an ambient condition (25 °C) and after being exposed to elevated temperatures (200 °C, 400 °C, 600 °C and 800 °C) 165
Figure 8.5 A comparison of microstructural modification in Jodhpur sandstone at an ambient condition (25 °C) and after being exposed to elevated temperatures (200 °C, 400 °C, 600 °C and 800 °C) 166
Figure 8.6 A comparison of microstructural modification in Gondwana sandstone at an ambient condition (25 °C) and after being exposed to elevated temperatures (200 °C, 400 °C, 600 °C and 800 °C) 167
Figure 8.7 A comparison of pore-space evolution in Dholpur sandstone at room temperature (25 °C) and after the thermal treatment (200 °C, 400 °C, 600 °C and 800 °C) 168
Figure 8.8 Average porosity and porosity profiles of the three coordinate directions for Dholpur sandstone. Plate a, plate b, plate c, plate d and plate e represent 25 °C, 200 °C, 400 °C, 600 °C and 800 °C, respectively. Plate f represents the comparison of the total porosity, connected pore spaces, and non-connected pore spaces of Dholpur sandstone at different temperatures 169
Figure 8.9 TG-DTA curve for Dholpur sandstone 170
Figure 8.10 A comparison of pore-space evolution in Jodhpur sandstone at room temperature (25 °C) and after the thermal treatment (200 °C, 400 °C, 600 °C and 800 °C) 171
Figure 8.11 Average porosity and porosity profile of the three coordinate directions for Jodhpur sandstone. Plate a, plate b, plate c, plate d and plate e represent 25 °C, 200 °C, 400 °C, 600 °C and 800 °C, respectively. Plate f represents the comparison of total porosity, connected pore spaces, and non-connected pore spaces of Jodhpur sandstone at different temperatures 172
Figure 8.12 A comparison of pore-space evolution in Gondwana sandstone at room temperature (25 °C) and after thermal treatment (200 °C, 400 °C, 600 °C and 800 °C) 173
Figure 8.13 Average porosity and porosity profiles of the three coordinate directions for Gondwana sandstone. Plate a, plate b, plate c, plate d and plate e represent 25 °C, 200 °C, 400 °C, 600 °C and 800 °C, respectively. Plate f represents the comparison of total porosity, connected pore spaces, and non-connected pore spaces of Gondwana sandstone at different temperatures 174
Figure 8.14 A comparison of porosity (a) and the ratio of non-connected pores to connected pores (b) in three sandstones after thermal treatment 175
Figure 8.15 TG-DTA curve for Gondwana sandstone 176

Figure 8.16 A comparison of the Thermogravimetric analyses of the three sandstones 176
Figure 8.17 Comparison of the PNM of Dholpur sandstone at 25 °C, 200 °C, 400 °C, 600 °C and 800 °C (white represents the value beyond the values used for the legend) 178
Figure 8.18 Comparison of pore-network attributes of Dholpur sandstone at different temperatures 179
Figure 8.19 Comparison of the PNM of Jodhpur sandstone at 25 °C, 200 °C, 400 °C, 600 °C and 800 °C (white represents the value beyond the values used for the legend) 180
Figure 8.20 Comparison of pore-network attributes of Jodhpur sandstone at different temperatures 181
Figure 8.21 Comparison of the PNM of Gondwana sandstone at 25 °C, 200 °C, 400 °C, 600 °C and 800 °C (white represents the value beyond the values used for the legend) 182
Figure 8.22 Comparison of pore-network attributes of Gondwana sandstone at different temperatures 183
Figure 8.23 Studied volume for the analysis of progressive deformation of sandstone 185
Figure 8.24 A comparison of pore-space evolution at different stress levels 186
Figure 8.25 A comparison of total porosity, connected pore spaces, and non-connected pore spaces at different stress levels 187
Figure 8.26 Comparison of the PNM at different stress levels 188
Figure 8.27 Comparison of pore-network attributes at different stress levels 189
Figure 8.28 Maximum values of various pore attributes at different stages of loading 191
Figure 8.29 Maximum values of various throat attributes at different stages of loading 191

List of Tables

Table 2.1 Coal blocks allotted to major Indian PSUs for UCG development (Singan and Ranade, 2017) 15
Table 3.1 Elemental distribution in the studied sandstone 33
Table 3.2 Results of the nanoindentation hardness test of the sandstone 36
Table 3.3 Geomechanical properties of the rocks used for comparison 37
Table 3.4 Dominant mineral phases in the three sandstones (figure 3.10) 41
Table 4.1 Thermal expansion of rock-forming minerals in different crystallographic axes (Skinner 1966; Somerton 1992) 68
Table 4.2 Chemical reaction of various minerals as a result of heating 69
Table 4.3 various stress threshold values of thermally treated sandstone at different temperatures 76
Table 4.4 Summary of the reviewed sandstones along with the sandstone used in the current investigation 78
Table 5.1 Normalised cumulative AE counts at different stages of applied stress in multiple cycles 87
Table 5.2 Experimentally determined average geomechanical properties of the rock 95
Table 5.3 Regression analysis for independent variable and dependent variables 101
Table 6.1 Recommended geometrical dimensions of SCB specimen (Kuruppu et al. 2014) 107
Table 6.2 Fracture toughness values of Manoharpur sandstone at different temperatures that range between ambient and 600 °C 113
Table 6.3 Fracture toughness values of Dholpur sandstone at different temperatures that range between ambient and 600 °C 113
Table 6.4 Mode I and mode II fracture toughness along with the effective fracture toughness in different notch angles at different strain rates 130
Table 6.5 Mode I and mode II energy-release rates along with the total energy rates in different notch angles at different strain rates. In the sample names, S1, S2, S3, and S4 represent the strain rates at which those specimens were loaded 131
Table 6.6 Maximum load (P_{max}) and local minimum load (P_{min}) with different strain rates . 139
Table 8.1 Parameters used for micro-CT scanning 159
Table 8.2 Summary of pore spaces and their evolution with the elevated temperatures for the three sandstones 174

Table 8.3 Various Pore-network attributes as a function of temperatures in three sandstones 184
Table 8.4 Statistical distribution of pore-network attributes at different stress levels..... 189

Chapter 1 Introduction

1.1 Clean energy and its importance in the current scenario

At present, the consumed global energy comprises oil (36 per cent), coal (28 per cent), natural gas (24 per cent), and renewable energy (7 per cent), which includes hydro, solar, and nuclear (6 per cent) energies. Most of the petroleum reserves are distributed unevenly in the world: the Middle East comprises 63 per cent of the total global reserves and holds the position of dominant supplier to various countries. After petroleum, coal is the second largest energy commodity worldwide. Coal contributes to over 30 per cent of the world's primary energy consumption; more than 40 per cent of the electricity production worldwide comes from coal consumption in thermal power plants. Unfortunately, petroleum oil is in danger of being in short supply in the near future (Demirbas, 2016). In the 21st century, the problem of increasing CO_2 emission during the production of electricity from coal needs to be addressed, while also ensuring access to energy. Technological improvements in all aspects of extraction need to be implemented for coal to remain competitive when compared to other energy sources in developed and developing countries of the world (AAPG Energy Minerals Division, 2015). Since India is a developing country, rising economic growth demands additional energy sources. As a first step towards development, coal is being used as the primary source of energy because it is found in abundance and is easier to extract than any other source of energy. India ranks third in coal production, and most of its energy demands are being fulfilled by coal. However, while using these conventional sources of energy, various environmental issues need to be addressed. In such scenarios, the future trend for energy supply is moving towards various alternative or unconventional energy sources. Some of the unconventional sources of energy are underground coal gasification (UCG), shale gas, geothermal energy, and coal bed methane.

UCG is the process of converting deep-seated coal into usable syngas. During UCG, the injection and the producing wells are linked, which is followed by the injection of air/oxygen/mixture of air and oxygen and steam. The coal is then ignited in situ, which converts it into useful syngas that is a mixture of hydrogen, methane, carbon dioxide, and carbon monoxide. **Figure 1.1** shows the status of global UCG in different counties across the world; the green circle represents sites that have been tested previously, and the yellow circles represent the sites that have been planned or identified for the development of UCG.

Geothermal energy contributes to the global energy demand through electric power production, thermal reservoirs for heat pump, and for direct heating and cooling; of these, electric power

production is mostly associated with geothermal energy extraction. **Figure 1.2** shows the development of geothermal energy in different countries; the portions marked with red, orange and yellow represent the installed geothermal energy in the ranges, > 500 MW, 100 – 500 MW and < 100 MW, respectively.

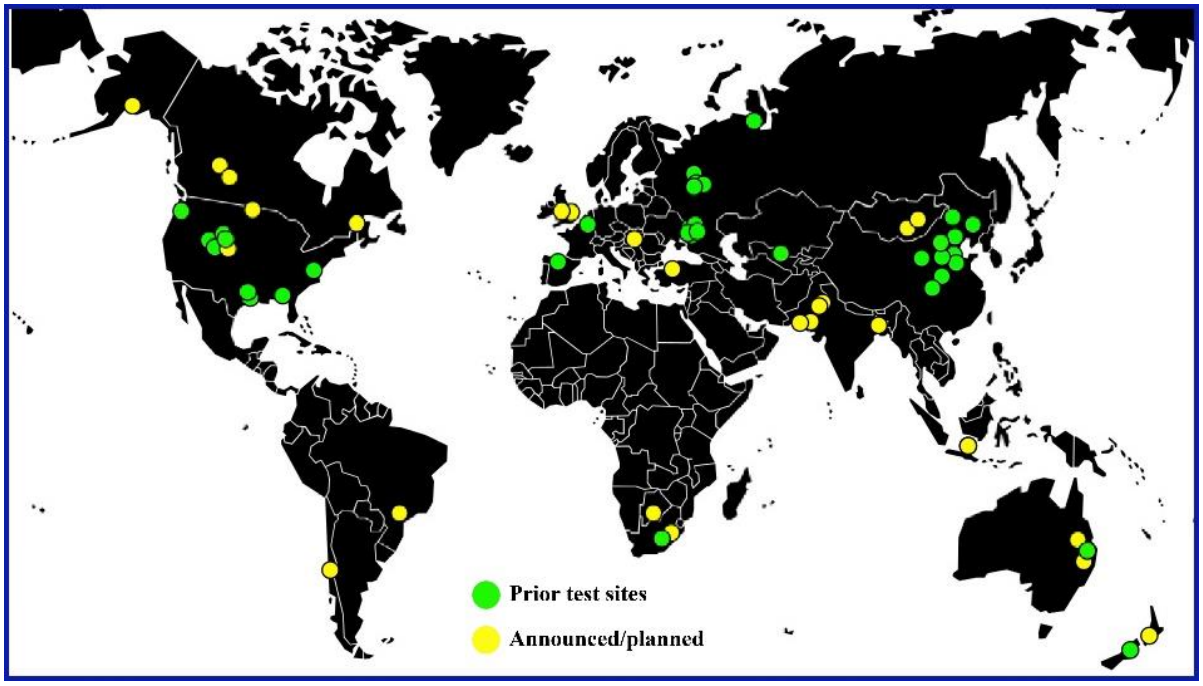

Figure 1.1 *Announced or planned UCG test sites around the world* (Lawrence Livermore National Laboratory, 2012)

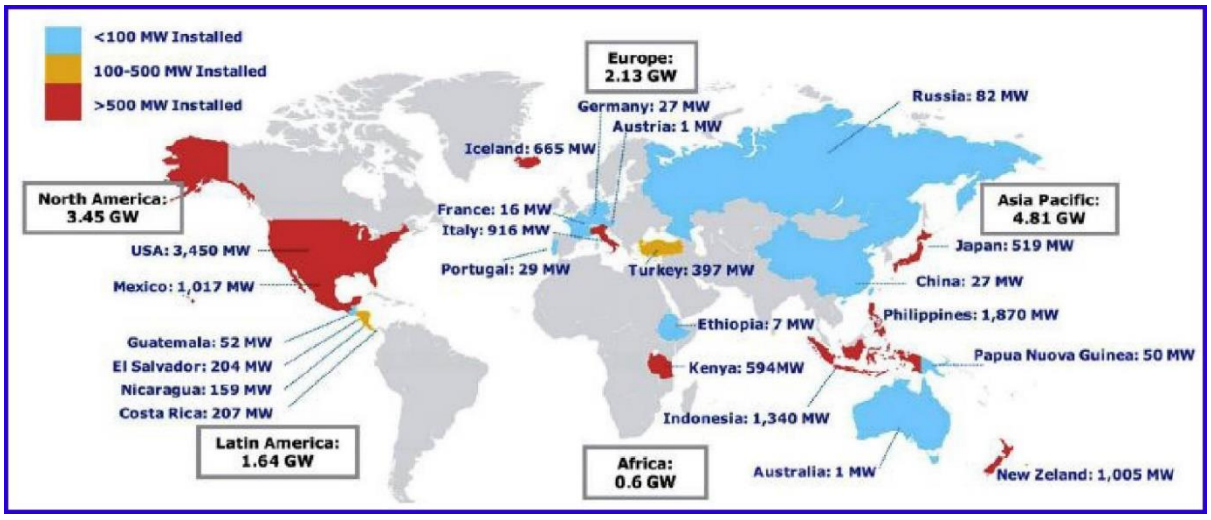

Figure 1.2 *2015 installed geothermal capacity* (Bertani, 2015)

Since organic-rich shale is a source rock in the generation of petroleum, it is considered an important component in the petroleum industry. Previous research indicates the presence of sufficient hydrocarbons in mudrocks that can be commercially developed by using advanced drilling and improved technology. However, thus far, a significant amount of petroleum has

been produced from shale or tight oil reservoirs in North America due to the improvements in multistage hydraulic fracturing and directional drilling (AAPG Energy Minerals Division, 2015).

The methane gas entrapped in the structure of coal is called coal bed methane (CBM). Not only does the coal combustion introduce various greenhouse gases (GHGs) into the atmosphere, during coal mining, the CBM is also released to the atmosphere. Capture of this entrapped gas from coal can prove to be a source of power production, which will then meet energy demands. CBM can be used domestically as a natural gas; it can also be used in the production of electricity in power plants (Prabu and Mallick, 2015). Out of the various sink sites for CO_2 sequestration, coalbeds are preferred over other sites because CO_2 is stored in the coal surface as an adsorbed phase, thereby enhancing desorption of CH_4. In addition to the sources of unconventional energy mentioned above, nuclear energy can prove a vital source in the mitigation of the modern energy demands. The cost of producing electricity in nuclear power plants by using nuclear fuel is not very small when compared to the total costs of the production of electricity through other energy sources.

In an Indian scenario, all the sources of unconventional energy techniques mentioned above are less explored. Various types of research and development are required for the successful implementation and development of new energy-engineering projects. With modernisation, the rapid growths in population and urbanisation have increased energy demands. To meet the energy, unconventional sources of energy, such as UCG need to be investigated.

1.2 Application of high-temperature rock behaviours

All the unconventional sources of energy mentioned above are associated with moderate-to-high temperatures during the course of their production phase, which involves various engineering applications as listed below:

- Wellbore stability

During the drilling of a wellbore, the differential temperatures at the top and bottom cause variations in stress distribution. The extent of the drilling-induced yielded zone around the wellbore is dependent on temperature changes in which heating enlarges the yielded zone and cooling reduces it.

- Water flooding and CO_2 storage

Water flooding, which is the injection of water into the reservoirs, is a secondary recovery method that is used in oil production. The process lasts for more than a month and, sometimes, even for a year. The thermal mismatch between the injecting fluid and the reservoirs can make substantial alterations in the reservoirs rocks, resulting in an improvement in the injectivity of water.

The process of carbon capture and storage involves injection of low-temperature CO_2 into the heated reservoir rocks that result in a reduction in the confining stress that facilitates fracturing. The low temperature associated with the injected CO_2 changes the stress condition at the lower part of the caprock that leads to its shear or tensile failure.

- Hydraulic fracturing

During hydraulic fracturing, cooling facilitates the formation and coalescence of the fracture, whereas heating inhibits it. However, controlled fracture propagation, delay in fracture-initiation and closure of fracture are achieved by using warm water. Additionally, the temperature change is responsible for the adjustment of the orientation of hydraulic fractures.

- Enhanced oil recovery (EOR) and hot fluid injection

Thermal EOR is associated with cyclic injection of steam. Steam flooding and in situ combustions, which bring different degrees of alterations to the formation rocks and modify the viscosity of the oil, facilitate the easy flowage through the reservoirs, which results in a better rate of production. Such a repetition of injection of steam and in situ combustion changes the properties of the surrounding rocks.

- Nuclear waste disposal

At the disposal sites, radiations from the nuclear waste increase the borehole temperature, which causes the rocks and the pore water to expand. It may also increase the probability of producing thermal cracks and eventually rock failure.

- Geothermal energy extraction

The process involves repeated circulation of cold water into the hot reservoirs to extract the heat that is present in the reservoirs in the form of steam or warm water. The thermal mismatch between the temperature of the circulating fluid and the reservoirs weakens the surrounding rocks and the effect is even more pronounced due to the circulating of the fluids being repeated.

- UCG

UCG is one of the most suitable of methods to extract deep-seated unmineable coals. However, many safety concerns such as the effects of temperature on the surrounding rocks of coal seams impede the successful implementation of such projects. During the combustion of UCG, the temperature ranges from 1000 °C to 1200 °C, and under the influence of such high temperatures, the physical, mechanical and hydrological properties of the associated rocks are altered; this, sometimes, results in subsidence of the surface, underground water contamination and product gas leakage.

1.3 Motivation

When compared to the various sources of unconventional energies, highest level of temperature is observed in the case of UCG, in which the temperature ranges from 1000 °C to 1200 °C at the ignition point of the gasifier. Subsequently, the surrounding rocks are exposed to high temperatures. In most cases of UCG, the surrounding associated rocks are sandstones. Additionally, in the Indian context, an extensive analysis of sandstone is lacking in the literature. These are important factors, for which sandstone was chosen for the current investigation. Although, all of the applications mentioned above require knowledge of the high-temperature behaviour of rocks, all experimental investigations and this entire research work is predominantly inclined towards understanding rock responses at high temperatures.

1.3.1 Rock mechanical aspects of UCG

At greater depths, due to the influence of temperatures, the engineering applications mentioned above make various changes to the stress field and to the pore pressure in the surrounding and overburden rocks. The application of rock mechanics is quite important for the development and stability of the extending cavity under high temperatures and pressure conditions. The various rock mechanical aspects that are associated with these applications are (1) borehole stability, (2) cavity development, (3) damage induced to overlying strata and (4) surface subsidence due to the failure of the overburden.

During UCG, cavity development and cavity filling are the main aspects. Cavity and borehole stability are predominantly dependent on the rock deformation at high temperatures. Cavity development induces fractures in the overlying strata and reduces the pore fluid pressure, which leads to surface subsidence and formation damage. During UCG, for successful and extended lateral development, there must be a balance between the consumption of coal and rock failure. The heat that is produced due to gasification leads to a temperature of about 1000 °C at the wall of the cavity, which gradually reduces towards the surrounding rocks where the maximum

temperature lies between 800 °C and 900 °C. In comparison to the atmospheric pressure, the gas pressure within the gasifier cavity is high, and as long as the injection pressure (<five MPa) is lower than the overburden pressure (~20 MPa); the effect of injection pressure is insignificant. The heat that is generated due to the UCG alters the temperatures in the surrounding rocks over time and space. The cavity walls are confined by the surrounding wall, and the expansion due to the exposure to high temperatures causes thermally induced stress. The various changes during UCG operation (1) rock mechanical properties such as strength parameters, elasticity, plasticity; (2) rock creep at certain rates; (3) development of thermally induced stresses and (4) increase in pore pressure due to heated water and steam.

1.3.2 Hydrogeological aspects of UCG

Good flow/hydrological characteristics of rocks drives the process forward in applications such as geothermal energy extraction, enhanced oil recovery and hot fluid injection, hydraulic fracturing, and water flooding and enhanced coalbed methane (ECBM), whereas enhancement in the permeability of the rocks during processes such as the UCG and nuclear waste disposal drives the process backward.

Impermeable overlying and underlying strata with very little porosity and deformability are suitable for UCG because the strata act as a barrier between the coal seam and the surrounding aquifer, and limit the degree of subsidence due to their low deformability. For disposal of nuclear wastes, formations that have low hydraulic conductivity and low porosity, such as granites and soft clay formations are preferred. During UCG, to avoid contamination of the groundwater, the presence of a fresh water aquifer in the surrounding area of the UCG site is not desirable. During gasification, the groundwater contamination occurs due to the escape of hot product gases through the cracks and fissures in the surrounding rocks. Hence, the porosity and permeability of the surrounding rock as a function of temperature is quite important. Additionally, the groundwater contamination can be a result of the post-burn leaching when the burnt coal-ash is exposed to water. However, sometimes, the gasification cavity collapses, resulting in a direct connection between the coal and the surrounding aquifer (Mohanty, 2017). In such a situation, the surrounding overlying and underlying rocks cool rapidly under the influence of the water ingress. This rapid cooling of the overburden rocks may result in drastic reduction in the strength parameters of the rocks and may induce surface subsidence. High pressure within the gasification chamber prevents the ingress of water into it. However, with depth, pressure increases, and the overburden permeability facilitates the movement of the enhanced product gases to the surrounding aquifers, which causes groundwater contamination.

The main hydrogeological aspects of the UCG projects are (1) rapid cooling or quenching of the strength of the surrounding rocks, and (2) variation in the porosity and permeability of surrounding rocks as a function of temperatures.

In such engineering applications, different levels of structural damages are developed in the associated rocks due to their exposure to high temperatures. Such structural damages vary from macro to micro levels. The successful implementation of engineering projects that involve such applications requires mechanical characterisation of the associated rocks.

1.4 Objective and approach

During underground coal gasification, geothermal energy extraction, and nuclear waste disposal, the surrounding rocks are exposed to a high temperature, which alters the mechanical and flow properties of the rocks. Periodic heavy spilling or rapid influx of water due to the intersection of a fracture results in rapid cooling and quenching of the rock. During UCG, the temperature rises to approximately 1000 °C, which creates a thermal stress in the associated rocks. In addition, as the gasification process continues, there will be a gradual loss of coal mass at the site of the UCG, which creates a variation in the stress condition of the surrounding rocks. Major stress change occurs due to gasification-induced excavation (the internal pressure in the gasification cavity and the induced stress due to the opening of the cavity) and a high temperature. High temperatures result in decomposition of the clay minerals, widening of cracks that are already present and generation of a few new cracks. In response to these modifications, the porosity and the permeability of the rocks are altered. Various organic compounds are created during UCG and are deposited at the edge of the cavity; this cavity needs to be kept away from groundwater. The high temperatures and pressures of such a process result in the enhancement of the hydrological properties in the surrounding rocks. This alteration of the hydrological properties facilitates the leakage of these organic compounds to the nearby aquifers.

Four main objectives were finalised for the current research work by considering all aspects (mentioned above) of rocks behaviour due to high temperatures. The main objectives of the work are as follows:

1. Assessment of the influence of high temperature on various physico-morphological and thermomechanical behaviours of sandstones in unconfined and confined conditions.
2. Investigation of the effect of the cyclic loading unloading and strain rates on rocks.

3. Investigation of fracture mechanical attributes as a function of high temperatures and the strain rates.
4. Investigation of microstructural modifications due to the influence of high temperatures.

The first objective describes the influence of temperature on various physical and mechanical strength parameters of rocks in both an unconfined condition and in situ high-temperature and high-pressure triaxial conditions. The strength parameters include compressive strength, Brazilian tensile strength, Young's modulus, Poisson's ratio, cohesion, angle of internal friction and damage factors. The second objective describes the behaviour of post high-temperature sandstone in response to loading and unloading cycles. In addition, the second objective illustrates the effect of the loading rate on the mechanical attributes of rocks. The third objective of the research work deals with the assessment of fracture mechanical attributes such as the fracture toughness and the energy-release rate in response to high temperatures and the strain rates. The fourth and final objective of the research work assesses microstructural modifications in response to high temperatures. Microstructural observations are made by using micro-CT techniques. The various pore-network attributes are assessed by using the technique to better visualise the effect of thermal treatment on the microstructure of sandstone. Additionally, the final objective describes the comparison of the pore-network modelling of sandstones after being exposed to high temperatures.

The outcome of the research work can also be useful to the other areas of research such as (1) geothermal energy extraction, (2) formation damage due to steam soak-enhanced oil recovery, (3) compactions due to production in hot reservoirs, (4) enhanced oil recovery by in situ combustion, (4) thermal drilling in sediments and (5) high-temperature resistance of concrete.

1.5 Structure of the thesis

- Chapter 2 includes existing literature. The various research works that are focused on the investigating of the mechanical and physical properties of sandstones have been incorporated into this chapter.
- Chapter 3 describes the rock type that is used in the research work, and its general geology; also indicated the geographical occurrences and the stratigraphy of the rock. In addition, it includes the preliminary material characterisation of the studied sandstone, which includes the x-ray diffraction (XRD) analysis, energy dispersive x-ray spectroscopy (EDS) analysis, grain-size analysis, and hardness test.

- Chapter 4 contains the experimental results of various physical and mechanical properties of thermally treated sandstone, rapid-cooled sandstone and sandstone under high temperatures. The degree of damage that is caused by the effects of the temperature is quantified. Additionally, this chapter includes the results of the various physico-morphological and thermomechanical properties of the rock as a function of temperatures.
- Chapter 5 includes results of the effect of different loading-unloading cycles and the strain rates on the strength parameters of rocks. Three types of loading-unloading cycles were used for a better assessment of the effect. In the first type, the thermally treated specimens are loaded up to a certain stress level and are maintained for a time span of five minutes, which is followed by their unloading; the same cycle was repeated five times. In the second type, the load is being increased with every cycle until the failure of the thermally treated specimen. In the third type, the cycles were based on the acoustic characteristics of the specimens. The samples are cyclically loaded up to crack-initiation stress, thereby a loading up to the crack damage stress followed by the crushing of the specimen. The second part of the chapter includes the mechanical behaviour of rocks under varying strain rates.
- Chapter 6 includes results of the fracture mechanical attributes in response to varying temperatures and strain rates. The assessment of mechanical attributes includes the measurement of the fracture toughness and the energy-release rate of the rocks.
- Chapter 7 includes results of the high-temperature, high-pressure behaviour of the rock. The highest temperature and pressure achieved during the experiment are 300 °C and 60 MPa, respectively. After the axisymmetric triaxial testing of the specimens, the failed samples were analysed to observe the grain boundary characteristics, which would afford better insight into the shear failure and shear bands that form at different confinements.
- Chapter 8 includes the results of the microstructural modification that occurred due to the influence of high temperatures. The various aspects that are estimated in the chapter are pore-space evolution, and pore-network modelling of rock in response to high temperatures. Micro-CT, which was carried out with the help of image analysing software AVIZO, was implemented for the assessment of the rock mechanical attributes mentioned above.
- Chapter 9 summarises the research work, which is followed by important conclusions that are drawn based on the experimental results. Additionally, the chapter includes recommendations for future work.

Chapter 2 Review of literature

2.1 Underground Coal Gasification

In order to avoid the emission of toxic gases into the atmosphere as a result of the burning of fossil fuels, various studies are being carried out to establish clean coal technologies; these studies include UCG, oxyfuel combustion, SOx and NOx reduction in boilers, and chemical looping combustion (Prabu and Mallick, 2015). The worldwide reserves of coal seam gas are estimated at 256 trillion m^3, which is considered to be a major source of energy (Hamawand et al., 2013). For the first time, in 1868, a German scientist, Sir William Siemens developed the idea of gasifying coal underground. However, at the same time, Russian scientist, Dmitri Mendeleev suggested his method to control and direct underground coal fires by using the drilling production and injection-well techniques. Subsequently, in 1909, Anson Betts received the first patent record for UCG (Elahi, 2016).

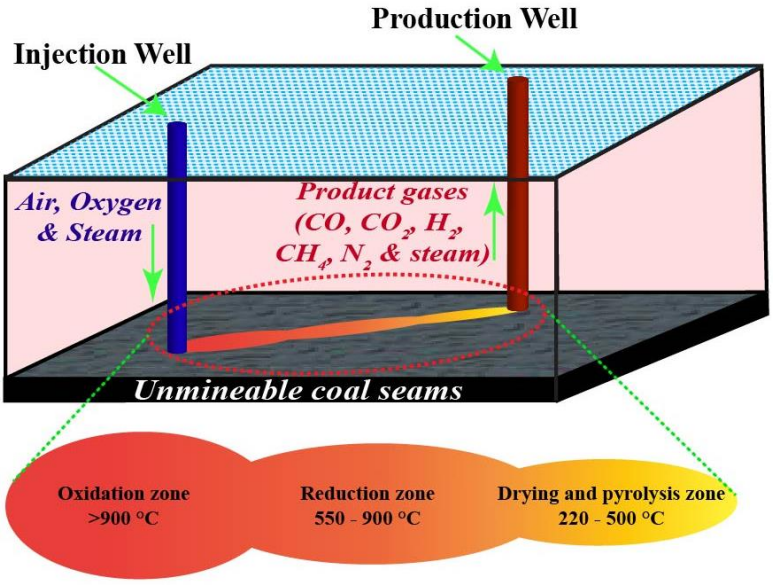

Figure 2.1 *Schematic of underground coal gasification*

Underground coal gasification is a technique that is used for the exploration of energy from unmineable coal seams that are either uneconomical to explore by conventional coal mining techniques or are inaccessible and lack of modern mining methods. The most effective approach for the utilisation of coal while also controlling pollution is underground coal gasification, in which coal is converted to product gases deep inside the earth (Jain, 2017; Blinderman and Klimenko, 2018). Oxygen, air, or a mixture of both is sent deep into the earth through an injection well to the unmineable coal seams, where the coal is gasified and converted to synthetic gas or syngas. Syngas is a mixture of flammable gases such as carbon

monoxide (CO), carbon dioxide (CO_2), methane (CH_4), hydrogen (H_2), nitrogen (N_2) and steam. Syngas can be used as fuel in heat and power generation, and as chemical feedstock for different chemical products (Elahi, 2016). The schematic of UCG is represented in **Figure 2.1**. The technique of UCG is clean and green in the generation of electricity from coal, with benefits such as a clean environment, low mining safety concerns and the ease of exploitation of low-grade coal resources (Khadse et al., 2007; Bhutto et al., 2013; Akanksha et al., 2017).

2.1.1 Methods of UCG implementation

Broadly, the methods of UCG projects can be classified into three categories:

- The linked vertical wells (LVW) method: This is the most common UCG method, in which both the injection and production wells are drilled vertically and are connected by forming a linking channel by means of hydraulic fracturing, explosive fracturing, and electric-linking (**Figure 2.2a**). In the case of steep coal seams, an inclined injection well is drilled to the bottom of the coal seams and a vertical producing well is drilled towards the top of the coal seam (**Figure 2.2b**). These types of UCG projects are more suited to shallow coal seams and are mostly used in projects in China, South Africa, New-Zealand and Uzbekistan (Tian, 2013).

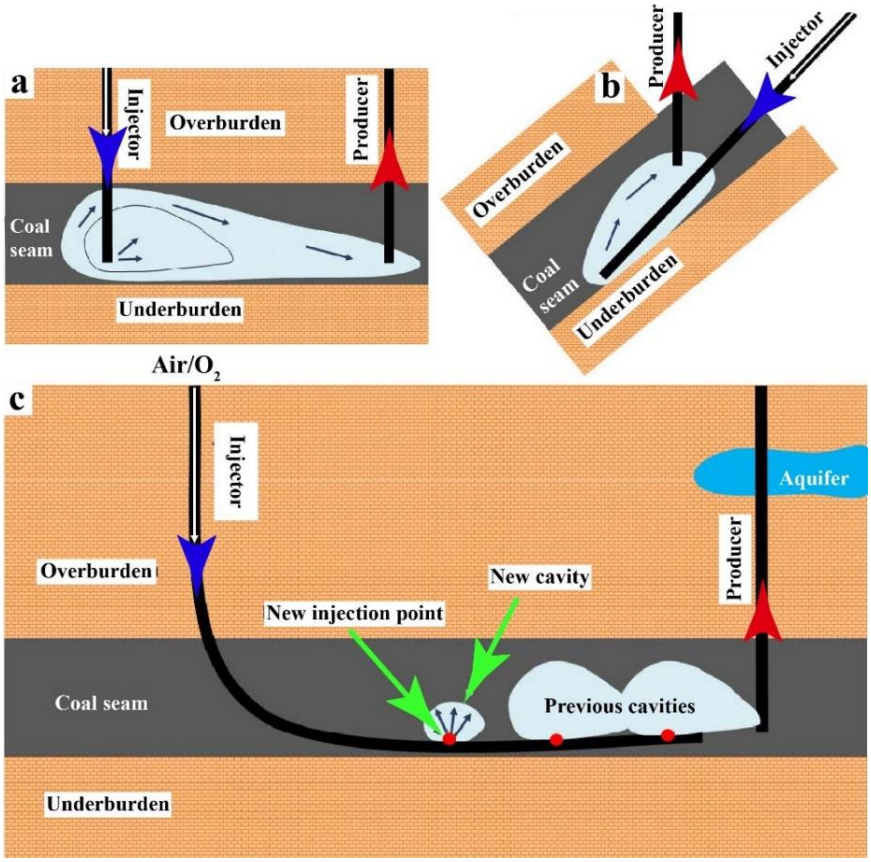

Figure 2.2 *Schematics of the types of UCG projects: (a) LVW, (b) steeply dipping coal seams, and (c) controlled retraction injection point (CRIP) (modified after Elahi, 2016)*

- The controlled retraction injection point (CPIP) method: In comparison to LVW, CPIP type of UCG projects is quite new. In this method, an injection well is drilled by directional drilling up to producing well. Initially, a gasification cavity is formed at the end of the injection well, and upon complete conversion of the coal at that site, the injection point is retracted to another point away from the producing well (**Figure 2.2c**).
- The long-tunnel large-section two-stage method: This is a new technique for UCG, in which air and water vapour are supplied circularly in two stages. In the initial stage, air is blown into the gasifier, which helps in the burning of coal and results in an increase in the temperature and the storage of heat in the coal seam. The second stage involves the injection of steam, which that decomposes when it comes into contact with the heated coal to form H_2 and CO (Tian, 2013) (**Figure 2.3**).

Of the three methods that are used for UCG, CRIP is the most efficient; It enables greater consistency in the quality of the gas that is produced and is the only industrial-scale technique that is capable of gasification of unmineable deep-seated coal seams (Kempka et al., 2009; Tian, 2013).

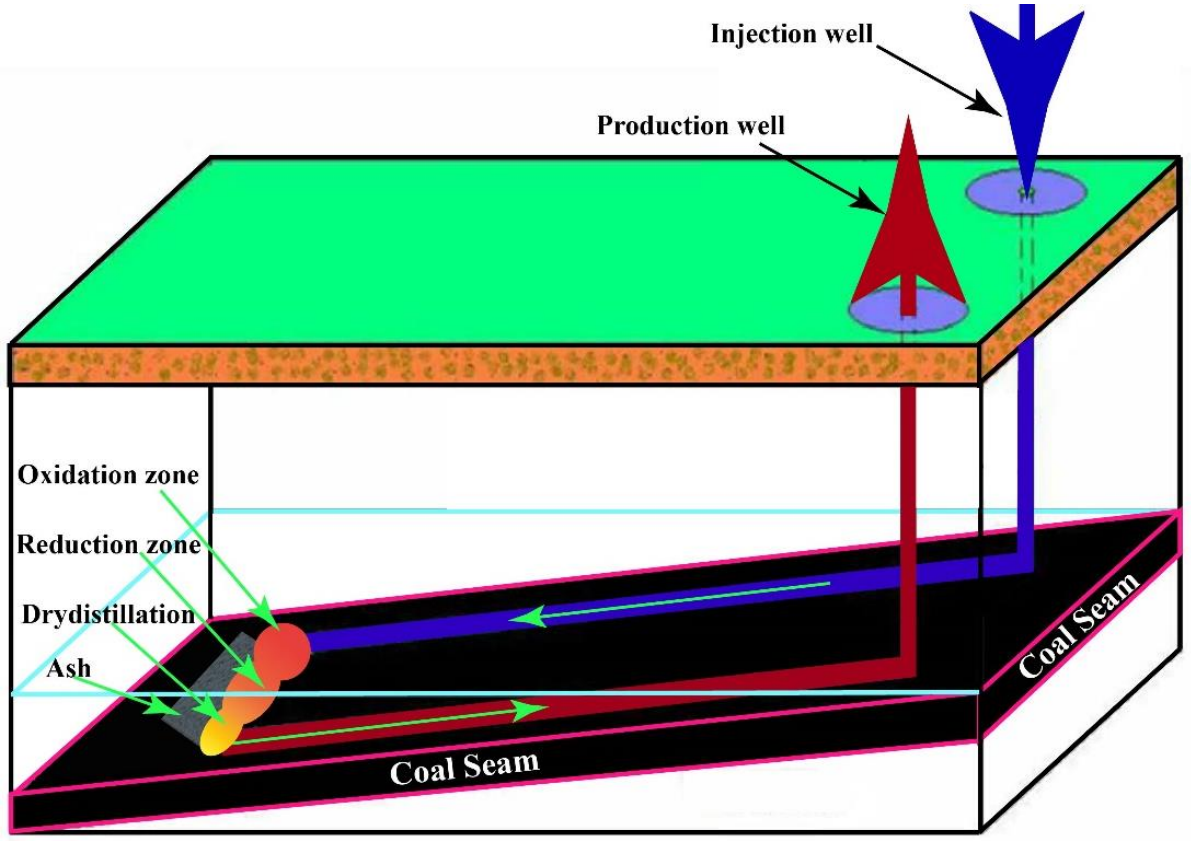

Figure 2.3 *Schematic of the long-tunnel large-section two-stage method (modified after Deng (2007))*

2.1.2 Development of UCG in India

Coal is the backbone of the structure of world energy. India has a long history of commercial coal mining. Between 2016 and 2017, India's coal production increased by 3.7 per cent from 639.23 million tonnes during 2015–2016 to 662.79 million tonnes during 2016–2017, making it the third largest coal-producing country after China and the United States (Indian Bureau of Mines, 2018).

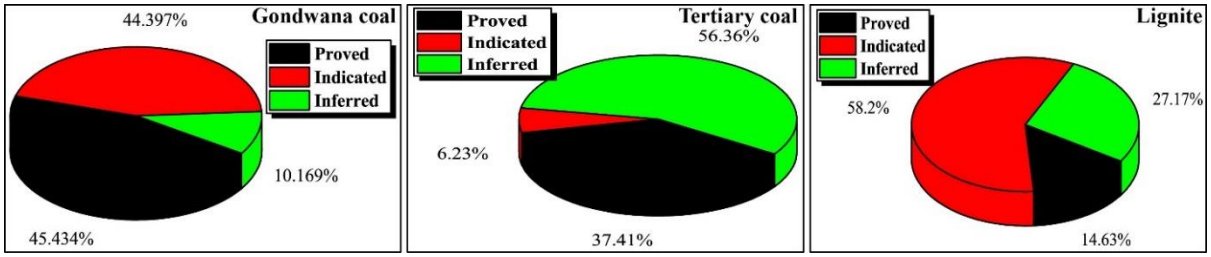

Figure 2.4 *Distribution of different types of coals and lignite in India (Indian Bureau of Mines, 2018)*

Indian coal deposits are predominantly found in Gondwana sediments, mainly in the eastern and central parts of peninsular India, as well as in Assam and Sikkim in the northeastern part of India. In addition to Gondwana coal, Tertiary coal-bearing sediments are found in Arunachal Pradesh, Assam, Meghalaya, and Nagaland. Indian coals are largely sub-bituminous to bituminous in rank. The occurrences of Indian lignite deposits are predominantly confined to the Tertiary sediments in the southern and western parts of peninsular India in Tamil Nadu, Kerala, Puducherry, Rajasthan, Gujarat, and Jammu Kashmir. Both coal and lignite contain large amounts of ash and have a low calorific value, which necessitates washing and certain other procedures prior to their being used. In India, the various explorations that were made by the geological survey of India (GSI) and the central mine planning and design institute (CMPDI) have led to an estimation of the reserves of coal at 315.149 billion tonnes, at a depth of up to 1200 metres; of this, 143.058 billion tonnes of reserves are proven, 139.311 billion tonnes of reserves are indicated and 32.779 billion tonnes of reserves are inferred. The distribution of proven, indicated and inferred coal reserves of different coal types and lignite has been represented in **Figure 2.4**.

The state-wise distributions of Gondwana coal, tertiary coal, and lignite in India have been represented in **Figure 2.5** and **Figure 2.6**. Out of the total reserves, 5.313 billion tonnes, 27.517 billion tonnes and 1.708 billion tonnes of coal are of prime-coking, medium-coking, and semi-coking type, respectively. The remaining 180.615 billion tonnes of coal falls under the category of non-coking coal, which comprises a high amount of sulphur (Indian Bureau of Mines, 2018).

A major portion of Indian coal and lignite deposits are located at a depth of below 300 m and below; with the existing coal mining methods, it is uneconomical to mine from such great depths.

Out of the total estimated coal reserves, only a sixth portion is accessible through open cast mining, whereas, of the total reserves, nearly 66 per cent can be considered to be a potential candidate for the development of UCG projects (Jain, 2017). In addition to coal, lignite exhibits certain unique properties such as high reactivity, spontaneous combustion, and high moisture content with a low carbon content, which renders it suitable for UCG.

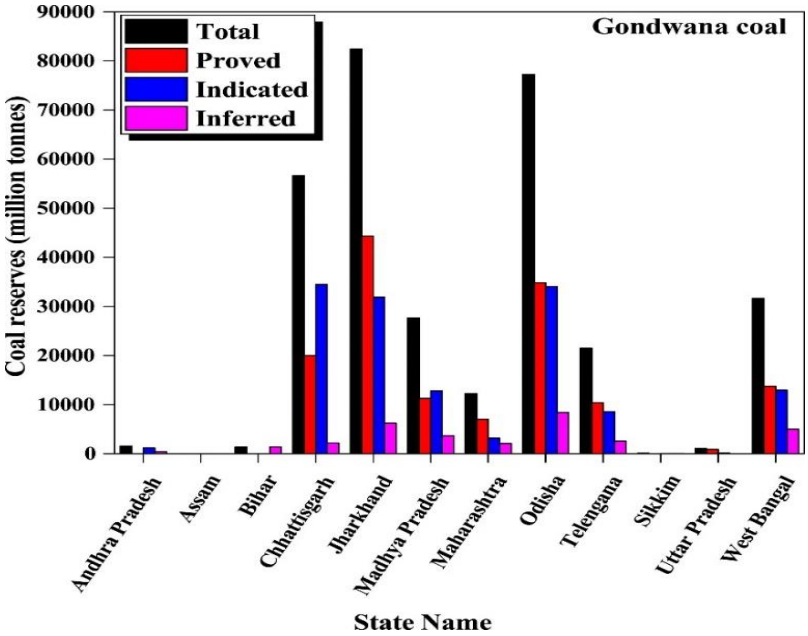

Figure 2.5 *Occurrence of Gondwana coal in different states of India (Indian Bureau of Mines, 2018)*

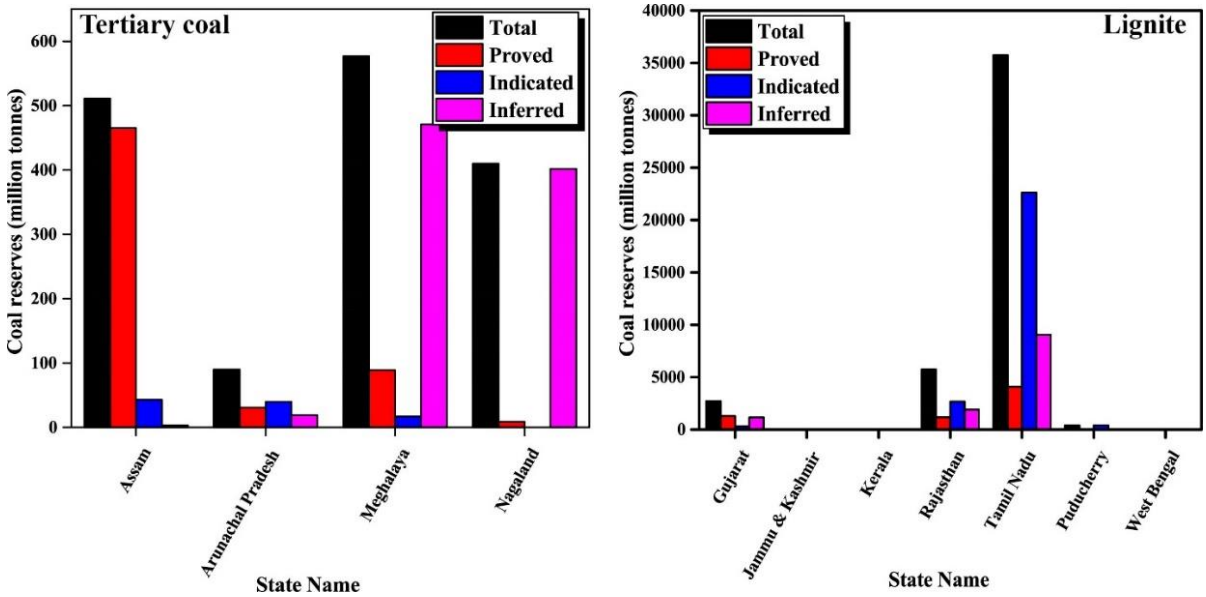

Figure 2.6 *Occurrence of tertiary coal and lignite in different states of India (Indian Bureau of Mines, 2018)*

The process of coal gasification involves multiple levels, which make its successful implementation quite challenging. The progress of UCG is always associated with issues such as the loss of heat and other valuable syngases to the surroundings, groundwater contamination, and potential instability of the ground surface. Small changes in the underground reactor can have significant influence on the rate of gasification. The successful exploitation of the inaccessible unmineable coal/lignite deposits necessitates the development of levels of expertise in the characterisation of the coal and geological conditions.

In mid-1980, the first Indian attempt at UCG was taken up by the collaboration of oil and natural gas corporation (ONGC) and coal India limited (CIL) under the technical collaboration of the union of Soviet socialist republics (USSR). A lignite block at Merta Road in Rajasthan was found suitable; however, its pilot appraisal could not be done due to problems such as groundwater contamination. Subsequently, in 2005, ONGC and CIL collaboratively made another attempt. Out of the five prospective sites suggested by CMPDI, Kasts block at Raniganj coalfield was selected for pilot-scale studies of UCG. In the later period, various public sector undertakings (PSU) have been involved in the successful implementation of UCG in India along with technical collaboration with certain foreign countries. So far, PSUs such as ONGC, Gujarat industries power company limited (GIPCL), CIL, CMPDI, and gas authority of India limited (GAIL) have achieved considerable progress (Singan and Ranade, 2017). **Table 2.1** summarises the development of UCG in India and represents the various coal and lignite blocks that have been allotted to different PSUs.

Table 2.1 *Coal blocks allotted to major Indian PSUs for UCG development (Singan and Ranade, 2017)*

Major PSU in India	Coal/Lignite	UCG site	References
Oil and Natural Gas Corporation (ONGC) + NMRC – Skochinsky Institute of Mining, Russia + Gujarat Industries Power Company Limited (GIPCL), Gujarat	Lignite	Vastan Site, Gujarat	Kumar et al. (2010)
ONGC	Lignite	Kasta Block, Raniganj	Kumar et al. (2010)
Coal India Limited (CIL) – Abhijeet Group + Ergo Exergy	Inferior coking coal	Kaitha block – Ramgarh Coal fields of CCL	Ergo Exergy (2015)
CMPDI + CIL		Thesgora C Block in Pench-Kanhan Coal fields of WCL	Bose (2011)

GAIL + Ergo Exergy	Lignite	Barmer, Rajasthan	(Ergo Exergy-GAIL, 1999; Working Group on Underground Coal, 2007)
Centre for Mine Planning and Development India (CMPDI) + Coal India Limited (CIL)	Coal	Yellendu (Dip side), Telangana	Ministry of Coal (2015)
CMPDI + CIL	Coal	Bandha-Singrauli Main Basin, MP	Ministry of Coal (2015)
CMPDI + CIL	Lignite	Sindhari West, Barmer, Rajasthan	Ministry of Coal (2015)
CMPDI + CIL	Lignite	Chokla North, Barmer, Rajasthan	Ministry of Coal (2015)
CMPDI + CIL	Lignite	Nimbalkot, Barmer, Rajasthan	Ministry of Coal (2015)
CMPDI + CIL	Lignite	Nagurda, Barmer, Rajasthan	Ministry of Coal (2015)
CMPDI + CIL	Lignite	Dungra, Surat, Gujarat	Ministry of Coal (2015)

2.2 Effect of temperature on physico-mechanical properties

Successful implementation of these engineering applications requires a detailed understanding of the physico-morphological and mechanical properties of rocks under high temperature and pressure conditions. Additionally, subsurface fire, geothermal water, magma intrusion, and explosions are components of very high temperatures, and they affect the physical and mechanical properties of the surrounding rocks. Exhaustive knowledge of the physical and mechanical attributes of rocks can be useful in the utilisation and reinforcement of rock constructions after they are exposed to fire or explosion. Therefore, the study of heated rocks has gained importance in rock mechanics.

Under the influence of temperature, most rocks undergo volumetric strain that can be either extensional or compressional. Within the elastic domain, the applied temperature is proportional to the behaviour of the rock. Depending upon the nature of the constraint and the increase or decrease of the temperature, increase or decrease in the confining stress occurs (Stephens and Voight, 1982). In reservoir conditions, the wellbore surroundings are subjected to various pressure and stress accumulations, and additional thermal alterations results in significant modification to various geomechanical attributes of the associated rocks. Such effects are capable of crushing the sand grains, shear or tensile stress zones around the borehole, wellbore stability, fracturing, fracture slip, shearing and reduction of the intergranular cohesion (Gupta and Civan, 1994; Wang and Dusseault, 2003). In the reservoir condition, the associated high temperature provides considerably influences the fluid-rock system. Often, the Young's modulus of the rocks is greatly influenced because of induced thermal stress (Stephens and

Voight, 1982). Additionally, porosity and permeability of the reservoir are influenced by the temperature change. Under higher confining pressures, heating of the formation rocks results in the expansion of the solid grains into the pore volume, thereby reducing the permeability of the formation (Palciauskas and Domenico, 1982); whereas, in certain conditions, shear dilation of fracking of the formation rocks results in an increment in the permeability (Palciauskas and Domenico, 1982; Azad and Chalaturnyk, 2011). The cooling of the formation due to fluid injection results in fracturing or fracture reactivation, which reduces the compressive stresses within the cooled region and increases the permeability of the rocks. Hydraulic diffusivity of the porous media and thermal expansion and contraction of the pore fluid affects the behaviour of the pore pressure within the reservoir, depending upon the inward or outward flows around the wellbore (Wang and Papamichos, 1994). The heat flow in the porous media is due to conduction and convection. High-permeable rocks and low-permeable rocks are associated with convective and conductive heat flow, respectively (Hou and Luo, 2012). The brittle and ductile nature of rocks are also influenced by the temperature variations, depending upon mineralogy, structural characteristics, and temperatures and confining pressures (Yu et al., 2015). The combined effects of stress, temperature, and pressure can be studied by the theory of thermoporomechanics, which includes thermoelasticity and thermoplasticity. According to the theory of thermoplasticity, thermal stress is capable of causing significant yield and damage to any material.

2.2.1 Effect of temperature on mechanical properties of sandstones

The geomechanical properties of rocks are highly influenced by temperature variations, which are predominantly dependent on mineralogical factors such as the amount of adhesion between the constituent minerals, their nature of bonding, chemical reactions, thermal expansion, and phase changes. However, the degree of influence is also dependent on the structural characteristics of rocks, such as total pores, interconnected pores, fracture, and grain boundary and sorting (Somerton, 1992; and Sygala et al., 2013). Since the nature of the factors that contribute to the thermal characterisation of rocks is diverse, it is quite difficult to obtain generic results from the experimental results (Uribe-Patino et al., 2017). Most of the time, the elastic modulus, and the strength properties of the rocks are altered when exposed to temperatures, which can be due to thermal expansion and thermal stress accumulation due to chemical reactions and/or due to constraining in any direction. The uniaxial compressive strength and sonic velocity of thermally treated Bandera, Berea and St. Peter sandstone specimens display a decreasing trend in the breaking strength and sonic velocity, which can be

explained in terms of an increasing fracture index that can be observed through microscopic thin sections. The degree of alteration is much higher in confining conditions than in the unconfined condition (Somerton, 1992). A uniaxial compressive test at different temperatures resulted in a fluctuation in the elastic modulus and strength properties, when the temperature was increased. From room temperature to 200 °C, an increasing trend was observed in most of the sandstones in the existing literature. However, after 600 °C, an abrupt decrease in the compressive strength and Young's modulus was observed. Mechanical properties such as Brazilian tensile strength, uniaxial compressive strength and bending strength of a well-cemented sandstone at high temperatures were investigated by Rao et al. (2007). In all the studied properties, an increasing temperature was found up to 200 °C, which was followed by a decreasing trend up to 300 °C.

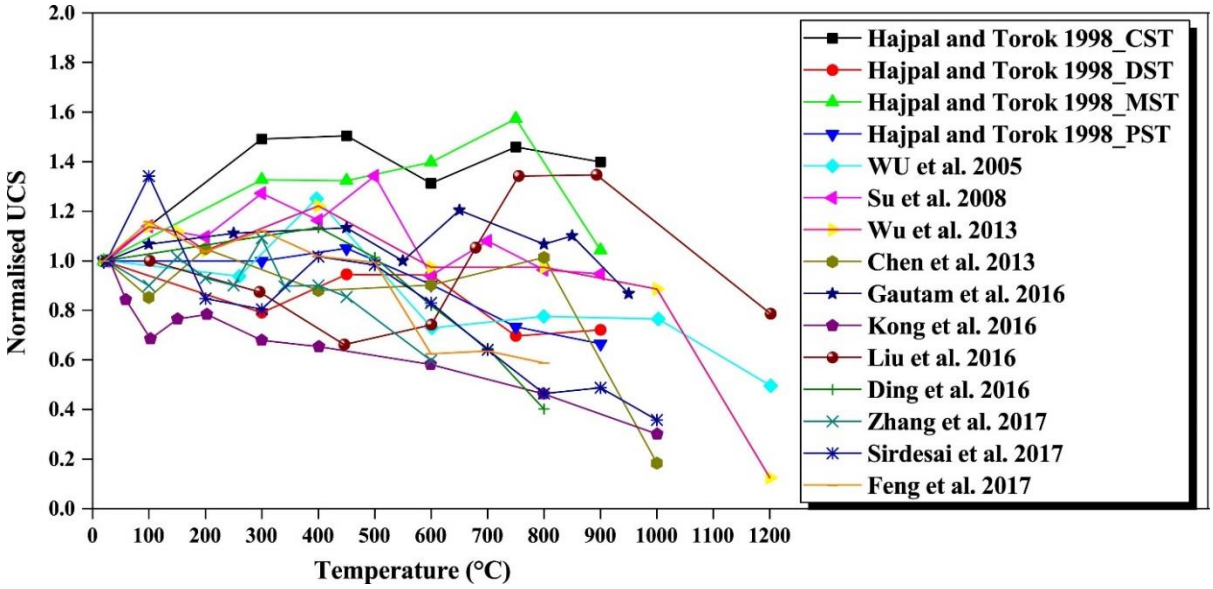

Figure 2.7 *Comparison of the UCS of thermally treated sandstones*

Over the last few decades, various experiments have been conducted to characterise the influence of temperatures on rocks, which indicates that there is a considerable impact of the temperature on the petrophysical, thermal and geomechanical properties of rocks. In most of the cases, thermal alteration tends to induce nonlinear behaviour and plasticity. For a rock that is well cemented and hard, the thermal damage leads to nonlinear behaviour due to microfractures whereas, in an uncemented and weak rock, the thermal damage results in plasticity due to the relative movement of mineral grains. Thus far, many researchers have examined the effects of temperature on the various physical and mechanical strengths and parameters of rocks. These parameters include UCS, tensile strength, elastic modulus, P-wave velocity, mass loss, porosity, peak strain, Poisson’s ratio, fracture toughness, cracks and

Acoustic Emission (AE) (Jaeger and Cook, 1976; Meredith, 1983; Heuze, 1983; Meredith and Atkinson, 1985; Bazant and Prat, 1988; Whittaker et al., 1992; Brede, 1993; Hajpál and Török, 1998; Al-Shayea et al., 2000; Rao et al., 2007b; Wu et al., 2007, 2013; SU et al., 2008; Dwivedi et al., 2008; Zhang et al., 2009, 2017; Vishal et al., 2011; Ranjith et al., 2012b; WU et al., 2012; Yin et al., 2012; Chen et al., 2013; Mahanta et al., 2016b; Lü et al., 2017).

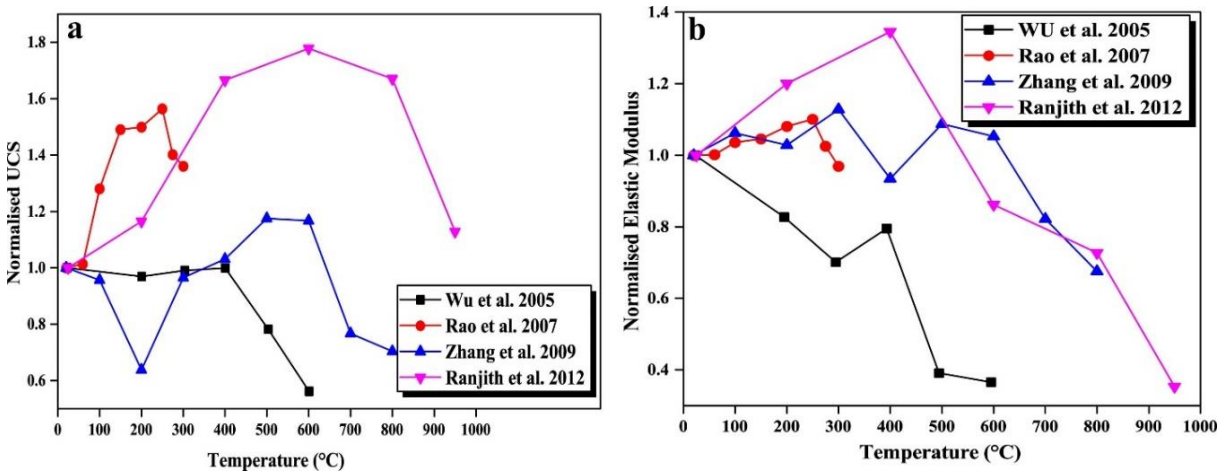

Figure 2.8 *Comparison of the UCS of sandstones at high temperatures*

When the temperatures are increased, thermal properties such as the heat capacity increases; whereas, thermal conductivity and thermal diffusivity decrease (Somerton, 1992). For the temperature increase from 90 °C to 800 °C, Somerton and Boozer (1960) observed a reduction of 60 per cent in the thermal diffusivity of the studied rocks.

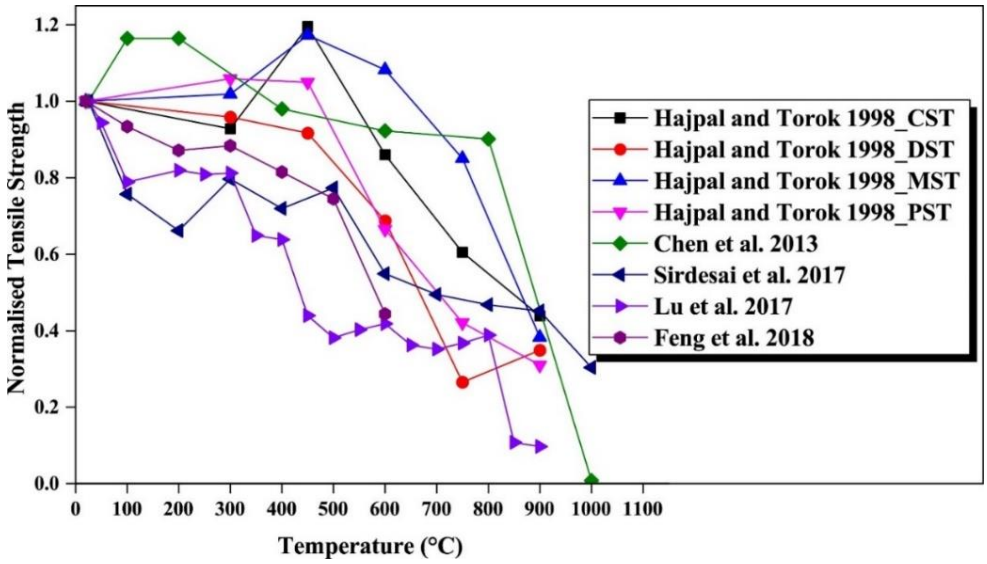

Figure 2.9 *A comparison of the tensile strength of different thermally treated sandstones*

Hajpál and Török (1998) studied mechanical properties such as the indirect tensile strength and the compressive strength of four thermally treated sandstones; they reported the different degrees of influence on the different types of sandstone. Similarly, Lü et al. (2017) investigated

the influence of temperature on the tensile strength, longitudinal wave velocity and mass loss rate of quartz-dominated Linyi sandstone. Sirdesai et al. (2017) investigated the degree of alteration of Dholpur sandstone that was exposed to high temperatures. They reported the variation in different mechanical properties such as the UCS, tensile strength, Young's modulus and Poisson's ratio of the sandstone, as a function of temperature.

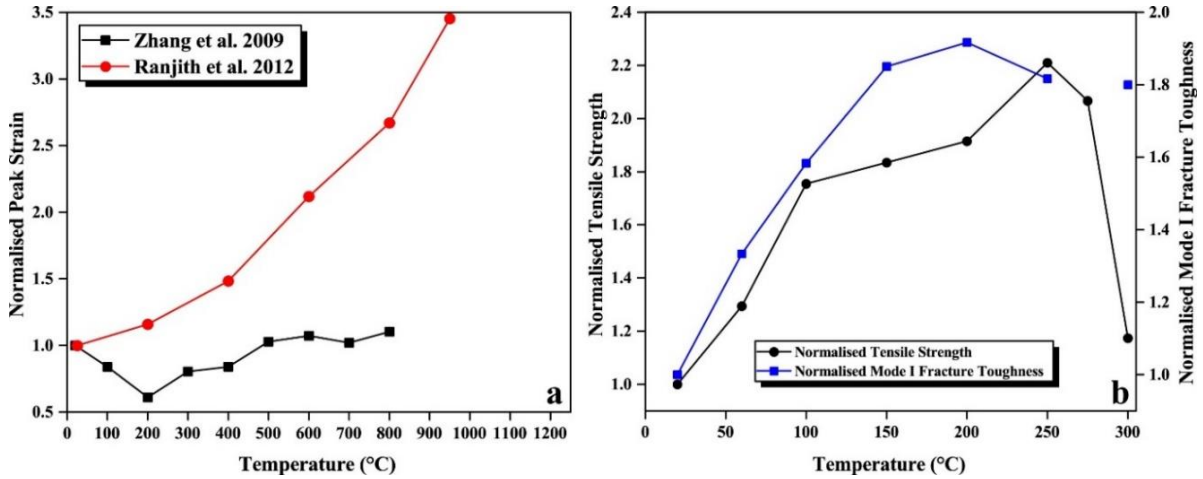

Figure 2.10 *A comparison of the peak strain, tensile strength, and fracture toughness of sandstones at high temperatures*

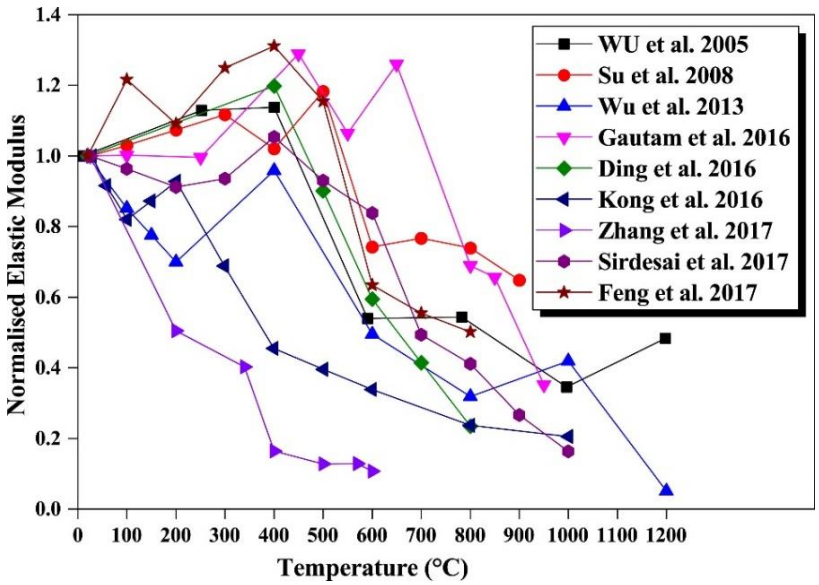

Figure 2.11 *A comparison of the Young's modulus of thermally treated sandstones*

Wu et al. (2013) and Zhang et al. (2017) are among researchers who investigated the effect of temperatures on thermally treated sandstone. Wu et al. (2013) investigated the peak stress, peak strain, elastic modulus, and Poisson's ratio of thermally treated Jiaozuo sandstone and reported a gradual decrease in elastic modulus and increase in failure/peak strain when temperatures were increased. In addition to the various properties investigated by Wu et al. (2013), Zhang et al. (2017) studied the porosity variation of Linyi sandstone as a function of temperature and

reported a slight decrease in porosity up to 400 °C, which indicates an increase in porosity up to the maximum temperature (600 °C) in their study.

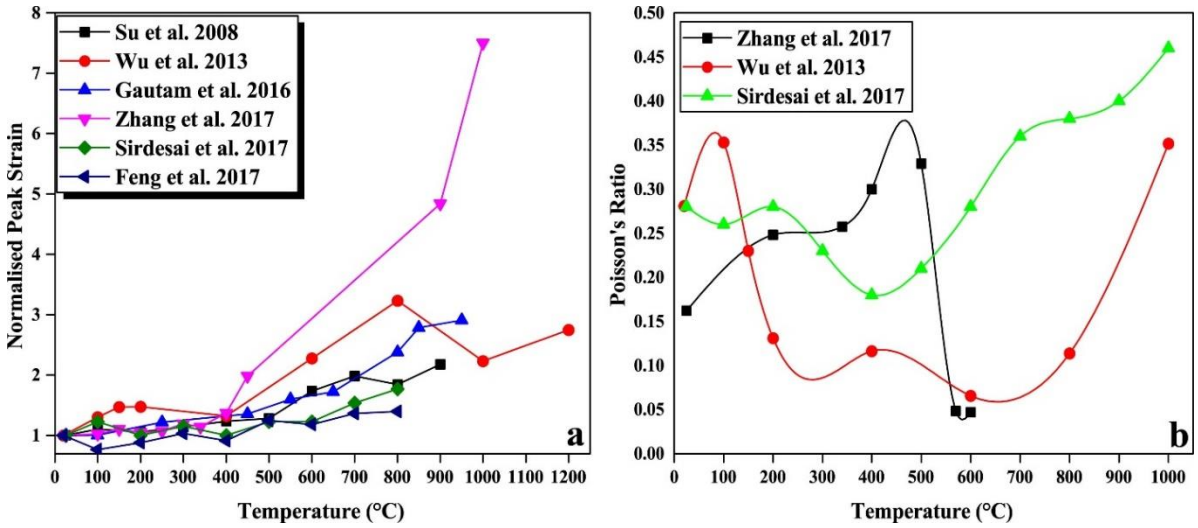

Figure 2.12 *A comparison of peak strain and Poisson's ratio of thermally treated sandstones*

Lü et al. (2017) studied the effect of the temperature on the tensile strength of thermally treated sandstone and reported a significant impact on the tensile strength, which they attributed to the loss of water and degradation of minerals as well as to induced thermal stress. The entire temperature window was divided into four phases: room temperature – 300 °C, 300 °C – 600 °C, 600 °C – 800 °C and 800 °C – 900 °C. In the initial temperature increase from room temperature to 400 °C, adsorbed water in the dominant mineral phases dehydrates, which result in progressive mass loss that is accompanied by microcracks due to the mismatched thermal expansion of minerals. These induced microcracks result in the shifting of the dominant pore size and in an increase in the void ratio (Liu et al., 2016).

Under thermo-mechanical loading (air-dried to 450 °C), the microcracks start to close, increasing the density of the rock (Zhang et al., 2014). During this stage of loading, moisture that is present within the rock evaporates due to thermal loading; simultaneously, due to mechanical loading, preexisting microcracks start to close, which results in an increment in the density of the rock, thereby increasing the elastic modulus. New microcracks are generated along with the rock as a result of the thermal stress, and the structure of the rock is changed. New microcracks are generated, which provides further sites for crack initiation. Thermal heating results in thermal cracking, which is due to the differential thermal expansion of minerals. Different minerals have different thermal expansion coefficients and even the same mineral has a different thermal expansion along a different crystallographic axis. The rapid decrease in the elastic modulus from 650 °C to 950 °C is due to the thermal softening of rocks,

which results in a decrease in the cohesion of the rock, facilitating the failure with very little peak load; this results in a decrease in the elastic modulus of the rock (Zhang et al., 2014).

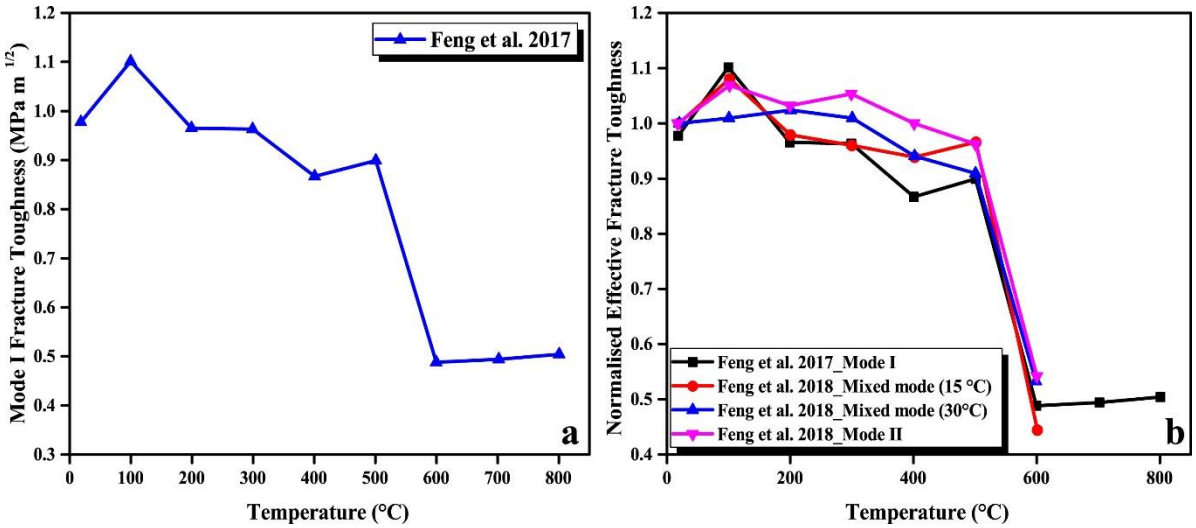

Figure 2.13 *A comparison of the fracture toughness of thermally treated sandstones*

The experimental study of the measurement of fracture toughness is useful in rock and material science for recognition of stress responses in rocks, metals, ceramics, concrete and such others. From the perspective of rock engineering, the effect of thermal treatment in rocks plays a crucial role in different engineering applications such as rock drilling, ore crushing, deep petroleum boring, geothermal energy extraction, deep burial of spent nuclear fuel, and waste disposal (Kranz, 1983; Homand-Etienne and Houpert, 1989; Balme et al., 2004; Nasseri and Mohanty, 2008; Yin et al., 2012, 2015; Ozguven and Ozcelik, 2014).

Safe and successful effectuation of modern geotechnical engineering projects such as nuclear waste disposal (Sundberg et al., 2009), underground coal gasification (Roddy and Younger, 2010), CO_2 sequestration (Rutqvist et al., 2002), geothermal heat energy (Zhao, 2000), construction in fire-exposed rocks (Zhan and Cai, 2007), hydraulic fracturing for oil and natural gas recovery (Whittaker et al., 1992; Papanastasiou, 1999; Funatsu et al., 2014a) necessitates the knowledge of the thermo-mechanical behaviour of rocks. The geomechanical properties of a rock gradually decrease with increasing temperatures in the thermal treatment that induces microcracks due to differential thermal expansion. Other mineralogical factors such as grain expansion, dehydration, decomposition, phase transition and re-crystallisation add further complexities to the experimental observations (Yin et al., 2012).

There is a decrease in the fracture toughness of a rock when it is treated at elevated temperatures until it reaches an elasto-plastic transition phase. It may be observed that that damage within rocks is introduced in the form of microcracks due to thermal treatment. However, the degree

of influence on the mechanical properties are rock type- and temperature-dependent (Balme et al., 2004; Yin et al., 2012). Nasseri and Mohanty (2008) experimentally observed that from 250 °C to 850 °C, with gradual thermal treatment, the number, and the average opening distances of microcracks gradually increase, resulting in a decrease in the P-wave velocity as well as in the fracture toughness of Westerly granite. According to Yavuz et al. (2010), the P-wave velocity in carbonate rocks increases from room temperature to 100 °C, possibly due to the dilation of calcite grains, and then gradually decreases with an increase in the temperature due to thermal damage above 150 °C. Funatsu et al. (2004) evaluated the fracture toughness of Kimachi sandstone and Tage tuff and observed that the fracture toughness gradually decreases up to 75 °C, after which it gradually increases up to 125 °C. Zhang et al. (2017) studied the uniaxial compression strength and the porosity of sandstone that was heated to different temperatures, from room temperature to 600 °C. The experimental results indicated an increase in the pore volume at 600 °C when compared to the room temperature. The uniaxial compressive strength and the elastic modulus were increased slightly, from 25 °C to 400 °C, which led to a quick decrease to 600 °C; they attributed this decrease to the transformation of kaolinite and quartz. A comparison of various mechanical properties such as UCS, tensile strength, elastic modulus, peak strain, Poisson's ratio and fracture toughness of thermally treated sandstones and sandstones at high temperatures has been shown from **Figure 2.7** to **Figure 2.16**.

Triaxial tests provide a platform to extract valuable information about the rocks in in situ pressures and temperatures. However, due to the experimental constraints, these types of tests barely exceed 200 °C. Despite the limitation, these tests are crucial in the investigation of the effect of temperature on the strength properties of rocks (Uribe-Patino et al., 2017). Even if the triaxial tests of thermally treated rocks do not represent the true in situ reservoir temperature and pressure condition, significant and valuable information can be extracted from these types of tests. A friable and non-homogeneous reservoir sandstone that was cored from the Potiguar basin in Brazil displayed a decreasing bulk compressibility when the temperature was increased from 80 °C to 150 °C. The average reduction in the shear failure limit, cohesion, Young's modulus, and Poisson's ratio was observed in the temperature window from 24 °C to 80 °C. However, the angle of internal friction barely changed in that temperature range (Araújo et al., 1997).

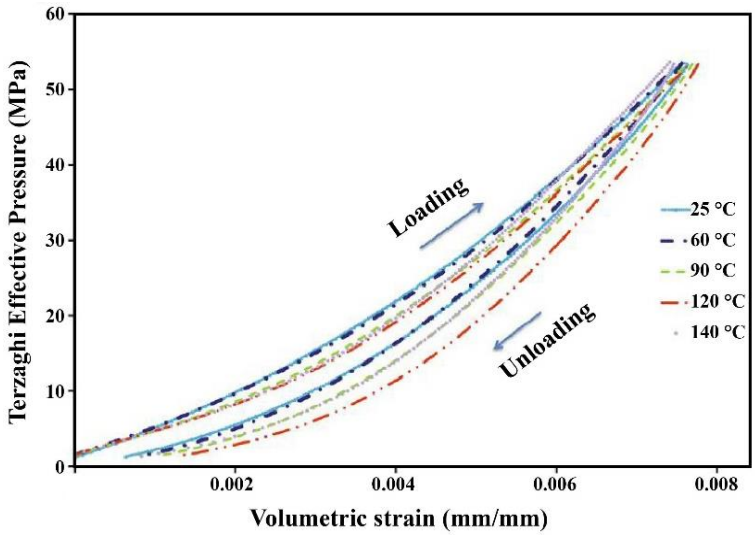

Figure 2.14 *Volumetric strain under various effective pressure and temperatures (Hassanzadegan et al., 2014)*

The high-temperature triaxial tests of high-cohesive Flechtinger sandstone displayed an increase in the irreversible deformation of the rocks after the loading-unloading cycle (Hassanzadegan et al., 2014). However, they reported diverse responses of the rocks to heating under different confining pressures. When temperatures were increased, low confining stresses were observed, along with a decrease in the static bulk modulus, increase in the porosity and rapid variation in wave velocities (**Figure 2.14** and **Figure 2.15**). However, high confining stress was observed, along with an increase in static bulk modulus, decrease in the porosity and moderate variations in wave velocities. Such behaviours were explained in terms of increment in low-aspect-ratio microfractures when temperatures were increased (**Figure 2.16)**. At a high temperature, the frequency of low-aspect-ratio microfractures was found to increase; whereas, high-aspect-ratio microfractures were found to decrease. The low-aspect-ratio microfractures and high-aspect-ratio microfractures are characterised by closing under low confining stress and high confining stress, respectively. The behaviour of rocks under low confining stress and high-temperature conditions is controlled by a high content of open low-aspect-ratio microfractures, due to which the rocks are found to be more compliant;, whereas, the behaviour of rocks under high confining stress and high temperatures are controlled by less open high-aspect-ratio microcracks, due to which the rocks are found to be much stiffer (Hassanzadegan et al., 2014). Based on the experimental results, Arias-Buitrago (2015) reported thermally induced structural alteration to the samples after 180 °C, by which the shear failure limit, internal friction and cohesion of the reconstituted oil sand decreased when temperatures were increased. Additionally, a decrease in the porosity and Young's modulus was reported in the

condition of heating at a high confining pressure, and an increase in porosity was observed in the condition of heating at a low confining pressure.

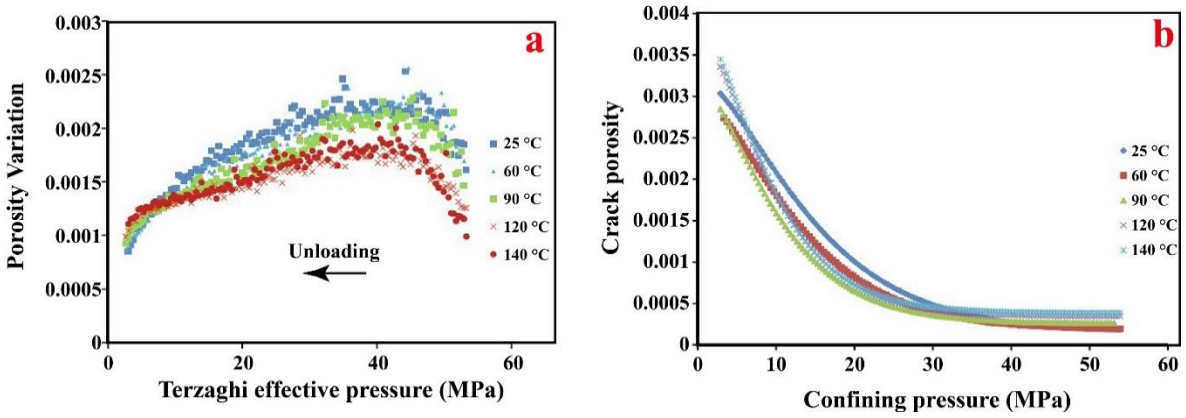

Figure 2.15 *Porosity and crack porosity variation under different pressures at different temperatures (Hassanzadegan et al., 2014)*

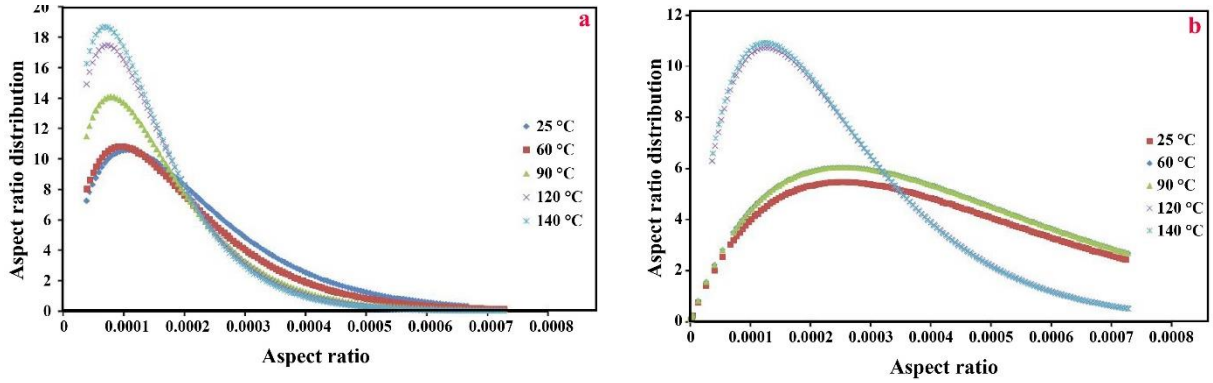

Figure 2.16 *Aspect ratio distribution for loading (a) and unloading (b) condition at different temperatures (Hassanzadegan et al., 2014)*

Yu et al. (2015) conducted triaxial tests with different confinements on thermally treated red sandstone. As per their results, from room temperature to 200 °C, an increasing trend of Young's modulus was found, which was followed by a decreasing trend of Young's modulus up to 600 °C. They suggested that the increase in Young's modulus from 20 °C to 200 °C was due to the closure of the primary pores and the preexisting cracks; whereas, the decrease in Young's modulus in the temperature window from 200 °C to 600 °C was due to the thermal degradation of the sample. Beyond, 800 °C, severe thermal damage was observed in the sandstone.

2.2.2 Effect of temperature on physical properties of sandstones

Tian et al. (2012) have reviewed the various physical properties of sandstones such as bulk modulus, porosity compressional wave velocity, and permeability after high-temperature treatment.

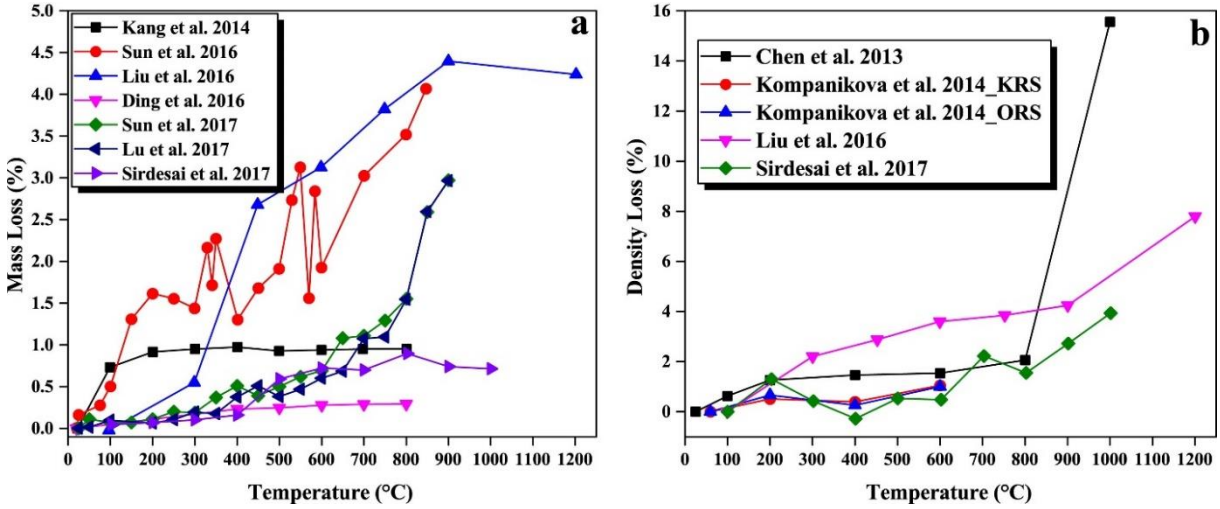

Figure 2.17 *A comparison of mass loss and density of different thermally treated sandstones*

Below 200 °C, mass loss is generally due to the evaporation of the free water that is present in the pore volume. In thermally treated sandstones, above 200 °C, the mass loss is either due to the clay minerals that loose absorbed water, hydroxyl, and oxygen or due to the organic materials and carbonates that disintegrate into carbon dioxide, oxides, and water. In thermally treated Sichuan sandstone, after 200 °C, a mass loss of one per cent was observed. However, the mass loss remained unchanged after 600 °C. In thermally treated Pingding-shan sandstone, the reported average mass loss was below one per cent even after 900 °C (Tian et al., 2012).

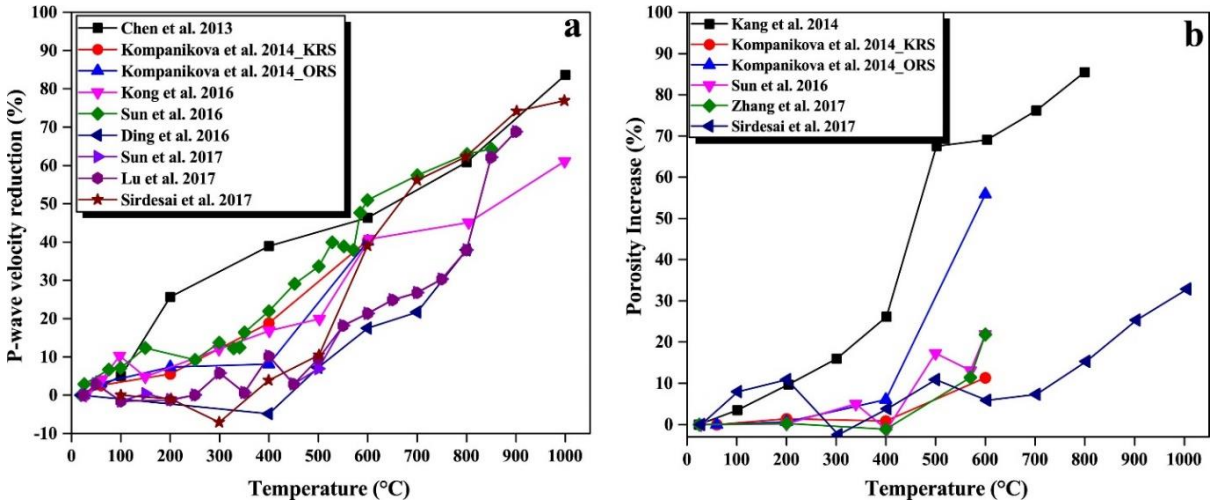

Figure 2.18 *Comparison of P-wave velocity and porosity of various sandstones*

Sun et al. (2017) studied the temperature effect on P-wave and microstructural variation of Linyi sandstone from room temperature to 1000 °C. They divided the total temperature window: at up to 300 °C, substantial disruption appeared in the interior of the specimens; whereas, in the range from 300 °C to 700 °C, major thermal damage to the specimen was observed; they attributed this to the combined action of thermal decomposition, thermal dehydration, and the thermal stress that was induced by heating.

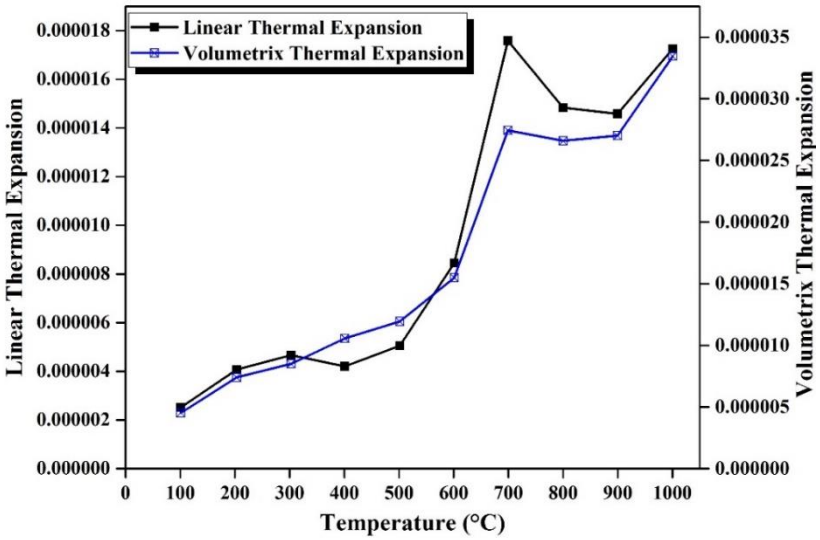

Figure 2.19 *A comparison of linear expansion and volumetric expansion of sandstones (Sirdesai et al., 2017a)*

Depending upon the different grain arrangements and the composition of the cementing material, the porosity of sandstones varies from 0.7 per cent to 34 per cent (Tian et al., 2012). After exposure to a high temperature, the change in porosity in sandstones is either due to the thermal expansion-driven structural damages in the rocks or the different chemical degradations of minerals. In general, with an increasing temperature, the porosity of most sandstones is found to have an increasing trend. However, in some of the sandstones, an initial decrease in the porosity is observed. The temperature of porosity is predominantly dependent on the initial porosity, and slightly dependent on the cementing materials (Somerton, 1992; Tian et al., 2012; Mahanta et al., 2016b; Sirdesai et al., 2017a). Both under and after high temperatures, the compressional wave velocities of rocks decrease with increasing temperatures (Somerton, 1992).

Although the thermal expansion of rocks is not significant in magnitude, it has quite a significant effect on the structure of the rocks. Rocks are assemblages of different essential and accessory minerals, and these minerals do have variable responses to the thermal effect. The differential thermal expansions of different mineral grains produce significant thermal stresses inside the rock, where major stresses are concentrated along the grain boundaries (Somerton and Boozer, 1960; Somerton, 1992). Upon exceeding the tensile or shear strength limits, the produced thermal stress results in widening of the existing cracks or, sometimes, even in the formation of new microcracks, inducing permanent structural damage inside the rock (Tian et al., 2012; Mahanta et al., 2016b).The same mineral could have differential thermal expansions

along different crystallographic axes, which also results in the development of thermal stress (Somerton, 1992).

A comparison of various physical properties such as mass loss, density, P-wave velocity, porosity, and thermal expansion of thermally treated sandstones has been shown from **Figure 2.17** to **Figure 2.19**.

2.3 Effect of temperature on the flow behaviour of sandstone

The various experiments that were conducted to assess permeability alteration of rocks due to temperatures can be divided into flow-based or volumetric-based experiments (Uribe-Patino et al., 2017). Based on flow-based experiments, the grounds for permeability variations can be microstructural rearrangements and pore structure change in the rock; the fluid-rock interaction between the flowing fluid and the minerals; different effects such as the variation in porosity, tortuosity and resistivity; clay reactions; and confining pressure (Somerton and Mathur, 1976; Udell and Lofy, 1989; Uribe-Patino et al. 2017).

Rosenbrand et al. (2014) reported that kaolinite migration could be a possible cause for the reduction mechanism; whereas, Hassanzadegan (2013) suggested an inelastic response of the rock as a possible cause of the effect. Sometimes, under low confinements, an increasing temperature results in an increasing permeability whereas, under high confinement, an increasing temperature results in decreasing permeability. In the case of uncemented and soft sandstones, movements or rearrangements of the sand grains dominate the inelastic response (Arias-Buitrago, 2015).

Volumetric strain-based experiments assume that pore-volume change due to volumetric strains predominantly brings about changes in permeability. Scott et al. (1994) reported an increment in the deviatoric stress due to the temperature increment, which promotes shear failure. An increasing temperature results in a volume expansion that is greater than the theoretical thermal expansion, which can be attributed to the shear strains or dilatancy. Depending upon the dilatant or contractant nature of the shear failure, permeability can be irreversibly increased or decreased, respectively (Zoback and Byerlee, 1976). The inelastic mechanism in different rock types, which is responsible for the permeability variation can be of different types such as the opening and closure of cracks in crystalline rocks, relative grain movement in porous clastic rocks, and grain crushing in uncemented rocks (David et al., 1994). For an example, the influence of temperature and pressure on the permeability of sandstone has been represented in **Figure 2.20**.

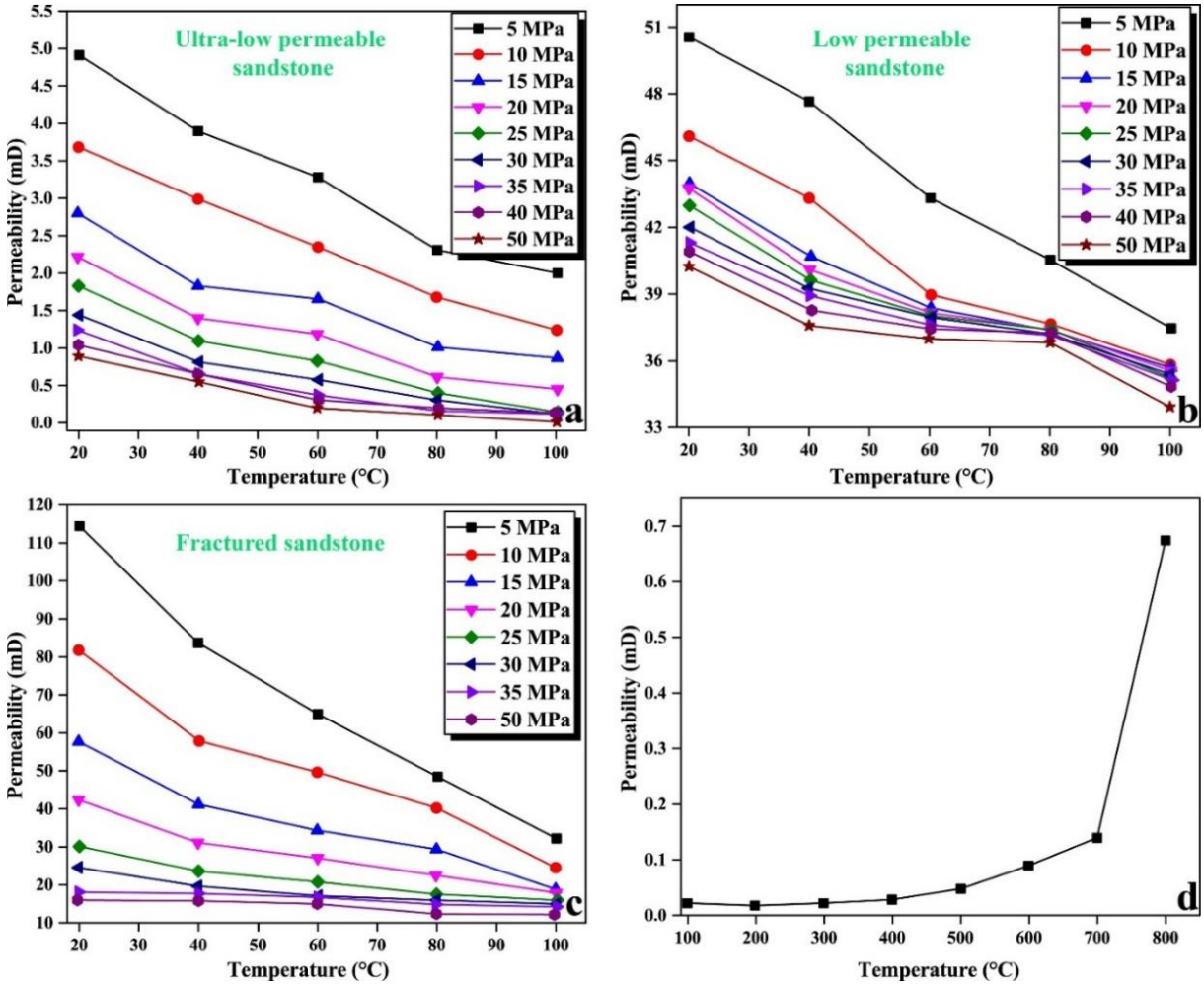

Figure 2.20 *Influence of temperature and pressure on the permeability of sandstone* (Guo et al., 2017)

2.4 Knowledge gap

Based on the literature review, it is quite clear that most of the thermo-mechanical characterisations of sandstone have been concentrated in the various physical and mechanical aspects. However, no microstructural observation was encountered in the literature. Therefore, in addition to the various mechanical and physical aspects of the sandstone, the microstructural responses of sandstone are one of the primary goals of the research work, which will better explain the thermal behaviour of sandstones under and after exposed to high temperatures.

Chapter 3 Materials and general methodology

Sandstone is one of the most widely distributed rocks and works as a reservoir rocks for oil and gas storage. It is also associated with UCG as the surrounding rock. Additionally, when the rock mechanical aspects of Indian rocks are considered, it is clear that sandstone has not been explored in much detail, and that a large amount of research is required in this aspect. Hence, sandstone was selected for the current research work.

3.1 Location and general geological information about sandstone

Jodhpur sandstone, which is used in the current study, belongs to the Jodhpur area of Rajasthan, India (**Figure 3.1)**. Jodhpur sandstone belongs to the Marwar Supergroup, which is a sequence of horizontal sedimentary beds that are nearly two-kilometres thick. The Marwar Supergroup is unconformably overlain by the Malani suits of igneous rock and by the Bap boulder beds. The age of the Marwar Supergroup is believed to be Upper Proterozoic to Lower Cambrian. The Marwar Supergroup is further divided in three groups: Jodhpur group at the bottom, Nagaur group at the top, and the Bilara group, which is sandwiched between the Jodhpur and the Nagaur groups (Khan and Sogani, 1973). The Jodhpur and the Nagaur groups are composed predominantly of siliciclastic rocks, and the Bilara group is composed of carbonates and evaporates (Pareek, 1984; Srivastava, 2012). Coarse- to fine-grained Jodhpur sandstone beds are horizontal, undisturbed, and unmetamorphosed (**Figure 3.2**) (Chauhan et al., 2004).

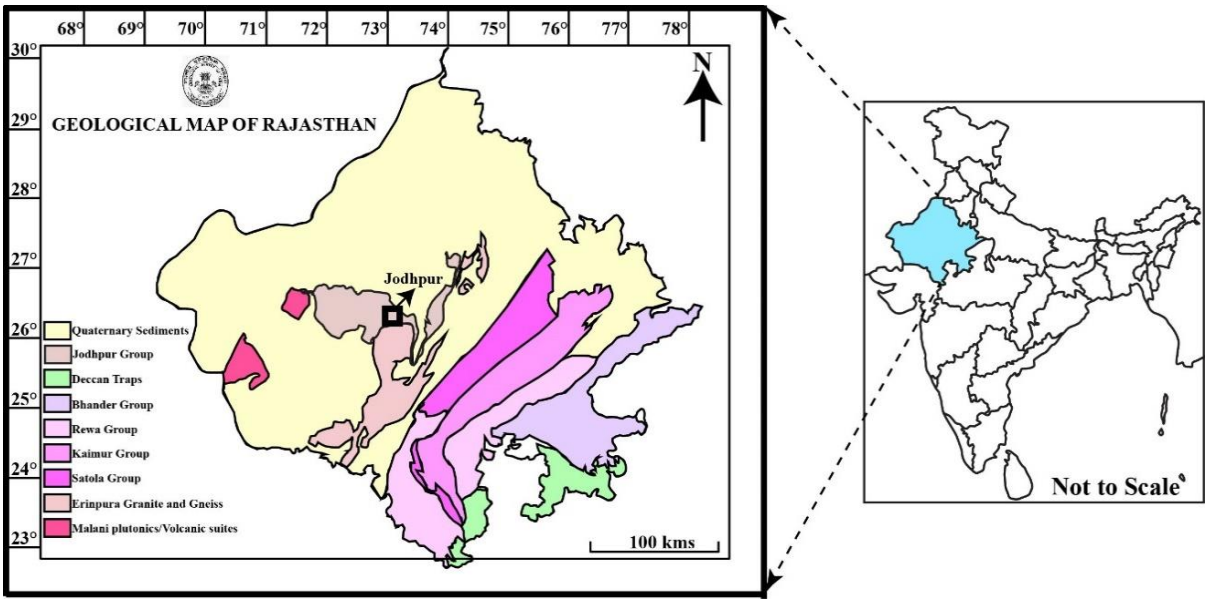

Figure 3.1 *Geological map of the studied rock type. The image on the left shows the geological map of Rajasthan, indicating the Jodhpur area*

Generally, the sandstones of the Jodhpur group are quartz-arenite and, occasionally, feldspathic, sub-feldspathic and subarkose arenite. Sandstones of the Jodhpur groups are mostly silica-cemented, are deposited in a marginal marine environment, and are mineralogically mature (Awasthi and Parkash, 1981). The Jodhpur group has been further subdivided as the Pokaran boulder bed, the Sonia sandstone and the Girbhaker sandstone by Pareek (1984). Later on, Chauhan et al. (2004) carried out certain modification in the classification of the Jodhpur group. They classified the Jodhpur group as the Pokaran boulder bed and the Jodhpur group, which includes the Sonia sandstone and the Girbhaker sandstone.

Supergroup	Group	Formation	Lithology
		Bap boulder beds	
		Unconformity	
Marwar Supergroup	Nagaur Group	Tunklian sandstone	Brick red sandstone, siltstone and red claystone
		Nagaur sandstone	Brick red sandstone, siltstone & red and green clay beds
	Bilara Group	Pondlo dolomite	Cherty dolomitic limestone
		Gotan limestone	Interbedded dolomite and limestone
		Dhanapa dolomite	Dolomitic limestone with cherty lenses
	Jodhpur Group	Jodhpur sandstone	Reddish yellow gritty sandstone with reddish brown clay beds
		Pokaran boulder bed	Conglomerate
		Unconformity	
Malani igneous complex/Aravalli rocks			

Figure 3.2 *Lithostratigraphic succession of the Marwar Supergroup, western Rajasthan, representing the stratigraphy of Jodhpur sandstone (Pareek, 1984; Chauhan et al., 2004)*

The current study investigates the effects of temperature on sandstone from the Jodhpur Group of the Marwar Supergroup in Rajasthan, India. For the future, it has been proposed that a few lignite-based underground gassfires be established in Rajasthan; this is the main motivation for considering Jodhpur sandstone for the current study, along with the investigation of its thermo-mechanical responses to varying temperatures.

3.2 Mineralogical characterisation and hardness test of sandstone

3.2.1 Petrographic study

At room temperature, sandstone is predominantly a quartz-dominated rock with a few opaque phases. The quartz grains that are present show side-to-side contact with each other.

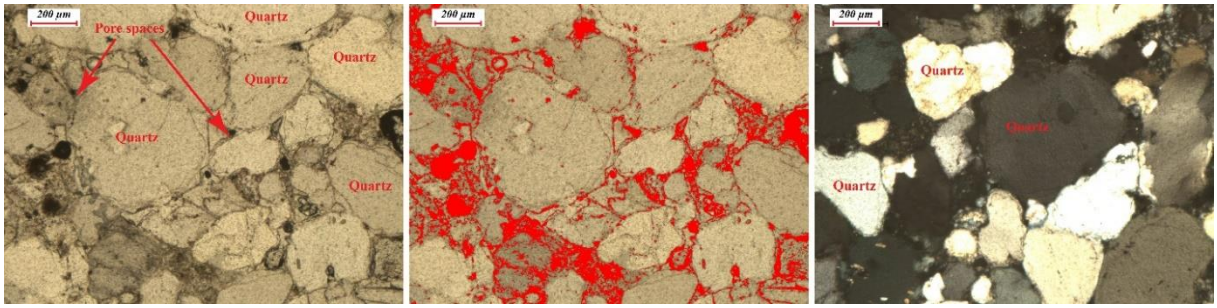

Figure 3.3 *Petrographic micrographs of the sandstone at room temperature*

Well-developed boundaries between the quartz grains can be observed. Quartz grains possess a medium relief and are triangular to subrounded. The subrounded shape of the quartz minerals indicates high textural and mineralogical maturity. The higher percentage of quartz indicates its textural maturity. The rock is rich in quartz grains, which indicates a quartz-rich source rock (**Figure 3.3**).

3.2.2 XRD analysis

XRD analysis was used for the identification of the composition of rocks at an ambient temperature. XRD analysis was performed by using an X-ray PANalytical Diffractometer (Empyrean) with a start position [°2θ] of 4.0 to the end position [°2θ] of 80.0, with a step size [°] of 0.020. These XRD data were then processed using X'Pert Highscore Plus software. The patterns that were obtained from the XRD analysis were compared to the JCSD-2013 database for identification of different mineral phases within these rocks.

3.2.2.1 Room-temperature XRD analysis

The XRD analysis at room temperature shows the dominance of mineral phases such as quartz, dickite, calcite, kaolinite, alkaline feldspar, spinel in Jodhpur sandstone.

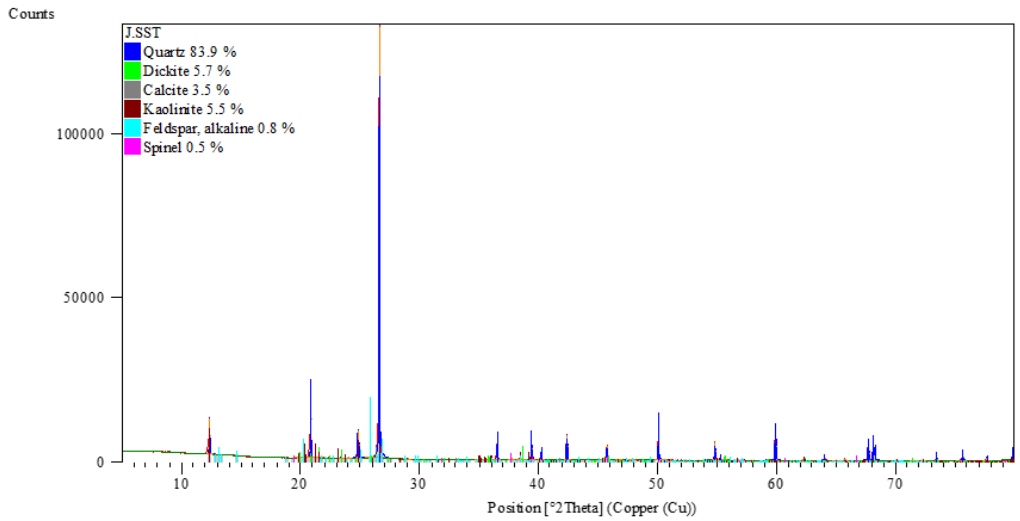

Figure 3.4 *XRD Analysis of the studied sandstone, indicating major mineral phases in the sandstone*

In addition to quartz, the studied sandstone contains few clay minerals in the form of kaolinite and dickite and carbonate mineral in the form of calcite accounts for nearly 3.5 per cent of the sandstone (**Figure 3.4**).

3.2.2.2 High-temperature XRD analysis

A high-temperature XRD analysis of Jodhpur sandstone represents the removal of peaks that correspond to the clay minerals (dickite and kaolinite) after 700 °C, indicating their complete decomposition by that temperature (**Figure 3.5**).

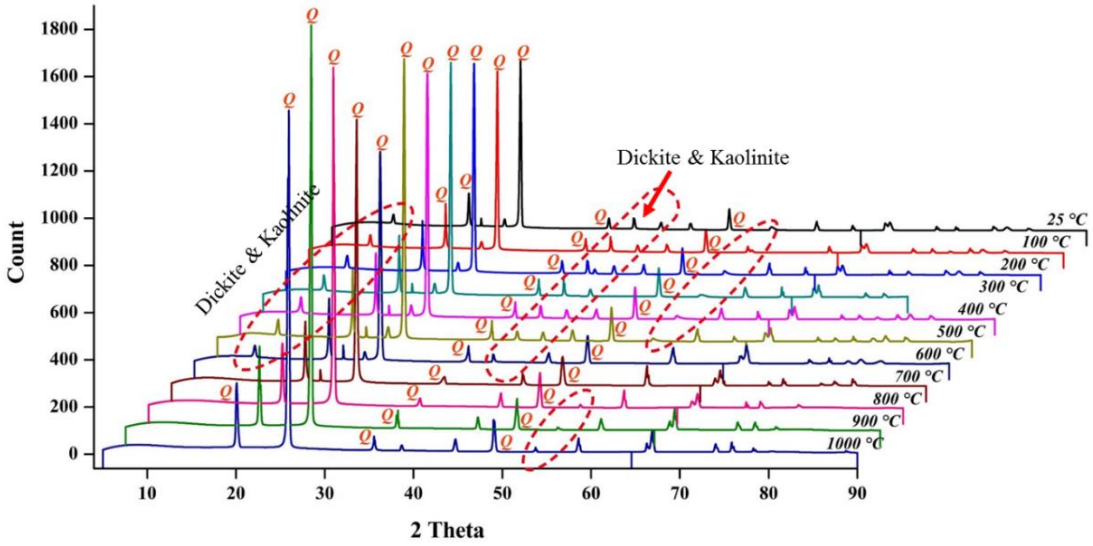

Figure 3.5 *High-temperature XRD analysis of the sandstone*

3.2.3 EDS analysis

Energy Dispersive X-ray Spectroscopy (EDS) shows a high amount of Si and O, and a trace amount of Al, Mg, and Ca in the studied sandstone (**Figure 3.6** and **Table 3.1**).

Table 3.1 *Elemental distribution in the studied sandstone*

Element	Weight per cent
C	6.75
O	56.53
Mg	0.02
Al	0.20
Si	36.53
Ca	0.02
Totals	100.00

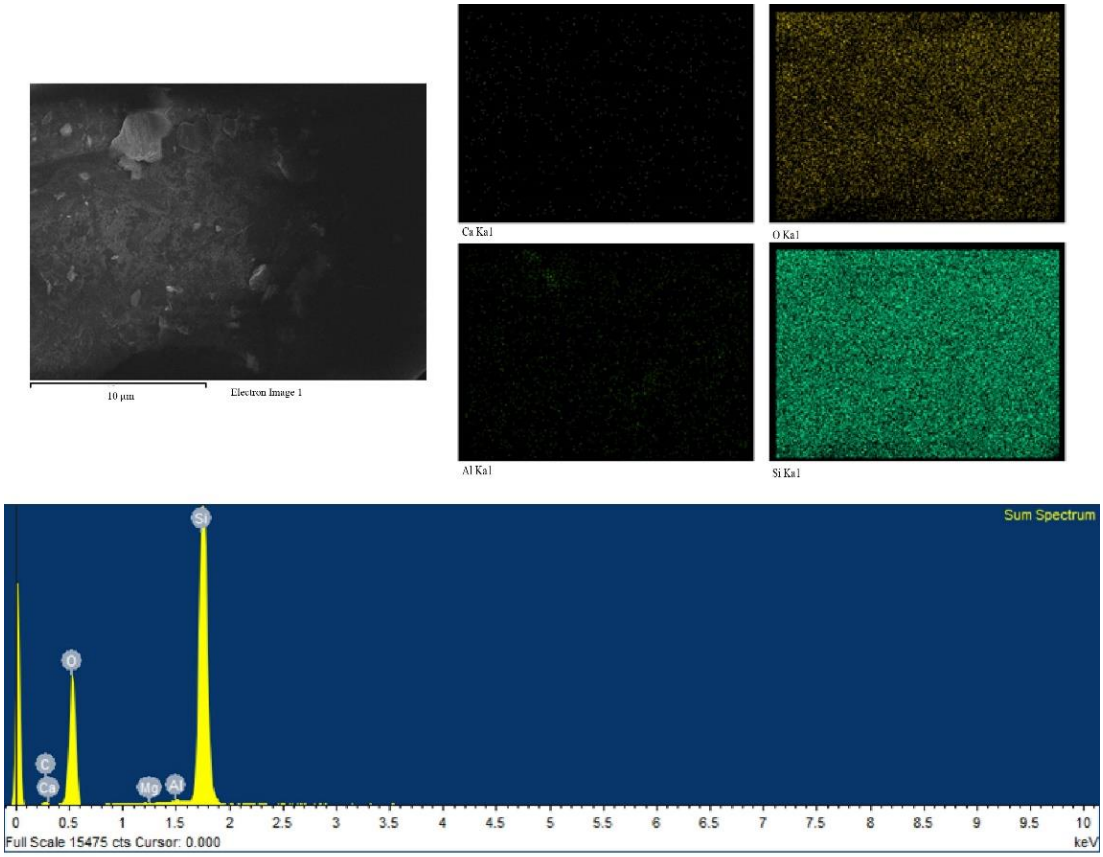

Figure 3.6 *EDS Analysis of the sandstone indicating the presence of dominant elemental phases in the sandstone*

3.2.4 Grain-size analysis

Grain-size analysis is an important aspect from the perspective of sedimentary rock classification. The percentage frequency distribution of the grain size in the studied sandstone is represented in **Figure 3.7**.

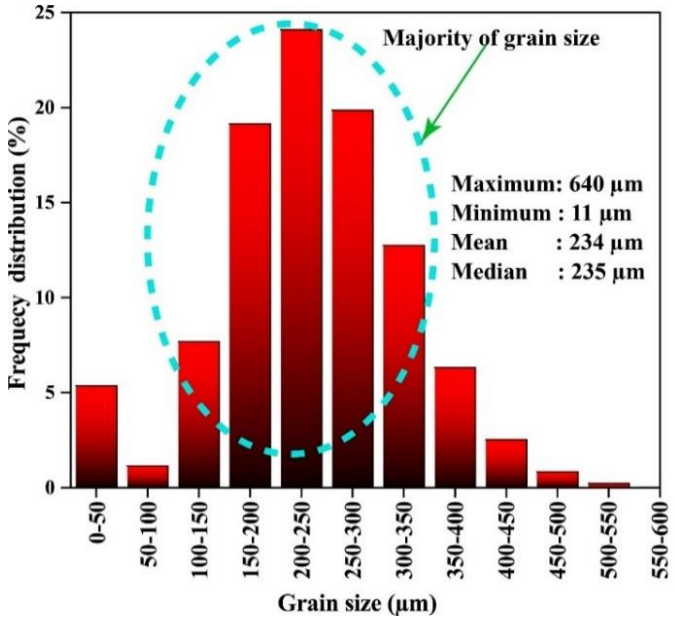

Figure 3.7 *Grain-size analysis of the sandstone*

The maximum and minimum grain sizes of the sandstone are 640 µm and 11 µm; whereas, the average grain size is 234 µm. The sandstone displays a unimodal nature of grain size-variation by which 89 per cent of the grains lie between 100 and 400 µm, and approximately 63 per cent of the grains lie between 200 and 300 µm. Based on a grain-size analysis, the sandstone falls under the category of fine- to medium-grain sandstone (Sam Boggs, 2006).

3.2.5 Nanoindentation hardness test

The hardness of the studied sandstone was measured using nono-indentation techniques by which the hardness can be found by dividing the indentation load by the projected contact area. The known geometry of the indenter and its depth of penetration were used for the estimation of the contact area (A). **Figure 3.8** represents the load curve in comparison with the displacement curve of the nanoindentation. **Table 3.2** summarises the resulting hardness for the sandstone that is found to be 9.307 GPa. However, the hardness value 4.281 GPa and 3.702 GPa seem to be the results of the indentation on the matrix of the sandstone whereas the rest of the values seem to be of the results of the indentation on the grains of the sandstone. While considering the average hardness of the sandstone, only the grains hardness was considered excluding the matrix hardness.

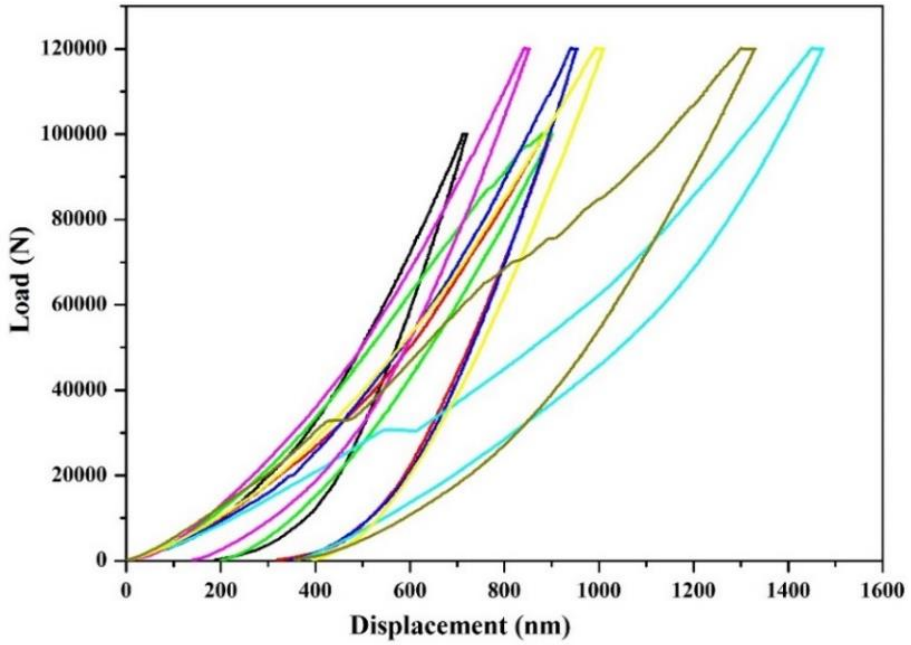

Figure 3.8 *Load versus displacement curve of the nanoindentation analysis used for the measurement of hardness of the studied sandstone*

Table 3.2 *Results of the nanoindentation hardness test of the sandstone*

Number of indents	Contact depth (H_C) (nm)	Maximum load (P max) (N)	Area (nm^2)	Hardness (H) (GPa)	Average H (GPa)
1	451.107	120005	7596209.94	15.798	
2	633.193	100002.4	13640161.1	7.331	
3	946.296	120001.2	28029136.2	4.281	
4	714.014	120003.4	16873981.8	7.111	
5	574.367	120007.7	11498552	10.436	9.307
6	1024.745	120007.6	32415852.2	3.702	
7	704.062	119997	16457623.8	7.291	
8	550.762	99997.7	10689729.4	9.354	
9	661.544	100000.9	14736222.7	6.786	
10	519.380	99995.8	9659379.8	10.352	

3.3 Other rock types used for comparison

The current study mostly investigates the various responses of Jodhpur sandstone. However, in different parts of the thesis, a few other types of sandstone and shale have been included in the experimental investigation to ensure a better comparison of the experimental results. These rock types include Dholpur sandstone, Rajasthan, India; Manoharpur sandstone, Odisha, India; Gondwana sandstone, Jharkhand, India; and Jhiri shale, Madhya Pradesh, India. Different types of sedimentary rocks were selected based on their diverse mineralogy and a few other factors (discussed earlier). A brief description of the general geology and mineralogical descriptions of the rock types that were used have been presented in the section below.

3.3.1 Dholpur sandstone

Dholpur is situated in the eastern most part of Rajasthan, India, and **Figure 3.10a** shows its geological map. Dholpur sandstone belongs to the Upper Bhander group of the Vindhyan Supergroup (**Figure 3.9**). Dholpur sandstone is mostly monomineralic, with quartz being the dominant mineral phase, constituting nearly 95 per cent of the rock; the matrix comprises less than 5 per cent of the rock (**Figure 3.11a**). The rock is composed mostly of equidimensional quartz grains that are well sorted and subrounded to rounded. Quartz grains are arranged close to each other, illustrating their compactness (Sirdesai et al., 2015, 2016b; Mahanta et al., 2016b). **Table 3.3** shows some of the basic geomechanical properties of the rock.

Based on physical observation and macroscopic details, it is found that Dholpur sandstone varies slightly in grain sizes. These properties do affect the mechanical strength and fracture toughness of rocks. Based on these observations, two sets of samples were selected for the

fracture toughness test (**in Chapter 6**). From these two sets, specimens with a smaller grain dimension were considered to be 'set a', and specimens with comparatively larger grains were considered to be 'set b'. However, on a broader scale, both set 'a' and set 'b' represent the same rock type.

Table 3.3 *Geomechanical properties of the rocks used for comparison*

Rock type	UCS (MPa)	P-wave velocity (m/s)	Water absorption (%)	Density (gm/cm^3)	Porosity (%)
Dholpur sandstone	35.40	2594	3.39	2.294	7.79
Jhiri shale	34.31	3829	4.09	2.470	10.13
Manoharpur sandstone	36.74	2273	5.16	1.278	6.59
Gondwana sandstone	72.47	3270	2.19	2.537	5.52

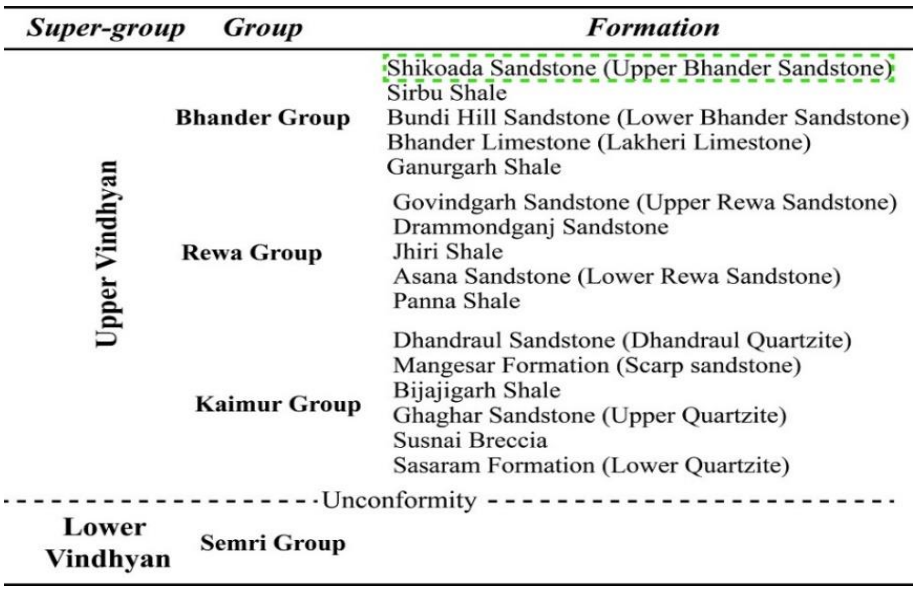

Figure 3.9 *Stratigraphic cuccession of the Vindhyan Supergroup, representing the stratigraphy of Dholpur sandstone (After Bhattacharya, 1996; Valdiya, 2016)*

3.3.2 Manoharpur sandstone

The specimens of Manoharpur sandstone were collected from Odisha, India, and **Figure 3.10c** represents its geological map. Manoharpur sandstone belongs to the lower Kamthi formation of the Lower Gondwana Supergroup. It has minerals such as quartz, kaolinite, dickite, muscovite, siderite, phlogopite and anatase (**Figure 3.11b**).

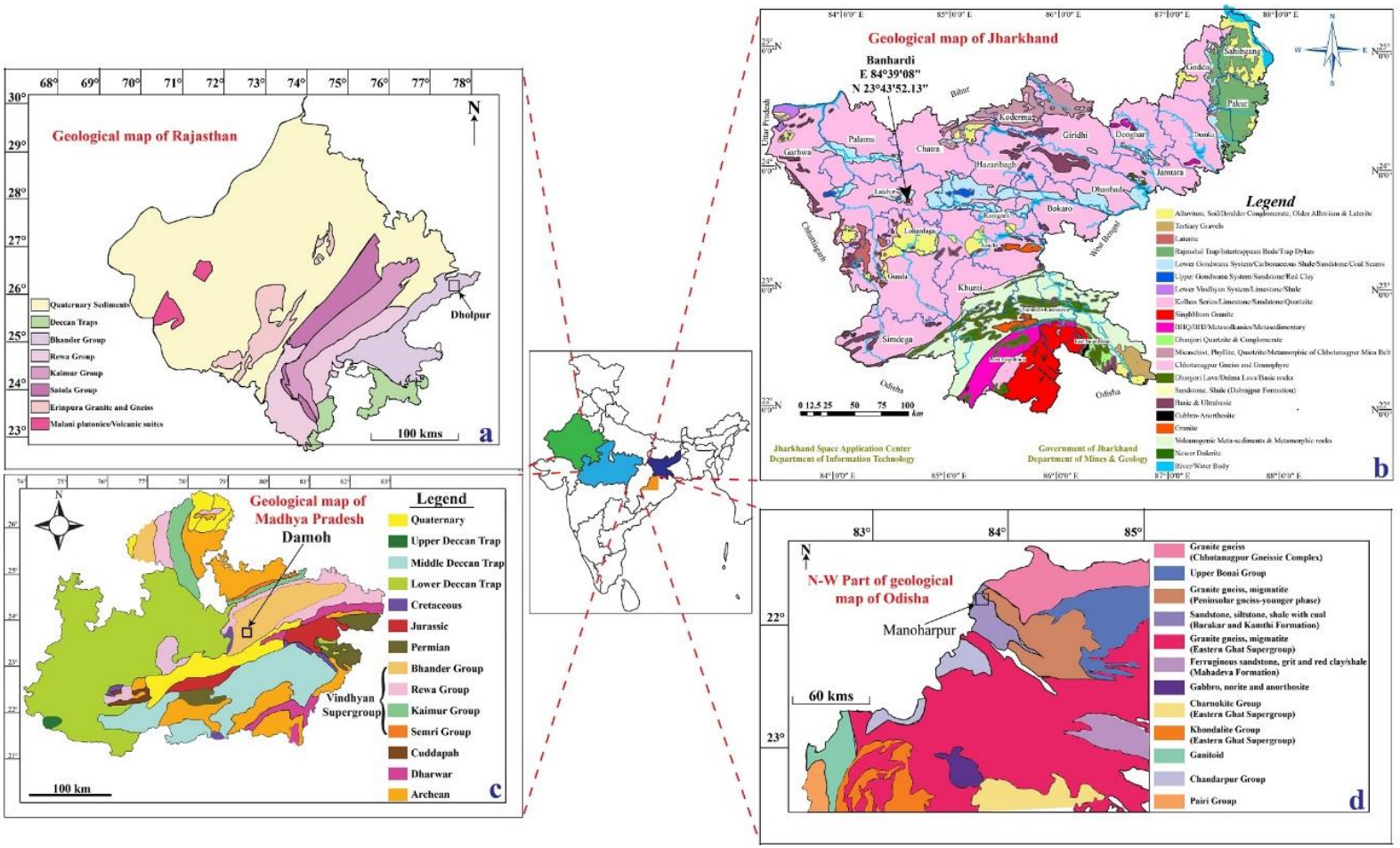

Figure 3.10 *Geological map of the sedimentary rocks that have been used for comparison in the current study. The map at the top left represents the geological map of Rajasthan, India and indicates the location of Dholpur sandstone (a); the map at the top right represents the geological map of Jharkhand, India, and indicates the location of Gondwana sandstone (b); the map at the bottom left represents the geological map of Madhya Pradesh, India, and indicates the location of Jhiri shale (c); the map at the bottom right represents the geological map of Odisha, India, and indicates the location of Manoharpur sandstone (d)*

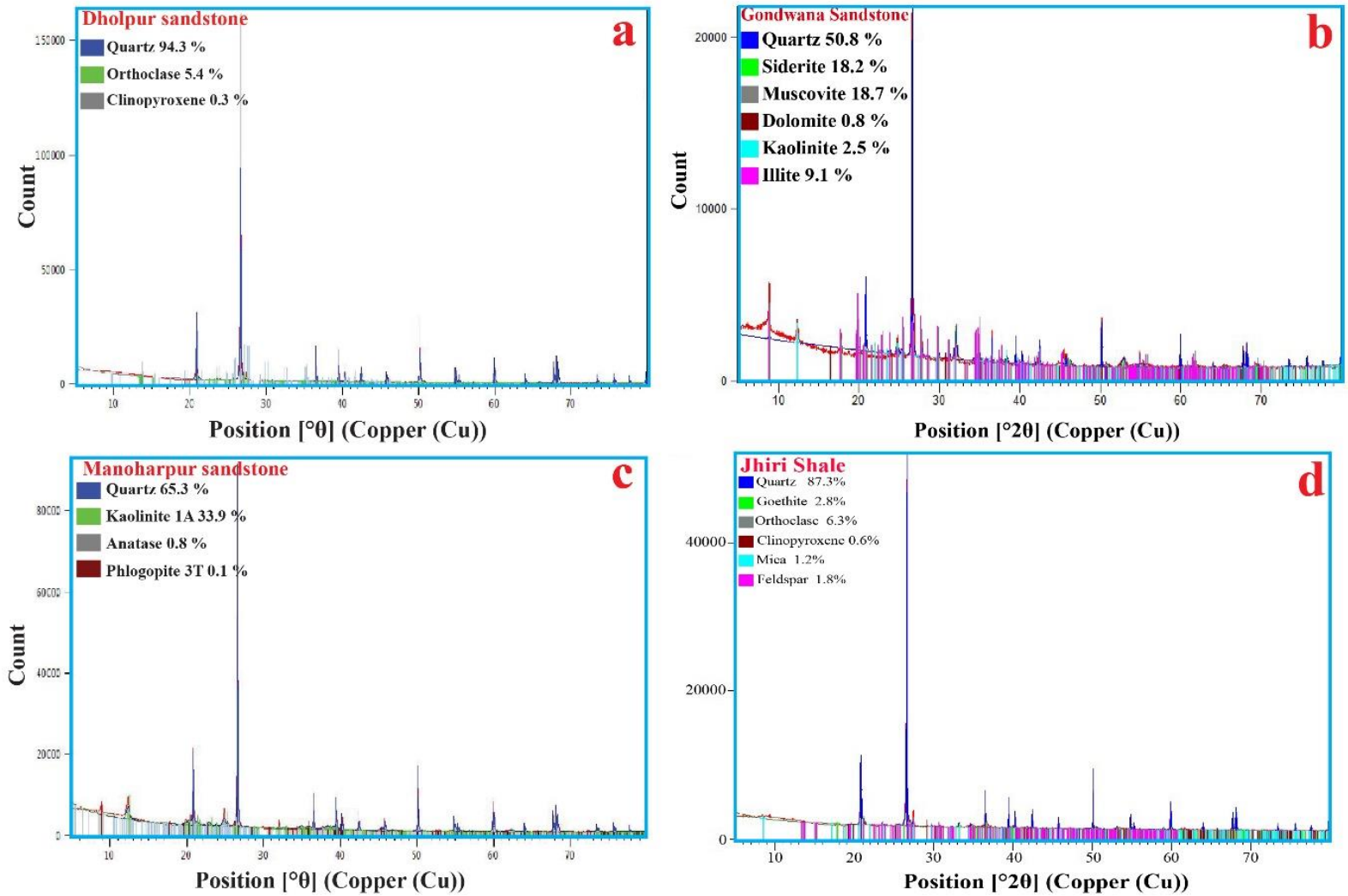

Figure 3.11 *XRD analysis, indicating the presence of different mineral phases within the different rock types that are used for comparison in the study. 'a' represents Dholpur sandstone; 'b' represents Gondwana sandstone; 'c' represents Manoharpur sandstone; and 'd' represents Jhiri shale.*

3.3.3 Gondwana sandstone

Gondwana sandstone belongs to the Banhardi area of Jharkhand, India (**Figure 3.10d**). In Peninsular India, the Gondwana Supergroup has its strata along three major river valleys, namely, Koel–Damodar, Son–Mahanadi, and Pranhita–Godavari. The Gondwana sandstone, used in the current investigation, belongs to the Barakar Formation of the Lower Gondwana Supergroup in the Damodar basin (**Figure 3.12**).

Group	Age		Formation
Upper Gondwana	Cretaceous	Lower	
	Jurrasic	Upper	
		Middle	Dubrajpur
		Lower	
	Triasic	Upper	Mahadev
		Middle	
		Lower	Panchet
Lower Gondwana	Permian	Upper	Raniganj
		Middle	Barren Measure (Kulti)
		Lower	Barakar Karharbari Talchir

Figure 3.12 *Stratigraphic of the Gondwana succession in the Damodar Basin, representing the stratigraphy of Gondwana sandstone (Valdiya, 2016)*

The Barakar formation is a fluvial-alluvial deposit that consists of the conglomerate, sandstones, siltstones and shales with thick beds of coal (Noori and Rais, 2014; Valdiya, 2016). The Gondwana sandstone is massive and heterogeneous; its colour ranges from grey to greyish-white, and grain size ranges from fine to coarse. The XRD analysis of the sandstone suggests that it is a clay-rich sandstone with nearly 30 per cent of clay content in the form of siderite; illite and kaolinite (**Figure 3.11b** and **Table 3.4**).

3.3.4 Jhiri shale

Representative samples of shale were collected from Damoh district in the state of Madhya Pradesh. The location from which these samples were collected is present in the northeastern part of the state, nearly 220 km away from Bhopal, the capital of the state. Geologically, it comprises the rocks of Rewa and the Upper Bhander groups of the Vindhyan Supergroup (Prasad and Rao, 2006). The geological map of the state Madhya Pradesh, indicating the location of the study area is shown in **Figure 3.10b**. The rock is medium- to fine-grained shale.

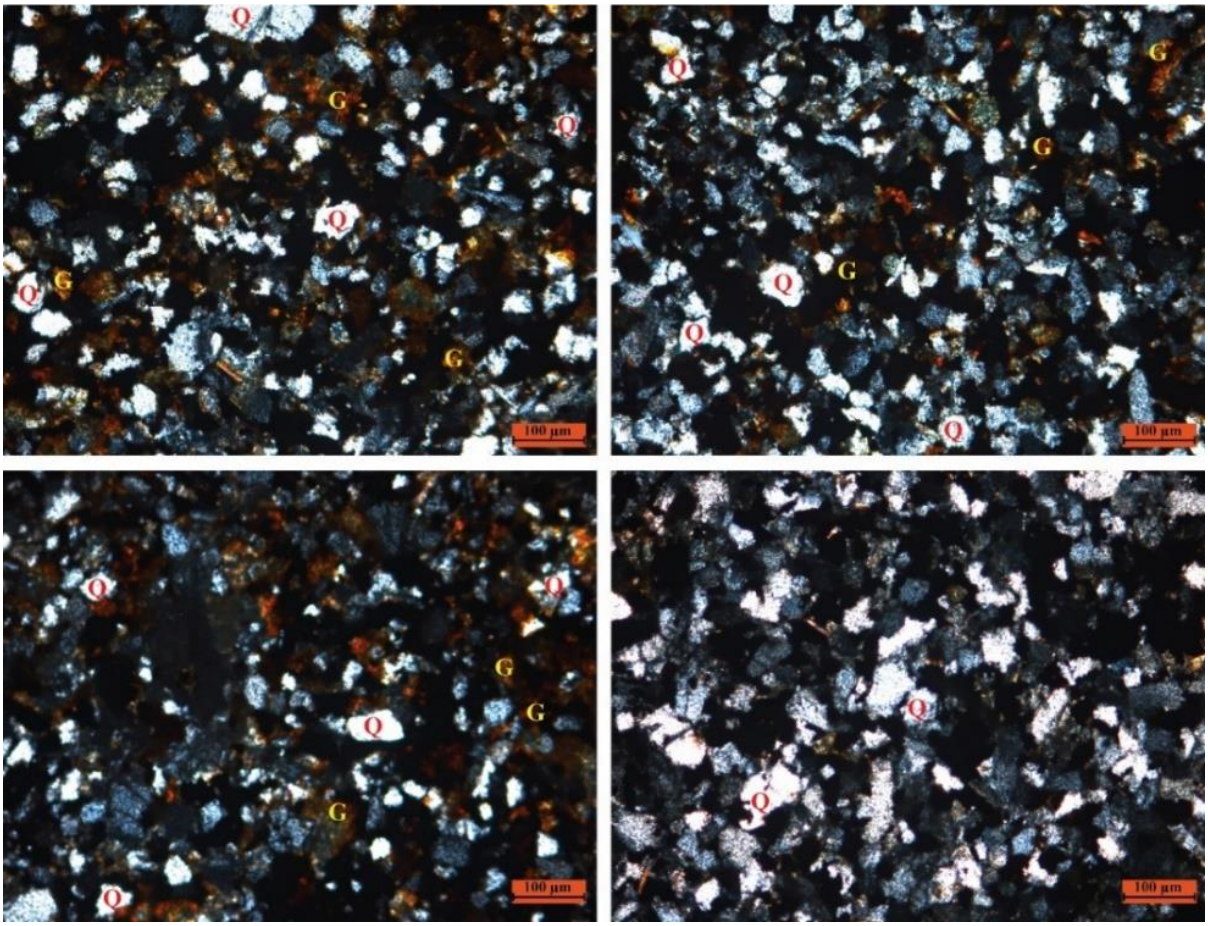

Figure 3.13 *Micrographic thin section images of Jhiri shale, which indicate a significant presence of minerals such as quartz and goethite in the rock*

The various geomechanical properties of other rock types are represented in **Table 3.3**. XRD analysis was performed in order to identify the different mineral phases that were present in the rock. The X-ray diffractograms are presented in **Figure 3.11d**. The XRD suggest the presence of various mineral phases such as quartz, illite, goethite, feldspars, orthoclase, and mica minerals. Of these, quartz is the dominant mineral phase and forms more than 80 per cent of the rock (**Figure 3.13**).

Table 3.4 summarises the various dominant mineral phases that are present in Jodhpur sandstone Dholpur sandstone, Manoharpur sandstone, Gondwana sandstone, and Jhiri shale. Among these sandstones, Manoharpur sandstone is the most clay-rich rock with minerals such as kaolinite, which constitute nearly 33 per cent of the rock; whereas, Dholpur sandstone is devoid of any significant clay minerals. Jodhpur sandstone contains nearly 11.2 per cent of clay minerals (dickite and kaolinite) along with some carbonate mineral in the form of calcite.

Table 3.4 Dominant mineral phases in the three sandstones (***Figure 3.11***)

Sandstone Type	Dominant Mineral Phases

Jodhpur Sandstone	Quartz (83.9 %), Dickite (5.7 %), Kaolinite (5.5 %), Calcite (3.5 %),
Dholpur Sandstone	Quartz (94.3 %), Orthoclase (5.4 %)
Manoharpur sandstone	Quartz (65.3 %), Kaolinite (33.9 %)
Gondwana Sandstone	Quartz (50.8 %), Siderite (18.2 %), Muscovite (18.7 %), Illite (9.1%), Kaolinite (2.5 %)
Jhiri shale	Quartz (87.3 %), Goethite (2.8 %), Orthoclase (6.3 %)

3.4 Specimen preparation, and the methodology of the heat treatment used for experimental investigation

From the outcrop, blocks of 30 x 30 x 15 cm^3 of the studied sandstone were collected. As per the ASTM standard, the minimum specified diameter of the specimen should not be less than 47 mm. With this in mind, the blocks of sandstone were cored into cylindrical specimens that had a diameter of 51 mm. As per ISRM standards, the end-face of the specimens should be flattened to 0.002 mm. To achieve the recommended standard and to avoid other end-face irregularities, the end-faces of the prepared cylindrical specimens were ground with the help of a face grinder and a v-block, as shown in **Figure 3.16a**. The specimens were prepared as per the recommendations of American society for testing and materials (ASTM) such as ASTM D3967-08, (2008); ASTM D4543 (2008); and ASTM D7012–14 (2004). **Figure 3.14** and **Figure 3.15** represent the cylindrical and disc specimens, respectively.

Figure 3.14 *Prepared cylindrical specimens for the UCS test that is 51 mm in diameter and 102 mm in length*

Figure 3.15 *Prepared disc specimens for the indirect tensile test that is 51 mm in diameter and 25 mm in width*

The prepared core specimens were subjected to different temperatures in an electric furnace (**Figure 3.16b**). The maximum temperature that was achieved for thermal treatment is 900 °C. Prior to the thermal treatment, the specimens were dried at 105 °C for 24 hrs to remove natural moisture. Various temperatures such as 100 °C, 200 °C, 300 °C, 400 °C, 500 °C, 600 °C, 700 °C, 800 °C, and 900 °C were achieved in order to enable thermal treatment.

The heat treatment is done in three stages (**Figure 3.16c**):

a. To avoid any thermal shock during the treatment, the heating rate was fixed at 5 °C/min until the target temperature was reached.
b. Once the target temperature was achieved, the specimens were kept at the same set of temperatures for three hours to enable homogeneous heat distribution throughout the specimen.
c. After the scheduled time, the specimens were cooled to room temperature.

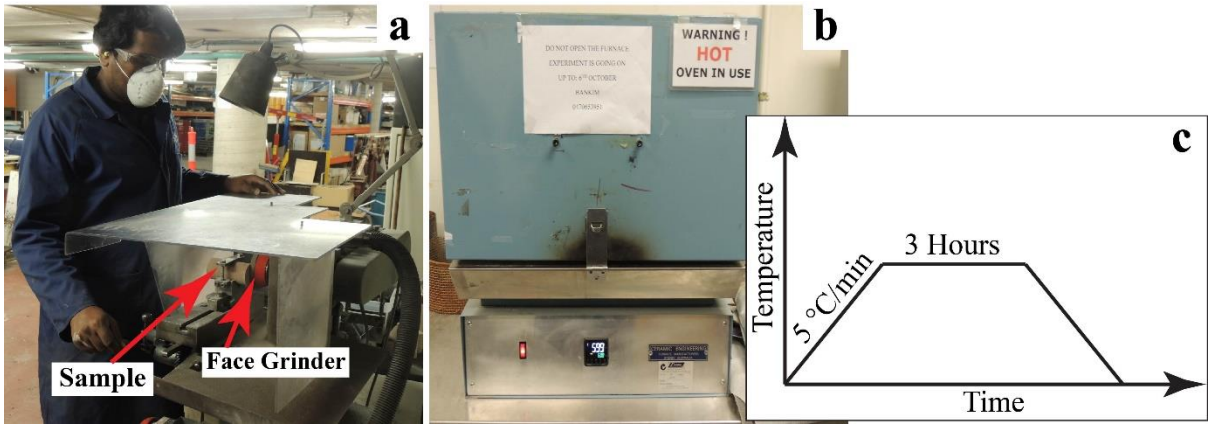

Figure 3.16 *Face grinding of the specimens prior to testing (a). The furnace used for the thermal treatment (b), along with the heating process (c)*

Upon exposure to different degrees of heating, various structural damages were induced in rocks. When the studied sandstone was exposed to temperatures such as 950 °C and 1000 °C

(**Figure 3.17**), surficial thermal cracks were observed; hence, keeping this in mind, the maximum temperature for the experimental investigations was set to 900 °C, and different experiments were conducted accordingly.

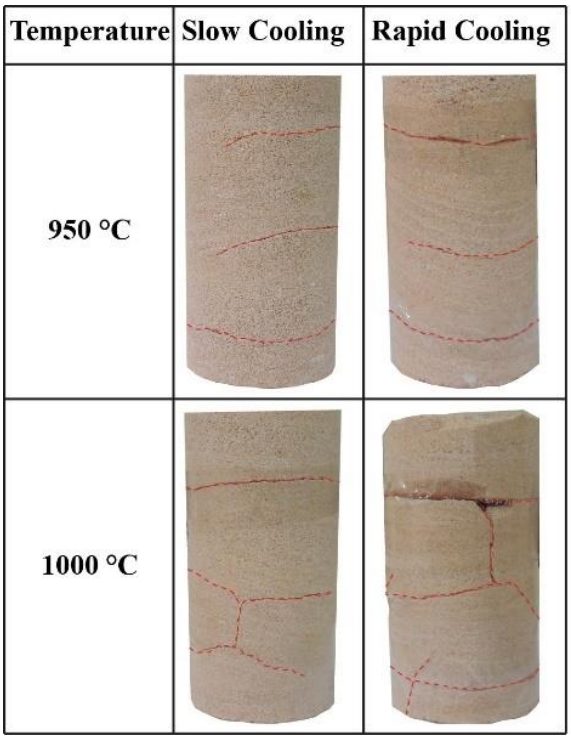

Figure 3.17 *Structural damages induced in Jodhpur sandstone at 950 °C and 1000 °C for both rapidly cooled and thermally treated specimens*

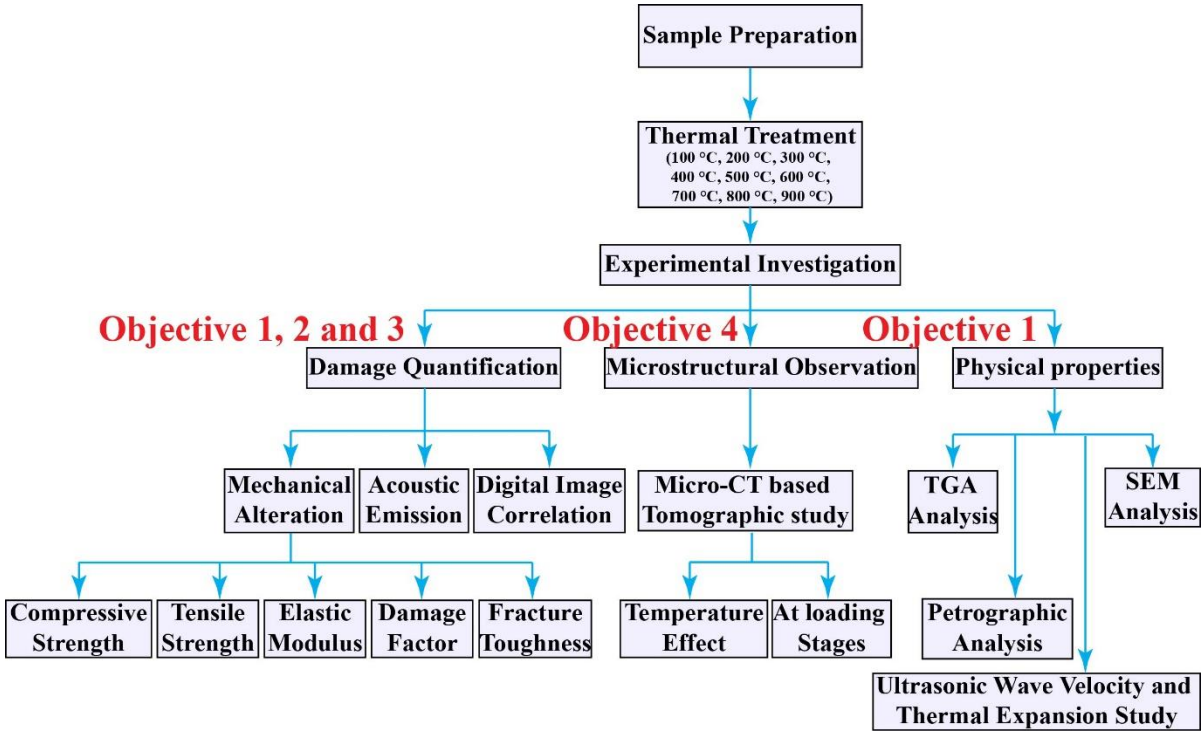

Figure 3.18 *Schematic diagram of the workflow that was followed in the current investigation*

In most of the experimental analyses during the research work, specimens with dimensions mentioned above were used. However, additionally, at certain stages of the experimental investigation, specimens that had different dimensions were also used. These modifications in the specimens were due to experimental limitations. Therefore, whenever specimens that had a different dimension were used, their dimensions were mentioned in the methodology section of those experiments.

After the treatment and prior to testing, the specimens were wrapped in polyethene sheets to prevent the thermally treated specimens from being exposed to any moisture. **Figure 3.18** represents the schematic workflow that is followed to achieve the different objectives of the research work.

Chapter 4 Experimental investigation of the physical and mechanical behaviour of sandstones with varying temperatures

4.1 Investigation of physico-morphological responses

4.1.1 Macroscopic observation

Prior to 400 °C, Linyi sandstone is dark red, which turns to brick red in the interval between 500 °C and 700 °C. Thereafter, it changes to a khaki colour, when the temperature exceeds 800 °C. The change in colour as a function of temperature is predominantly due to the transition of iron elements from a state of low valence to a state of high valence (Sun et al., 2017). In general, when rocks are exposed to high temperatures, they undergo a certain amount of colour change that is predominantly dependent on the amount of Fe in the rocks. **Figure 4.1** and **Figure 4.2** represent the colour variation of thermally treated and rapid-cooled sandstone specimens, respectively. The EDS analysis (**Figure 3.6**) of Jodhpur sandstone does not indicate the presence of Fe in the sandstone; therefore, no significant colour change can be observed with an increase in temperature.

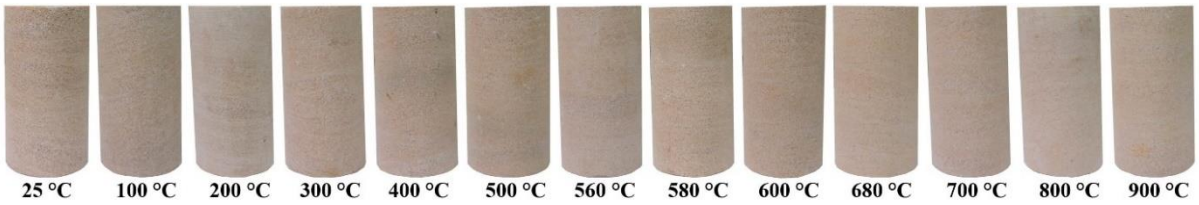

Figure 4.1 *Colour change in thermally treated sandstone specimens*

Figure 4.2 *Colour change in rapid-cooled sandstone specimens*

Upon exposure to a temperature of 950 °C and 1000 °C, macrocracks in the form of surface cracks and crossing cracks (on the side face) were introduced into the structure of the rocks (**Figure 3.17**). Additionally, high-temperature exposure to the rock resulted in the formation of a large amount of powder on the surface, which shows several stages of thermal damage due to heating.

4.1.2 Petrographic thin-section images of the sandstone

The petrographic micrographs of the thermally treated and rapid-cooled Jodhpur sandstone are shown in **Figure 4.3** and **Figure 4.4**, respectively. With the progressive increase in

temperature, a zigzag-corrugated boundary between the quartz grains can be observed (at 200 °C). With further increase in the temperature, at 400 °C, the roundness of the grains is preserved in a few places; at the sites, triangular contacts between the grains can be observed. A fused grain boundary can be observed up to a temperature of 400 °C, which indicates possible expansion of minerals as a result of the thermal stress.

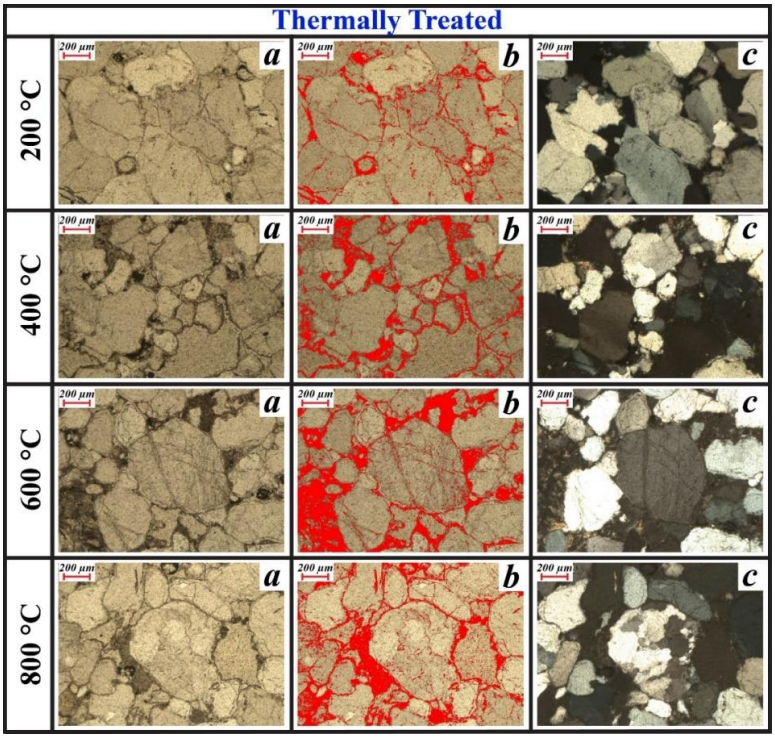

Figure 4.3 *Petrographic thin-section images of thermally treated Jodhpur sandstone*

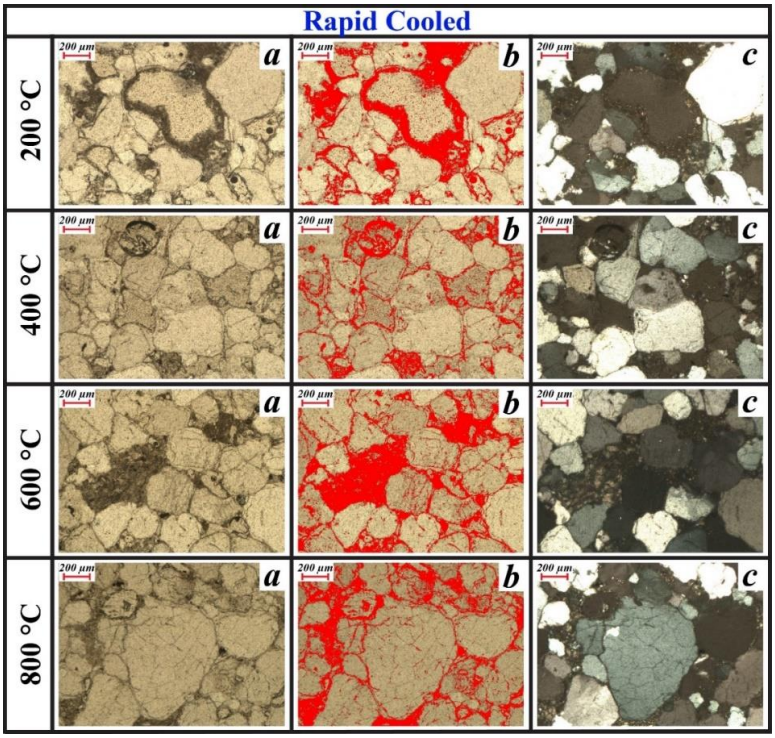

Figure 4.4 *Petrographic thin-section images of rapid-cooled Jodhpur sandstone*

Up to a temperature of 400 °C, the roundness of the grains disappear, and rarely is any rounded mineral observed at this temperature. The appearance of a fracture in the grains can be observed at up to 600 °C. Different types of cracks such as intergranular and transgranular cracks can be observed at this temperature (**Figure 4.5**). The micrographs of the sandstone at 800 °C indicate the presence of a new cementing material. A few polycrystalline quartzes can be observed at this temperature.

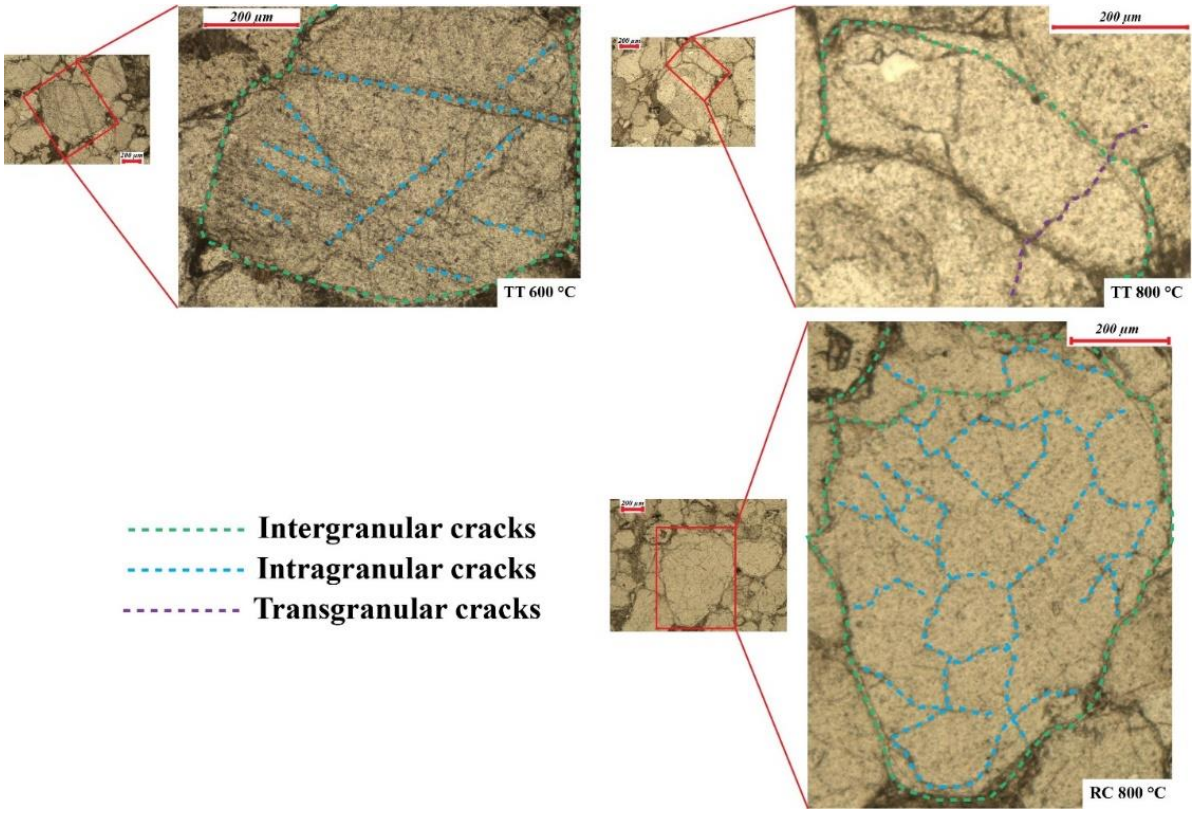

Figure 4.5 *Petrographic thin-section magnified images of Jodhpur sandstone at TT_600 °C, TT_800 °C, and RC_800 °C*

4.1.3 SEM study for surface morphology

An SEM (JSM-6390, JEOL) was used for the observation of microstructures that were present in the sample. The scanning was performed at 20 kV acceleration voltage at a working distance of 10–20 mm. Samples were carbon-coated on a carbon coater (EM ACE 200, Leica) prior to the SEM study. SEM images of the topography and morphology of the grain structures and the microfractures were taken. The SEM images of the rock are shown in **Figure 4.6**.

The effectiveness of the temperature in the structure of rocks and the evolution of the internal structure can be observed with the help of the SEM technique. The photomicrographs of the SEM, which are at 25 °C, represents the original pores and complete and large particles with a rough surface. The damage threshold of the sample is 400 °C. By 500 °C, there is a rapid

growth in the volume of the quartz, which results in parallel cracks in certain minerals. Further increase in temperatures results in the damage of the structure, which is indicated by the presence of induced microcracks and pore spaces (**Figure 4.6**).

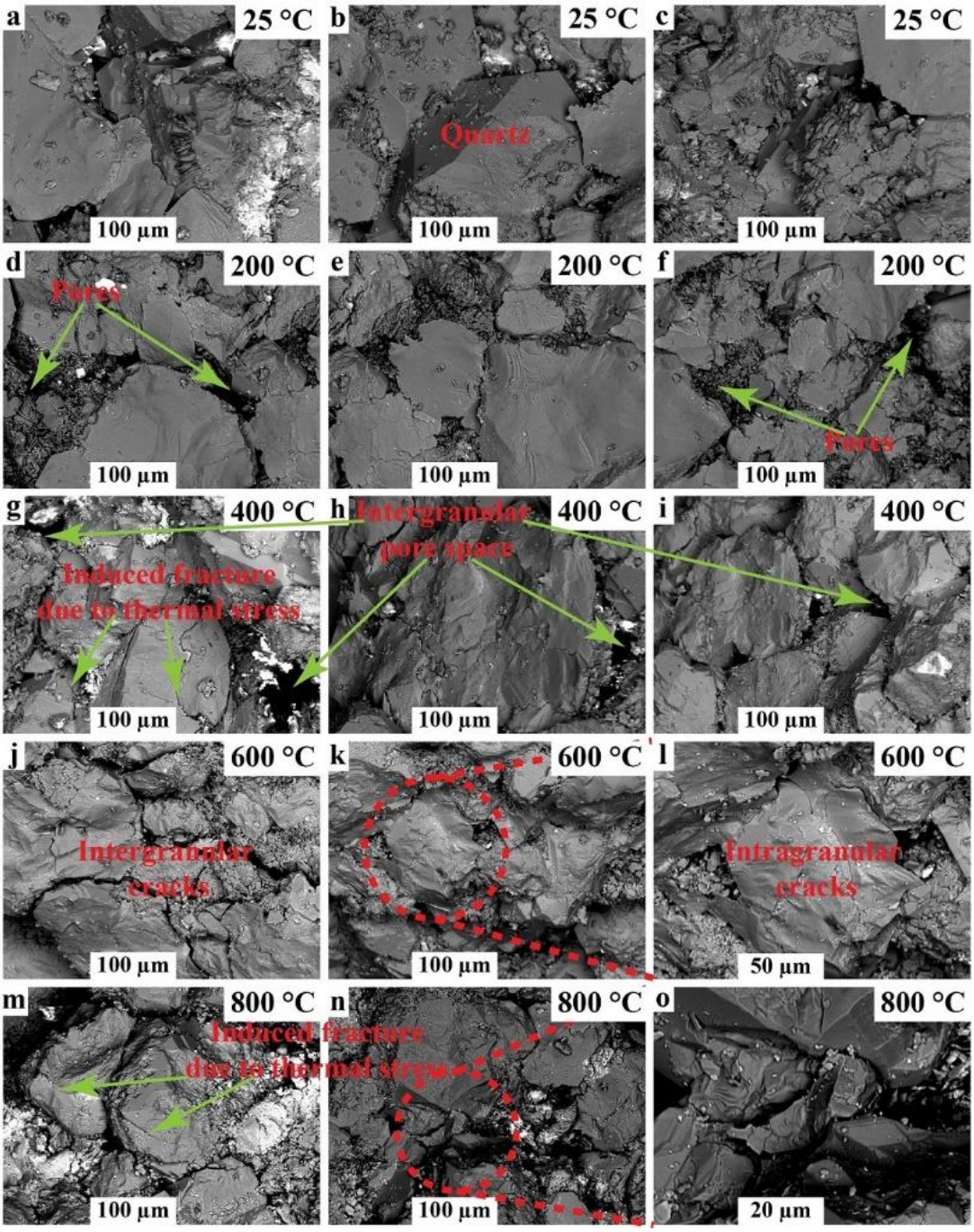

Figure 4.6 *SEM images of the sandstone at different temperatures*

4.1.4 Effect of temperatures on the seismic wave velocity of sandstones

The various elastic properties of the rocks propagate acoustic waves in the rocks. The propagation of P-wave velocity in rocks is influenced by the mineral composition, structure of the rock, degree of cementation, and occurrence of pores and cracks. Acoustic wave

measurements, when these factors are considered, play an important role in the classification of the rock. The extent of damage to the structure of the sandstone due to exposure to high temperatures can be observed in the change in the P-wave velocity; this is because the P-wave velocity of the rock is closely related to the mechanical properties and the physical properties (structural characteristics, density, moisture content, porosity and such others.) of the rock. Hence, indirectly, the variation of the P-wave velocity due to the temperature reflects the variation of these properties of the rock. Therefore, the measurement of the P-wave velocity of the rock will evaluate the extent of the effect of heating on the rock.

Cylindrical specimens of Jodhpur sandstone, which were 51 mm in diameter and 102 mm in length, were used for the measurement of P-wave velocity by using the portable ultrasonic nondestructive digital indicating tester (PUNDIT) lab instrument. Two piezoelectric 54 kHz transducers are attached to the two end faces of the specimen along the axial direction. The transmitter converts the electrical pulses into mechanical pulses that travel through the length of the specimen, and the receiver converts the mechanical pulses into electrical pulses. Based on the travel time of the pulses through the specimens, the seismic P-wave velocity is determined. During measurements that would enable the removal of the air gap and ensure better contact between the specimen and the transducer, a layer of couplant was coated on the end-surface of the specimen. The schematic of the measurement of the ultrasonic wave velocity has been represented in **Figure 4.7**.

Figure 4.7 *Experimental setup used for the measurement of the P-wave velocity of the sandstone*

With a progressive increase in temperature, from room temperature to 100 °C, an increase in the P-wave velocity was observed for both the thermally treated and rapid-cooled specimens. After 100 °C, the P-wave velocities followed a decreasing trend up to 800 °C. However, in rapid-cooled specimens, the decreasing trend is quite sharp whereas, in thermally treated specimens, the decreasing trend was gentle up to 400 °C, followed by a sharp decreasing trend up to 800 °C. For both types of specimens, no significant increase or decrease was observed in the temperature window from 800 °C to 900 °C (**Figure 4.8**).

In the temperature window between 25 °C and 300 °C, on the one hand, the free water that is present in the rock turns into steam and escapes from the open pore spaces, which increases the pore volume. On the other hand, the process of heating results in the expansion of the mineral grains, which fills certain pore spaces. Due to the combination of both these effects, the pore volume of the rock decreases at certain times and increases at others (Sun et al., 2017).

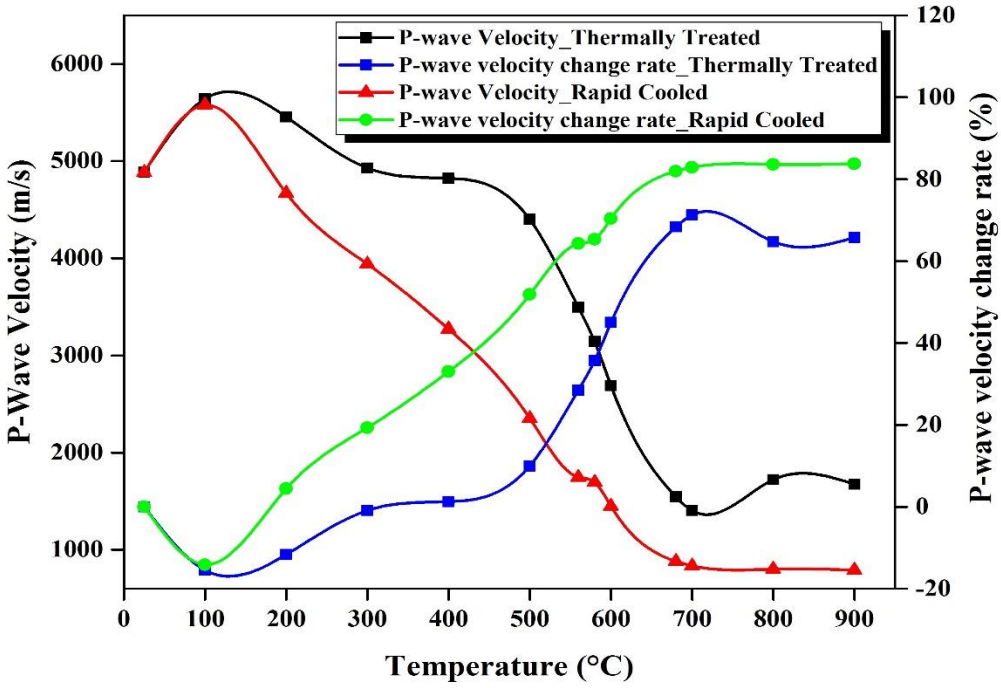

Figure 4.8 *Variation of P-wave velocities of Jodhpur sandstone in both thermally tretaed and rapid-cooled specimens*

At 400 °C, the P-wave velocity of thermally treated and rapid cooled specimen falls to 1.26 per cent and 33 per cent, respectively. In the second stage of the heating process, the decomposition of clay minerals and the removal of structural water turn into an increase in the amount of pore spaces, which results in a decrease in the P-wave velocity of the rock. Additionally, the phase transformation of α-quartz to β-quartz occurs at 573 °C. Although the transformation is reversible in nature, the lattice dislocation, expansion and other lattice defects cannot be

recovered completely, which affects the propagation of the P-wave in the rock. From 700 °C to 900 °C, the microcracks accumulate and connect with each other to form macrocracks that can be observed at the surface of the rock specimen. The thermal decomposition of calcite minerals in this temperature range further influences the structure of the rock, thereby influencing the propagation of the P-wave in the rock. Above 700 °C, the calcite decomposes and transforms to portlandite and CaO. By 900 °C, the calcite collapses completely, and the rock is broken down with the formation of cracks. In addition to this effect, β-quartz transforms to β-tridymite at 870 °C, which increase the volume of quartz grains by 16 per cent (Sun et al., 2017). These effects that take place from 700 °C to 900 °C result in a rapid decrease in the P-wave velocity. Up to 600 °C and 900 °C, the P-wave velocity of thermally treated specimens falls to 44 per cent and 65 per cent, respectively, whereas, in rapid-cooled specimens, it falls to 70 per cent and 83 per cent, respectively, when compared to room temperature.

4.1.5 Thermal expansion of sandstones in response to varying temperatures

The thermal expansions of Jodhpur sandstone have been shown in **Figure 4.9**. Both the linear and lateral expansions of the sandstone follow an increasing trend with increasing temperatures. However, the thermal expansion of the thermally treated sandstone specimens was significantly different when compared to the thermal expansion measured at the heated condition (soon after the temperature treatment).

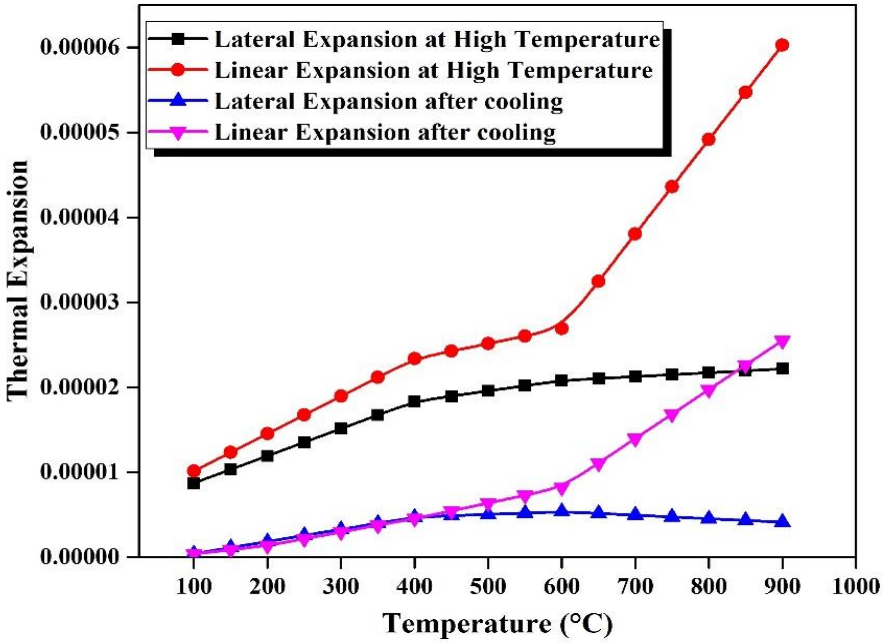

Figure 4.9 *Thermal expansion of the sandstone at a high temperature and after cooling to room temperature*

The expanded grains as a result of heat treatment contract with progressive cooling. However, significant irreversible structural damages remain in the structure of the rock. Under the influence of temperatures, the shapes, sizes, and masses of rocks are altered, which results in a change in the volume. In comparison to quartz-dominated rocks, carbonate rocks and rocks that have a high amount of clay exhibit greater variation in the density and in the volume change due to various chemical reactions in response to high temperatures (Yavuz et al., 2010; Sirdesai et al., 2017a). The high temperatures results in the enlargement of grains along different crystallographic directions, which facilitates the induction of microcracks into the structure of rocks (Den'gina et al., 1993). Factors such as the mineralogical composition, microfractures, pore spaces and fluid phases predominantly control the extent of thermal expansion in rocks (Siegesmund et al., 2000; Sirdesai et al., 2017a). Based on the experimental results, Somerton (1992) reported that largely quartz-rich rocks exhibit a behaviour that is similar to a pure quartz crystal. However, the presence of any other mineral does affect the behaviour of the rocks at high temperatures.

4.1.6 Mass loss of sandstone in response to varying temperatures

The analysis and characterisation of the internal damages that are introduced due to the temperature are quite difficult. Mass loss indirectly represents the change in the internal structure, which occurs due to high temperatures. In general, heating results in mass loss, which is primarily attributed to the loss of free water and constitutional water. Additionally, the formation of microcracks, widening of preexisting cracks and formation of powder enhance mass loss.

Mass loss increased exponentially along with the temperature (**Figure 4.10**). The complete profile of mass loss can be divided into three major parts based on the trend of the curve. In the temperature window from room temperature to 400 °C, the mass loss has no pronounced variation relative to the other two stages that occur later. In this stage, the free water that is present in the pore spaces turns into steam and escapes from the open pores (Jian-ping et al., 2010; Sun et al., 2017). Pore water possesses little mass; hence, the loss of pore water has no obvious effect on the mass loss curve. In the second stage (400 °C – 600 °C), the mass loss is predominantly due to the removal of the structural water and the dehydration and dihydroxylation of the clay minerals that are present in the rock.

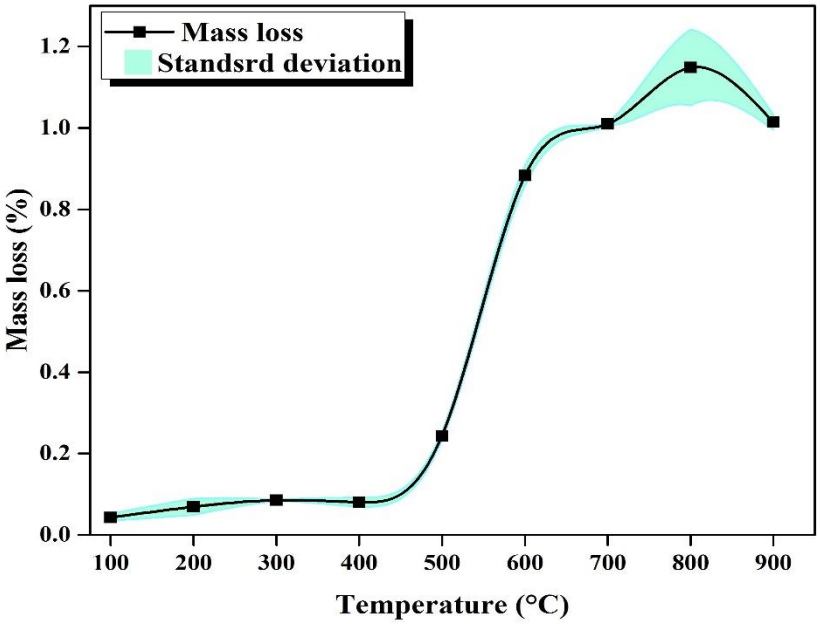

Figure 4.10 *Variation of mass loss of Jodhpur sandstone after exposure to high temperatures*

A rock is a heterogeneous body that comprises various mineral phases. The produced thermal stress results in the breaking of the links between mineral grains, which results in the breaking away of some of the particles, leading to further mass loss. However, the last stage (600 °C – 900 °C) of the curve does not possess any significant variation in comparison to the second stage. In the third stage, the decomposition of calcite or dolomite (carbonate minerals) occurs at nearly 700 °C; the carbon dioxide that forms as a result of the decomposition escapes, resulting in mass loss in that temperature range (Tian et al., 2012). In addition, during the third stage of the heating process, from 600 °C to 900 °C, the internal cracks accumulate and connect to form macrocracks gradually; this formation progresses from the inside to the surface in the form of wing cracks on end faces and cross cracks on the side face. Large amounts of powder and fragments break away from the surface of the rock, resulting in cracks in the mass loss in the third stage of the heating process (Sun et al., 2017).

4.1.7 Thermogravimetric analysis of sandstones

Thermogravimetric (TG) analysis was carried out at sophisticated analytical instrument facility (SAIF), IIT Bombay, India. The Perkin–Elmer diamond thermogravimetric/differential thermal analyser (DTA) (**Figure 4.11**) was used for the TG analysis of the studied sandstone. In this analysis, a certain weighted mass of the sample (nearly 100 g) was heated from room temperature to the required temperature at a constant rate of 5 °C/min. TG analysis was performed in an inert environment. The TG data were used for the measurement of the weight

loss; whereas, the DTA curve was used for the measurement of various chemical changes that occured in the samples due to exposure to high temperatures.

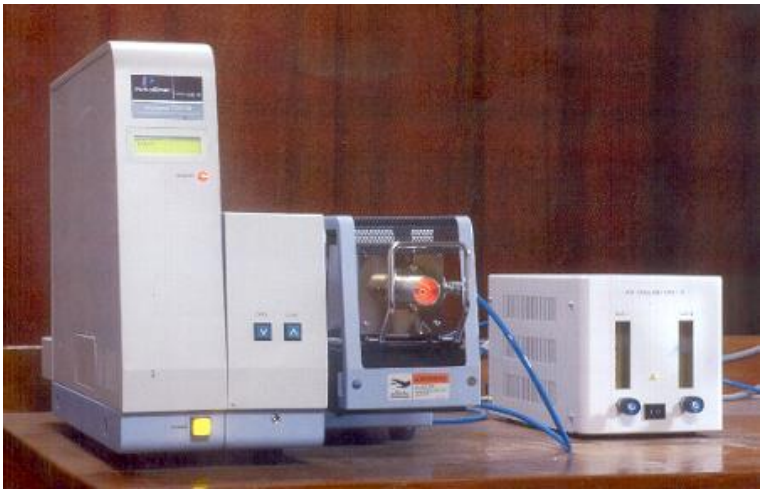

Figure 4.11 *Perkin Elmer Diamond thermogravimetric/differential thermal analyser*

Based on the studied TG/DTA results, a drastic loss of weight was observed in the range of 400 °C to 680 °C, which suggests a major structural damage in that temperature zone (**Figure 4.12**). The structural damage to the microstructure of the sandstone can be explained in terms of the decomposition and dehydroxylation of clay minerals (dickite and kaolinite) and the inversion of α-quartz to β-quartz at 573 °C. Minerals such as kaolinite, siderite, illite, calcite, dolomite, magnetite, pyrite and pyrrhotite undergo various chemical alterations in the range of 450 °C to 700 °C (Just and Kontny, 2012; Sun et al., 2015, 2016b). **Table 4.2** presents a list of minerals that undergo different chemical alterations at different temperature levels.

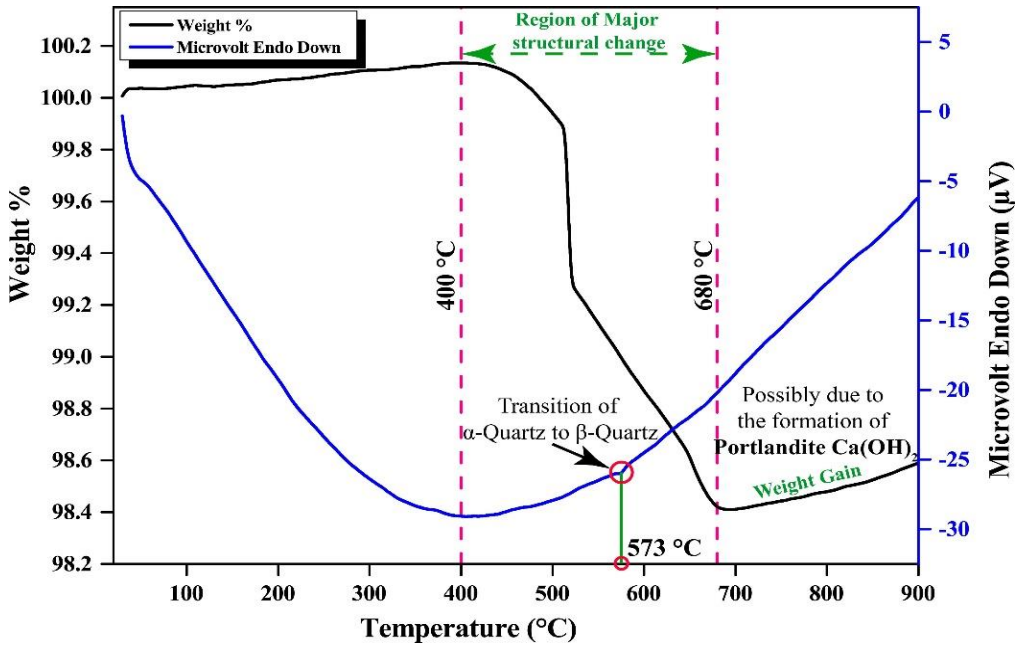

Figure 4.12 *Thermogravimetric Analysis of the studied sandstone*

In the studied sandstone, an increase in its weight was observed after 700 °C. This can be due to the formation of a new cementing material in the form of portlandite (Hajpal and Torok, 2004), which may be the by-product of the dihydroxylation of dickite ($Al_2SI_2O_5(OH)_4$) (Stoch and Wacławska, 1981) at 680 °C and the decomposition of calcite ($CaCO_3$) at approximately 700 °C (Barshad, 1972; Somerton, 1992). A segment of weight gain in the TG curve after 680 °C soon after the dehydroxylation of dickite indicates the formation of new cementing materials.

4.2 Investigation of thermo-mechanical responses

Overview

A coupled investigation by using AE, digital image correlation through *ARAMIS*, micro-CT techniques, and thermogravimetric analysis is performed to investigate the mechanical responses of sandstone to increasing temperatures. UCS, tensile strength, elastic modulus, and failure strain were investigated in response to different temperatures. UCS, tensile strength and elastic modulus of sandstone aligned with increasing temperatures in an overall decreasing trend. The maximum and minimum UCSs of sandstone were found to be at 400 °C and 700 °C respectively, and as compared to the ambient conditions, the UCSs at these temperatures were found to be 11 per cent more and 38 per cent less, respectively. The maximum and the minimum tensile strengths of the sandstone were observed at 300 °C and 700 °C, respectively, which are 5 per cent more and 70 per cent less, respectively, in comparison to the ambient conditions. Early crack initiation and crack damage phenomena in high-temperature treated specimens were observed from the AE results. The deformation was further analysed by using *ARAMIS*, and strain levels were visually quantified. The widespread distribution of high strain was observed in samples that were treated at 700 °C.

4.2.1 Experimental methodology

4.2.1.1 Mechanical strength tests

A height-to-diameter ratio of 2:1 for the UCS test and a thickness-to-diameter ratio of 0.5 for the tensile test is maintained in all the specimens. Mechanical tests for thermally treated and rapid cooled specimens are performed by using the Shimadzu compression machine that has a maximum capacity of 300 kN. During the compression test, the stress-strain behaviour of the thermally treated and rapid cooled sandstone was acquired, which was later analysed to determine Young's modulus and the damage factor. Prior to the test, electric strain gauges were attached to the surface of the specimens to measure the deformation of the specimen in response to the applied load. For the measurement of AE characteristic during the failure of the

specimens, AE sensors were attached to the specimens (**Figure 4.13**). In addition to the strain measurements by means of strain gauges, the digital image correlation (DIC) technique with the help of ARAMIS was also used to visualise the development of various strain fields on the specimens with progressive deformation (detail about the AE and ARAMIS setup has been mentioned in the next section). The experimental loading configuration of the compression machine along with the attached AE sensors and the well-focused ARAMIS system are represented in **Figure 4.14**.

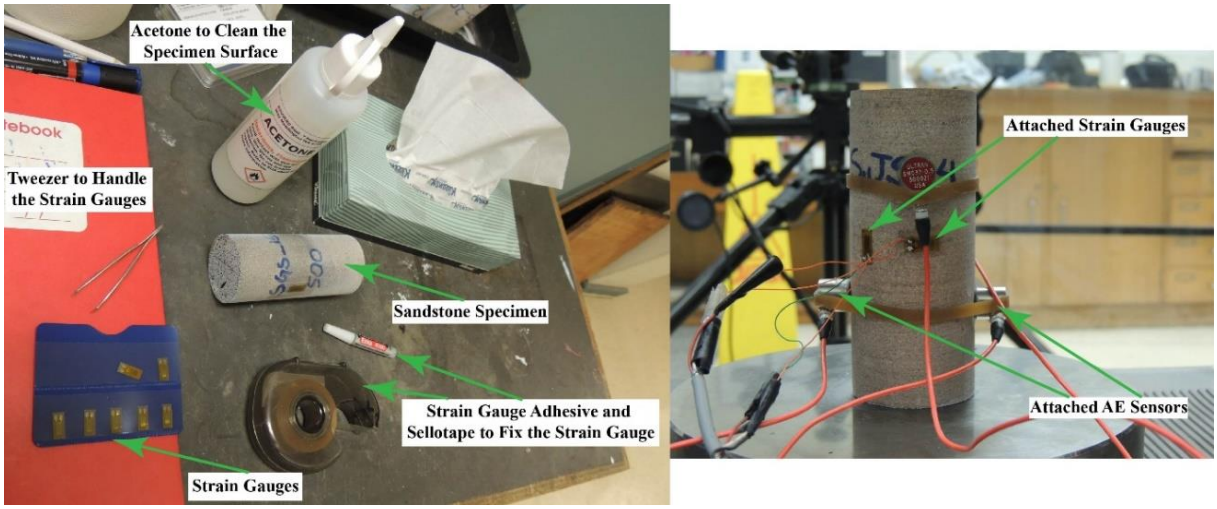

Figure 4.13 *Prearrangement of thermally tretaed and rapid cooling specimens prior to the mechanical testing*

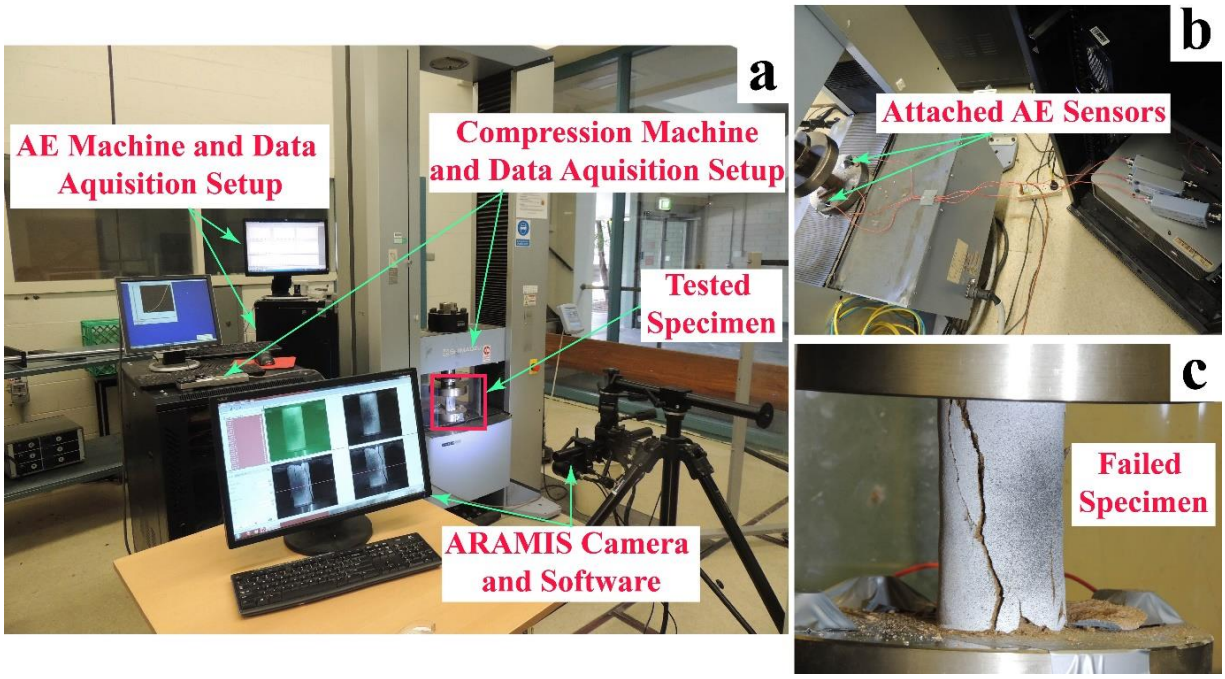

Figure 4.14 *Experimental setup for the measurement of UCS and tensile strength (a) for the thermally treated and rapid cooled specimens. The AE setup that is used for the measuring of acoustic events (b) and a failed specimen after the UCS test (c)*

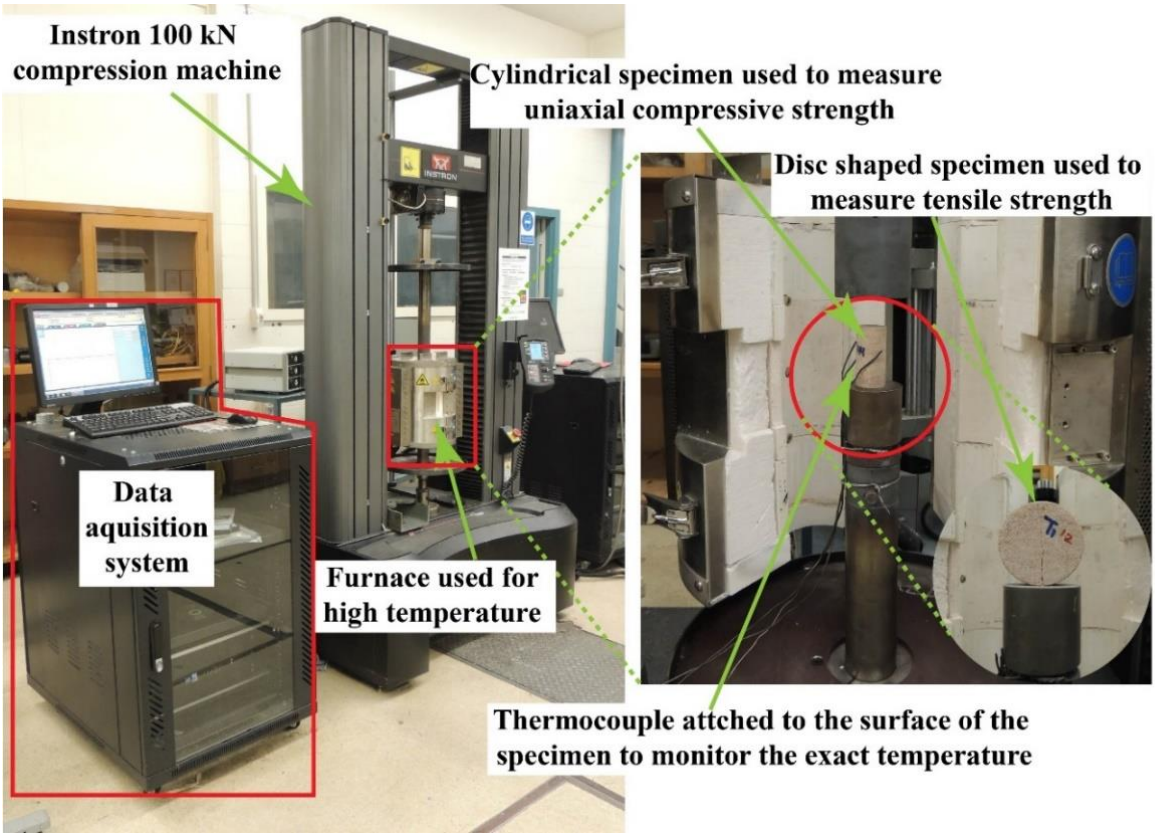

Figure 4.15 *Experimental setup for the measurement of UCS and tensile strength at high temperature condition*

For the in situ mechanical heating tests, Instron compression machine that has a maximum capacity of 100 kN was used. An electric furnace was attached to the Instron machine that was used to provide high temperature environment to the specimens. For the in situ high temperature mechanical tests, specimens having a dimension of 25 mm in diameter and 50 mm in length were used for the UCS test and specimens having a dimension of 51 mm in diameter and 25 mm in width were used for the tensile strength test. During the high temperature tests, thermocouples were attached to the surface to ensure the exact temperature of the specimens. Considering the experimental difficulties and limitations, the strain and elastic measurements for the high temperatures specimens could not be performed. The configuration of the setup for the high temperature mechanical tests has been represented in **Figure 4.15**. At each temperature, a set of three specimens for UCS and a set of two specimens for tensile strength were tested, and their average was reported in the manuscript.

4.2.1.2 Acoustic emission technique

The process of the brittle fracturing of a rock involves the growth of various microcracks that originate from different stress concentrates such as the grain boundaries, inclusions and void spaces that are present in the specimen. During the testing of the specimen, the AE technique

is used to monitor the different cracking events. The AE system that is used in the current investigation is a peripheral component interconnection (PCI) two-channel data acquisition system. This system consists of a band-pass filter that has a frequency in the range of 200–750 kHz and a nominal resonant frequency of 500 kHz. The hardware consists of sensors and an external amplifier.

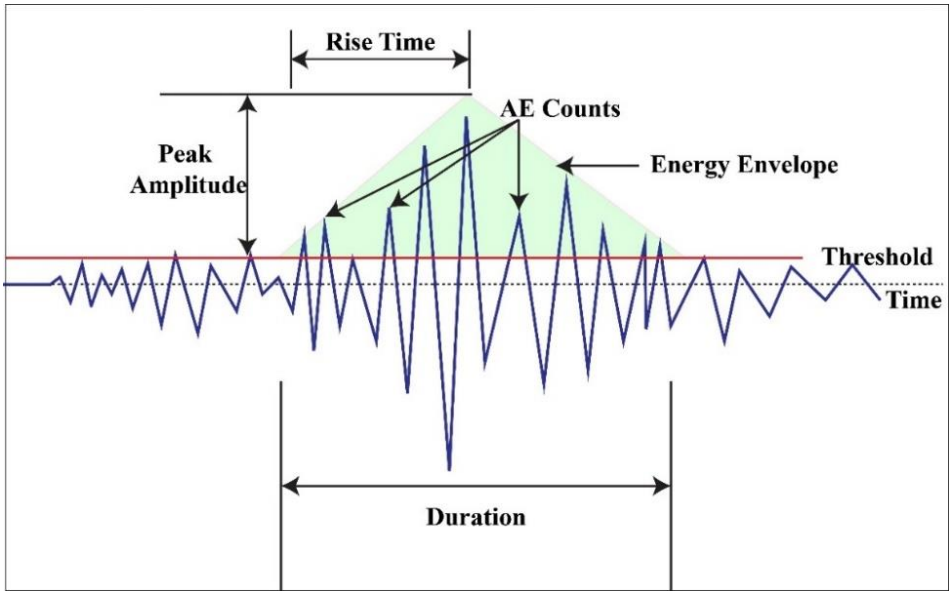

Figure 4.16 *Schematic diagram of the simple AE waveform* (Eberhardt et al., 1998)

During each test, three sensors were attached to the lower platen of the compression machine by applying a semisolid lubricant between the sensors and the platen to avoid an air gap. The external amplifier, which was set to a value of 40 dB, was used to amplify the low-frequency acoustic waves that were produced during the test. **Figure 4.14** represents the setup of the configured sensors and the AE system used in the current study. During the application of stress, certain elastic waves are generated as a result of the sudden release of the stored elastic energy. These elastic waves travel through the specimens towards the boundary where they are observed as an acoustic event and are captured by the AE machine with the help of certain sensors that are attached to the boundary surface of the specimen or to the base of the loading frame (Eberhardt et al., 1998; Hardy, 1977). **Figure 4.16** represents the schematic diagram of the acoustic waveform, and its details can be found in Eberhardt et al. (1998).

4.2.1.3 DIC using ARAMIS

ARAMIS digital speckle is a non-contact measurement system that is capable of measuring the three-dimensional deformation of the specimen by using natural light or white light. ARAMIS can identify the surface of the tested specimen by means of the camera images in which different coordinates are assigned to different image pixels. During the span of the testing time,

a series of images are captured by the ARAMIS camera at certain time intervals. The camera captures the geometric points in each image and acquires the surface deformation by tracking the movement of the geometrical points in the sequence of images. This technique is capable of analysing the three-dimensional deformation and the different strain components under both static and dynamic loading conditions (Hu et al., 2015). During the measurement procedure, the first image that is undeformed is considered the reference image, and the deformation is optimised by comparing the different pixels in the subsequent image series.

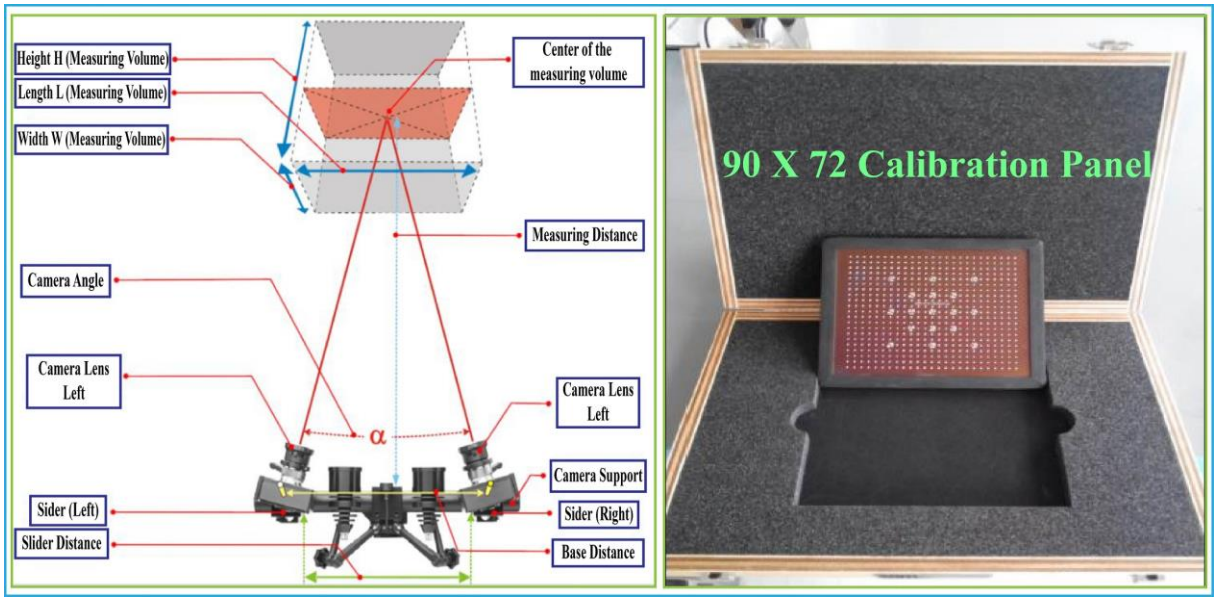

Figure 4.17 *ARAMIS setup and the calibration panel used prior to the measurement (modified after Hu et al., (2015))*

Broadly, ARAMIS system consists of the measurement system that includes two cameras, tripod to hold the camera, camera bracket, LED floodlight, sensors A/D converter and laser; and analysis system that includes the application software installed in a high-performance computer (Hu et al., 2015). The schematic diagram of the working principle of the ARAMIS technique has been represented in **Figure 4.17**. Before the measurements were made, various camera parameters were adjusted based on the specimen size, followed by the calibration of the measuring techniques. These adjustments included the measuring of the height, focal length, and camera angle. The focus of both the cameras was adjusted, considering the laser transmitter to be the symmetry axis. The adjustment was made in such a way that the focus of both the cameras convergeed at the midpoint of the specimen. Subsequent to the camera adjustment, a three-dimensional space-point calibration of the setup was required, which was an essential requirement that ensureed the accuracy of the measured quantity. The calibration was carried out with the help of a 90 x 72-calibration panel as shown in **Figure 4.17b**. The

values of the camera angle should lie in the range from 18 ° to 35 ° and a size deviation of 0.001 mm and a calibration deviation of 0.024 pixels must be attained to ensure the accurate measurements while using the ARAMIS measurement techniques. (Hu et al., 2015).

During the testing of a specimen, the ARAMIS system and the loading system can be combined by which the ARAMIS system measures the surface deformation of the specimen and the loading system acquires the loading profile during the test of the specimen. For accurate measurement of the deformation at the surface, the specimen requires a reasonable amount of variation in tone and contrast of the specimen. To achieve a better contrast and tone, the air-dried specimens were painted in white, which is followed by a spray of black dots over the white-painted surface of the specimen.

4.2.2 Results and discussion

4.2.2.1 Variation of mechanical strength parameters in response to temperatures

4.2.2.1.1 Effect of heating on stress-strain behaviour

The series of images that were captured by using the ARAMIS system were analysed to observe the different degrees of strain levels in the specimens with progressive deformations**. Figure 4.18** and **Figure 4.19** show a comparison of the ARAMIS-processed images at different temperatures for thermally treated specimens. **Figure 4.20** and **Figure 4.21** represent a comparison of the ARAMIS-processed images for both thermally treated and rapid cooled specimens. High-temperature specimens displayed the shear nature of the failure, and the induced macrofractures align at an angle to the applied stress. However, for a better comparison, in each case, the legends that were used to indicate the strain levels were normalised and scaled to an identical value. Hence, the ARAMIS-processed images represented a graphical comparison of the development of strain in the specimens rather than the true strain of the specimens during loading. **Figure 4.22** can be referred to for information about the true strain that developed in the specimens. When the frequencies of the legends for each ARAMIS-processed images for different temperatures were compared, the 700 °C represents a widespread frequency of the developed strains. However, no other case with such a widespread frequency of developed strains was noticed, which indicates maximum thermal alteration and damage in the case of 700 °C. The stress-strain curves of the studied sandstone after thermal treatment at different temperatures are represented in **Figure 4.22**. Specimens that were heated up to 500 °C demonstrated a brittle nature of fracturing, by which the axial strain gradually increased with the increase in compressive strength, followed by a sudden drop of the load after the failure of the specimen.

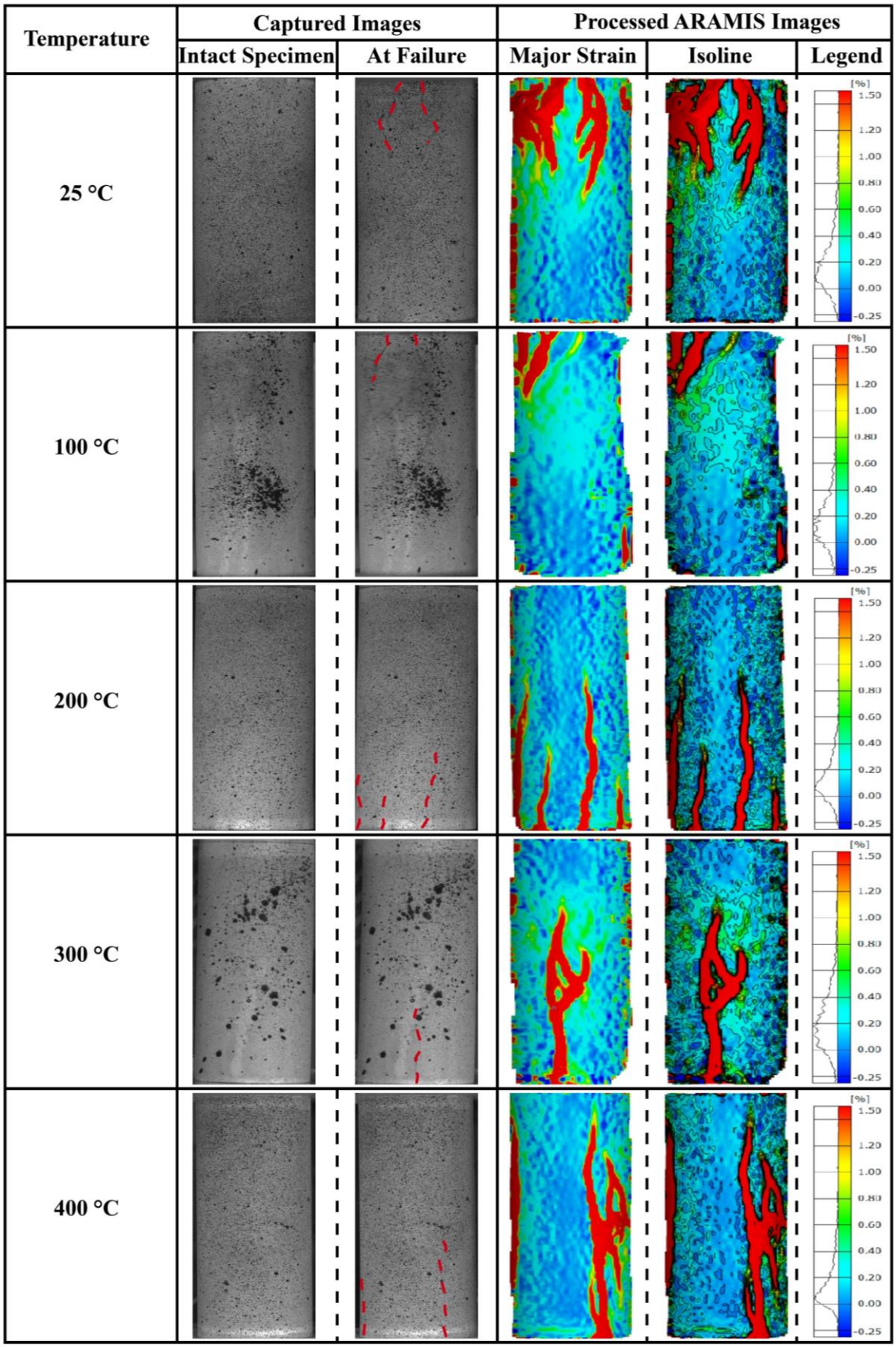

Figure 4.18 *Processed-ARAMIS images, indicating the developed strain in thermally treated specimens (25 °C – 400 °C)*

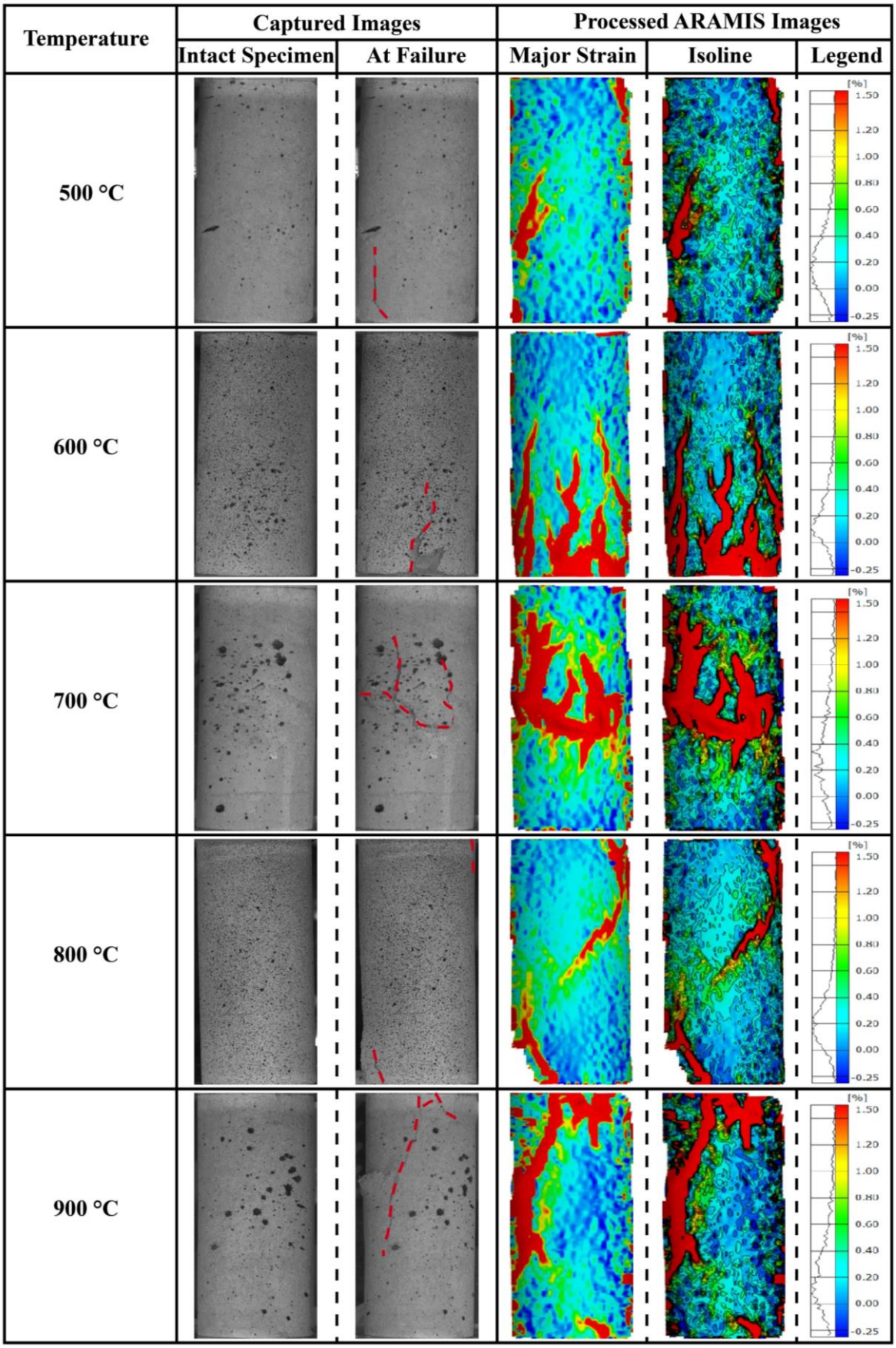

Figure 4.19 *Processed-ARAMIS images, indicating the developed strain in thermally treated specimens (500 °C – 600 °C)*

Temperature	Slow cooling		Rapid cooling	
	Major Strain	Legend	Major Strain	Legend
25 °C	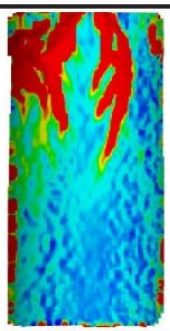	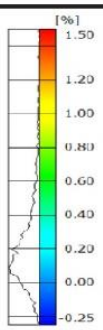		
100 °C	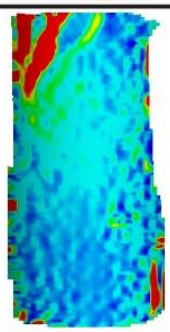	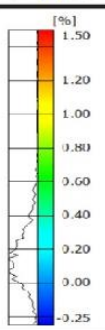	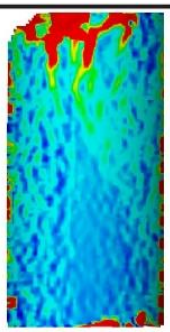	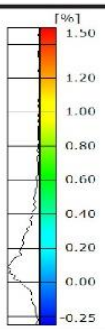
200 °C	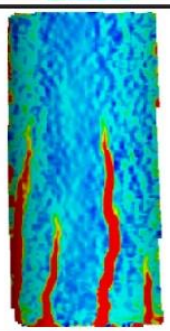	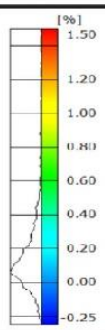	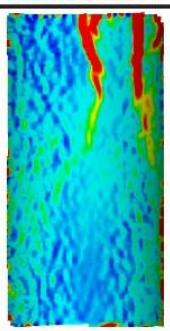	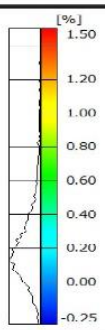
300 °C	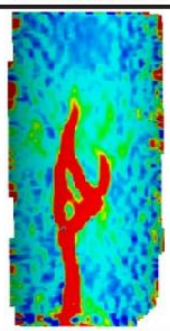	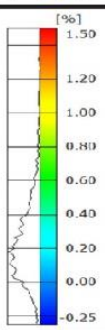	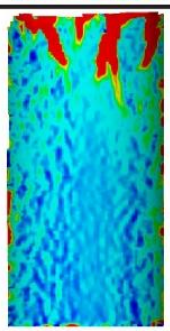	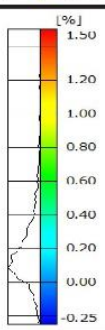
400 °C	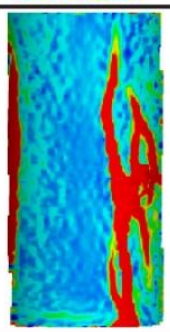	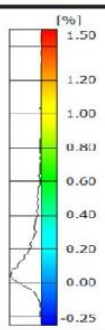	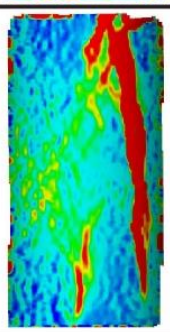	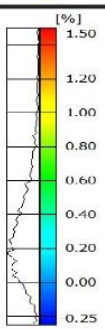

Figure 4.20 *Processed-ARAMIS images, indicating the developed strain in rapidly cooled specimens (25 °C – 400 °C)*

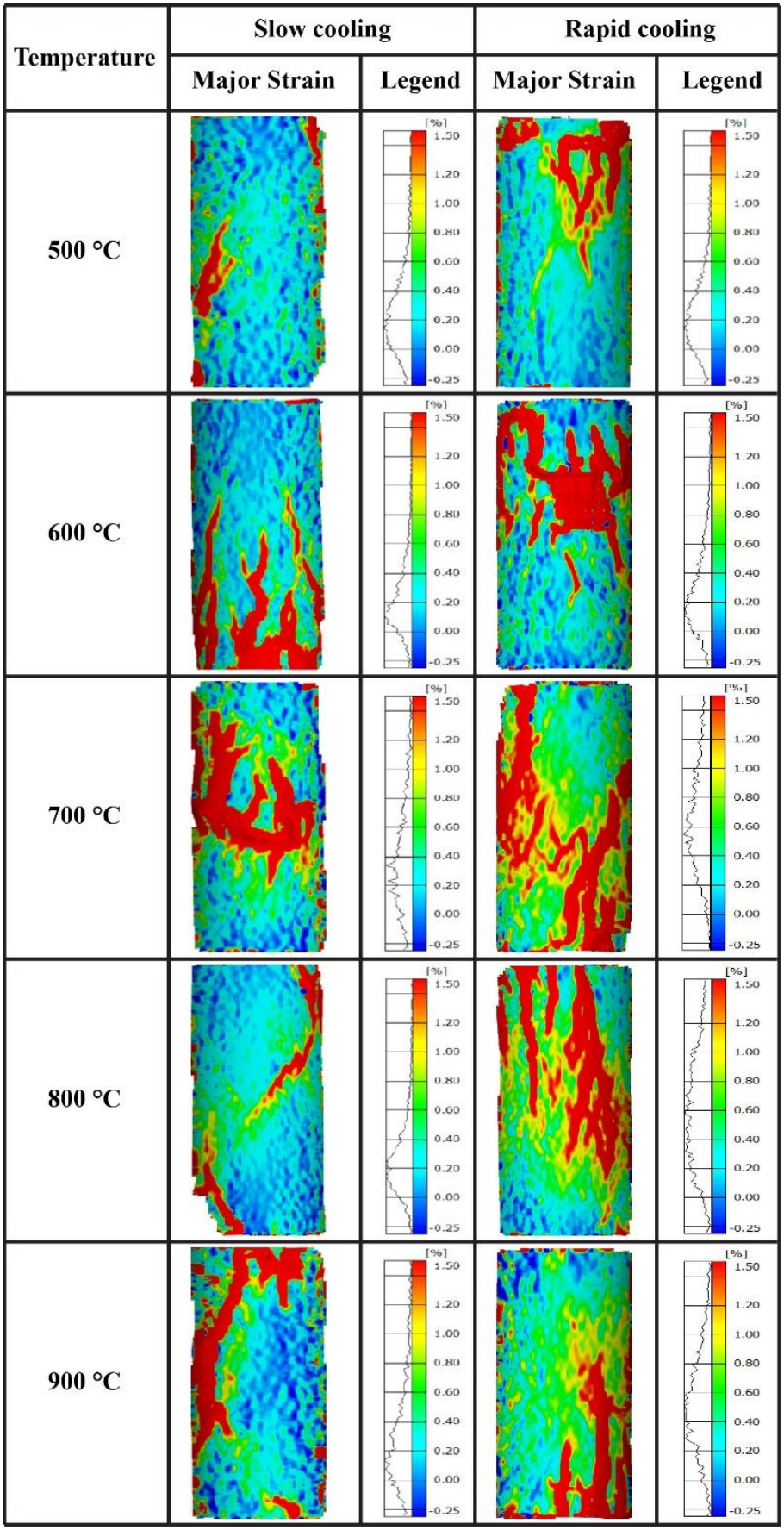

Figure 4.21 *Processed-ARAMIS images, indicating the developed strain in rapid cooled specimens (500 °C – 900 °C)*

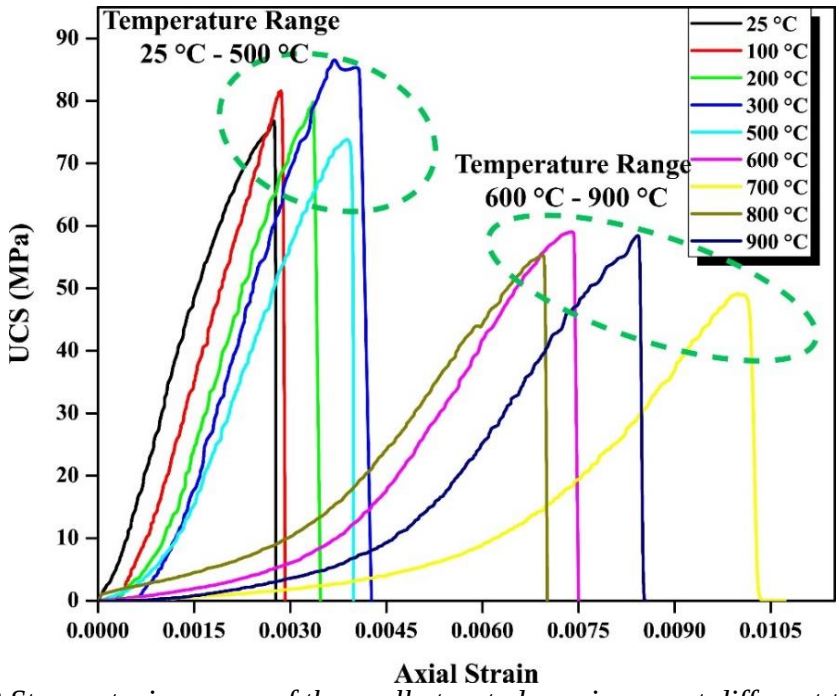

Figure 4.22 *Stress-strain curves of thermally treated specimens, at different temperatures*

However, stress-strain curves that correspond to higher temperatures were marked by their concave upward nature. This indicates the low stiffness and pseudo-ductility of the specimens in which the axial strain and the compressive stress followed a nonlinear correlation. For all the three conditions (thermally treated and rapid cooled and at high temperatures), the specimens that were subjected up to 500 °C displayed higher average-UCS values when compared to the specimens that were subjected to higher temperatures (**Figure 4.22 - Figure 4.25)**.

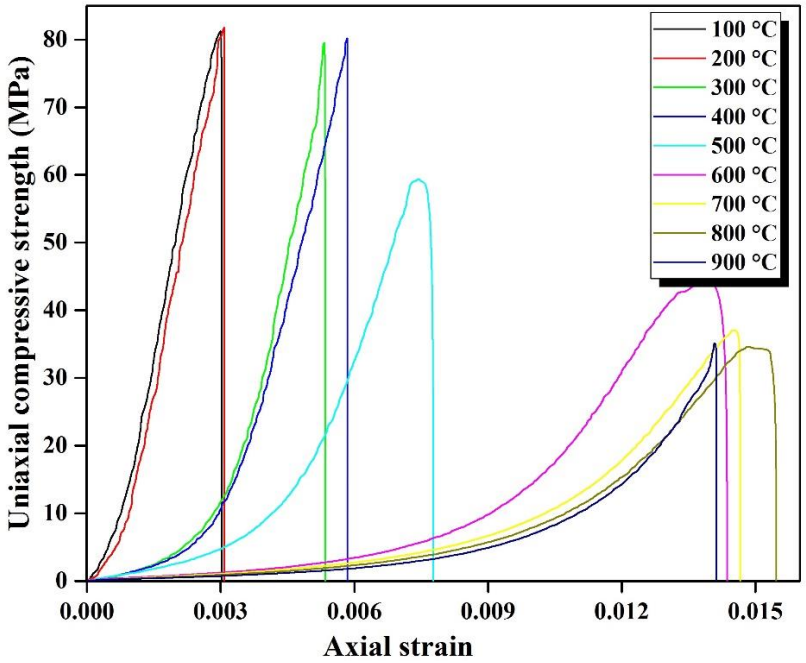

Figure 4.23 *Stress-strain curves of rapid cooled specimens, at different temperatures*

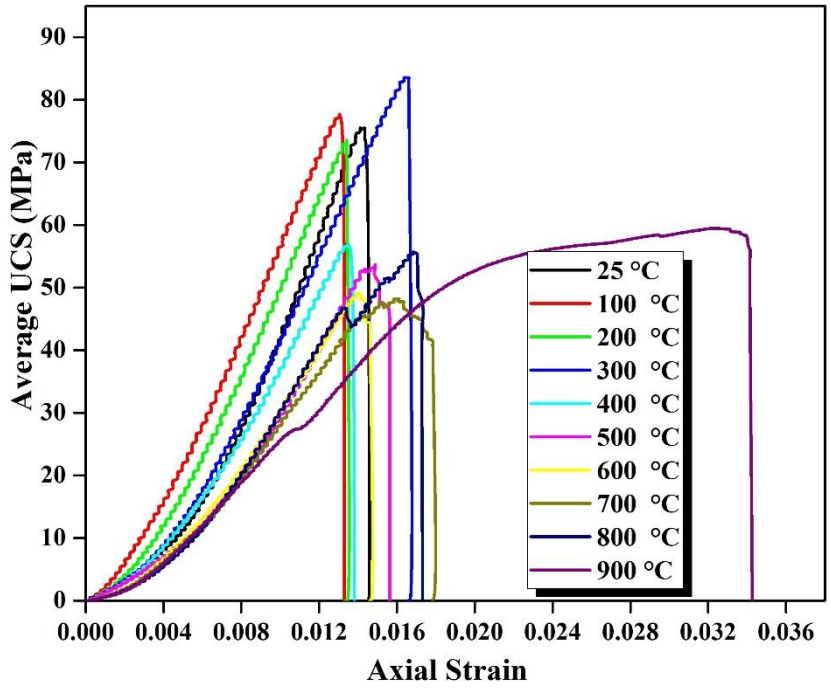

Figure 4.24 *High-temperature stress-strain curves of the studied sandstone*

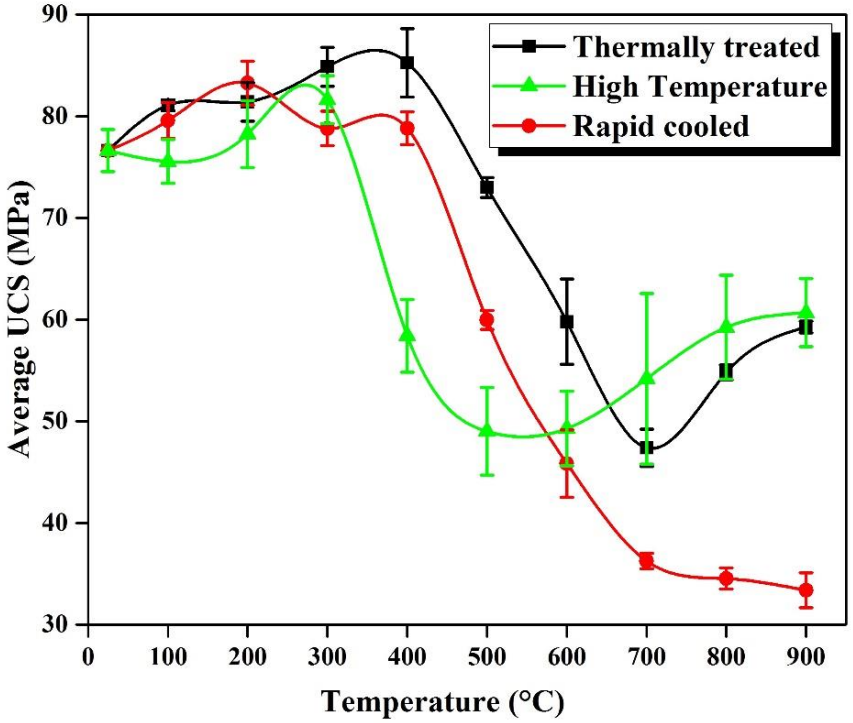

Figure 4.25 *Variation of UCS of the sandstone as a function of temperature*

The UCS of the sandstone increased by 11 per cent when the temperature was raised from room temperature to 400 °C. Thereafter, a sharp decreasing trend up to 700 °C, where it attained its minimum value, was observed, and after 700 °C, a slight increase in the compressive strength of the sandstone was noticed. The presence of microcracks does influence the mechanical and

flow behaviours of rocks. A progressive increase in temperature either induces new microcracks in the structure of the rock or extends the pre-existing microcracks. The thermal responses of rocks completely depend upon the presence of the dominant mineral phases and their responses to different degrees of heating. The average compressive strength increased from 76.62 MPa at 25 °C to 85.25 MPa at 400 °C and, thereafter, the trend of compressive strength followed a sharp decreasing trend up to 700 °C.

4.2.2.1.2 Effect of heating on the UCS and tensile strength

At elevated temperatures, minerals undergo different thermal expansions along the crystallographic axes; however, calcite contracts along the *c*-axis (**Table 4.1**). This mismatch in thermal expansion results in different thermal stress along different directions and, ultimately, new microcracks are induced in the microstructure of the rock, which results in the reduction of the mechanical strength of the rocks.

Table 4.1 Thermal expansion of rock-forming minerals in different crystallographic axes (Skinner, 1966; Somerton, 1992)

Mineral	Axis	Per cent expansion from 20 °C			
		100 °C	200 °C	400 °C	600 °C
Quartz	⊥c	0.14	0.30	0.73	1.75
	|| c	0.08	0.18	0.43	1.02
Orthoclase	|| a	0.05	0.14	0.48	0.90
	|| b	0.00	0.10	0.04	0.13
	⊥001	0.00	0.005	0.065	0.155
Plagioclase	|| a	0.09	0.22	0.50	0.83
	⊥010	0.03	0.06	0.16	0.29
Calcite	⊥c	0.19	0.48	1.12	1.82
	|| c	-0.04	-0.10	-0.18	-0.22
Hornblende	⊥100	0.05	0.12	0.29	0.48
	|| b	0.06	0.17	0.39	0.64
	|| c	0.05	0.13	0.29	0.46

Depending on the degree of heating and the mineral assemblages, the induced microcracks can be intergranular, intergranular and transgranular. Rocks that contain a significant amount of quartz, feldspar, mica and clay minerals show remarkable changes in response to elevated temperatures (Mahanta et al., 2016; P. G. Ranjith et al., 2012; Siegesmund et al., 2008; Tian et al., 2016). A detailed summary of the thermal expansions of some common rock-forming minerals is listed in **Table 4.2**.

Table 4.2 *Chemical reaction of various minerals as a result of heating*

Temperature (°C)	Mineral	Reaction	Reference
25–220	Ca-montmorillonite	Desorption	Barshad, 1972; Somerton, 1992
25–220	Mg-montmorillonite	Desorption	
400–625	Mg-illite	Decomposition	
455–642	Kaolinite	Decomposition	
554–723	Ca-montmorillonite	Decomposition	
573	Quartz	α-β inversion	
550	Siderite	Decomposition	Luo et al., 2016
580 and 680	Dickite	Dehydroxylation	Stoch and Wacławska, 1981
700–830	Ca-carbonate	Decomposition	Barshad, 1972; Somerton, 1992
790–950	Mg-illite	Decomposition	
816–908	Ca-montmorillonite	Decomposition	

The tensile strength of the specimen can be compared to the behaviour of the specimen's peak compressive strength, which exemplifies strength variations. At room temperature, the tensile strength of sandstone was found to be 6.324 MPa. With a progressive increase in temperature, from room temperature to 300 °C, the tensile strengths of the sandstone did not display any considerable variation, and thereafter, from 400 °C, the tensile strength of the sandstone decreased until 700 °C to 1.838 MPa (**Figure 4.26**).

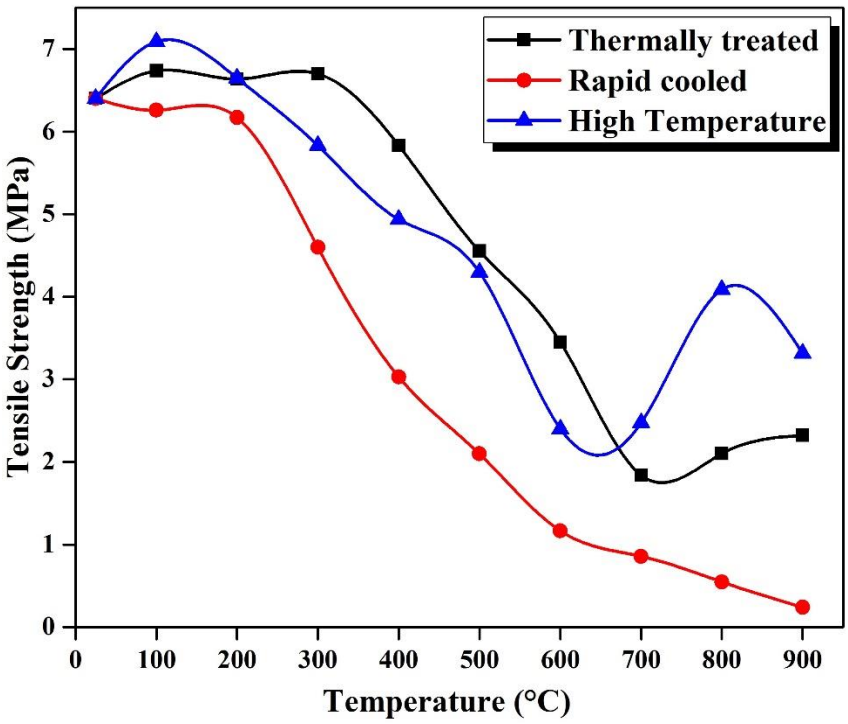

Figure 4.26 *Variation of tensile strength of the sandstone as a function of temperature*

4.2.2.1.3 Effect of heating on the elastic modulus and failure strain

Elastic modulus is a parameter that is used to describe the deformational behaviour of a material/rock, and it indicates the resistance that is offered by the material/rock to the introduced deformation. With increasing temperatures, Young's modulus of sandstone aligned with an overall decreasing trend.

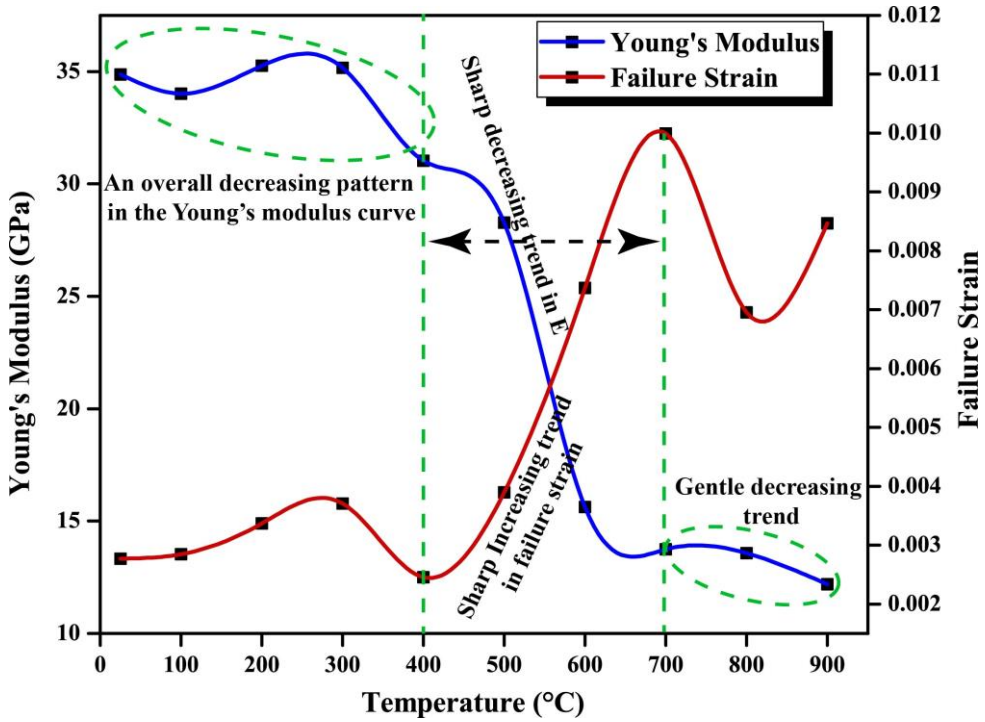

Figure 4.27 *Variation of Elastic modulus and failure strain of the sandstone for different thermally treated specimens*

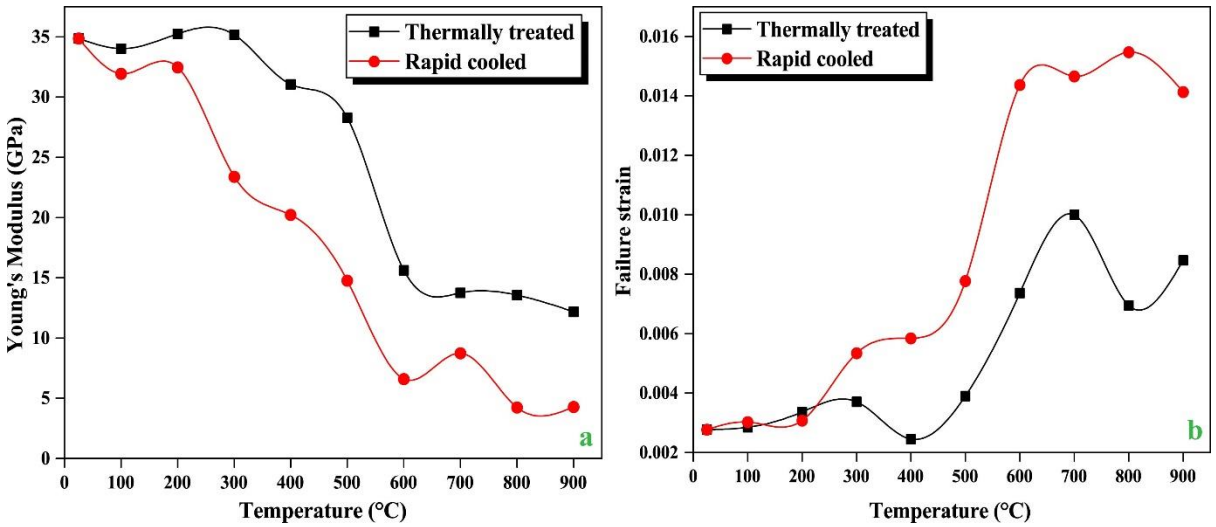

Figure 4.28 *Variation of Elastic modulus and failure strain of the sandstone for different thermally treated and rapid cooled specimens*

At room temperature, Young's modulus of sandstone was found to be 34.87 GPa. No significant change was observed in the rock's Young's modulus up to 400 °C. From 25 °C to 400 °C, Young's modulus of sandstone reduced by 11 per cent to 31.04 GPa at 400 °C. However, a sharp drop in Young's modulus was observed at 600 °C, when it reduced to 15.62 GPa.

When the thermal stress resulting from the differential thermal expansions among the different mineral phases exceeds the cohesion among the mineral particles, cracks start to develop. With the further widening of the cracks, more deformation is introduced to the structure of the rocks, thereby decreasing the elastic modulus of the rock (Zhang et al., 2017). A sharp decline in Young's modulus of the sandstone was observed in the window of 400 °C to 600 °C when compared to the window of 600 °C to 900 °C, where it followed a trend of a gentle decrease. At 900 °C, Young's modulus of the sandstone was found to be 12.186 GPa, which is 65 per cent lesser than the value at room temperature.

In case of failure strains, a sharply increasing trend was observed in the window of 400 °C to 600 °C. At room temperature, the failure strain was found to be 0.0027 and attains its maximum value at 700 °C. Up to 400 °C, the pattern for the peak strain followed a gently increasing pattern, whereas, after 400 °C, a rapid increase in the peak strain was observed (**Figure 4.27** and **Figure 4.28**). The progressive increase in the failure strain is due to the low stiffness and ductility of the specimens. As discussed earlier, upon exposure to higher temperatures, the specimens exhibit less stiffness along with some ductile behaviour, in comparison to the cases of lower temperature (**Figure 4.22** and **Figure 4.27**). **Figure 4.29** represents a comparison of the damage factor for both thermally treated and rapid cooled specimens.

4.2.2.1.4 Effect of temperature on damage factor and Poisson's ratio

With a progressive increase in temperature, the internal structure of the specimen is destroyed, as a result of which the peak stress and the peak strain of the rock gradually decreases and increases, respectively. The extent of the damage that is induced in the rock can be measured by the damage factor, which is mathematically expressed as

$$D(T) = 1 - \frac{E_T}{E_0}$$

Where,

E_T : Elastic modulus at temperature T °C

E_0 : Elastic modulus at room temperature

For the studied sandstone, an overall increasing nature of the damage factor was observed. The damage factor followed a sharp increment with a progressive increase in the temperature, from 300 °C to 600 °C (**Figure 4.29**).

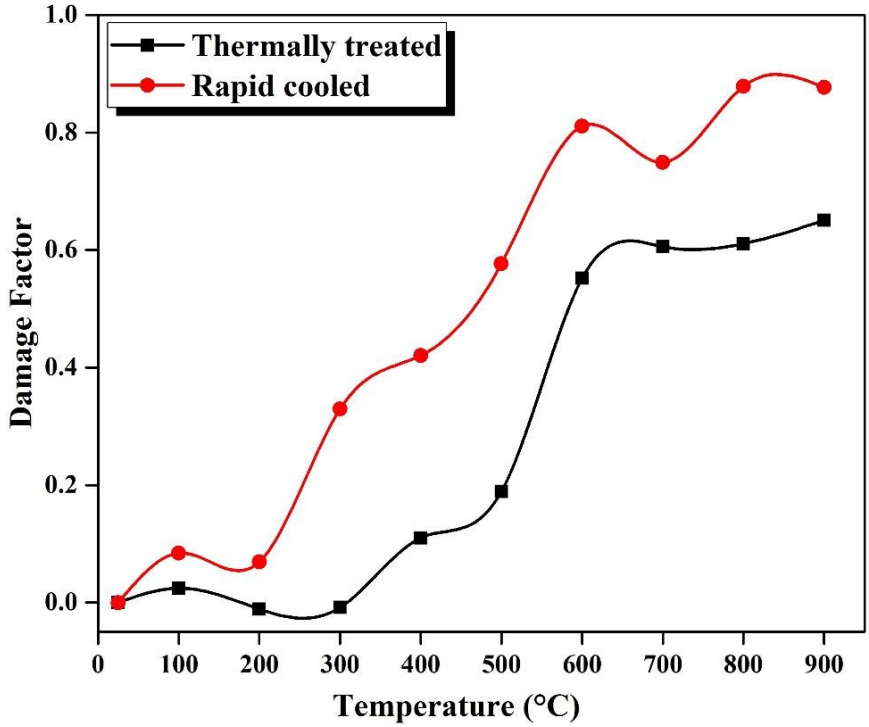

Figure 4.29 *Variation of damage factor as a function of increasing temperature*

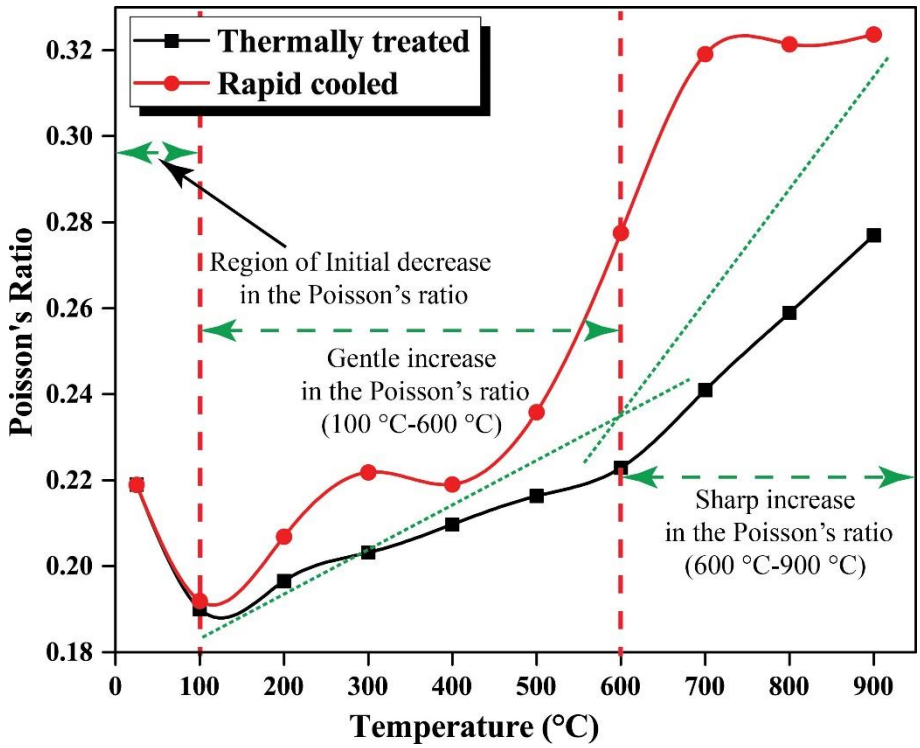

Figure 4.30 *Variation of Poisson's Ratio of the sandstone as a function of temperature*

Poisson's ratio is a measure of the transverse-extensional strain to the longitudinal-compressional strain of the material under applied compression. The change in the Poisson's ratio of sandstone across the range of the temperatures that have been studied can be divided into three broad regions.

An early reduction in the range from 25 °C to 100 °C, which led to a gentle increase of up to 600 °C, was followed by a sharp increase up to 900 °C. The Poisson's ratio was found to be 0.21 at room temperature, 0.22 at 600 °C, and 0.27 at 900 °C (**Figure 4.30**). An increment of 24 per cent in the Poisson's ratio value of the sandstone was observed when there was an increase in the temperature, from 600 °C to 900 °C. This increment may be due to a reduction in the rock's stiffness and the development of pseudo-ductility (Kumari et al., 2017).

4.2.2.1.5 Fracturing characteristic of thermally treated specimens by using AE

The continuous deformation of the specimen and its fracturing can be analysed by using the AE response of the specimen during its testing. During the laboratory testing of the rocks, a rapid growth of microcracks produces various acoustic events, which demonstrates good correlation with the inelastic strain rate. During loading and failure of the specimen, cumulative counts of the AE events can be used in the damage mechanics model for the quantification of damage accumulation and prediction of failure (Lockner, 1993). Progressive application of stress results in the formation of new microcracks in the specimen along the different weak zones. The density of induced microcracks/crack density is proportionate to the applied stress, and it reaches an optimum number before its failure. The whole event of cracking in response to applied stress can be imaged with the help of AE events, by which the major cracking events can be demarcated on the basis of AE counts or released AE energy (Kumari et al., 2017). Based on the stress-strain characteristics, the failure process can be divided into four different stages. According to Brace (1964), Bieniawski (1967) and Eberhardt et al. (1998), these stages can be defined as crack closure, linear-elastic deformation, crack initiation and stable crack propagation, crack damage and unstable crack propagation, and failure. Much more details about the different stages of cracking can be found in the references mentioned above. The crack-closure stage and the linear-elastic deformation stage are associated with the very negligible amount of acoustic counts/energy. However, with progressive loading, a gradual increment in the AE counts can be observed at the beginning of the crack initiation stage, and exponential increment of AE counts can be observed at the beginning of the crack damage stage. The AE responses for the different thermally treated and rapid cooled specimens are represented in **Figure 4.31** and **Figure 4.32**, respectively.

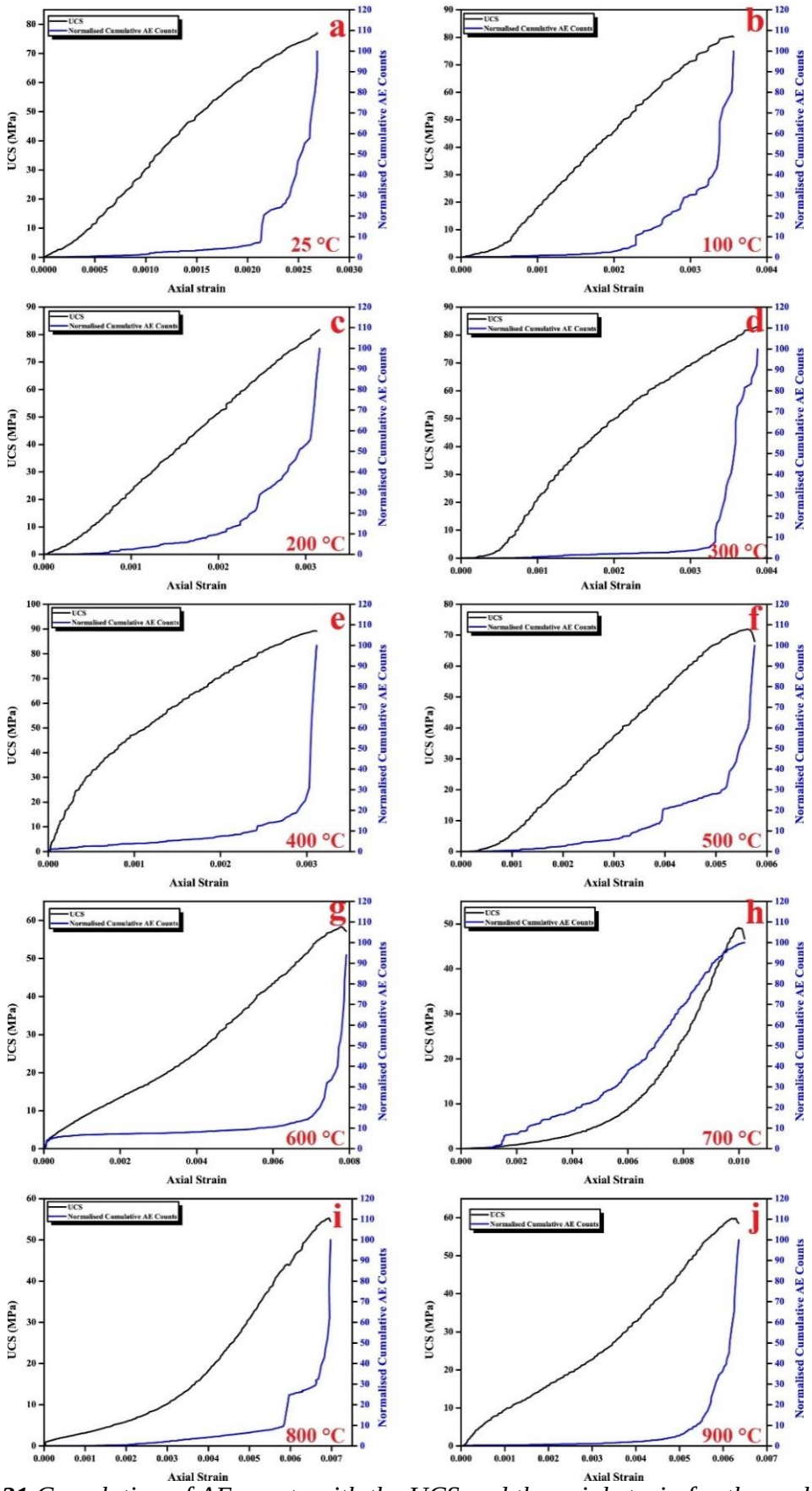

Figure 4.31 *Correlation of AE events with the UCS and the axial strain for thermally treated specimens*

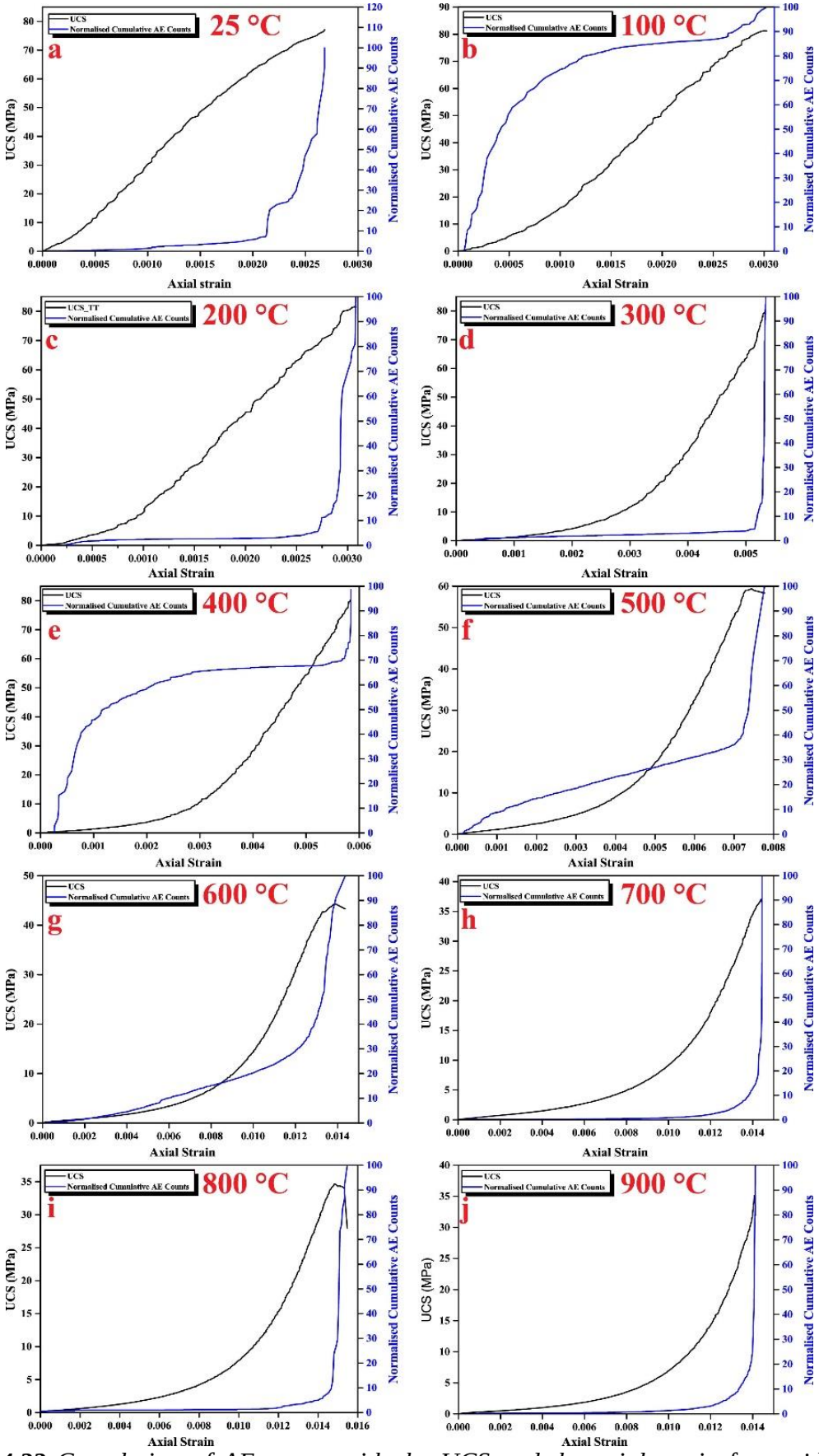

Figure 4.32 *Correlation of AE events with the UCS and the axial strain* for rapid cooled specimens

In the current study, the AE profile of the thermally treated specimens do not correspond to a demarcated crack-closure stage and, hence, the current study includes the identification of various crack initiations and crack damage stress thresholds by observing the linear and exponential increments in the cumulative AE-counts curve, respectively. Additionally, the different stress thresholds at different temperatures were normalised with the corresponding failure stress to obtain the stress threshold ratio.

$$Crack\ initiation\ stress\ threshold\ ratio = \frac{crack\ initiation\ stress\ threshold\ \sigma_{ci}}{Failure\ stress}$$

$$Crack\ damage\ stress\ threshold\ ratio = \frac{crack\ damage\ stress\ threshold\ \sigma_{cd}}{Failure\ stress}$$

Table 4.3 *various stress threshold values of thermally treated sandstone at different temperatures*

Temperature (°C)	CIST (MPa)	CDST (MPa)	UCS (MPa)	CISTR	CDSTR
25	32.051	70.744	77.126	0.416	0.917
100	34.094	71.421	80.411	0.424	0.888
200	29.623	74.069	81.735	0.362	0.906
300	32.394	70.662	82.915	0.391	0.852
400	27.606	79.350	89.273	0.309	0.889
500	21.433	51.119	71.936	0.298	0.711
600	18.623	43.655	58.387	0.319	0.748
700	8.360	30.932	49.178	0.170	0.629
800	14.640	38.513	55.266	0.265	0.697
900	15.854	41.220	59.791	0.265	0.689

CIST: crack initiation stress threshold; CDST: crack damage stress threshold; UCS, CISTR: crack initiation stress threshold ratio; and CDSTR: crack damage stress threshold ratio.

CIST, CDST at different temperatures, the normalised CISTR and CDSTR at different temperatures are represented in **Table 4.3** and plotted in **Figure 4.33**. From **Figure 4.33**, it can be inferred that upon exposure to higher temperatures, the CISTR and the CDSTR follow a decreasing pattern from room temperature to 900 °C, which indicates the early occurrence of both the crack initiation and cracks damage event in the thermally treated sandstone. In the room temperature case, the crack initiation and the crack damage stage started at around 41 per cent and 91 per cent of the failure strength, respectively. However, the crack initiation and the crack damage stage started at nearly 17 per cent and 62 per cent of the failure strength in the specimens at 700 °C, which suggested a possible reduction in the linear-elastic region and the stable crack propagation region in thermally treated specimens.

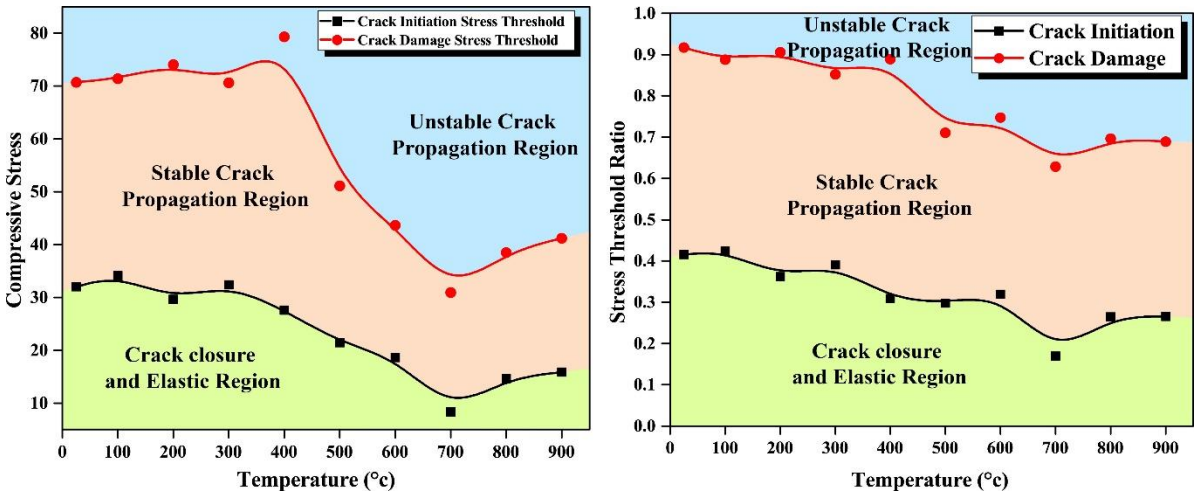

Figure 4.33 *Variation of different stress thresholds and the stress threshold ratio as a suction of temperatures*

Fredrich and Wong (1986) reported a considerable amount of increment in the intergranular crack density above 250 °C. Significant changes occurred above 400 °C because most of the minerals undergo chemical alterations after this temperature (Tian et al., 2012). In the range of 400 °C to 600 °C, the sandstone undergoes major physical and chemical changes. Quartz undergoes a phase transition at 573 °C, at which the low/α-quartz changes to high/ β-quartz, which is marked by a volume increment of two per cent due to the difference in the densities of the two phases (Schacht, 2004; Somerton, 1992; Somerton and Boozer, 1960). Furthermore, in the range of 500 °C to 600 °C, a drastic escalation of cracking can be observed (Glover et al., 1995; Reuschlé et al., 2006). The measurement of the fracture surface energy reveals the potential development of microfractures during the phase transformation of α-quartz to β-quartz (Blenkinsop, 2000; Wang et al., 1989). In most cases, phase transformation results in the formation of intergranular microcracks (Blenkinsop, 2000).

4.2.2.2 Comparison of the experimental results along with existing literature

In most cases, the alterations that are induced in rocks as a result of their exposure to high temperatures are due to chemical changes and thermal damages. Chemical changes include the different changes in mineralogical composition, whereas structural damages include the effects of thermal stress on the microstructure of the rocks (Brotóns et al., 2013; Chaki et al., 2008; Hajpál, 2002; Hajpal and Torok, 2004; Mahanta et al., 2016; N. Sirdesai et al., 2017; Yavuz et al., 2010). These chemical and the thermal damages in rocks are explained in terms of various physical (mass loss, P/S-wave velocity, and thermal expansion) and mechanical strength parameters (compressive strength, tensile strength, elastic modulus, Poisson's ratio, and damage factor).

Table 4.4 *Summary of the reviewed sandstones along with the sandstone used in the current investigation*

Sandstone Type	Site Of Sandstone	Heating Condition			Cooling Process	Dominant Minerals	Investigated Properties	References
		Maximum Temperature (°C)	Heating Rate (°C/min)	Heating Time (Hrs)				
Linyi Sandstone	Shandong, China	600	5	2	Furnace-cooled	-	Porosity, UCS, Peak strain, Elastic modulus, Poisson's ratio	Zhang et al. 2017
Jiaozuo Sandstone	Jiaozuo, China	1200	5	2	Furnace-cooled	Quartz, Feldspar, Mica, Sericite, Calcite	UCS/Peak stress, Peak strain, Elastic modulus, Poisson's ratio	Wu et al. 2013
Dholpur sandstone	Dholpur, India	1000	5	120	Air-cooled	Quartz, Feldspar, Mica, Pyroxene	UCS, Failure strain, Tensile strength, Young's modulus, Poisson's ratio	Sirdesai et al. 2017b
Linyi sandstone	Shandong, China	900	30	0.5	Furnace-cooled	Quartz, Dolomite/Ankerite, Feldspar Kaolinite	Tensile strength, Longitudinal wave velocity, Mass loss rate	Lü et al. 2017
Cottaer sandstone	Cottaer, Germany	900	# Heating procedure took 1 hr to reach the required temperature	6	Air-cooled	Quartz	Indirect tensile strength, UCS	Hajpál and Török 1998
Donzdorfer sandstone	Donzdorfer, Germany					Quartz		
Maulbronner sandstone	Maulbronner, Germany					Quartz		
Pliezhausener sandstone	Pliezhausener, Germany					Quartz		
Fangzhuang Sandstone	Jiaozuo, China	900	10	4	Furnace-cooled	Quartz, feldspar, Mica	UCS, Elastic modulus, Secant modulus, Peak strain	SU et al. 2008
Qinling Sandston	Quiling Mountain, China	1000	10	2	Air-cooled	Quartz, Clay	UCS, Tensile strength, Density loss, P-wave change rate	Chen et al. 2013
Jodhpur sandstone	Jodhpur, India	900	5	3	Air-cooled	Quartz, Dickite, Calcite, Kaolinite	UCS, Tensile strength, Elastic modulus, Peak strain	Current study

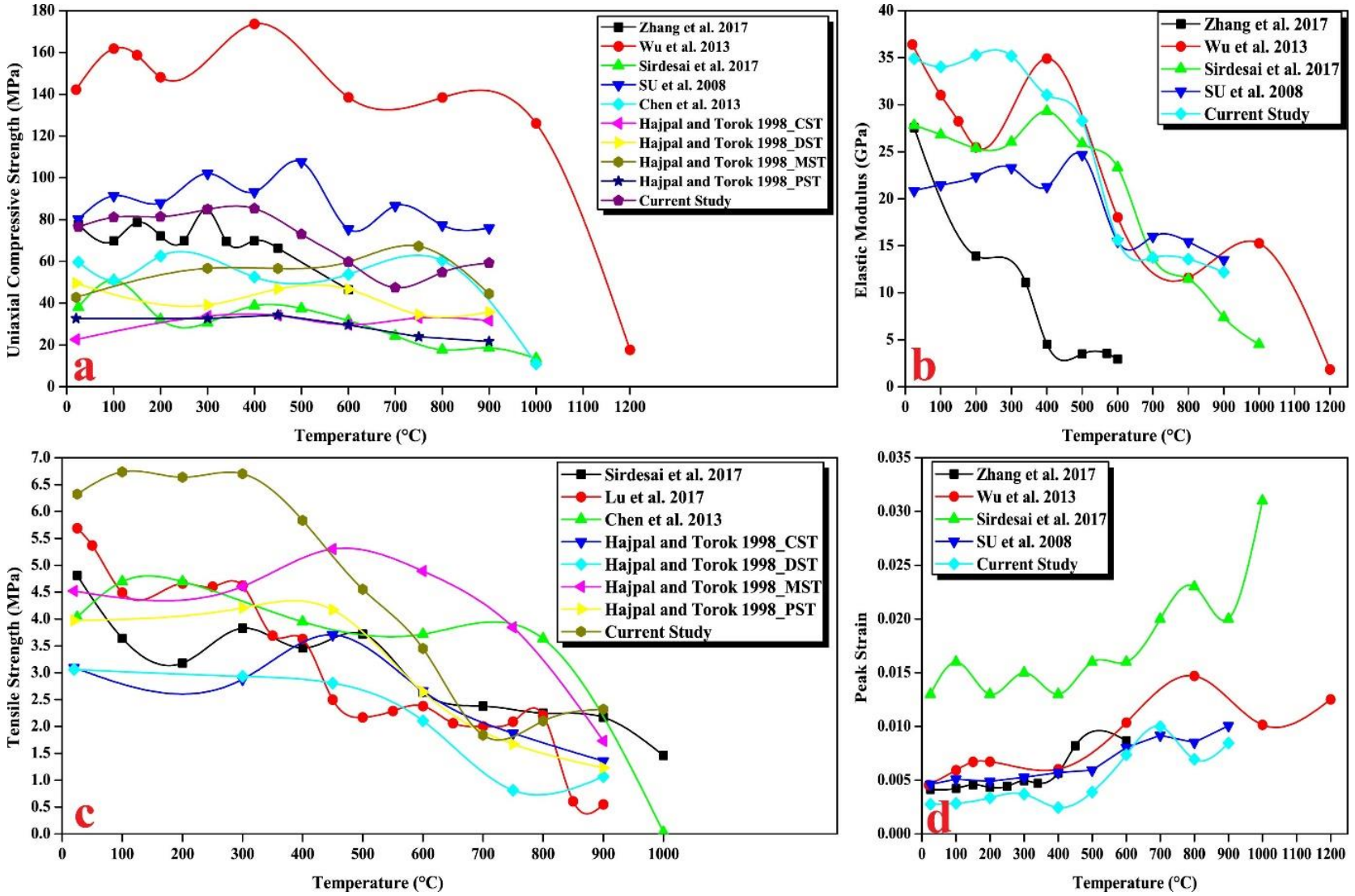

Figure 4.34 *Comparisons of different mechanical properties of different sandstones along with the sandstone used in the current study. Figures 22a, 22b, 22c and 22d represent the comparison of UCS, elastic modulus, tensile strength and peak strength of various sandstones, respectively*

Thorough knowledge of the thermal behaviour, rocks can be used in various engineering applications such as underground coal gasification; geothermal energy extractions; geological nuclear waste disposal and enhanced oil recovery. The thermal properties of the rocks are predominantly dependent on in situ temperature and pressure conditions. Additionally, the shape, the size of the grains, the geometry and structure of the pore, and the shape and density of the cracks do affect the behaviour of the rocks (Sun et al., 2016a). Sandstone exhibits a complex pore and pore-throat network of different sizes that range from the nanoscale to the micro-scale (Lai et al., 2017). Depending upon their types, mineralogy and structures, rocks display different thermal behaviours. **Table 4.4** summarises the different sandstones that were present in the literature in which comparable attempts were made to investigate the various mechanical attributes of the sandstone after they were exposed to high temperatures. The graphical comparisons of various sandstones are represented in **Figure 4.34**.

Chapter 5 Experimental investigation of the effect of cyclic loading-unloading and the strain rate on sedimentary rocks

5.1 Effect of the loading-unloading cycle on the mechanical and AE characteristics of sandstone

AE response is the phenomena of capturing the released elastic strain energy during the deformation and failure of the rock material. These strain energies occur predominantly due to the expansion of internal cracks and defects as well as due to the generation of new macrocracks and their breakage under applied stress (Meng et al., 2018). In 1950, the Kaiser Effect was first reported by Kaiser, based on the AE characteristics. Subsequently, Goodman (1963) found its applicability in the field of rock mechanics. Real-time monitoring of the process of generation, development, and coalescence of rock-fractures by using AE techniques has proved to be a useful tool in the understanding of the deformational behaviour of rocks. In general, the AE technique is used to understand the evolution of the fracture and to predict the failure states and type, which reveals the instability mechanisms that are based on the relationship between AE activity and rock damage. Based on the AE, a cyclic compression test of rocks reveals mechanisms that are more complicated than the conventional uniaxial and triaxial compression test (Meng et al., 2018). In a natural scenario, the various stress conditions that are observed via the cyclic loading-unloading failure modes in different engineering fields are quite complicated (Rao and Ramana, 1992; Li and Nordlund, 1993; Meng et al., 2018). Acoustic emission reflects the evolution of internal defects during the course of stress application and provides crucial information that clarifies the internal destruction of rock materials. The Kaiser effect in marble was investigated by Fu et al. (2015) by using the Brazilian splitting test and the three-point bending test, in which various relations between the AE, stress and strain were established. Under cyclic loading-unloading conditions, the progressive failure of rock materials was studied by Li and Nordlund (1993) and Rao and Ramana (1992); they reported ambiguity in the appearance of the Kaiser effect in all types of rock masses. Similar to the experimental analysis mentioned above, Yang and Jing (2013) made an attempt to investigate the AE characteristic of red sandstone in a triaxial compression setup with varying confinements and complex stress paths (Yang and Jing, 2013).

5.1.1 Experimental investigation

In the current investigation, thermally treated sandstones were exposed to complex stress paths, and their response to cyclic loading and unloading was investigated. For the purpose, three

different patterns of loading and unloading were followed. The various stress paths that were used in the experimental investigations are shown in **Figure 5.1**.

Cylindrical sandstone specimens of 51 mm x 102 mm were prepared. As mentioned in the previous chapters, the specimens were cored and cut into cylindrical shapes as per the standard suggestions in end-face grinding to remove end-face irregularities. Cyclic loading-unloading experiments were conducted on thermally treated sandstone specimens to observe the effect of cyclic stressed and unstressed conditions in sandstone. In addition, the validation of the Kaiser effect in the thermally treated sandstones was examined in the investigation.

The application of cyclic loading and unloading of the specimens was achieved by using the Shimadzu compression machine at the Civil Engineering Department, Monash University. All the loading and unloading patterns were displacement-rate controlled. In addition to the stress level, the loading and unloading rates also play a vital role in the rock behaviour, by which the higher loading rates stimulate the expansion and connectivity rate of the internal microcracks and thereby accelerate the progression of the damage in the rock. Considering this, in order to avoid any ambiguity in the experimental results, the loading and unloading of the specimens were performed with the same loading rate (0.1 mm/min).

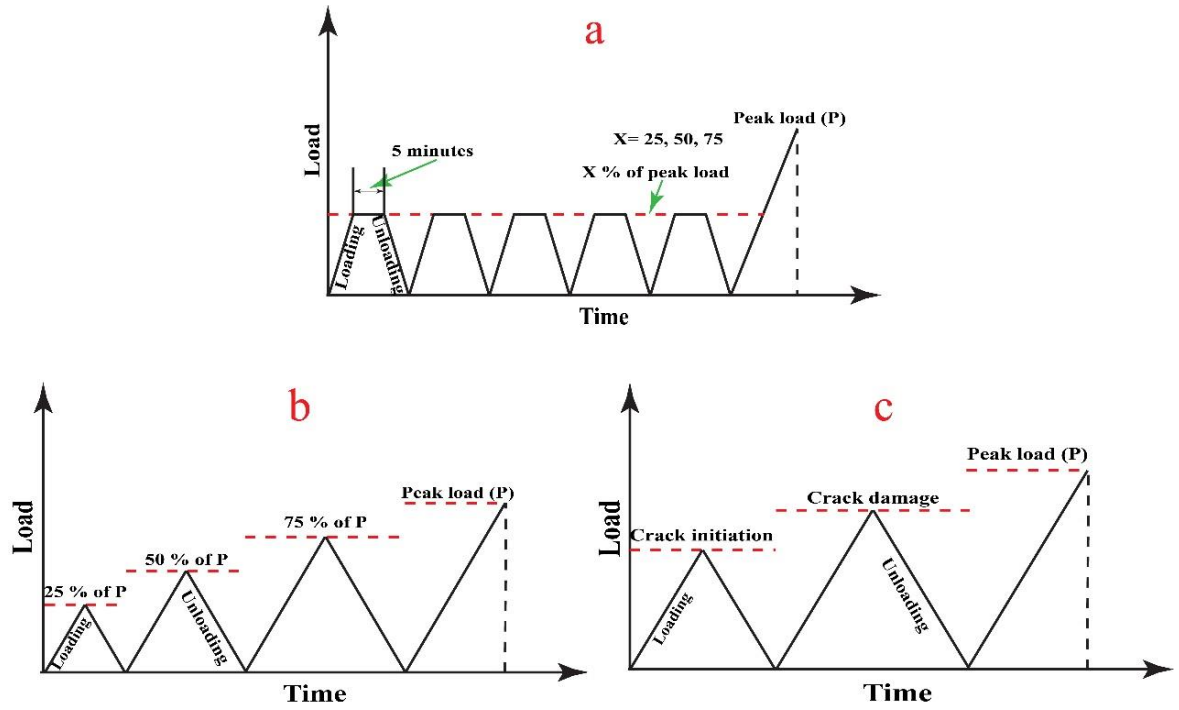

Figure 5.1 *Schematic of the different cyclic loading-unloading patterns follwed in the experiment*

For the development of a well-pronounced Kaiser effect, the preload stress should be between 30 per cent and 80 per cent of the ultimate strength. Below the lower boundary of this range, a low number of AE events are recorded, and this silence can be interpreted as the Kaiser effect. However, the suggested range is rock dependent, and it varies from rock to rock (Lavrov, 2003). Considering this, three different loading patterns were followed in the current investigation.

5.1.1.1 Multiple cycles at different stress levels of the peak load

In the first type of arrangement, the specimens were loaded to certain percentage (25 per cent, 50 per cent, and 75 per cent) of the peak load. Once the target load was achieved, the same stress condition was maintained for five minutes followed by unloading. The same loading-unloading cycle was repeated five times to observe different effect due to the cyclic loading and unloading (**Figure 5.1a**).

5.1.1.2 Incremental stress cycles based on certain percentages of the peak load

In the second type of arrangement, the specimens were loaded to certain percentages of the peak load followed by their unloading. In the following cycles, the load level was increase by 25 per cent and so on up to the peak failure of the specimens (**Figure 5.1b**).

5.1.1.3 Incremental stress cycles based on the acoustic characteristics

In the third type of arrangements, the specimens were loaded up to the crack-initiation point, which was followed by their unloading. In the subsequent cycle, the load was increased to the crack damage load and the peak failure load in the second and third cycles, respectively (**Figure 5.1c**).

Furthermore, in the result and discussion part of the analysis, the multiples cycles at the different stress levels, the incremental stress cycle based on a certain percentage of the peak load, and the incremental stress cycles based on the acoustic characteristics are referred to as case one, case two and case three, respectively.

5.1.2 Results and discussion

Rock engineering fields comprise various complicated stress conditions, and they frequently manifest the cyclic loading and unloading failure mode (Rao and Ramana, 1992; Li and Nordlund, 1993; Meng et al., 2018). Acoustic emission information is quite necessary and important in the understanding of the process of rock failure during the phenomenon of loading and unloading. Hence, in the current investigation, the rock behaviour that was exhibited through three different stress paths was observed with the help of the AE technique. For the

experimental investigation, thermally treated Jodhpur sandstone was used, and its AE characteristics were identified in response to different stress paths and temperatures.

In comparison to the conventional uniaxial and triaxial tests, the cyclic compression tests of rocks using the AE technique provides complicated mechanical features and detailed insight into the responses of rocks to applied load. Based on the information about rock damage and AE activity, information about the fracture evolution process, types and states of failure can be inferred and can be used to visualise the instability mechanism (Meng et al., 2018).

5.1.2.1 Multiple cycles at different stress levels of the peak load

The relation between the applied stresses along with time has been plotted in **Figure 5.2**, **Figure 5.4,** and **Figure 5.6** for the three conditions that were investigated in the current study. In cyclic loading and unloading tests, three specimens were used for each set. However, it is quite difficult to represents all the test results; hence, the results of only a few specimens were represented in this part of the research work. The single cycle AE responses of the sandstone have already been mentioned in **Chapter 4** and, hence, are not repeated here. Only cyclic AE responses of the sandstone have been included in this chapter.

For each cycle, the maximum AE counts were observed close to the unloading points. The unloading stage of the specimens was not involved with any AE activity, and the unloading stage had quiet periods in terms of AE counts; most of the AE events were produced during the loading stage of the specimen. However, repetition of the same stress level produced a certain amount of AE counts in case one.

Numerous AE events were recorded in the entire process of cyclic loading and unloading. Sandstone specimens that were exposed to different heating levels demonstrate various AE activities under different stress levels. **Table 5.1** represents the normalised cumulative AE counts of the thermally treated sandstone for multiple tested cycles at different stress levels.

Rocks generally undergo two types of deformation: elastic deformation and plastic deformation. Initiation of microcracks and the expansion of fractures are the predominant modes that contribute to the plastic deformation of the rocks. Although the deformation is recovered to some extent after unloading of the applied stress, large-scale plastic deformation results in continuous accumulation of rock damage.

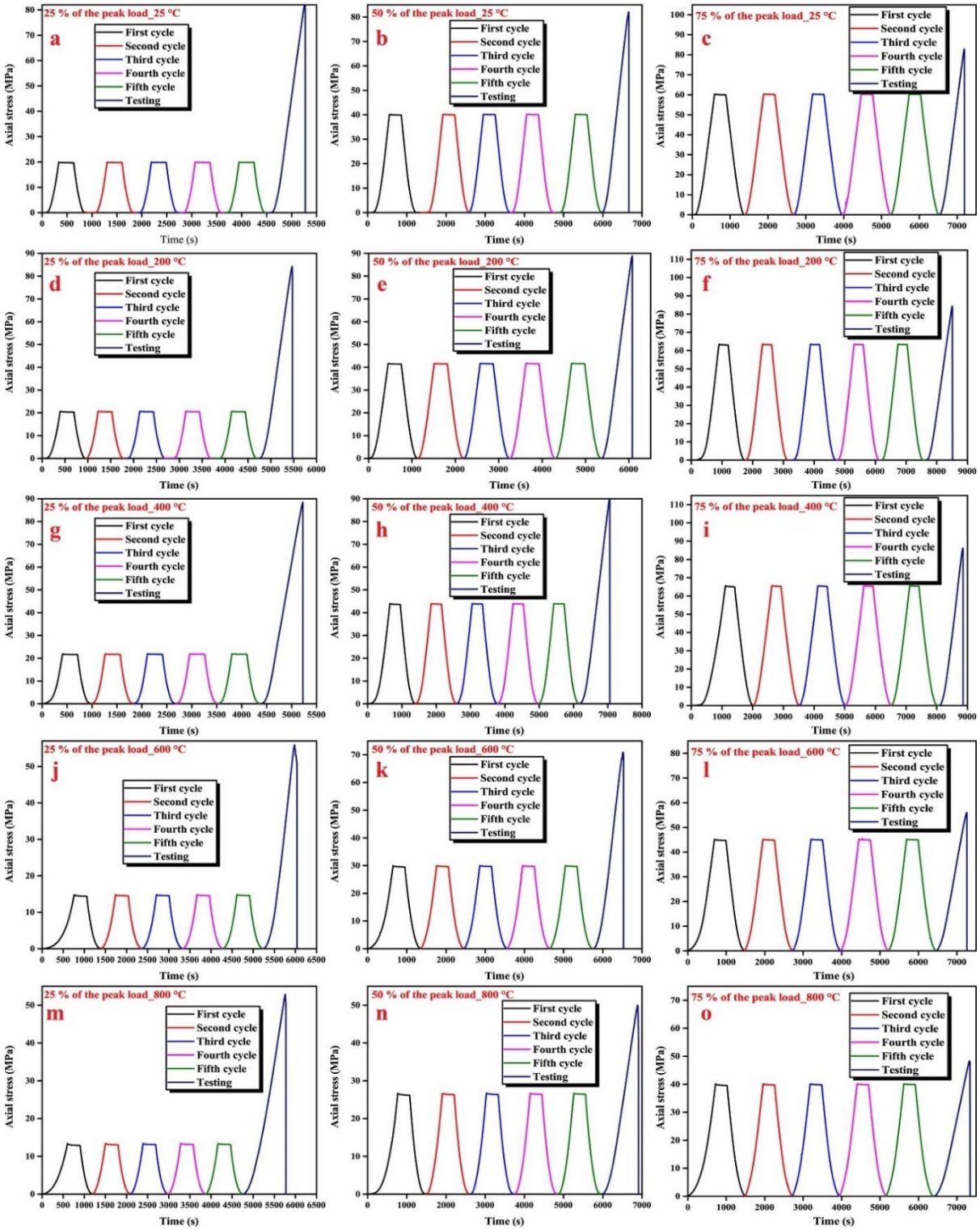

Figure 5.2 *Axial stress versus time curves of Jodhpur sandstone in multiple cycles at different stress levels of the peak load*

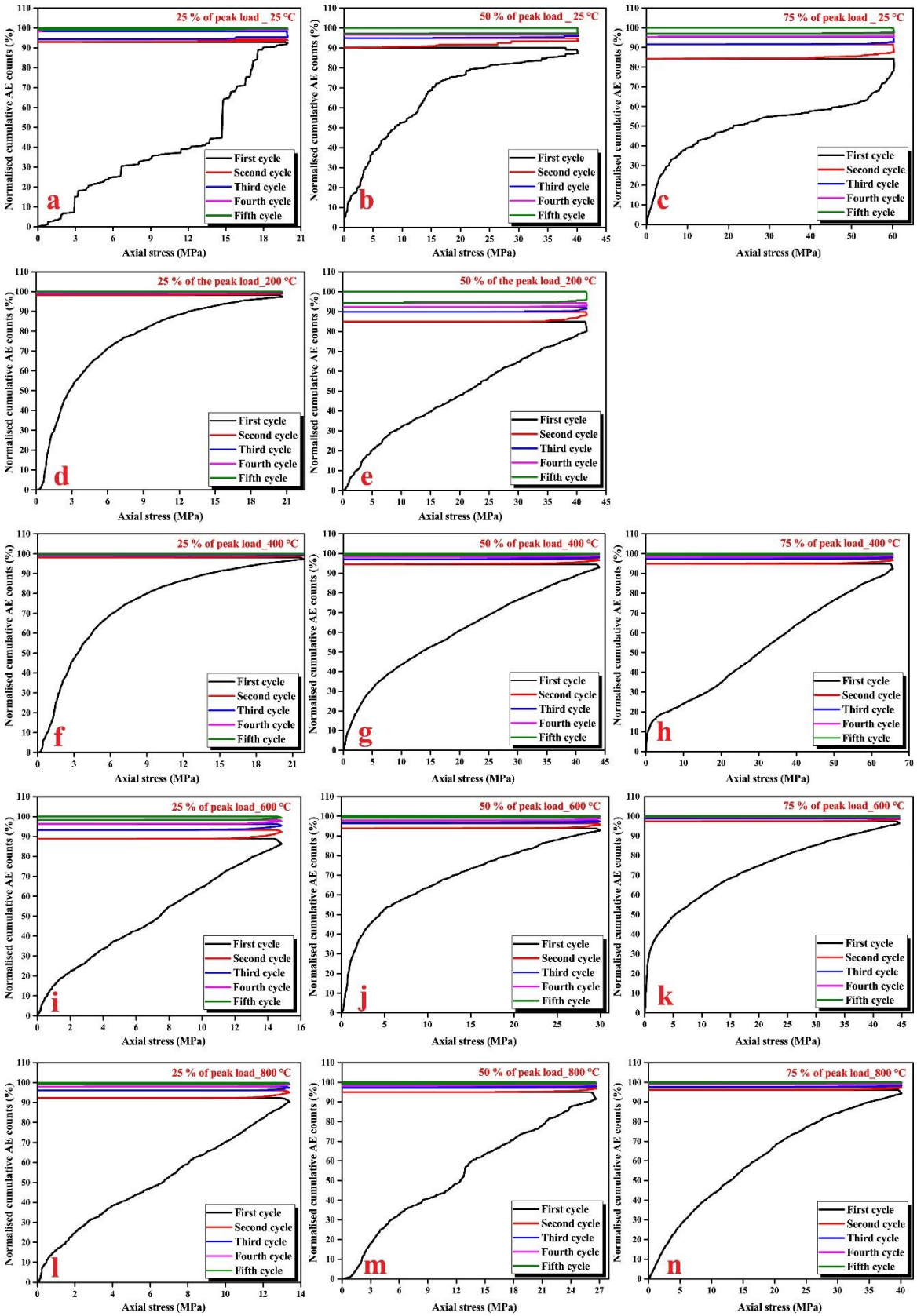

Figure 5.3 *Normalised cumulative AE counts of Jodhpur sandstone in multiple cycles at different stress levels of the peak load*

Table 5.1 *Normalised cumulative AE counts at different stages of applied stress in multiple cycles*

	Number of cycle	Normalised cumulative AE counts (%)		
		25 % σ_c	50 % σ_c	75 % σ_c
25 °C	First	92.985	90.177	84.213
	Second	94.345	94.904	91.557
	Third	98.280	96.675	95.331
	Fourth	99.126	97.276	97.087
	Fifth	100	100	100
200 °C	First	98.314	84.835	
	Second	99.436	89.831	
	Third	99.630	92.302	
	Fourth	99.892	94.226	
	Fifth	100	100	
400 °C	First	98.161	94.525	94.852
	Second	99.296	97.136	97.347
	Third	99.673	98.383	98.516
	Fourth	99.867	99.298	99.410
	Fifth	100	100	100
600 °C	First	88.838	93.837	97.375
	Second	93.248	96.365	98.799
	Third	96.268	97.766	99.327
	Fourth	98.263	99.220	99.715
	Fifth	100	100	100
800 °C	First	92.250	94.942	96.167
	Second	96.112	97.184	97.563
	Third	98.010	98.156	98.845
	Fourth	99.394	99.085	99.475
	Fifth	100	100	100

5.1.2.2 Incremental stress cycles based on certain percentages of the peak load

At room temperature, for both the second type and third type of loading and unloading cycles, a significant increment in the AE counts was observed when the applied load exceeded the previous maximum load, which indicated the Kaiser effect (discussed later) of the rock. However, in the thermally treated specimens, significant AE counts were recorded before the counts reach the maximum stress level of the previous cycle, indicating an inverse Kaiser effect or the Felicity effect (discussed later) (**Figure 5.5** and **Figure 5.7**).

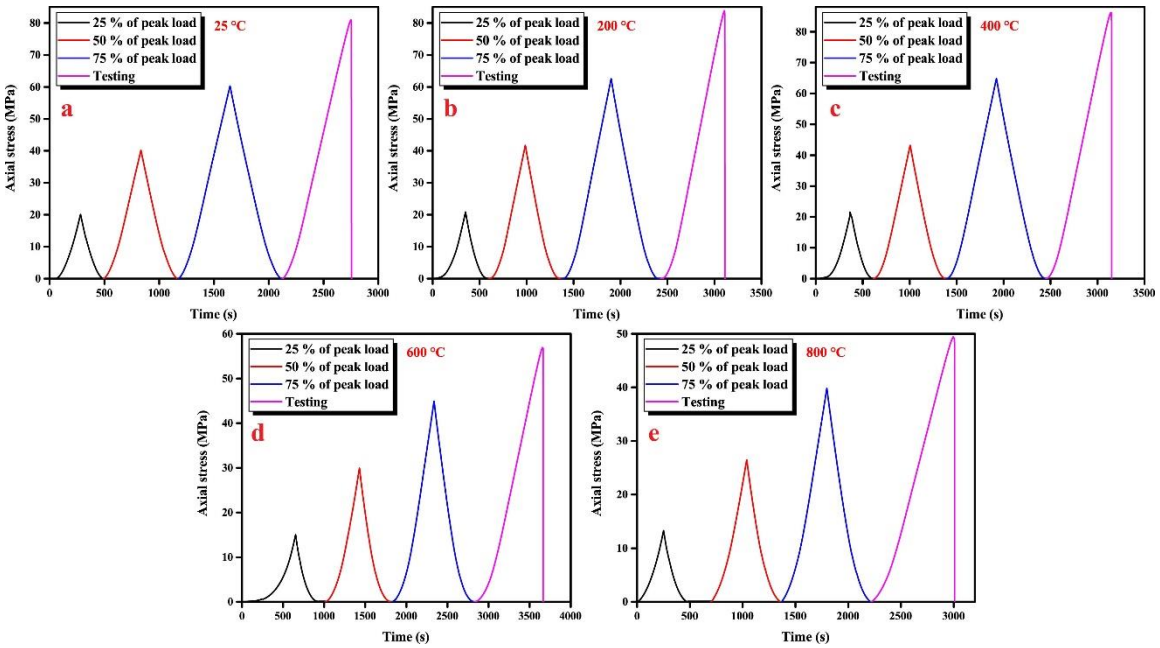

Figure 5.4 *Axial stress versus time curves of Jodhpur sandstone in incremental stress cycles at different stress levels of the peak load*

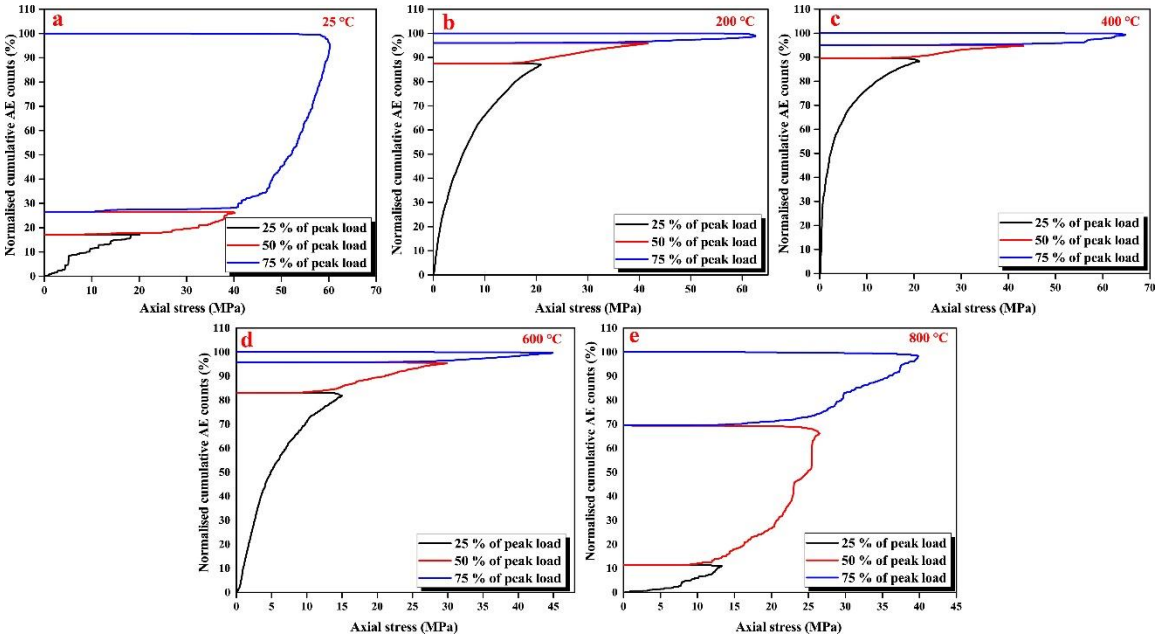

Figure 5.5 *Normalised cumulative AE counts of Jodhpur sandstone in incremental stress cycles at different stress levels of the peak load*

5.1.2.3 Incremental stress cycles based on acoustic characteristics

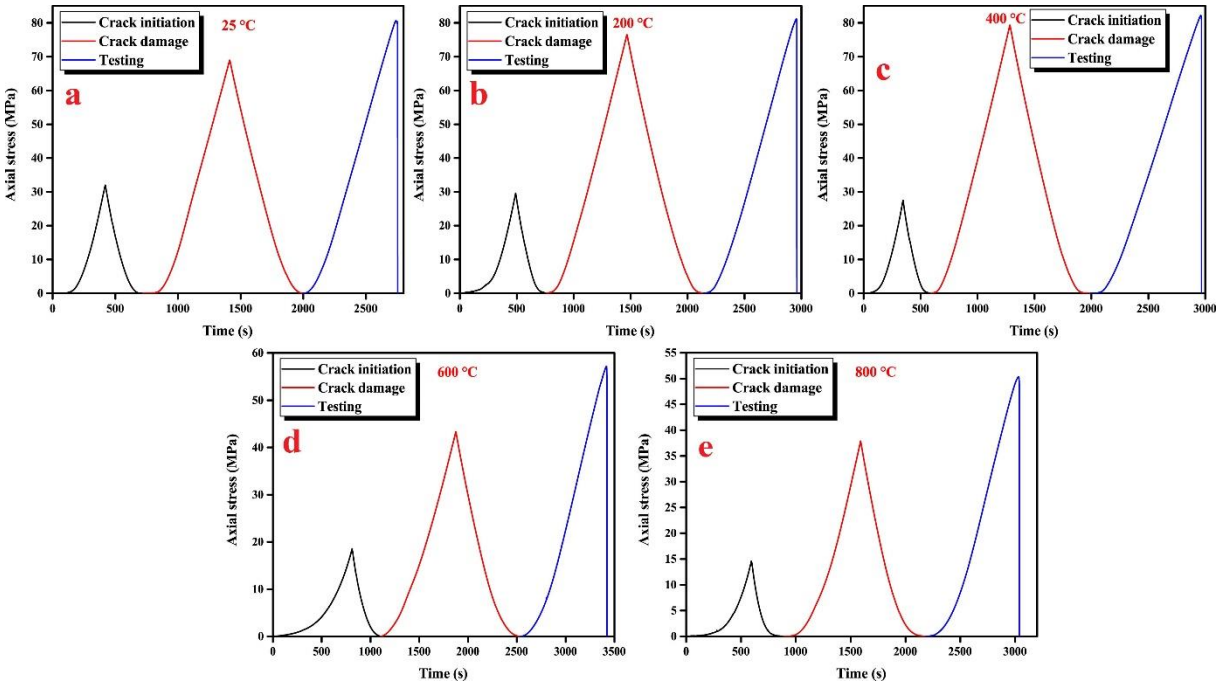

Figure 5.6 *Axial stress versus time curves of Jodhpur sandstone in incremental stress cycles based on acoustic characteristics*

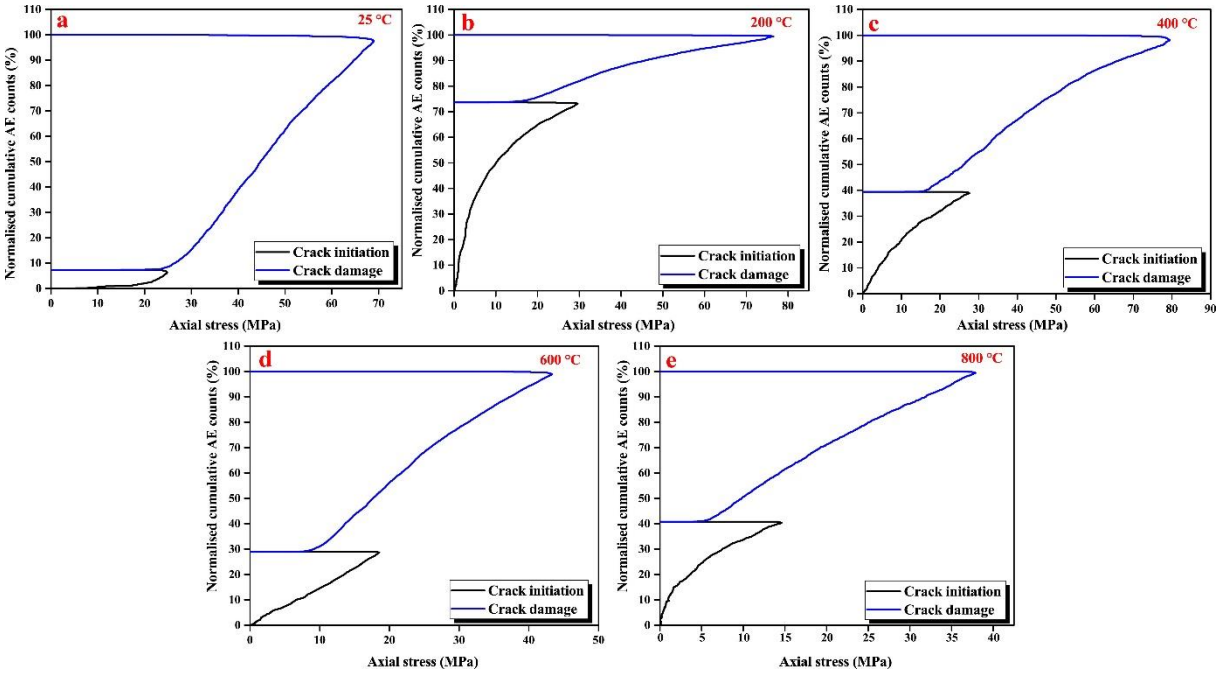

Figure 5.7 *Normalised cumulative AE counts of Jodhpur sandstone in incremental stress cycles based on acoustic characteristics*

5.1.2.4 The Kaiser effect and the Felicity effect in the failure and deformation stages of thermally treated specimens

The Felicity effect is an inherent property of rocks, which describes the irreversible degree of AE activity in rocks. During cyclic loading and unloading, the Felicity effect is the phenomenon of the beginning of significant AE counts before the current stress level exceeds the previous maximum stress levels. Mathematically, the Felicity effect is expressed in terms of the Felicity ratio as

$$FR_i = \frac{P_{i+1}}{P_{imax}}$$

Where,

FR_i : Felicity ratio in the i^{th} cycle

P_{i+1} : Stress level in the $i+1^{th}$ cycle when significant AE counts are produced

P_{max} : Maximum stress level in the i^{th} cycle

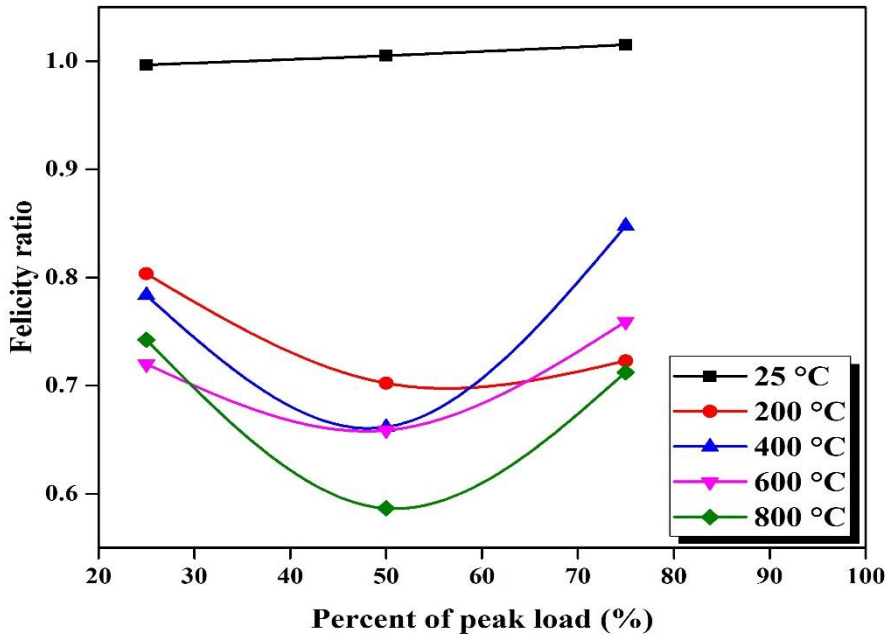

Figure 5.8 *Felicity ratio for the sandstone tested with incremental stress cycles based on certain percentages of the peak load*

According to the Kaiser effect, when the stress level in the current cycle exceeds the previous maximum stress level, significant increment in the AE counts is observed, which demonstrates the memory accuracy of the experienced stress level of rocks. Therefore, the Felicity ratio measures the accuracy of the Kaiser effect. In the condition at which FR ≥ 0, the Kaiser Effect

is effective, and the condition with FR < 0 represents the damaged state of the rock materials. The smaller the Felicity ratio values, the higher the degree of structural damage in the rocks.

Based on the AE characteristic, it was observed that in case two and case three, at room temperature, the Kaiser effect was quite satisfactory, and significant AE counts were produced when the stress level in the current cycle exceeded the maximum stress level of the previous cycle (**Figure 5.7** and **Figure 5.9**). However, in higher temperatures, the Kaiser Effect was not as significant as the room temperature in both case two and case three. In the case of high temperatures, a significant number of AE counts were observed well before the previous maximum stress. In such a situation, the accuracy of the Kaiser effect or the stress memory effect of the sandstone can be explained in terms of the Felicity ratio. **Figure 5.8** and **Figure 5.9** represent the Felicity ratio for both case two and case three, respectively. In case one, the same stress level had been repeated for five cycle; hence, the effectiveness of the Kaiser effect or of the Felicity effect was not determined.

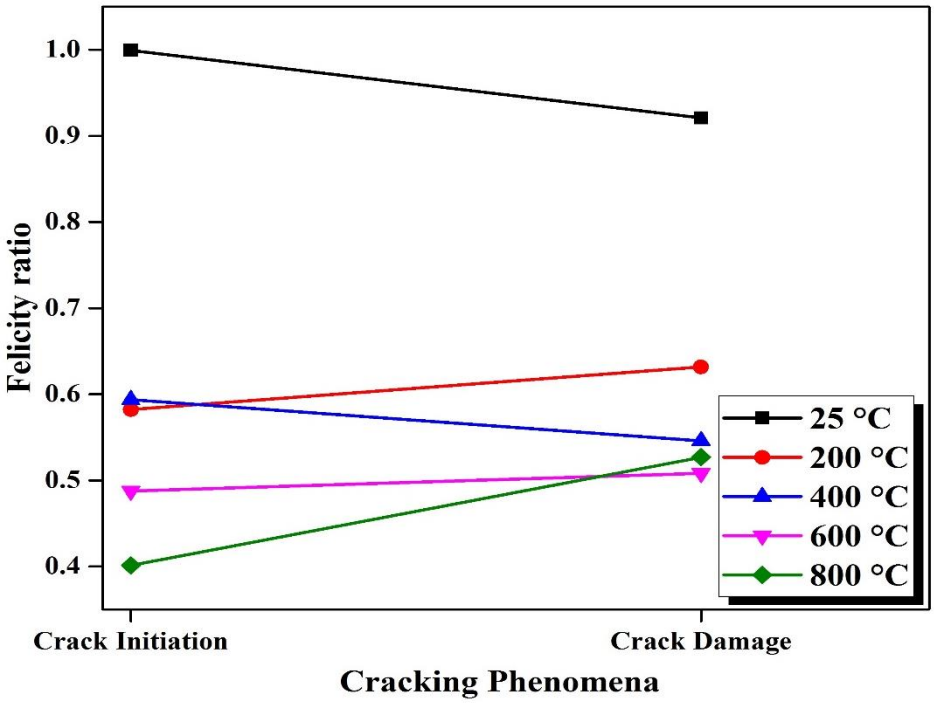

Figure 5.9 *Felicity ratio for the sandstone tested with incremental stress cycles based on acoustic characteristics*

5.2 Effect of strain rates on the mechanical properties of shale

5.2.1 Overview

The modern improved engineering technologies in the field of rock mechanics and the successful identification of the hydrocarbon potential of gas shales have turned the tight shale

formations as a profitable resource for the natural gas. In the current study, Jhiri shale was tested for its strength; deformational failure attributes and mechanism at different strain rates in order to understand the dependence of the deformation rate upon various geomechanical properties. The rock samples were subjected to varied strain rates during loading and the resultant geomechanical properties such as UCS, tensile strength (σ_t), Young's modulus (E), failure strain (ε_f), mode I and mode II fracture toughness (K_{IC} and K_{IIC}) and brittleness index (B_1 and B_2) were determined in each case. The stress-strain behaviour of the Jhiri shale was estimated at four different strain rates that varied from 1.7 x 10^{-2} s^{-1} to 7.9 x 10^{-5} s^{-1}. It was found that all of the mechanical parameters of the rock that are mentioned above, except for the failure strain, increased with increasing strain rates. Such behaviour of the rock due to the strain rates may be due to stress redistribution during grain fracturing. At a strain rate of 7.9 x 10^{-5} s^{-1}, UCS, tensile strength, mode I fracture toughness and mode II fracture toughness of Jhiri shale were found to be 25.45 MPa, 7.71 MPa, 0.171 MPa $m^{1/2}$ and 0.083 MPa $m^{1/2}$, respectively, which increased up to 50.57 MPa, 13.06 MPa, 0.565 MPa $m^{1/2}$ and 0.467 MPa $m^{1/2}$, respectively, at a strain rate of 1.7 x 10^{-2} s^{-1}. Critical and appropriate empirical equations have been proposed to evaluate the strain-rate dependency of the mechanical properties of the rock.

5.2.2 Background knowledge

After the successful exploitation of shale gas in the United States, studies on the geomechanics of shale is gaining momentum. Two key components to the success of shale gas story are directional drilling and hydraulic fracturing. The fracturing behaviour of shale under various in-situ conditions attracts the attention of scientists worldwide to resolve different critical problems in the field of geo-engineering like reservoir geomechanics, hydraulic fracturing, drilling, and blasting and geothermal energy tapping etc. With the aid of modern improved technologies in the field of rock mechanics (fracturing and drilling) and in the identification of the hydrocarbon potential of gas shales, tight shale formations have shifted from an otherwise uneconomic rock type to a lucrative resource of natural gas (Holmes et al., 2015; Vishal et al., 2015). It is known that the mechanical behaviour of rocks is controlled by the state or condition of the stress applied to it. Further, environmental factors such as pressure, temperature, humidity, water vapour, and strain rate, and intrinsic rock characteristics such as grain size, composition, and anisotropy affect the mechanical strength of rocks. The degree of anisotropy because of the preferred alignment and/or microcracks, the orientation of mineral grains, and minerals with preferred bands or veins strongly affect the directional strengths of the rocks. Understanding the mechanical behaviour of shales in good detail is quite a difficult task

because of their complex nature and heterogeneous structural features such as anisotropy, grain orientation, presence, and distribution of microcracks, and the segregation of minerals along the preferred orientation (phyllosilicate minerals). A detailed and better understanding of rock behaviour, strength, fracture pattern, and fragmentation will promote the better exploitation of the natural resource and will lead to a better design standard for engineering work in these rocks.

For a better development of design standards and structures, a better understanding of fracture behaviour and rock strength in different strain rates is required (Hokka et al., 2016). Several researchers have studied the effects of strain rate on different mechanical properties of rocks (Bieniawski, 1970; Cadoni, 2010; Chong and Boresi, 1990; Dragon and Mroz, 1979; Heap et al., 2009; Kumar, 1968; Liang et al., 2015, 2011; Mahmutoglu, 2006; Masuda et al., 1987; Sano et al., 1981; Zhang et al., 2000; Zhou et al., 2010). In rock mechanics, the prime focus is on the time involved and the energy required for the fragmentation of the rocks; in such a case, the strain rate can be a deciding factor in estimating these requirements (Blanton, 1981; Cleja-Tigoiu, 1991; Wasantha et al., 2015; Zhang et al., 2003). Different phenomena such as geological tectonic movement, and mining and blasting design can be explained by the time-dependent deformational behaviour of rocks (Bieniawski, 1970; Chong and Boresi, 1990; Li and Xia, 2000; Zhang and Zhao, 2014; Zhao et al., 1999).

The mechanical behaviour of various rocks under the influence of strain rate during compression (Liu and Xu, 2015; Xia et al., 2008), tension (Cho et al., 2003; Fourmeau et al., 2014), and bending (Dai et al., 2011; Dai and Xia, 2013) have been studied in the recent years. The strain rate dependency of the strength and ductility of Colorado oil shale was investigated by Lankford (1976), in which the failure strength was found to increase with the strain rate. Based on the experimental results on Kuru granite, Hokka et al. (2016) reported that the rock strength increased with an increase in the confining pressure and the strain rate. Yang et al. (2005) observed an increase in the peak strength as well as in the strain with the increasing loading rate. However, they reported that the failure mode of the rocks did not change with the strain rates. Mahmutoglu (2006) carried out experiments on thermally treated Mugla marble with strain rates varying from $2x10^{-5} – 5x10^{-7}s^{-1}$ and reported that the compressive strength of the rock decreased with a decrease in the strain rates. He also reported that the decrease of strength in the dry specimen was about 44 per cent while in a saturated condition, it was much higher. Ray et al. (1999) experimentally observed that the UCS of Chunar sandstone increased from 64 MPa to 99.5 MPa with an increase in the strain rate from $2.5 \times 10^{-1} – 2.5 \times 10^{1}\ s^{-1}$,

respectively. Cho et al. (2003) performed experiments to measure the dynamic tensile strength of rocks such as Inada granite and Tage tuff and found that the strength of these two rock types increased rapidly with increasing strain rates. Li et al. (2000) determined the dynamic tensile strength of Bukit Timah granite using four different values of strain rates and six different values of confining pressures. They observed that the compressive strength gradually increased with increasing strain rates and confining pressure. There is a considerable increase in the tensile strength of concrete with increasing loading rates (Reinhardt and Weerheijm, 1991). They attributed such a rock response to the kinetics of energy barriers and inertia effects in the vicinity of a running crack. It can be well inferred from the experiments performed by Gao et al. (2015), Dai and Xia (2013), Hokka et al. (2016) that the fracture toughness and the fracture strength of brittle materials are very sensitive to the loading rates. Li and Wang (2006) measured the dynamic fracture toughness of marble using the Hopkinson bar and observed that the toughness increased with the loading rates. Fukui et al. (2004) reported that the shear strength of Sanjome andesite was dependent on loading rates. They also reported that the cohesion of the rock increased by 6.1 per cent with an order of magnitude increase in the loading rate. Further, they reported that other geomechanical properties such as UCS, indirect tensile strength, and fracture toughness increased with the loading rate. Blanton (1981) investigated the mechanical behaviour of Charcoal granodiorite, Berea sandstone, and Indiana limestone across strain rates, from 10^{-4} s^{-1} to 10^{3} s^{-1}. He concluded that with increasing strain rates, the brittleness of Berea sandstone and Indiana limestone increased. Similarly, Fuenkajorn and Kenkhunthod (2010) and Okubo et al. (2013) performed the loading rate effect on the mechanical behaviour of various rocks and concluded that the peak strength and the elastic modulus of rocks increased in an exponential manner with the increase in the loading rate. They also reported that the UCS increased within a range of 1–10 per cent for every order of magnitude increase in the loading rate. The current study includes the experimental investigation of Jhiri shale under varying strain rates for a better understanding of the mechanical behaviour of shales. The strain rate was varied between low and intermediate rates in the range of 7.9×10^{-5} to 1.7×10^{-2} s^{-1}. For convenience of the readers, the different strain rates applied in these experiments are denoted by S1, S2, S3 and S4, in which S1= 1.7×10^{-2} s^{-1}, S2 = 1.3×10^{-2} s^{-1}, S3 = $3.8 \times 10^{-3} s^{-1}$ and S4 = 7.9×10^{-5} s^{-1}, respectively.

5.2.3 Experimental investigation

The experiment includes investigation of various geo-mechanical properties of rock like UCS, Young's modulus (E) and peak strain (ε_f), Brazilian tensile strength and brittleness index.

Except for brittleness index, all other rock properties were determined according to the standards of the International Society for Rock Mechanics (ISRM 1981).

In past few years, many researchers have considered brittleness index based on various approaches like UCS and tensile strength; mineral composition, porosity and grain size; stress-strain curve; penetration, impact, or hardness test; and geophysical method. However, for the current study, the brittleness indices (B_1 and B_2) were evaluated on the basis of compressive strength and tensile strength of the rock as described in the previous literature (Altindag, 2002; Altindag and Guney, 2010; Kahraman and Altindag, 2004).

$$B_1 = \frac{(\sigma_c * \sigma_t)}{2} \qquad B_2 = \frac{(\sigma_c - \sigma_t)}{(\sigma_c + \sigma_t)}$$

Where,

σ_C : UCS of the rock (MPa)

σ_t : Tensile strength of the rock (MPa)

5.2.4 Results and discussion

The investigated geomechanical properties at multiple strain rates are represented in **Table 5.2**, respectively. Strength increase as a function of strain rate is attributed to the micromechanical cause of rock deformation during loading. In rocks, there are two stages of strain increment: elastic strain and plastic strain. Elastic strain is independent of the strain rate as it occurs in a quick span of time. The plastic deformation component depends on the strain rate. Under a certain stress condition, the plastic strain develops completely if there is sufficient time before the next incremental stress. Under low strain rate conditions, the strain rates are quite low and there is sufficient time for the development of plastic strain in between two successive stress levels. In the case of high strain rates, the plastic strain does not get sufficient time before the next incremental strain, resulting in stiffening of the rock materials (Chong and Boresi, 1990; Wasantha et al., 2015; Zhang et al., 2008).

Table 5.2 *Experimentally determined average geomechanical properties of the rock*

$\dot{\varepsilon}$	**UCS (MPa)**	**E (GPa)**	ε_f	σ_t **(MPa)**	K_{IC} **(MPa m$^{1/2}$)**	K_{IIC} **(MPa m$^{1/2}$)**	B_1	B_2
7.9 x 10^{-5}	25.45	12.65	0.00209	7.71	0.171	0.083	99.07	0.533
3.8 x 10^{-3}	34.31	26.62	0.00167	9.48	0.225	0.176	163.74	0.568
1.3 x 10^{-2}	43.54	45.49	0.00126	11.28	0.343	0.231	244.47	0.587
1.7 x 10^{-2}	50.57	61.22	0.00114	13.06	0.565	0.467	331.12	0.590

$\dot{\varepsilon}$: strain rate; UCS; E: Young's modulus; ε_f: failure strain; σ_t: tensile strength; K_{IC}: mode I fracture toughness; K_{IIC}: mode II fracture toughness; B_1 and B_2: brittleness index.

The effect of strain rates in rock deformation can be explained from the energy point of view. Damage to materials is attributed to the induced microfractures. Under conditions of high strain rates, the development of microfractures in the material lags when compared to the increment of loading, that is, the response and the deformation speed of grains within the material are slower. The energy that was absorbed by the material as a result of loading cannot be consumed or released completely in a short period of time by developing microfractures; as a result, the absorbed energy is stored temporarily as material compression, thereby enhancing the strength of the material (Liang et al., 2011). At low strain rates, the fragments are large and the crack propagates further, whereas, at high strain rates, the fragments are small and the cracks are localised (**Figure 5.10b** and **Figure 5.10c**). A theoretical model explaining the strain rate effect on rocks like material has been included in **Appendix 1** The theoretical background for the strain-rate effect on the rock properties.

It was found that the failure strain at higher strain rates is quite low when compared to the failure strain at lower strain rates. Higher strain rates possess higher strength as compared to the low strain rate conditions. This is the reason for which the low strain-rate stress-strain curve always lying below the high strain-rate stress-strain curves (**Figure 5.10a**). With increasing strain rates, the strain at the peak strength/peak strain decreases (**Figure 5.12d**). In a variation of strain rate from 7.9 x 10^{-5} s^{-1} to 1.7 x 10^{-2} s^{-1}, the failure strain was reduced from 0.00209 to 0.00114 i.e. nearly about 45 per cent decrease in the failure strain.

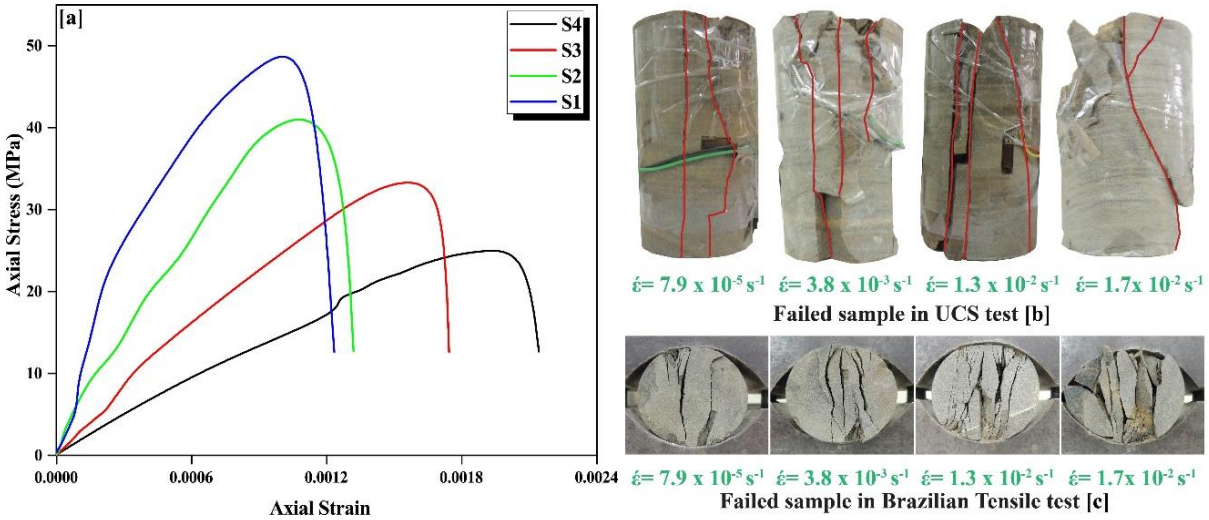

Figure 5.10 *Stress-strain curve of the rock at different strain rates (a). Fractured samples after compression test at different strain rates (b). Fractured samples recovered after Brazilian tensile tests at different strain rates (c)*

Figure 5.10a represents the stress-strain behaviour of the rock at different strain rates. It was found that the stiffness of the rock increased with the gradual increase in the strain rates. At a strain rate of 7.9 x 10^{-5} s^{-1}, Young's modulus of the rock was found to be 12.65 GPa that gradually got increased with an increase in the strain rate and reached up to 61.22 GPa at a strain rate of 1.7 x 10^{-2} s^{-1} (**Figure 5.12c**).

5.2.4.1 Macroscopic fracture failure

In the UCS test, with gradual increase of strain rates, there was extensive shear mode component during the fracturing. At a high strain rate, the mode of fracturing was completely in shear mode (**Figure 5.10b**). The shear mode fracturing that was obtained in the shale samples was in accordance with the findings of Liang et al. (2015). In the Brazilian tensile test, the number of fractures formed at lower strain rates was quite less compared to the high strain-rate case. At high strain rates (1.7 x 10^{-2} s^{-1}), a larger number of fractures were formed in the specimen, resulting in complete pulverisation and collapse of the specimen (**Figure 5.10c**). Nikolaevsky (1990) suggested a model that explains the fragmentation of specimens that are loaded at high strain rates. According to the model, when the crack growth velocity (the terminal velocity) is limited, a higher amount of stress causes the growth of small cracks, which emerge in front of the main cracks after the propagation of the main crack is arrested. During uniaxial compression, certain sites within the rock may be subjected to tensional stresses, which give rise to the nucleation/formation and growth of microcracks. Incremental strain rate increases the applied stress, leading to the activation of a higher number of such microcracks. On the contrary, at low strain rates, fewer and larger microcracks are activated.

5.2.4.2 Mesoscopic and microscopic fracture surface

Under low and quasi-static conditions of loading, sufficient time is available for stress redistribution. Therefore, the collective damage occurs along the weak parts that are adjacent to the crack tip and the crack propagates along the grain boundaries resulting in fractures that are intergranular in nature. However, in the case of high strain rates, the stress at the crack tip does not get sufficient time to spread away from the crack tip, as a result of which the crack propagates rapidly through the mineral grains, resulting transgranular cracks.

With further increase in the strain rate, there tends to be a greater dominance of the transgranular fracture, whereas, at lower strain rates there are principally intergranular fractures (Mahanta et al., 2017b; Wasantha et al., 2015; Zhang and Zhao, 2013). The SEM micrographs of the tested rock specimen represent the occurrence of intergranular fracture pattern as a result of a low strain rate that possesses rough fracture surfaces (**Figure 5.11c** and **Figure 5.11d**).

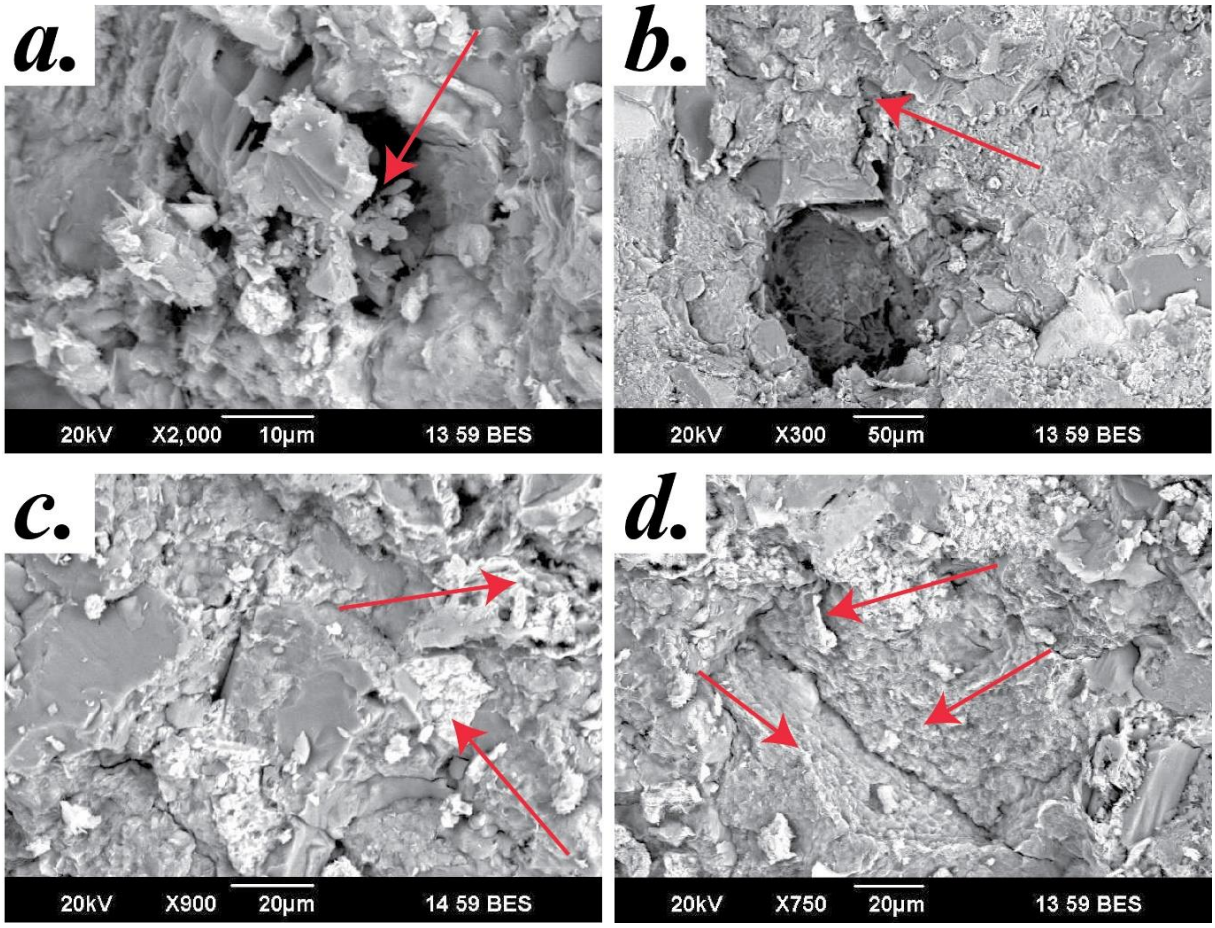

Figure 5.11 *SEM micrographs of the studied rock representing the pore spaces, different types of granular fractures and the presence of clay minerals in the rock* (Mahanta et al., 2017b)

5.2.4.3 Influence of strain rate on various mechanical strength parameters

With increasing strain rate, the UCS, as well as the tensile strength of rock, are gradually increasing (**Figure 5.12a,** and **Figure 5.12b**). At a strain rate of 7.9 x 10^{-5} s^{-1} the UCS and tensile strength of the rock were found to be 25.45 MPa and 7.71 MPa, respectively, which reached up to 50.57 MPa and 13.06 MPa, respectively, at a strain-rate of 1.7 x 10^{-2} s^{-1}. Under low strain rate conditions, the principal fracture mode has low energy consumption, resulting in lower UCS.

Under high strain rates, the energy input will be faster and higher, resulting in transgranular fractures that are more difficult to generate and propagate, which eventually leads to the high rock-strength. Any increase in strain rate causes an increase in the absorbed energy per unit volume in the number of induced cracks and in the area of the fracture surface, which leads to a high number of rock fragments at a variable scale (Hokka et al., 2016; Mahanta et al., 2018). The mineralogy of the rock also plays a significant role in the fracture behaviour of the rock. Hogan et al. (2012) reported that the quartz content has a strong influence on the fragmentation

process of the rock. Quartz is the dominant mineral phase present in the tested samples and that may have contributed to the fragmentation behaviour of shale under different strain rates.

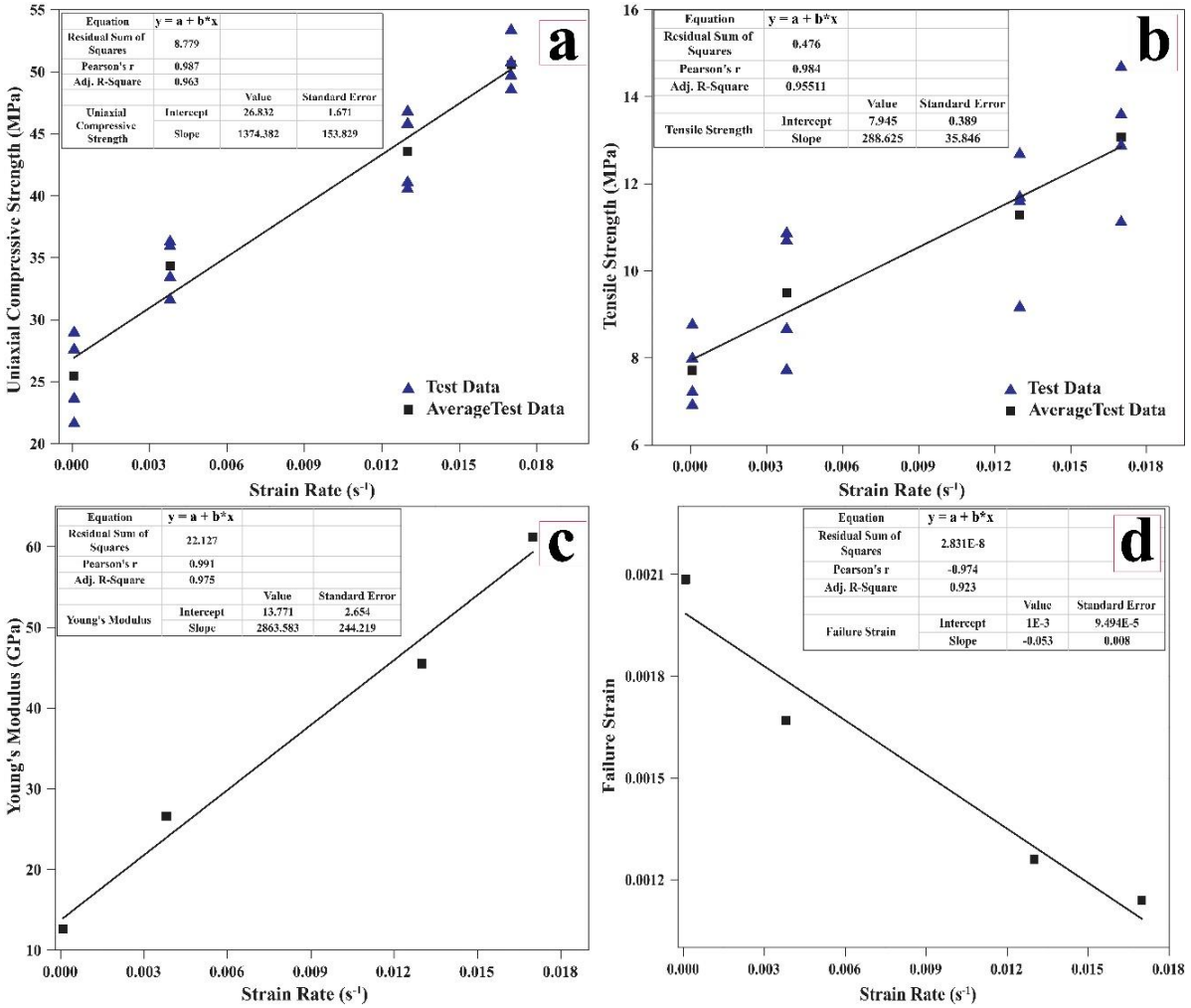

Figure 5.12 *Variation of UCS (a), tensile strength (b), Young's modulus, (c) and failure strain (d) with strain rates*

Fracture toughness data of the strain rate effect on the studies rock were collected from Mahanta et al. (2017) (explained in detailed in chapter 6.2). Both mode I and mode II fracture toughness of the rock was found with an increasing trend with the increasing strain rates which was in accordance with the experimental result observed by Dai and Xia (2013). At a strain rate of 7.9 x 10^{-5} s^{-1}, mode I and mode II fracture toughness of the rock were found to be 0.171 MPa $m^{1/2}$ and 0.083 MPa $m^{1/2}$, respectively. However, mode I and mode II fracture toughness were found to be 0.565 MPa $m^{1/2}$ and 0.467 MPa $m^{1/2}$, respectively, at a strain rate of 1.7 x 10^{-2} s^{-1} (**Figure 5.13a**, and **Figure 5.13b**).

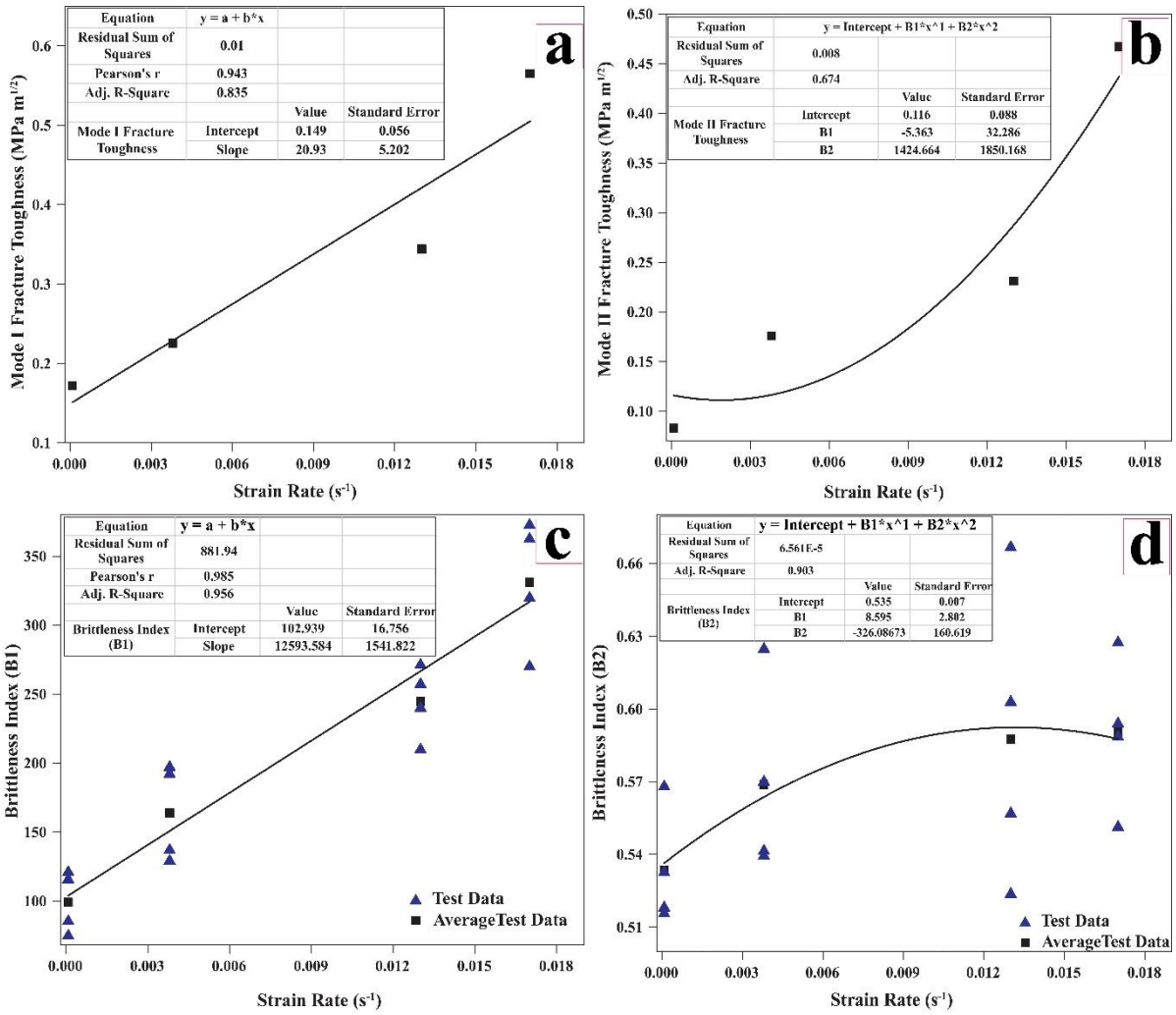

Figure 5.13 *Variation of mode I fracture toughness (a), mode II fracture toughness (b), brittleness index B_1 (c) and brittleness index B_2 (d) with strain rates*

Brittleness index B_1 and B_2 were found in an increasing trend with the strain rates which was in accordance with the finding of Duda and Renner (2013). UCS describes the compressibility of rock, whereas, tensile strength describes the cohesion of the bonds between the grains of the rock. The higher the difference between these two parameters, the higher the brittleness of the rock. In between B_1 and B_2, B_1 is more practical than B_2, as it can be used for the prediction of some brittleness-related rock properties such as fracture toughness (Kahraman and Altindag, 2004) and rock drillability (Altindag, 2002). Similarly, increasing loading rates promote the brittle nature of rock as rock-samples tend to break unstably (Duda and Renner, 2013; Zhang et al., 2016). In recent times, many authors have used this brittleness index to characterise different rock types, to estimate the drillability index, and in identifying the problems involved in borehole collapse and hydraulic fracturing (Holt et al., 2015; Hucka and Das, 1974; Özfırat et al., 2016; Rybacki et al., 2016; Zhang et al., 2016). Brittleness index, B_1 increased from 99.07 to 331.12, whereas brittleness index, B_2 increased from 0.533 to 0.590 when the strain

rate was increased from 7.9 x 10^{-5} s^{-1} to 1.7 x 10^{-2} s^{-1}, respectively (**Figure 5.13c** and **Figure 5.13d**).

5.2.4.4 Regression analysis based on the experimental results

The experimentally observed parameters were correlated with the different strain rates that were conducted in the experiments. Based on the observations, different types of curves (linear and polynomial) were fitted to the experimental data. All the regression analysis details are demonstrated in **Table 5.3**. The regression analyses of different geomechanical properties with strain rates are shown in **Figure 5.12** and **Figure 5.13**.

Table 5.3 Regression analysis for independent variable and dependent variables

Independent Variable	Dependent Variable	Correlation	Correlating Equation	R^2
Strain Rate	UCS	Linear	UCS= 1374.4$\dot{\varepsilon}$ + 26.833	0.97
Strain Rate	E	Linear	E= 3628$\dot{\varepsilon}$ + 11.626	0.99
Strain Rate	ε_f	Linear	ε_f= -0.09$\dot{\varepsilon}$ + 0.002	0.97
Strain Rate	σ_t	Linear	TS= 288.63$\dot{\varepsilon}$ + 7.945	0.97
Strain Rate	K_{IC}	Linear	K_{IC}= 20.931$\dot{\varepsilon}$ + 0.149	0.89
Strain Rate	K_{IIC}	Polynomial	K_{IIC}= 1424.7$\dot{\varepsilon}^2$ - 5.363$\dot{\varepsilon}$ + 0.116	0.89
Strain Rate	B_1	Linear	B_1= 12594$\dot{\varepsilon}$ + 102.94	0.97
Strain Rate	B_2	Polynomial	B_2= -326.09$\dot{\varepsilon}^2$ + 8.595$\dot{\varepsilon}$ + 0.535	0.96

5.2.4.5 Correlation between fracture toughness and brittleness index

In the field of rock fracture mechanics, fracture toughness is quite an important parameter. However, the evaluation of fracture toughness is relatively more difficult, compared to other rock properties like UCS, tensile strength. Therefore, if a good correlation can be established between these standard rock properties and fracture toughness, then a substantial information about the fracture toughness of the rock can be easily acquired.

Keeping this in mind, lastly, a correlation between both the fracture toughness (mode I and mode II) and brittleness index (B_1 and B_2) is established (**Figure 5.14**). From the analysis, it can be observed that brittleness index B_1 possesses strong correlation with both the measured fracture toughness values. Although the correlation between brittleness index B_2 and fracture toughness is not as strong as compared to the brittleness index B_1, still it holds a good correlation with fracture toughness with a coefficient of determination 0.82 and 0.86 for mode I and mode II, respectively.

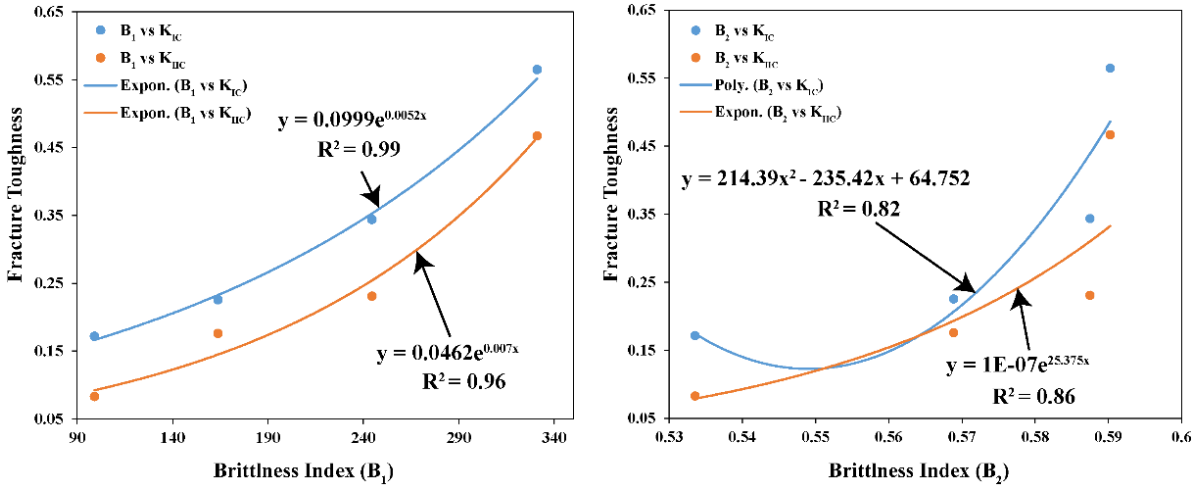

Figure 5.14 *Correlation between measured fracture toughness and brittleness index of the rock*

5.2.4.6 A comparison of the effect of strain rate on rocks

Among various mechanical strength parameters of rocks, tensile strength and the compressive strength are considered to be very important. Considering this at the end of the manuscript a comparison of tensile strength and compressive strength of various rock types that are already present in the literature and the results of the current experimental analysis has been done.

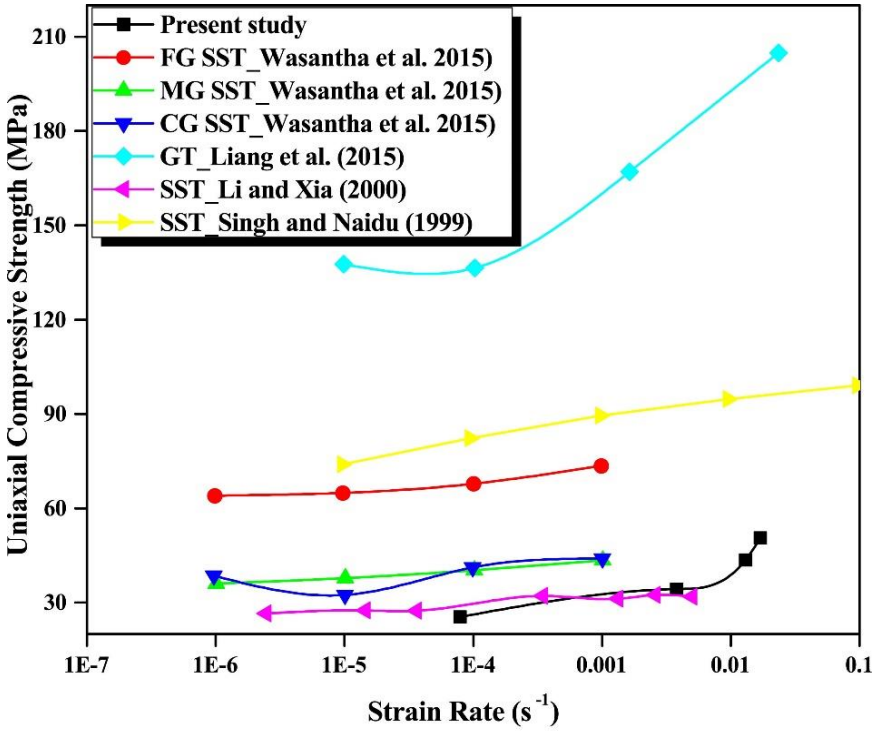

Figure 5.15 *Comparison of uniaxial compressive strength of various rocks with strain rates*

The comparison of uniaxial compressive strength and tensile strength of all the rocks are represented in **Figure 5.15** and **Figure 5.16**, respectively. In most of the case, the compressive

strength and tensile strength of rocks follow an increasing trend with the increase of the strain rates. However, the UCS of coarse grain sandstone (Wasantha et al., 2015), an initially decreasing trend was observed with increasing strain rates and in the later stage its UCS value increased with increasing strain rates. The current studied rock displayed a significant increase in its tensile strength values with increasing strain rates. However, the increment is not that much significant for the other mentioned cases.

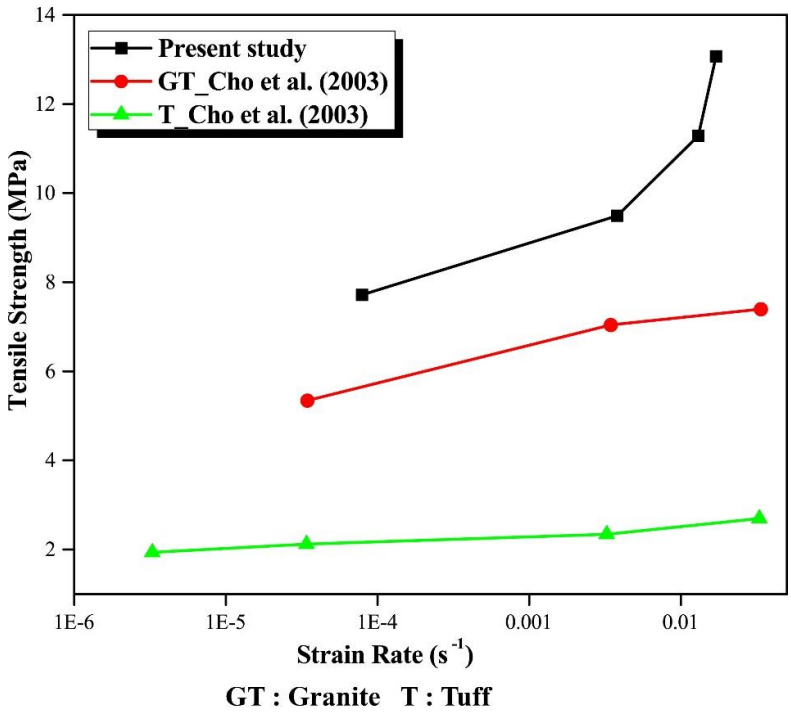

Figure 5.16 *Comparison of tensile strength of various rocks with strain rates*

Chapter 6 Experimental Investigation of Fracture Mechanical Attributes of sandstone and shale in response to varying temperatures and strain rates

6.1 Influence of temperature on the fracture mechanical attributes of sandstones

6.1.1 Overview

An experiment was carried out to measure the static mode I fracture toughness of Manoharpur sandstone and Dholpur sandstone after thermal treatment at different temperatures that ranged from ambient conditions to 600 °C. The three-point bending method was applied using cracks straight through semi-circular bending (CSTSCB) specimens that were fabricated according to ISRM standards. Three different rocks were used to measure the degree of influence of thermal treatment on fracture toughness in different rocks. In addition, petrographic and XRD analyses were carried out to identify the compositions of these rocks. Finally, SEM analysis was performed in order to measure the micro-cracks that were induced within these rocks as a result of thermal treatment. The experimental results demonstrated that, up to a temperature range of 100 °C, the fracture toughness of Manoharpur sandstone, and Dholpur sandstone increased by 40 per cent, and 65 per cent, respectively, when compared to the ambient condition, and thereafter decreased with a gradual increase of temperature. At 600 °C, when compared to the ambient condition, the fracture toughness of these rock types decreased by 59 per cent, and 30 per cent for Manoharpur sandstone and Dholpur sandstone, respectively.

6.1.2 Preparation of CSTSCB Specimen

Rock cores with diameters of 72 mm, and 50 mm were obtained from blocks of Manoharpur sandstone and Dholpur sandstone, respectively. The cores were sliced into discs of the required thickness that is shown in **Table 6.1**, according to the standards suggested by ISRM. The discs were cut into halves to form semi-circular bending (SCB) specimens. A straight notch that was perpendicular to the diametral core at the centre of each SCB specimen was then introduced using a diamond blade of a thickness of 1mm with the appropriate notch length according to the recommendation. The notch length in each specimen was measured as an average taken on both the sides of the SCB specimens. Special care was taken during core drilling and notch preparation to avoid micro-mechanical damage to the CSTSCB specimens.

Thirty-eight specimens from the three types of rocks were divided into eight groups for the thermal treatment experiment: room temperature (28 °C), 60 °C, 100 °C, 150 °C, 200 °C, 450 °C, 550 °C and 600 °C. The specimens were thermally treated in an electric furnace at a rate of 2 °C/min. After reaching the required temperature, the temperature was maintained for three hours for the equilibrium treatment of the samples. The samples were then cooled to room temperature at a lower rate to avoid cracking due to rapid cooling.

6.1.3 Determination of mode I fracture toughness using CSTSCB specimens

Fracture toughness is one of the most important parameters in the field of fracture mechanics and represents the energy or, in other words, the material resistance that is required to initiate brittle failure around the crack tip (Ayatollahi, 2015; Ayatollahi and Alborzi, 2013; Kanninen and Popelar, 1985; Liu, 1983). The fracture toughness of a given rock can be evaluated under any definite type and magnitude of loading because it can be explained in terms of the stress intensity factor (Ayatollahi, 2015). To date, four different methods have been suggested by ISRM (2007) for the measurement of fracture toughness, namely the short rod specimen method (SR) (Matsuki et al., 1991; Ouchterlony, 1988), the chevron bend specimen method (CB) (Ouchterlony, 1990), the crack chevron notched Brazilian disc (CCNBD) specimen methods (Fowell, 1995) and the crack straight through semi-circular bend (CSTSCB) specimen method (Kuruppu et al., 2014).

In past few years, the SCB specimen proposed by Chong et al. (1987) has gained the attention of many researchers including Lim et al. (1993; 1994), Kuruppu (1997; 1998; 2000), Kuruppu and Chong (2012), Kuruppu et al. (2014) and Ayatollahi (2015) for the measurement of fracture toughness, because of factors such as convenient sample preparation, simple geometry, minimal requirement of machining, loading configuration and the convenience of the experimental set-up that can be achieved by applying three-point compressive loading using a common laboratory load frame and low requirement of materials (Aliha et al., 2012; Ayatollahi, 2015; Ayatollahi and Aliha, 2007; Chong and Kuruppu, 1984; Kuruppu et al., 2014). Normally, geo-materials are weak under extensional force and, hence, the applied force for the measurement of fracture toughness should be such that it promotes tensile fracturing. Kuruppu and Chong (2012) experimentally demonstrated that SCB specimens are suitable for measurement of fracture toughness at elevated temperatures, high strain rates, and high confining pressures.

In SCB specimens, cracks can be created by introducing a straight notch through the sample, as is demonstrated in **Figure 6.1**. The fracture toughness value is not influenced by factors such as low displacement rate but is influenced by the size of the specimen (Kataoka et al., 2014; Lim et al., 1994a). In general, fracture toughness is measured as level I, which is based on the maximum failure load; this load does not include non-linear material behaviour. Fracture toughness is also measured as level II, which includes non-linearity correction in order to include non-linear behaviour within the material. However, the CSTSCB method provides the only level I fracture toughness (Kuruppu et al., 2014). For the testing of SCB specimens Chong et al. (1987), suggested the following size prerequisite, as mentioned in
Table 6.1.

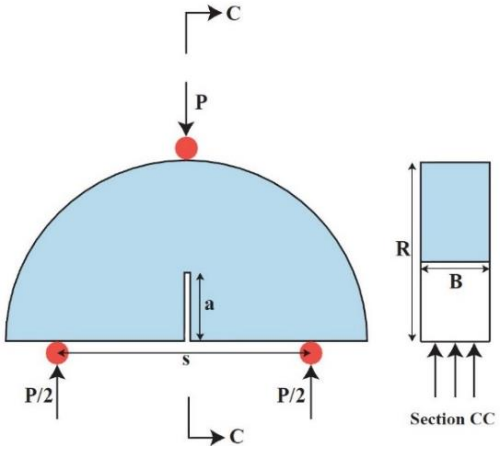

Figure 6.1 *Specimen geometry and loading configuration for the CSTSCB specimen*

Fracture toughness can be calculated by using the following formula that was proposed by Kuruppu et al. (2014);

$$K_{IC} = \frac{P^{max}\sqrt{\pi a}}{2BR} Y'$$

Where,

K_{IC} : Critical stress intensity factor corresponding to the initiation of fracture (MPa√m),

P^{max} : Experimental peak load (kN),

B : Thickness of the SCB specimen (mm),

R : Radius of the SCB specimen (mm), and

Y' : Non-dimensionless stress intensity factor for mode I loading

$$Y' = -1.297 + 9.516\left(\frac{s}{2R}\right) - \left(0.47 + 16.457\left(\frac{s}{2R}\right)\right)\beta + \left(1.071 + 34.401\left(\frac{s}{2R}\right)\right)\beta^2$$

Where, β=a/R

According to the method suggested by ISRM, the non-dimensional stress intensity factor is only valid for $\beta \geq 0.2$. However, that is not sufficient for a strong mode I stress field near the notch. Hence, a larger β is recommended.

Table 6.1 *Recommended geometrical dimensions of SCB specimen* (Kuruppu et al., 2014)

Descriptions	Range
Thickness (B)	Larger of 0.4D or 30 mm
Crack Length (a)	$0.4 \leq \beta \leq 0.6$
Span length (s)	$0.5 \leq S/2R \leq 0.8$

6.1.4 Experimental work

The experimental work included the determining of various geo-mechanical properties of the above-mentioned rocks. The main objective of this study was to measure the variation of the fracture toughness of the rocks as a function of elevated temperature. In order to support the findings of the study of fracture toughness, petrographic analysis, XRD analysis, and SEM studies were also performed to provide a qualitative understanding of the associated mechanism.

6.1.5 Geo-mechanical properties

Different geo-mechanical properties for the three different rocks were measured according to the standards provided by the ASTM and ISRM, in order to enable a better understanding of the geomechanical behaviour of these rocks. These properties included uniaxial compressive strength (ASTM D7012-13, 2013) tensile strength (ASTM D3967-08, 2008), P-wave velocity (ASTM D2845-08, 2008) and water absorption, density, unit weight and porosity (ISRM, 2007). All the values of geo-mechanical parameters that are provided are based on the basis of five test samples and their average is reported as per ISRM standards.

6.1.5.1 Petrographic study

Petrographic analyses of the rocks at elevated temperatures are shown in the following **Figure 6.3**. Manoharpur sandstone is medium-to very coarse-grained sandstone, which is composed of rounded to sub-rounded quartz grains with a clay matrix. Dholpur sandstone is a clean and well-washed rock that comprises mostly quartz minerals and is free of silt and clay. The rock is composed of mostly equidimensional quartz grains that constitute more than 95 per cent of the rock, and the matrix comprises less than 5 per cent of the rock. Quartz grains are in close contact with each other, illustrating their compact nature. The quartz grains are well sorted and sub-rounded to rounded.

'c' and 'd' in **Figure 6.3** represent intragranular and intragranular fractures in the quartz grain in Manoharpur sandstone at 600 °C. 'h' in **Figure 6.3** represents Dholpur sandstone at 600 °C, which shows some sort of induced intragranular fracture in quartz grains as a result of thermal

heating. Nevertheless, the intensity of these induced fractures in Dholpur sandstone is lower when compared to the two other rocks.

6.1.5.2 SEM study

SEM images of all the rocks at different temperatures are shown in **Figure 6.2**. A scanning electron microscope (JSM-6390, JEOL) was used for the observation of micro-fractures that were induced as a result of the thermal treatment. The scanning was performed at 10 kV, 15 kV and 20 kV acceleration voltage at a working distance of 10-20 mm. Samples were carbon-coated (25 mm) on a carbon coater (EM ACE 200, Leica) prior to the SEM study. SEM images of the topography and morphology of the grain structures and micro-fractures were taken (**Figure 6.2**).

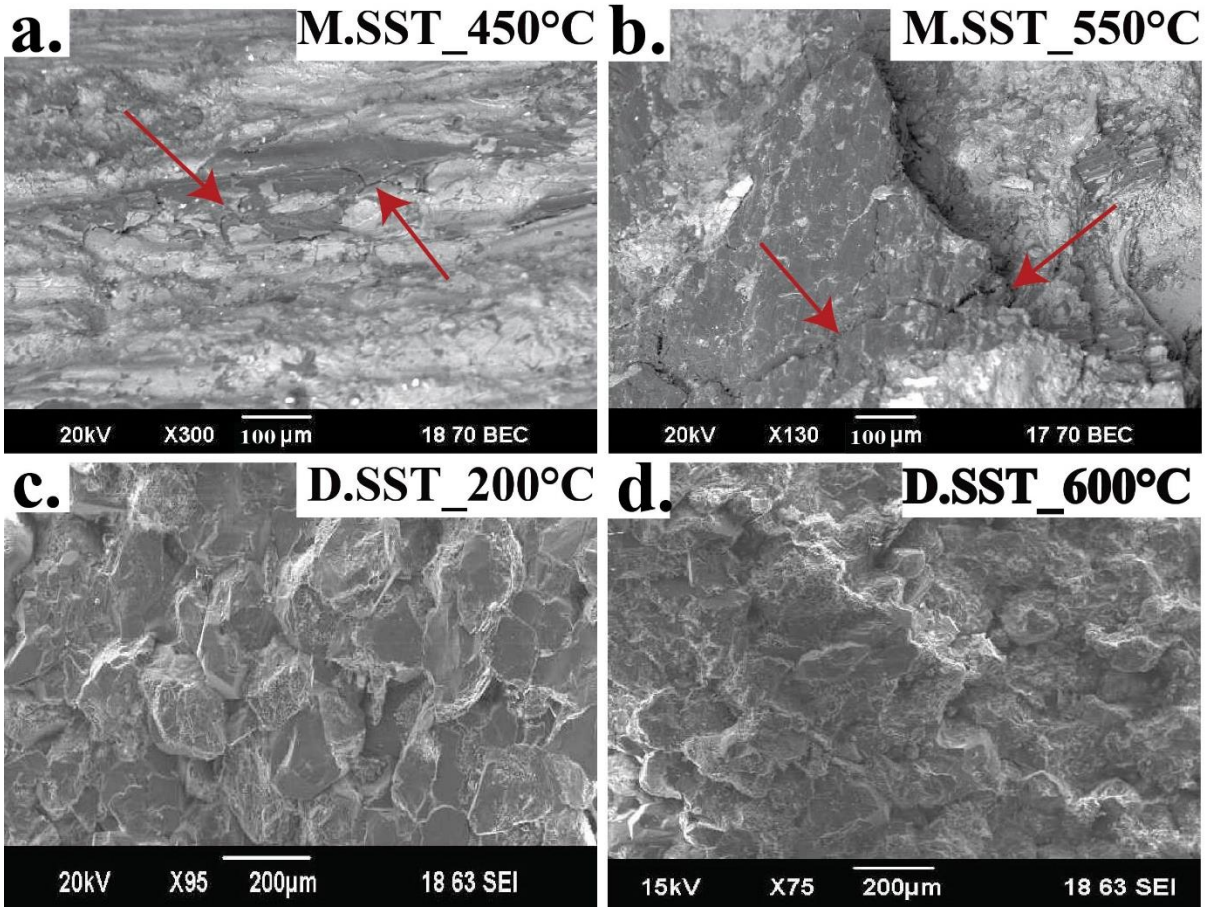

Figure 6.2 *SEM images of the three types of rock at different temperatures that show the development of micro-fractures within the rocks as a function of temperature increment. 'a' and 'b' represent Manoharpur sandstone; and 'c' and 'd' represent Dholpur sandstone*

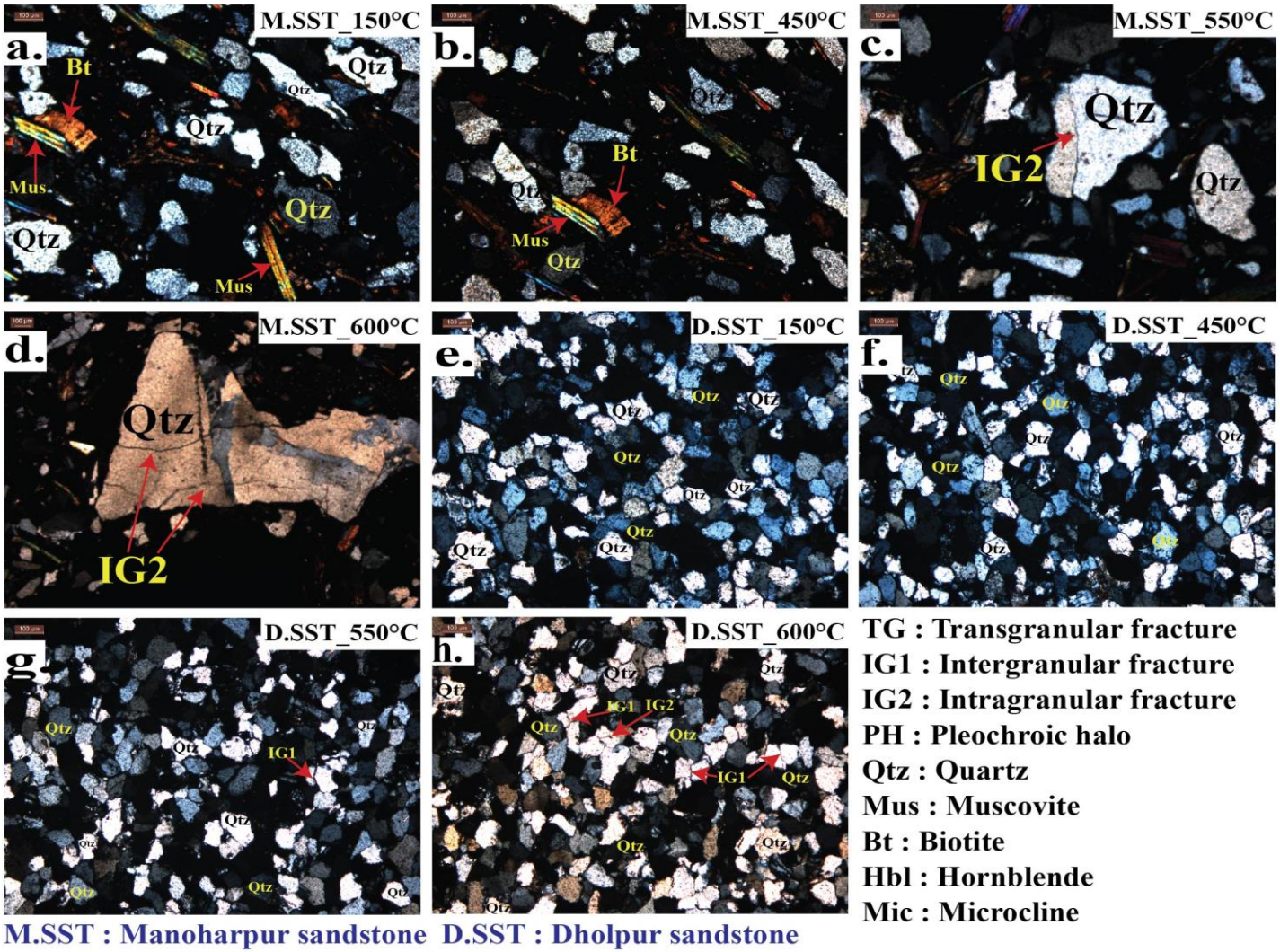

Figure 6.3 *Petrographic thin section of rock types, of which, all others except for 'f' are taken under the crossed polarised light. 'a', 'b', 'c' and 'd' represent Manoharpur sandstone at 150 °C, 450 °C 550 °C and 600 °C, respectively. ''j', 'k', 'l' and 'h' represent Dholpur sandstone at 150 °C, 450 °C, 550 °C and 600 °C, respectively*

6.1.6 Results and discussion

It can be inferred from the petrographic analysis of these rock types that when the temperature of treatment increases, different types of micro-fractures (intragranular, intergranular and transgranular) are being induced in these rocks based on their mineralogical composition. In the case of Dholpur sandstone, the number of induced fractures is less, which may be due to its monomineralic nature.

From the petrographic and XRD analyses of these rocks, it can be inferred that quartz, mica, feldspar, and clay minerals are prominent mineral phases within these rocks (**Figure 3.11)**. The volume expansion of quartz and mica is four times higher than feldspar. Therefore rocks composed of mainly quartz, feldspar, mica and some amount of clay always show remarkable changes with increasing temperatures in thermal treatment (Siegesmund et al., 2008; Tian et al., 2012).

The SEM study of different rocks that are treated at elevated temperatures revealed the appearance of thermally induced micro-fractures as a result of differential expansion of the minerals that are present within these rocks (**Figure 6.2**). In **Figure 6.2**, a and b are SEM images of Manoharpur sandstone at 450 °C and 550 °C, which demonstrate that at 450 °C, micro-fractures have started to appear in the rock, but at 550 °C these micro-fractures are densely present. If these two SEM images are compared, it can be observed that the cracks at 550 °C are wider than those at 450 °C. The SEM images of Dholpur sandstone did not exhibit induction of micro-fractures up to a thermal treatment range of 600 °C. It is possible that higher temperature treatment is required for the initiation of large micro-fractures within these rocks because of their mono-mineralic and hard-bonding nature. A few minor cracks can be observed in the images taken at 200 °C and 600 °C, possibly due to the monomineralic nature of the rock. The fracture surface of Dholpur sandstone indicates that the fracture surface at 200 °C is much rougher than the fracture surface at 600 °C, possibly because the roughness of the fractures gradually decreases, as the induced fractures become transgranular with increasing temperature.

6.1.6.1 Load and load line displacement curve

It can be observed that increasing the temperature of the thermal treatment causes the strength in rocks to gradually decrease (**Figure 6.4**). This also shows the change in the stiffness of these rocks with increasing temperature.

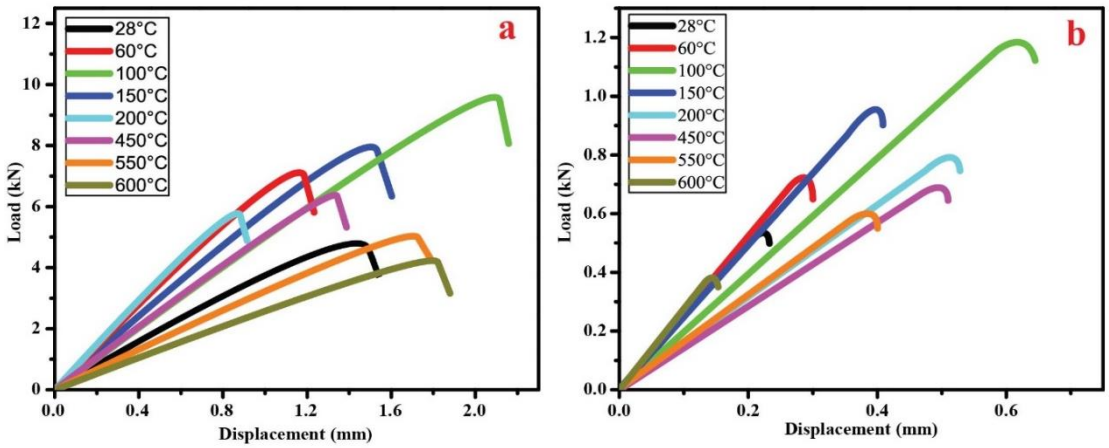

Figure 6.4 *Load and displacement curves for all the rocks at various temperature where 'a' and 'b' represent Manoharpur sandstone and Dholpur sandstone, respectively*

6.1.6.2 Change in physical appearance

The major physical changes that appeared after the thermal treatment were those in the colour of the specimens as well as the changes in the mass and the porosity. These are well demonstrated in **Figure 6.5** – **Figure 6.7**. **Figure 6.7** illustrates the changes in the colours of the specimens, and the macro-fractures initiated in Manoharpur sandstone after treatment at 600 °C. **Figure 6.5** indicates the loss of weight compared to room temperature in all three rocks as a function of elevated temperature, whereas **Figure 6.5** demonstrates the comparison of the change in porosity in these rocks at room temperature and at 600 °C. In Manoharpur sandstone, the loss of weight up to 200 °C was almost constant, after which the weight loss gradually increased up to 7 per cent, 10 per cent and 11 per cent at 450 °C, 550 °C and 600 °C, respectively, compared to room temperature.

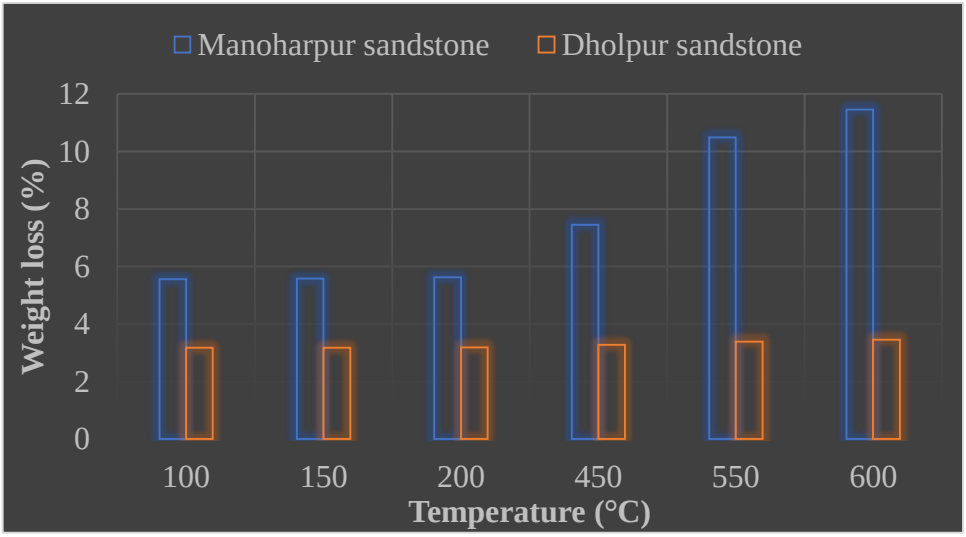

Figure 6.5 *Weight loss in different rocks as a function of elevated temperature, compared to room temperature*

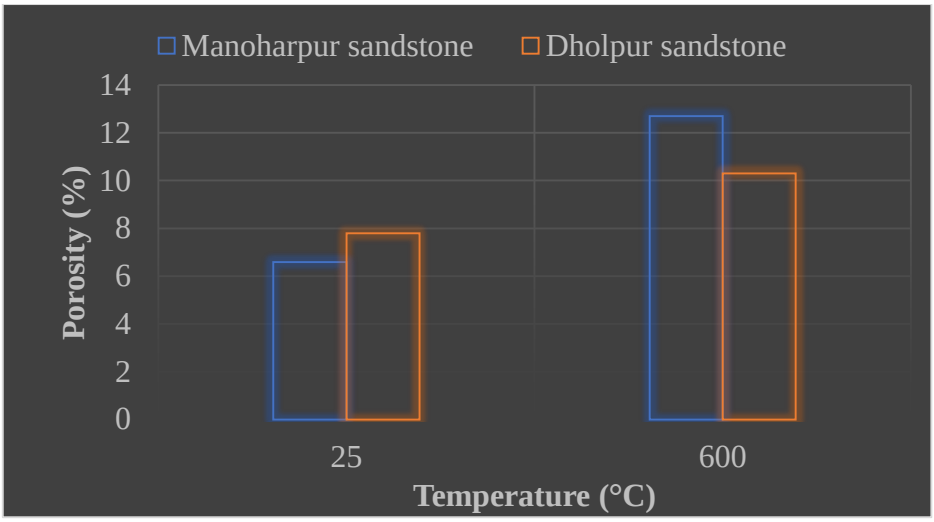

Figure 6.6 *Comparison of the change in porosity in different rocks at room temperature and after treatment at 600 °C*

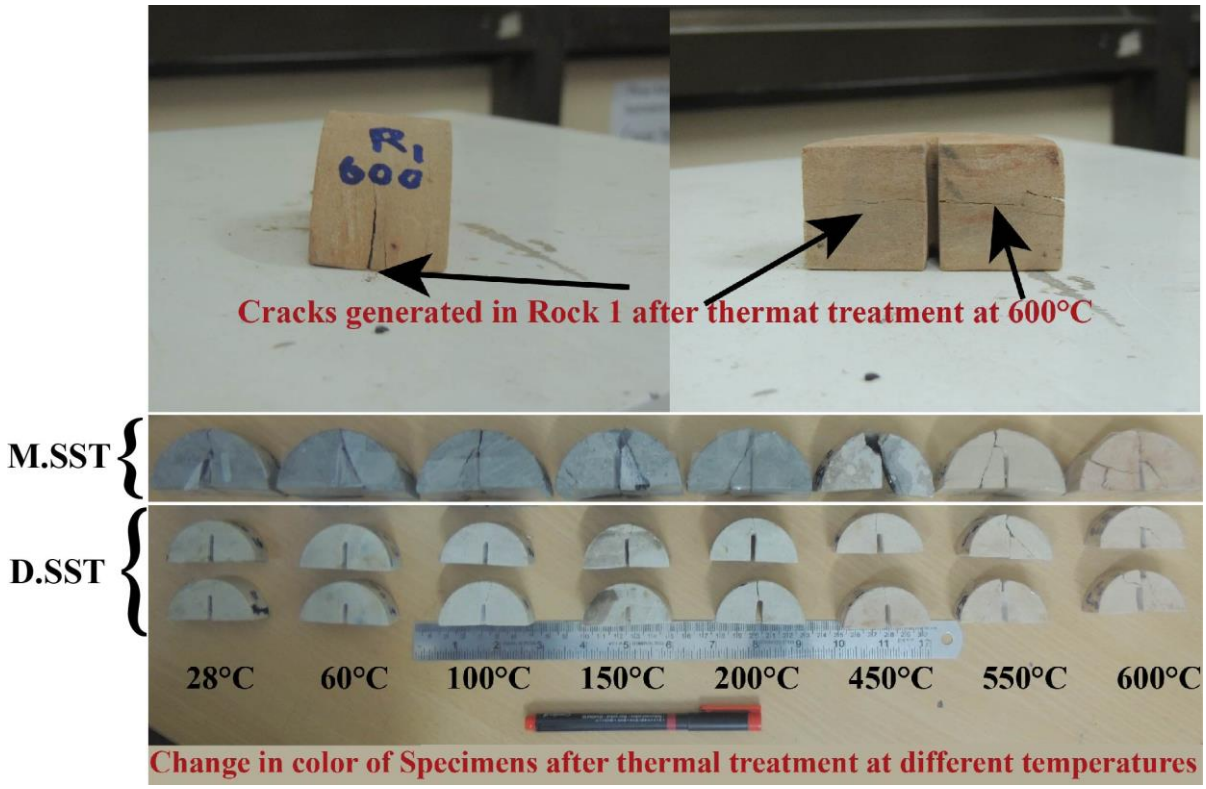

Figure 6.7 *Change in physical appearance of sample specimens after thermal treatment at different temperatures*

Thermal treatment results in thermal reactions in different minerals. For clay, the mineral desorption reaction releases all the absorbed water that is in between the layers and in structural channels, whereas the bound water in the form of hydroxyl ions is driven out as a result of the decomposition reaction that is indicated by mass loss (Tian et al., 2012). For Dholpur sandstone, the weight loss was approximately constant throughout the temperature range, and the rocks show a very marginal difference in weight loss after treatment at 600 °C that is 3.45

per cent compared to the ambient condition. In all the rocks, the weight loss in the range of 200 °C may be due to desorption of different volatiles, gases, and water from these rocks.

Thermal treatment results in changes in the rocks, including both, morphological variations such as increased lustre of flaked surfaces and darkening in colour, and crystalline damages such as micro-fracturing (Balme et al., 2004; Domanski and Webb, 2007), which can be inferred from **Figure 6.5** and **Figure 6.7**. **Figure 6.6** demonstrates the increment of porosity in rocks after thermal treatment. The increment in porosity in Manoharpur sandstone, and Dholpur sandstone is around 92 per cent, and 32 per cent, respectively, compared to ambient temperature; this increase in porosity in these rocks may be due to the induced micro-cracks that are the result of heat treatment (Balme et al., 2004; Tian et al., 2012).

Table 6.2 *Fracture toughness values of Manoharpur sandstone at different temperatures that range between ambient and 600 °C*

Specimen	**Temperature** (°C)	**NDSIF** (Y′)	**Failure Load** (kN)	**Fracture Toughness** (MPa $m^{1/2}$)
R1_28	28	4.783	4.38	2.89
R1_60	60	4.604	7.12	3.34
R1_100	100	4.268	9.52	4.05
R1_150	150	3.960	7.93	3.20
R1_200	200	4.783	5.73	2.89
R1_450	450	3.960	6.36	2.50
R1_550	550	3.680	5.02	2.39
R1_600	600	3.103	4.2	1.17

Table 6.3 *Fracture toughness values of Dholpur sandstone at different temperatures that range between ambient and 600 °C*

Specimen	**Temperature** (°C)	**NDSIF** (Y′)	**Failure Load** (kN)	**Fracture Toughness** (MPa $m^{1/2}$)
R3_28a	28	6.759	0.53	0.78
R3_28b	28	6.136	0.55	0.72
R3_60a	60	5.355	1.15	1.09
R3_60b	60	7.465	0.73	1.02
R3_100a	100	5.595	1.24	1.26
R3_100b	100	6.136	1.17	1.36
R3_150a	150	5.137	1.27	1.09
R3_150b	150	6.437	0.96	1.23
R3_200a	200	6.437	0.99	1.07
R3_200b	200	7.465	0.81	1.12

R3_450a	450	6.437	0.82	0.87
R3_450b	450	5.595	0.74	0.67
R3_550a	550	6.136	0.64	0.81
R3_550b	550	6.136	0.63	0.63
R3_600a	600	7.102	0.38	0.52
R3_600b	600	6.759	0.39	0.51

6.1.6.3 Fracture toughness vs tensile strength

The specimens in both tensile strength test and fracture toughness test form two fractured surfaces under the influence of loading and in both the cases failure of the specimen is caused as a result of the extension of a single crack or the coalescence of few micro-cracks in the same plane. From this point of view, there may be an inherent relationship between fracture toughness and tensile strength of rocks (Whittaker et al., 1992; Zhang, 2002). Keeping this in mind, the tensile strength and the fracture toughness data were correlated. In the last few years many authors have tried to establish relation between fracture toughness and tensile strength of rocks (Gunsallus and Kulhawy, 1984; Haberfield and Johnston, 1989; Vavro and Souček, 2013; Whittaker et al., 1992; Zhang, 2002). Fracture toughness and tensile strength data for all the two rocks at ambient conditions are plotted with some previously proposed relation.

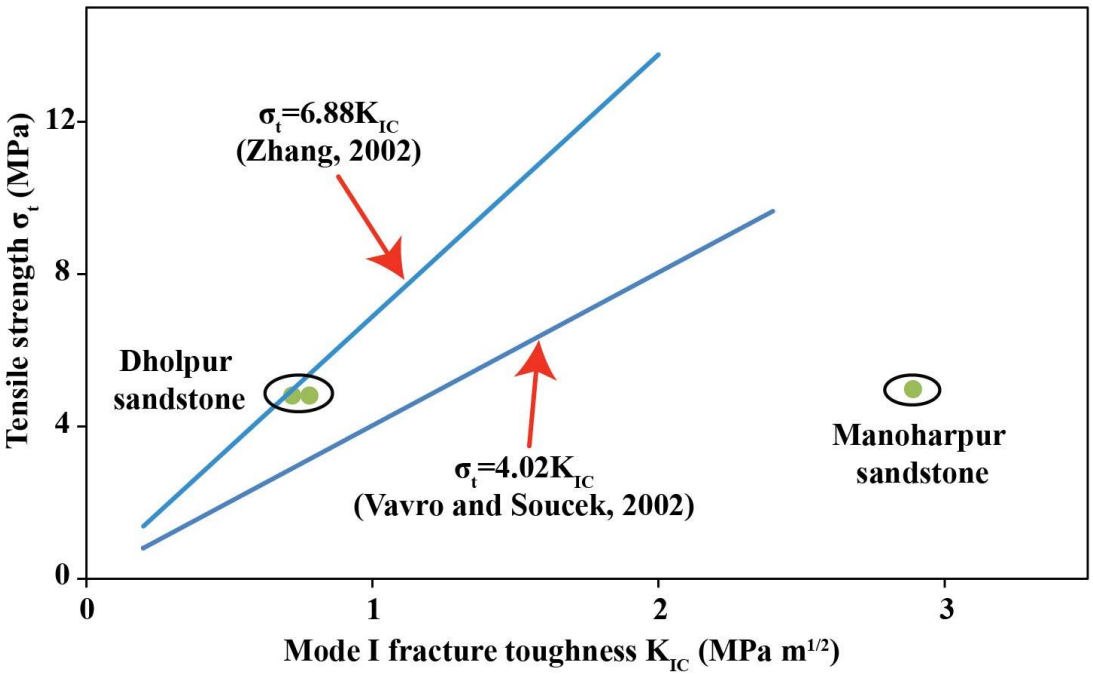

Figure 6.8 *Fracture toughness vs tensile strength of three different rocks at ambient condition*

The correlation data as shown in **Figure 6.8** illustrates that the fracture toughness and tensile strength of Dholpur sandstone is in good accordance with the relation proposed by Zhang

(2002) and Vavro and Souček (2013). Whereas the values of Manoharpur sandstone is not in accordance with the proposed relation. This variation of Manoharpur sandstone may be due to its mineralogical composition.

6.1.6.4 Temperature vs fracture toughness

Three sets of specimens (one set for Manoharpur sandstone and 2 sets for rock Dholpur sandstone) were tested, in order to better understand the variation of the fracture toughness of rocks due to thermal treatment. **Table 6.2** and **Table 6.3** represent the fracture toughness of Manoharpur sandstone, and Dholpur sandstone, respectively, at elevated temperatures**. Figure 6.9** clearly demonstrates that the specimens with smaller grains are having higher fracture toughness, compared to the specimens with little bit larger grain size. Rocks with finer grain size possess high strength, compared to the rocks with larger grain size. Strength and fracture toughness of rocks are directly proportional to each other. Thereby, rocks with finer grain possess a higher value of fracture toughness, compared to the rocks with larger grains (Fredrich et al., 1990; Jian-an and Sijing, 1985; Kahraman and Altindag, 2004; Sabri et al., 2016).

Figure 6.9 indicates the variations of fracture toughness at different temperatures within these rocks. From **Figure 6.9**, it can be observed that the value of the fracture toughness of three rocks shows an increasing trend up to 100 °C and thereafter a decreasing trend, possibly due to the increment in the width of the damage zone by the thermal treatment which causes the increased level of thermal damage (Balme et al., 2004; Yin et al., 2012). For Manoharpur sandstone and Dholpur sandstone, the fracture toughness value increases sharply with increasing temperature up to a temperature range of 100 °C. Up to 100 °C, the increase in fracture toughness values for Manoharpur sandstone, and Dholpur sandstone is around 40 per cent, and 65 per cent, respectively. This is in accordance with the findings of Yin et al. (2012), who measured the dynamic fracture toughness of Laurentian granite; Funatsu et al. (2004) who evaluated the effect of temperature on the static fracture toughness of Kimachi sandstone and Tage Tuff; Al-Shayea et al. (2000) who found that the fracture toughness of limestone increased about 25 per cent at 116 °C when compared to ambient conditions; and Meredith (1983) who investigated the variation of mode I fracture toughness in rocks such as black Gabbro, Westerly granite and synthetic quartz due to thermal treatment in a temperature range of 20 °C to 400 °C using double torsion tests. Meredith (1983) reported that the fracture toughness increased slightly with the gradual increase of temperature in the range of 20 °C to 100 °C. The increase in the fracture toughness up to a temperature range of 100°C to 150°C is because of micro-crack closure due to thermal expansion, which may lead to suppression of

the linkages between existing micro-cracks; this suppression may lead to an increment in the fracture toughness of materials (Balme et al., 2004). Atkinson et al. (1982) found a similar result by performing experiments on Westerly granites, whereas Whittaker et al. (1992) summarised these findings and mentioned that the variation of the fracture toughness of a material according to the temperature is dependent on the material and gradually increases in the temperature range between 20 °C 100 °C. Zhang et al. (2001) reported a decrease in the fracture toughness value of gabbro in the same temperature range, which may be due to the textural and mineralogical differences in these rocks.

Manoharpur sandstone contains a large amount of clay minerals, and the structural water (chemically bonded water) and lattice water (chemically non-bonded water present in the crystal structure) associated with the clay minerals is released when the temperature rises above 100 °C, causing rapid contraction. The hardening of clay minerals is due to the dehydration or dry-caking of the interlayers and the absorptive water above 100 °C, which results in the increase of the coefficient of friction between mineral particles, leading to an increase in the fracture toughness, above 100 °C (Funatsu et al., 2004, 2014a). In general, clay minerals (kaolinite) become non-plastic at 400 °C and when the temperature is raised to a range above dehydration but below dehydroxylation, clay minerals lose adsorbed, hydration and lattice water (Escalera et al., 2012). As a result, the interlayer spaces collapse and the pore space in the rock is changed, along with its plasticity. In contrast, temperatures above dihydroxylation destroy the layer structures of these clay minerals. Generally, the interlayer water present in clay minerals is lost in the temperature range from 80 °C to 100 °C. (Yilmaz, 2011, 2003). Heating kaolinite to 200 °C results in a reduction in the grain size, leading to the shrinkage and disintegration; this may be due to the complete removal of absorbed water (McCabe et al., 2010; Wang et al., 1990). In all clay minerals, most adsorbed water is lost at a temperature of below 150 °C (Ramachandran and Kacker, 1964). For Dholpur sandstone, this increment in fracture toughness values may be due to the closure of the original cracks that are caused by the thermal expansion of mineral grains (Funatsu et al., 2004; Yin et al., 2012).

Thereafter, a gradual decrease in fracture toughness values for all three rocks up to a temperature range of 600 °C was observed, which might be due to the development of micro-cracks that are induced as a result of tensile stresses due to differential thermal expansion between adjacent mineral grains in the rocks. This is similar to the findings of Meredith and Atkinson (1985), who conducted experiments on granite and gabbro using double torsion tests and reported the decrease in fracture toughness after 110 °C. The thermal expansion introduces

micro-cracks, which reduce the shear fracture resistance, thereby reducing the effective stress intensity factor (Funatsu et al., 2014a). Under the influence of thermal temperatures below the melting temperature, new micro-cracks are induced and pre-existing micro-cracks become widespread and widen. After cooling down, the damage or changes induced due to heating remains permanent (Gautam et al., 2015). At higher temperatures, differential expansion between the mineral phases present in these rocks reopens the cracks and reduces the toughness (Balme et al., 2004). In general, within a rock, the maximum stress is concentrated along the mineral grain boundaries. If this induced stress due to thermal treatment exceeds the tensile or the shear strength of rocks, either new cracks will develop along those boundaries, or existing cracks will migrate, resulting in irreversible structural damage (Somerton, 1992; Tian et al., 2012). The findings of this experiment are in accordance with the results of Nasseri et al. (2009), who evaluated the fracture toughness of thermally treated Westerly granite up to a temperature range of 850 °C and observed a decreasing trend in the fracture toughness from untreated specimen to specimens treated at 850 °C. This is possibly due to a variation in the thermal coefficient of expansion of minerals such as quartz, feldspar, and mica, as a result of grain-grain boundary opening and increased micro-crack density. From **Figure 6.9**, it can be observed that in the temperature range of 550 °C to 600 °C, there is a marked decrease in the fracture toughness value of Manoharpur sandstone, that is, about 50 per cent; this may be due to the α-β quartz phase transition at 573 °C, which increases the differential expansion between quartz and other constituted minerals, resulting in open micro-cracks within the specimen. For the three types of rocks, the decrease in the fracture toughness value at 600 °C is around 59 per cent, 36 per cent and 30 per cent, respectively, when compared to the ambient conditions. For Dholpur sandstone, the fall in the fracture toughness value at 600 °C is lower than that of the other two rocks, which may be due to the monomineralic nature of the rock or the structural damage induced as a result of differential thermal expansion along the crystallographic axes of the same mineral (Somerton, 1992; Tian et al., 2012).

Normally, the increasing and decreasing rates of different physicomechanical properties of rocks depend not only on the temperature to which a rock is exposed but also on environmental conditions such as the thermal treatment path, the heating/cooling rate and the temperature history (Tian et al., 2012). The primary cause of the change in the physical properties of different rocks after thermal treatment is structural damage that is induced as a result of mineral thermal expansion and thermal reaction (Tian et al., 2012). Untreated rock specimens are expected to be tough initially, but an increase in treatment temperatures results in thermally

induced micro-cracks, which blunts the crack tip and results in a higher amount of plastic energy dissipation in the propagation zone (Balme et al., 2004).

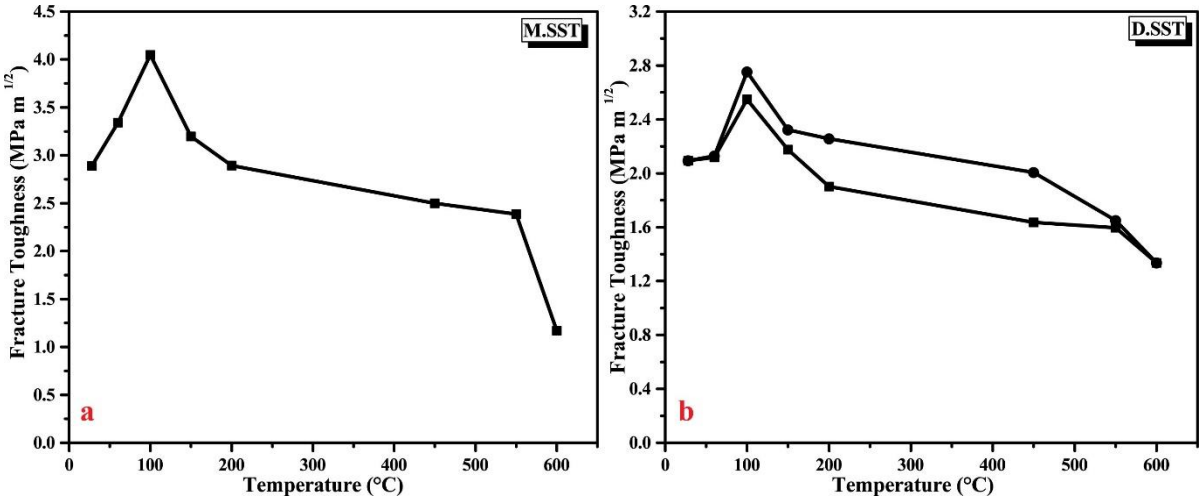

Figure 6.9 *Variation of fracture toughness in the rocks with elevated temperature, of which, 'a' represents Manoharpur sandstone and, b represents Dholpur sandstone, respectively*

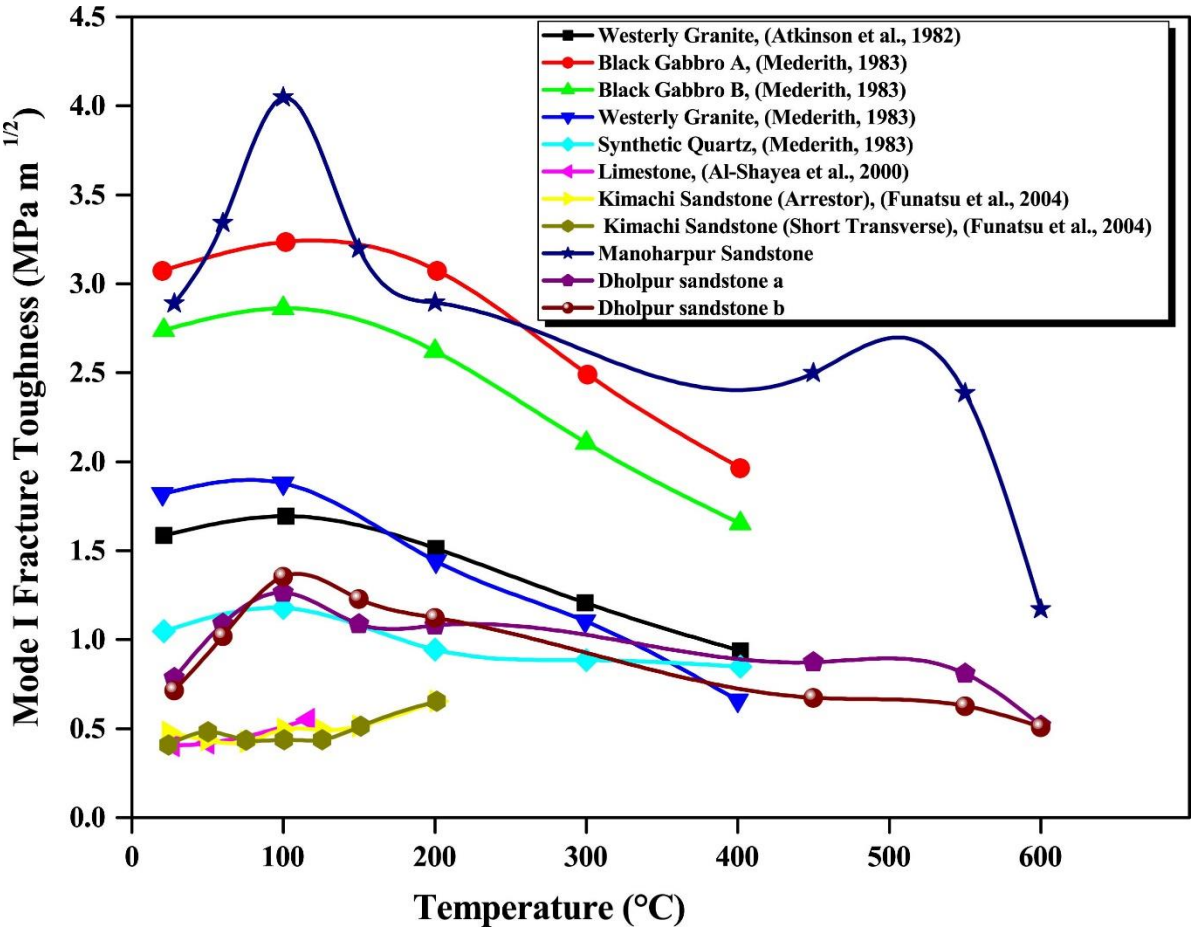

Figure 6.10 *Comparison of the effect of thermal temperature on measured mode-I fracture toughness of various rocks (adapted after Al-Shayea et al., 2000; Funatsu et al., 2004; Whittaker et al., 1992)*

Heating is expected to cause micro-fracturing and a decrease in the fracture toughness due to a decrease in the surface energy of the rocks and crack linkage, which results in a steady decrease in toughness along with the increase in temperature until the elasto-plastic transition is achieved, resulting in tearing of the specimen (Balme et al., 2004; Darot et al., 1985). **Figure 6.10** represents comparisons of previously reported mode-I fracture toughness for various rocks along with the current study as a function of temperature.

6.2 Influence of strain rate on the fracture mechanical attributes of shale

6.2.1 Overview

The aspect of enhanced energy extraction in the field of rock mechanics requires a detailed understanding of rock fracture mechanics. Common examples are hydraulic fracturing of gas shales and geothermal energy systems. Resolving rock fracture behavioural patterns and its properties such as fracture toughness and energy-release rate during fracturing is important for the successful implementation of such scientific projects. These properties are a function of different environmental factors such as temperature, humidity, water vapour, pressure, and strain rate. In this study, the effects of various strain rates on the fracture toughness as well as the energy-release rate of gas shales were investigated. The three-point bending method was applied using notched semicircular bending shale specimens that were fabricated as per international standards. The fracture toughness and the energy-release rates were measured for three different modes, namely, mode I, mixed mode (I – II), and mode II. In addition, XRD analysis was carried out to identify the composition of the select shales. Finally, SEM analyses were performed in order to acquire an insight into the effects of strain rate on fractures at microstructural scales. The experimental results indicate that the fracture toughness and the energy-release rate for all the three modes are a function of strain rates. At lower strain rates, the fracture toughness and the strain-energy-release rates for all the modes are comparable but vary significantly at higher strain rates. At high strain rates, the strength and stiffness of the shale increases, which in turn increases the fracture toughness and, eventually, the energy-release rate of the shale. For all the strain rates, mode I require the minimum application of energy, while mode II requires maximum energy for the onset of crack growth. The energy-release rate in mode I is maximum, in comparison with the two other modes. The findings of this investigation will be useful in achieving a better and comprehensive understanding of some aspects such as initiation, propagation, and failure of shales during hydraulic fracturing for the extraction of hydrocarbons.

6.2.2 Background knowledge

The advent of modern technologies in the field of drilling and fracturing of shale formations has transformed these shale formations from an otherwise uneconomic rock type to a profitable resource of natural gas. Shale gas is natural gas that is generated and stored in tight and impermeable shale formations. If exploited scientifically and properly, shale gas can efficiently contribute to the energy supply. The primary challenge in the exploitation of shale gas is the extremely low permeability of the host rock. In order to produce gas from shale reservoirs, the formations are hydraulically fractured and permeability is induced in the system. Hydraulic fracturing has led to a sharp rise in gas production from shale, resulting in an energy boom at reduced gas prices (Arora and Cai, 2014; Middleton et al., 2015). In the year 2000, shale gas accounted for nearly 1 per cent of the gas contribution in US energy sector, which reached up to 20 per cent in 2010 and, at the end of 2012, around 24 per cent of the US gas demand (Kerr, 2010; Weijermars, 2014). The international energy agency (IEA) predicts that approximately 14 per cent of global gas production will comprise shale gas by 2035 (Hammond and O'Grady, 2016).

Successful hydraulic fracturing depends on a profound understanding of the geomechanical behaviour of the rock and the regional in situ stress distribution. More specially, the fracture toughness is of concern, among other important aspects. Hydraulic fracturing is performed in three stages: the opening of the fractures, the propagation of the fractures, and the flow of fluid through the fractures (Asadi et al., 2013). The first two stages are primarily dependent on the fracturing behaviour of the rock and its response to various stresses. Fracture toughness represents the resistance offered by a rock material to the growth of a crack (Griffith, 1921; Irwin, 1957). Depending upon the geometry of the specimen, the loading configuration, and the displacement modes, crack growth can be classified into three different modes: mode I (crack opening mode/tension mode), mode II (crack sliding mode/in-plane shear mode) and mode III (crack tearing mode/anti-plane shear). The critical value of the stress intensity factor at which the crack starts to propagate is called the fracture toughness (K_{IC} in the case of mode I, K_{IIC} in the case of mode II and K_{IIIC} in the case of mode III), which plays a crucial role in hydraulic fracturing (Rummel and Winter, 1982). Thus, it is essential to study the fracture toughness of shales for each mode of failure in order to optimise the hydraulic fracturing of gas shales for methane recovery.

Cracks in a rock mass are subjected to very complex conditions because of the random orientation of cracks with respect to the loading direction, as a result of these conditions, brittle

fractures in rocks may grow due to a combination of two major fracture modes, that is, mode I and mode II (Ayatollahi and Aliha, 2007). While recent studies have focused on the mode I fracture propagation in rock, most of the realistic cases involve both the tensile mode (mode I) and the shear mode (in-plane shear mode II). Therefore, for a better understanding of the common mechanisms that are responsible for the propagation of fractures in rock, it is imperative to develop the understanding of fracture toughness as well as critical stress intensity factors in mode II and mixed-mode (I-II) conditions (Aliha et al., 2006; Funatsu et al., 2014b).

The field of fracture mechanics has earned increasing importance in the recent years and has addressed challenges that involve rock mass fracture behaviour in various applications. Fracture mechanics can be applied to the appropriate designing of hydraulic fracturing for oil and natural gas recovery, geothermal energy extraction, rock mass stability in slopes as well as in excavation and for interpretation of rock fragmentation patterns during blasting and rock bursts (Funatsu et al., 2014b; Gale et al., 2007; Germanovich et al., 1994; Papanastasiou, 1999; Scavia, 1990; Thallak et al., 1993). The strength and the deformational behaviour of a rock are affected by the state of the stress applied to it. They are also influenced by environmental factors such as temperature, humidity, water vapour, pressure and strain rate, as well as by some other rock properties such as composition, grain size and anisotropy (Donath and Fruth, 1971; Lajtai et al., 1991; N. N. Sirdesai et al., 2016). In addition, mineralogy, fabric, and texture have a robust influence on such behaviours. The anisotropy may exist due to the preferred orientation of mineral grains, microcracks and minerals along preferred bands or veins (Valente et al., 2012).

The mechanical response of a rock to varying strain rate or loading rate plays a crucial role in the design of rock structures, slopes, dam foundations and underground excavations (Gautam et al., 2016; Khandelwal et al., 2013; Singh and Naidu, 2000). This rate is applied in many fields such as blasting, exploration, and earthquake, in which the rocks encounter a high rate of loading. Many researchers in the past few decades have focused their research on these quasi-static and dynamic behaviours of rocks (Bieniawski, 1970; Cadoni, 2010; Liang et al., 2015; Mahmutoglu, 2006; Masuda et al., 1987; Zhang et al., 2000; Zhou et al., 2010).

For the better development of design standards and structures, an enhanced understanding of rock behaviour, rock strength, and fracture behaviour to different strain rates is essential (Hokka et al., 2016). In the past few years, rock behaviour at different strain rates was studied by many researchers. Xia et al. (2008) and Liu and Xu (2015) studied the behaviour of rocks

in a compression mode, Fourmeau et al. (2014) studied it in a tension mode, whereas Dai et al. (2011) and Dai and Xia (2013) studied it in a bending mode. Hokka et al. (2016) experimentally observed the effects of strain rate and confining pressure on Kuru granite and found that the rock strength increases with an increase in strain rate and confining pressure. From some previous experimental works performed by Dai and Xia (2013); Gao et al. (2015); and Hokka et al. (2016), it can be inferred that the fracture strength and the fracture toughness of brittle materials are highly sensitive to the loading rate. In the current study, attempts were made to investigate the dependency of the fracture toughness of the rock in mode I, mixed mode and mode II with varying strain rates. Experimental studies were conducted in order to understand better the fracture behaviour in gas shales with different strain rates. The strain rate was varied in the range of 7.9×10^{-5} to 1.7×10^{-2} s^{-1} that comes under the quasi-static regime of strain rate. For the convenience of the readers, the different strain rates that were applied in these experiments are denoted by S1, S2, S3 and S4, in which S1=1.7×10^{-2} s^{-1}, S2 =1.3×10^{-2} s^{-1}, S3=$3.8 \times 10^{-3}$$s^{-1}$ and S4=7.9×10^{-5} s^{-1}.

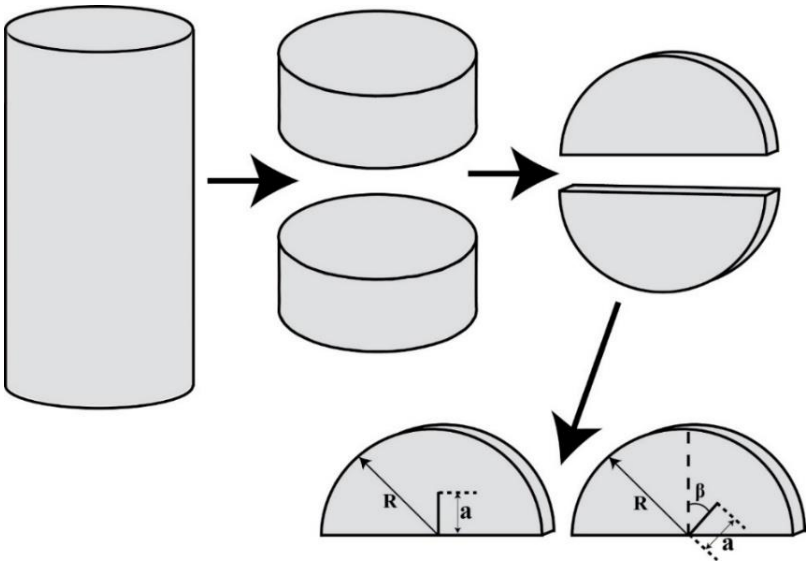

Figure 6.11 *Schematic diagram of the preparation of the SCB specimens*

Blocks of shale were collected from the exposed rock-mass section. **Figure 6.11** represents the schematic diagram of the sample preparation. Rock cores with diameters of 50 mm were obtained and sliced into discs of required thickness (23.2 ±1 mm, for this experiment), according to the standards (Kuruppu et al., 2014; Lim et al., 1994b, 1993). The discs were then cut into halves to obtain SCB specimens. A straight notch at the centre of each SCB specimen, with required inclination of mode I, mode II and mixed-mode I/II fracture toughness was then introduced using a diamond blade of a thickness of 1 mm for an appropriate notch length of 13.5±0.5 mm, according to the standards. The measurement of the artificially–induced notch

length in each specimen was taken as an average of both the sides of the SCB specimens. During core drilling and notch preparation, special care was taken to avoid micromechanical damage to the specimens. During the preparation of the specimens, uniform geometry was maintained so that there would not be any difference in the notch length and the thickness of the specimens.

6.2.3 Testing methodology

The initiation of unstable fracture propagation can be predicted by using the critical value of the stress intensity factor, the strain-energy-release rate, or simply the energy-release rate. In this study, the main intention was to measure the critical stress intensity factors and the energy-release rate for different modes (I, I/II, II) of failures at varying strain rates.

6.2.3.1 Fracture toughness determination

With the advent of research in the domain of hydraulic fracturing, some aspects of different modes of rock failures such as mixed modes in rock, mechanics have been clearly understood. A number of laboratory testing techniques and test specimens have been proposed for the determination of the fracture toughness of brittle materials for different modes. A few of these suggested techniques are centrally cracked Brazilian discs (Atkinson et al., 1982b; Chang et al., 2002; Khan and Al-Shayea, 2000; Shetty et al., 1987); single edge cracked rectangular plate subjected to four-point bending (He et al., 1990; Huang and Wang, 1985; Maccagno and Knott, 1989); compact shear and tension specimen (Banks-Sills and Bortman, 1986; Mahajan and Ravi-Chandar, 1989) and the edge-cracked semi-circular bending specimen (Aliha et al., 2006; Ayatollahi and Aliha, 2006; Chong and Kuruppu, 1984; Chong et al., 1987; Kuruppu and Chong, 2012; Lim et al., 1994a, 1993; Mahanta et al., 2016).

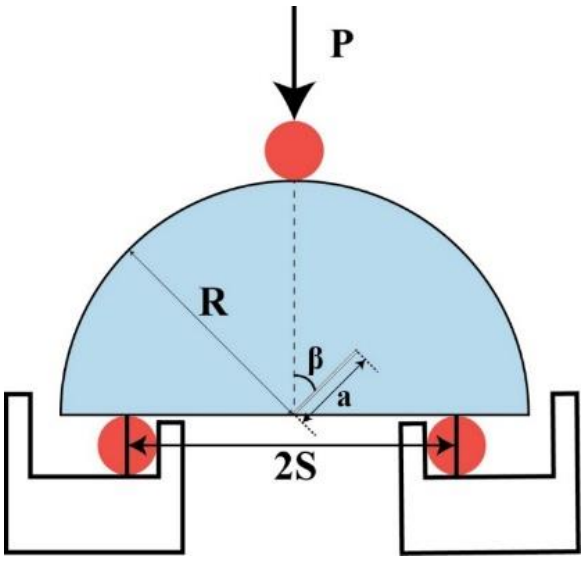

Figure 6.12 *Loading configuration of the semicircular bending specimen*

Among these, the SCB specimen that is loaded in the three-point bending method is widely accepted for the estimation of mode I, mode II and mixed-mode (I/II) fracture toughness. Geomaterials are weak under extensional force and, hence, the applied force for the measurement of fracture toughness should be such that it promotes tensile fracturing. Tensile fracturing can be easily achieved by the three-point bending method in which the mode of applied load is compression. However, the material breaks because of the induced tensile and shear stress at the crack tip based on the nature of the loading.

The SCB specimen is commonly used because of the simplicity of its geometry, test procedure, low machining requirement for the specimen preparation, application of compressive loads in preference to tensile loads, ability to encompass the full range, from pure mode I to mode II (Ayatollahi and Aliha, 2007; Kuruppu and Chong, 2012; Lim et al., 1994a). **Figure 6.12** shows a schematic diagram of the specimen with a radial edge crack of length, *a*, which is introduced from the centre of the semicircle. The SCB specimen is placed in the three-point bending arrangement, as shown in **Figure 6.12**. A vertical load, *P*, is imposed until the specimen fails. Mode I and mode II fracture toughness as well the critical stress intensity factors for the mixed mode (I/II) can be estimated with different combinations of three parameters: normalised crack length (*a/R*), normalised span ratio (*S/R*) and direction of crack line relative to the vertical direction (β). When β is zero, the specimen is subjected to a pure mode I condition, irrespective of *a/R* and *S/R*. With a gradual increase in β, various mixed mode, as well as mode II conditions, can be achieved, depending upon the *a/R* and the *S/R*.

The critical stress intensity factors can be measured in terms of fracture load, *P*, as:

$$K_I = \frac{P}{2RB}\sqrt{\pi a}\, Y_I\left(\frac{a}{R}, \frac{S}{R}, \beta\right)$$

$$K_{II} = \frac{P}{2RB}\sqrt{\pi a}\, Y_{II}\left(\frac{a}{R}, \frac{S}{R}, \beta\right)$$

Where K_I and K_{II} are the mode I and mode II stress intensity factors, respectively, at the onset of brittle fracture and *B* is the thickness of the specimen and Y_I and Y_{II} are non-dimensional stress intensity factors for mode I and mode II, respectively. Y_I and Y_{II} are also called geometry factors that depend on *a/R*, *S/R* and β. In the past, authors such as Chong and Kuruppu (1984), Lim et al. (1993), Ayatollahi and Aliha (2007) have analytically and numerically calculated the values of Y_I and Y_{II} for SCB specimens by using finite element models for various combination of *a/R*, *S/R* and β. According to the results reported by Lim et al. (1993) and Ayatollahi and Aliha (2007), for *a/R* = 0.5 and *S/R* = 0.5, the angle, β, which corresponds to the pure mode II loading in the SCB specimen, is 40°; that is, Y_I becomes zero at this angle and it corresponds to the pure mode II condition.

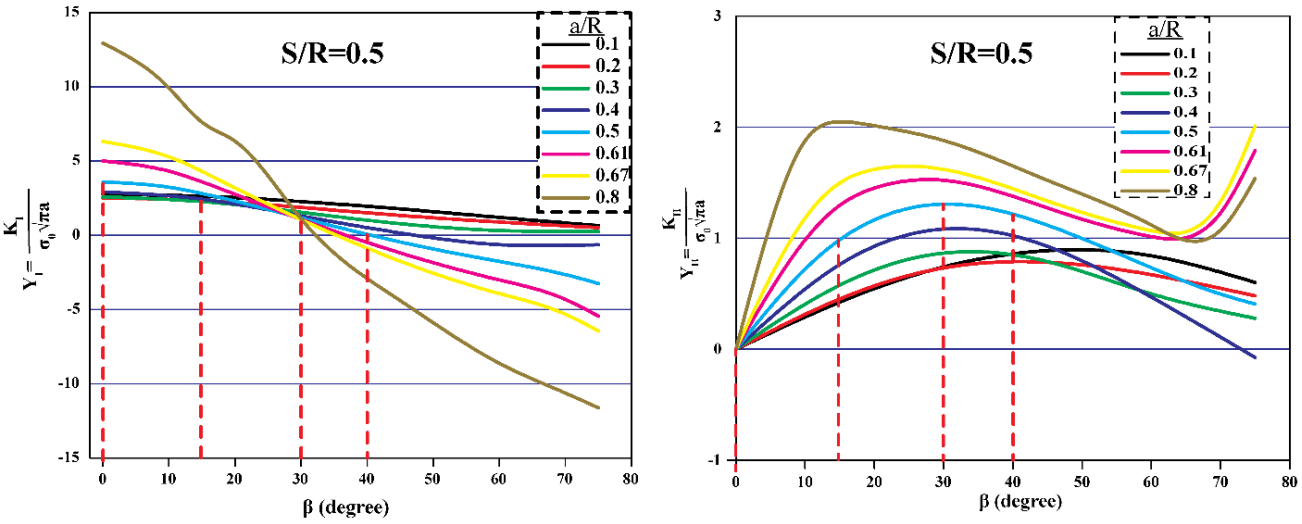

Figure 6.13 *Normalised stress intensity factors Y_I and Y_{II} (modified after Lim et al. (1993))*

Figure 6.13 represents the normalised stress intensity factors, which are being used for the current study, with different *a/R* and *β* values and *S/R* equal to 0.5. Therefore, in order to get mixed-mode fracture results, it is quite sufficient to vary the angle between 0° and 40° (Ayatollahi et al., 2015; Lim et al., 1994a).

In this study, two angles, 15° and 30°, were used to determine the mixed-mode fracture toughness of shales. In order to represent the mixed-mode fracture toughness results, the effective stress intensity factor, K_{eff}, was calculated as

$$K_{eff} = \sqrt{K_I^2 + K_{II}^2}$$

The total energy-release rate of each mode can be summed and evaluated as $G_{TOT} = G_I + G_{II} + G_{III}$. A detailed derivation of the G_{TOT} has been included in **Appendix 2** Energy-release rate.

$$G_I = \frac{K_I^2}{E}$$

$$G_{II} = \frac{K_{II}^2}{E}$$

$$G_{III} = (1+\nu)\frac{K_{III}^2}{E} = \frac{K_{III}^2}{2\mu}$$

6.2.3.2 Applied energy

Elastic potential energy is the energy that an object has in it due to being deformed. Any object that can deform and then returns to its original shape does have some elastic potential energy. The applied energy is equal to the work done on the crack surface for its propagation, and the work done on the system is equal to the applied load multiplied by the displacement (**Figure 6.14**).

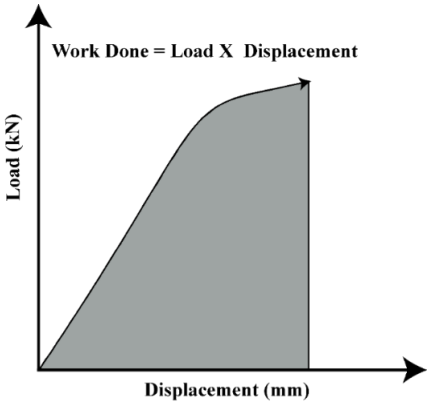

Figure 6.14 *Schematic diagram of applied load and the displacement*

6.2.4 Experimental investigation

Experimental work includes the estimation of various geomechanical properties of the shales. The main objective of the current study was to estimate the different modes of fracture toughness including mode I, mode II and mixed-mode I/II. In addition to this fracture toughness study, XRD analysis, and SEM studies were also performed for a better understanding of the associated mechanism. It is a medium-to fine-grained shale. Quartz grains are rounded to sub-rounded, and the clay matrix consists predominantly of goethite. Quartz grains are in close contact with each other indicating a high degree of compaction.

6.2.4.1 SEM study

An SEM was used for the observation of microstructures that were present in the sample. SEM images of the topography and morphology of the grain structures and the microfractures were taken. The SEM images of the rock are shown in **Figure 5.11**.

6.2.5 Results and discussion

Figure 6.15 represents the failed specimens, each with a different notch angle. It also represents the failure angle with the initial notch line. **Figure 6.16** represents the load that is applied to the specimen and the displacement for different strain rates that have a different notch angle. During loading, signals from the load cell and the displacement gauge are continuously recorded to obtain the load versus displacement curve.

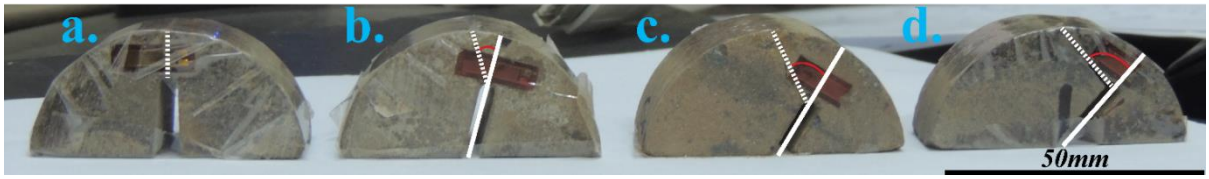

Figure 6.15 *Shale specimens of different notch angles (a: 0°, b: 15°, c: 30°, d: 40°)*

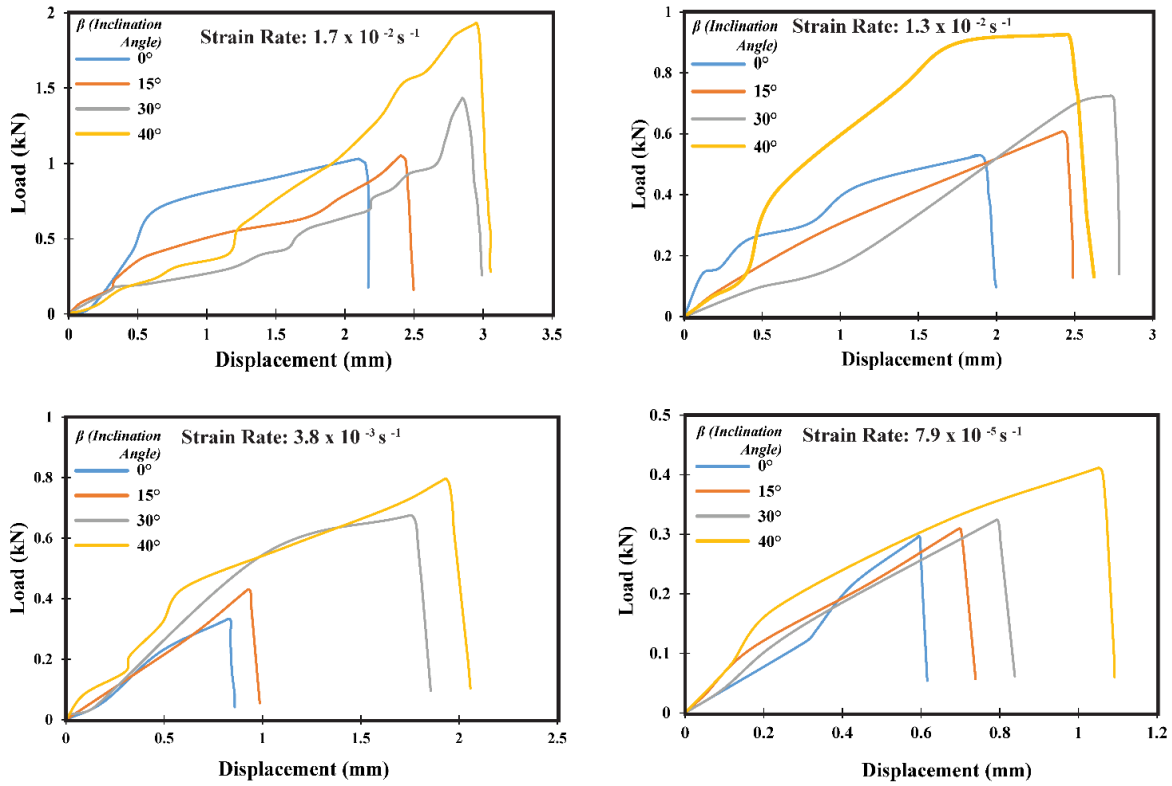

Figure 6.16 *Load versus displacements curves for different strain rates*

Under a low strain rate, intergranular (IG-I) fracturing was the dominant mode of fracture on the fracture surface. Under such conditions of loading, the fracture surfaces are rougher, when compared to that of the specimens that failed at a high strain rate. With an increase in the strain rate, the transgranular fractures become dominant over the intergranular fractures and, as a result, the fracture path becomes straighter and possess a lesser rough fracture surface when compared to the low strain rate condition (Zhang and Zhao, 2013). Under low strain rates, the stress field near the crack tip has sufficient time for redistribution to other parts of the grains and, as a result, there may be more damage along the weak parts near the crack tip, that is, along the grain boundary; the resultant dominant mode of fracture is intergranular.

In a static compression test, the strain rate is slow and, as a result, the plastic strain gets enough time to develop more or less fully before the next incremented load is applied. At a high strain rate, the loading is fast and the plastic strain component may not get enough time to develop fully until the next incremental load is applied. Consequently, it appears that the material has stiffened because of the incomplete development of the plastic strain due to insufficient time (Chong et al., 1980; Chong and Boresi, 1990; Wasantha et al., 2015). It is difficult for transgranular fractures to form compared to the intergranular fractures because transgranular fractures require a high input of energy.

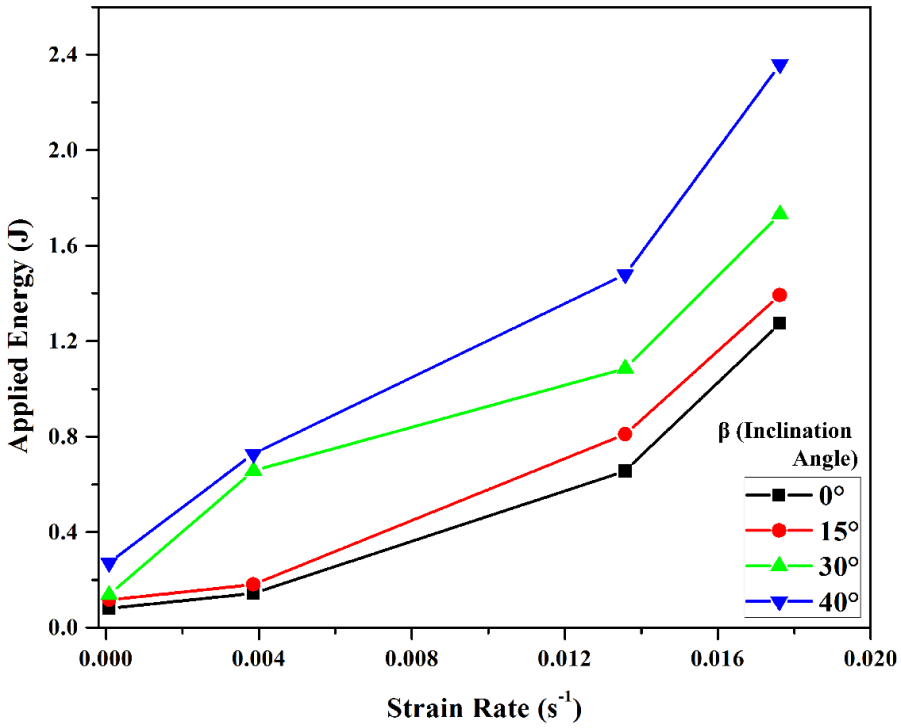

Figure 6.17 *Strain rate and applied load with different modes: 0° for mode I; 15° and 30° for mixed mode; and 40° for mode II*

Figure 6.17 represents the load that was applied to specimens that were tested with different strain rates for the evaluation of fracture toughness and critical stress intensity factors. For all types of modes such as mode I, mixed mode (I/II) and mode II, the applied energy increases gradually with increasing strain rates. From **Figure 6.17**, it can be inferred that at slower strain rates, the applied energy for all the modes are quite equivalent. However, as the strain rate increases, the applied energy gradually increases for different modes based on their mechanism of fracture propagation, that is, tensile opening, shearing opening, or a combination of both. The roughness of the fracture surface is dependent on the fracture modes or the failure mechanisms. Rougher fracture surfaces are a result of intergranular fracture formation, whereas transgranular fractures are seen in flatter surfaces or surfaces that are less rough because of higher energy absorption during the fracture process (Liang et al., 2015; Mecholsky and Mackin, 1988; Zhang and Zhao, 2013).

Since the absorbed energy is utilised in the formation of new fracture surfaces, high-energy absorption suggests that large surface areas are created during the failure process. From the study, it can be inferred that in all the strain rates, mode II has the maximum applied energy because of the formation of a large surface area after the failure of the specimen. Mode I involves a minimum area, in comparison to the mixed mode and mode II conditions and, hence,

requires the least applied energy for failure. Mode I opening involves tensile opening and is devoid of any shear movements. In a high strain rate condition, many pre-existing cracks are activated at the same time. These induced microcracks absorb more energy in comparison to a single macroscopic crack, resulting in an increase of the fracture energy. As a result of a high strain rate, the rock is fragmented into more pieces through multiple crack growths (Dai and Xia, 2013). During compression, certain locations of the rock materials may be subjected to tension, which gives rise to the nucleation and growth of microcracks. With an increasing strain rate, the applied stress progressively increases, which is responsible for a higher rate of activation of microcracks. The number of activated microcracks is directly proportional to the applied stress. Therefore, at low strain rates, a few relatively large microcracks are activated, leading to a few large broken pieces of the specimens, whereas, in a high strain rate, a greater number of and relatively small microcracks are activated, resulting in smaller broken pieces of the specimen (Chong and Boresi, 1990). At high strain rates, many pre-existing cracks are activated at the same time and these induced microcracks absorb more energy when compared to a single macroscopic crack, resulting in an increase in the fracture energy (Dai and Xia, 2013).

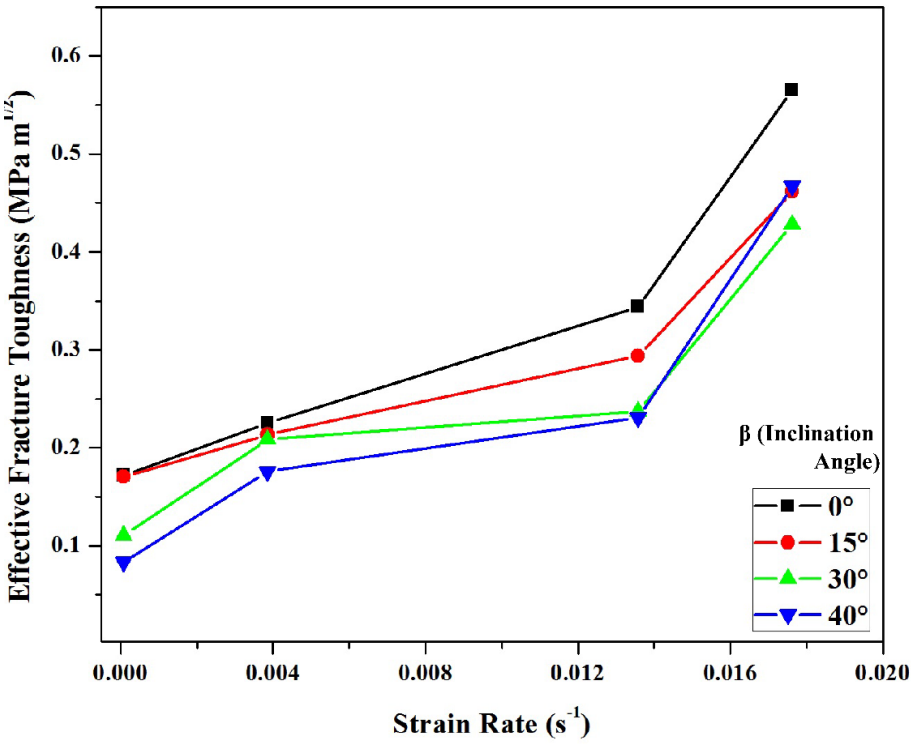

Figure 6.18 *Variation of effective fracture toughness in response to increasing strain rates*

The fracture toughness of any material is directly proportion to the load applied before the failure of the specimen. As in the case with increasing strain rates, the load required to break

the specimen increases, which in turn increases the fracture toughness of the material because both are dependent on each other. The effective fracture toughness for different strain rates is measured according to the relation mentioned for effective stress intensity factor. The relationship between the shale fracture toughness for different modes and the strain rate is shown in **Figure 6.18**, which indicates that fracture toughness gradually increases with increasing strain rates, which is in accordance with the observations of Dai and Xia (2013). Dai and Xia (2013) experimentally established the rate dependence of the fracture toughness anisotropy of Barre granite and found that the fracture toughness increased linearly with the loading rate. **Table 6.4** represents experimentally measured effective fracture toughness for different strain rates. In the sample names, S1, S2, S3, and S4 represent the strain rates at which those specimens were loaded (**Table 6.4**).

Table 6.4 *Mode I and mode II fracture toughness along with the effective fracture toughness in different notch angles at different strain rates*

Sample Name	**Applied Load** (kN)	**Mode I Fracture Toughness** (MPa $m^{1/2}$)	**Mode II Fracture Toughness** (MPa $m^{1/2}$)	**Effective Fracture Toughness** (MPa $m^{1/2}$)
0°_S1	1.029	0.565	0.000	0.565
0°_S2	0.529	0.344	0.000	0.344
0°_S3	0.359	0.225	0.000	0.225
0°_S4	0.294	0.172	0.000	0.172
15°_S1	1.049	0.436	0.152	0.462
15°_S2	0.608	0.277	0.097	0.294
15°_S3	0.378	0.201	0.070	0.213
15°_S4	0.304	0.161	0.056	0.170
30°_S1	1.431	0.285	0.319	0.428
30°_S2	0.833	0.158	0.177	0.237
30°_S3	0.588	0.139	0.155	0.208
30°_S4	0.323	0.074	0.082	0.110
40°_S1	1.928	0.000	0.467	0.467
40°_S2	0.998	0.000	0.231	0.231
40°_S3	0.796	0.000	0.176	0.176
40°_S4	0.420	0.000	0.083	0.083

Figure 6.19 represents the fracture toughness for all the three modes at different inclinations of the notch angles at different strain rates. With a gradual increase in the inclination of the notch angle, the mode I fracture toughness gradually decreases and, at 40° inclination of the

notch, it converges to zero. Simultaneously, the mode II fracture toughness gradually increases from zero at 0° and attains the maximum value at 40° inclination of the notch angle.

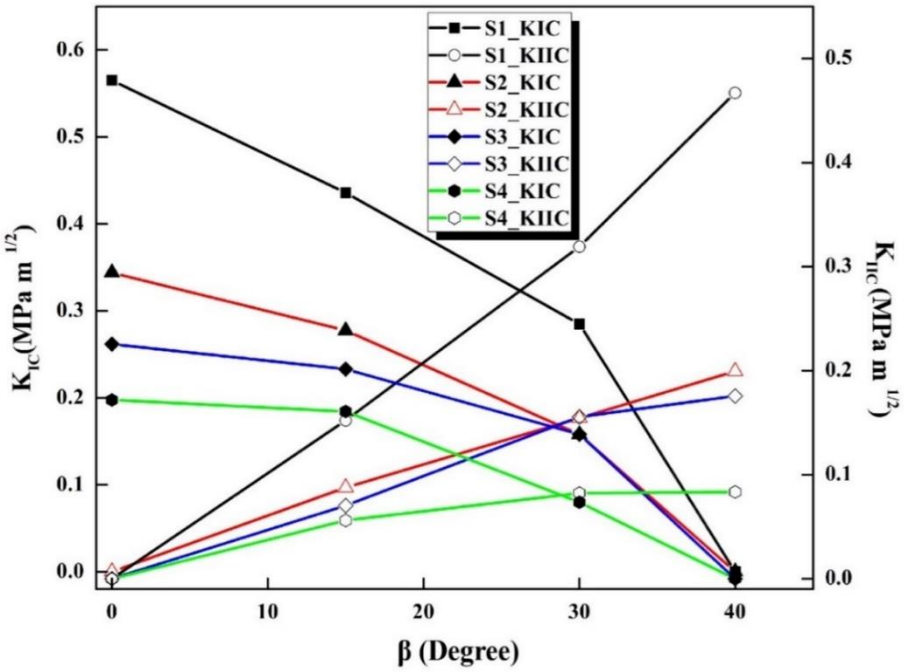

Figure 6.19 *Fracture toughness for different modes with different notch angles at the variable strain*

Table 6.5 *Mode I and mode II energy-release rates along with the total energy rates in different notch angles at different strain rates. In the sample names, S1, S2, S3, and S4 represent the strain rates at which those specimens were loaded*

Sample Name	**Applied Energy** (J)	**Mode I Energy-Release Rate** (J/m^2)	**Mode II Energy Release Rate** (J/m^2)	**Total Energy Release Rate** (J/m^2)
0°_S1	1.275	15.186	0.000	15.186
0°_S2	0.656	5.626	0.000	5.626
0°_S3	0.144	2.419	0.000	2.419
0°_S4	0.080	1.405	0.000	1.405
15°_S1	1.393	9.033	1.101	10.134
15°_S2	0.810	3.662	0.446	4.108
15°_S3	0.181	1.930	0.235	2.165
15°_S4	0.116	1.230	0.150	1.380
30°_S1	1.731	3.862	4.844	8.707
30°_S2	1.086	1.186	1.487	2.673
30°_S3	0.657	0.917	1.150	2.067
30°_S4	0.137	0.257	0.323	0.580
40°_S1	2.359	0.000	10.372	10.372
40°_S2	1.479	0.000	2.529	2.529

40°_S3	0.728	0.000	1.468	1.468
40°_S4	0.271	0.000	0.331	0.331

The energy-release rate for the plane stress condition can be measured according to the relation given by earlier. The energy-release rates for mode I and mode II fracture toughness under the plane stress condition at different strain rates were calculated; subsequently, the total energy-release rate was calculated by summing the values for both the modes. **Table 6.5** represents the mode I and mode II energy-release rate along with the total energy-release rate that corresponds to each strain rate.

Figure 6.20 represents the increment of the strain energy as a function of the strain rates. Towards the lower strain rates, the energy-release rates in all the three modes that have been tested in the current study have comparable energy-release rates. However, with increasing strain rates, the variations in the energy-release rates gradually become increasingly pronounced. Among all the strain rates, the mode I energy-release rate is higher than that of the mixed mode and mode II. In the case of the mode I opening, there is a very small involvement of the fracture surface, which produces a high energy-release rate. Similarly, in the mode II condition, the area involvement is high, which produces a small energy-release rate and the value of the intermediate energy-release rate is sandwiched between the values of mode I and mode II.

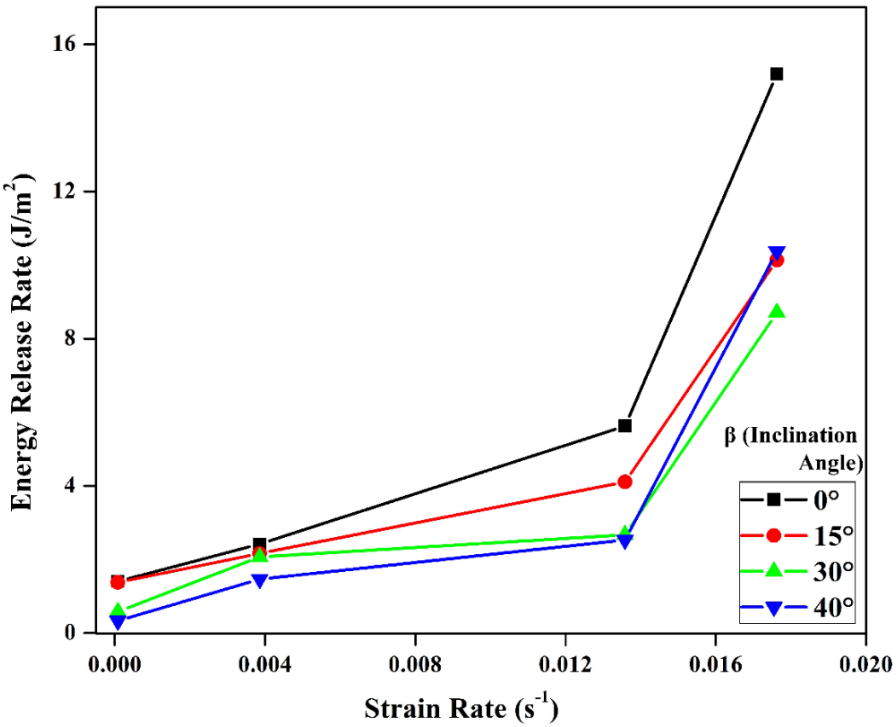

Figure 6.20 *Total energy-release rates at different strain rates*

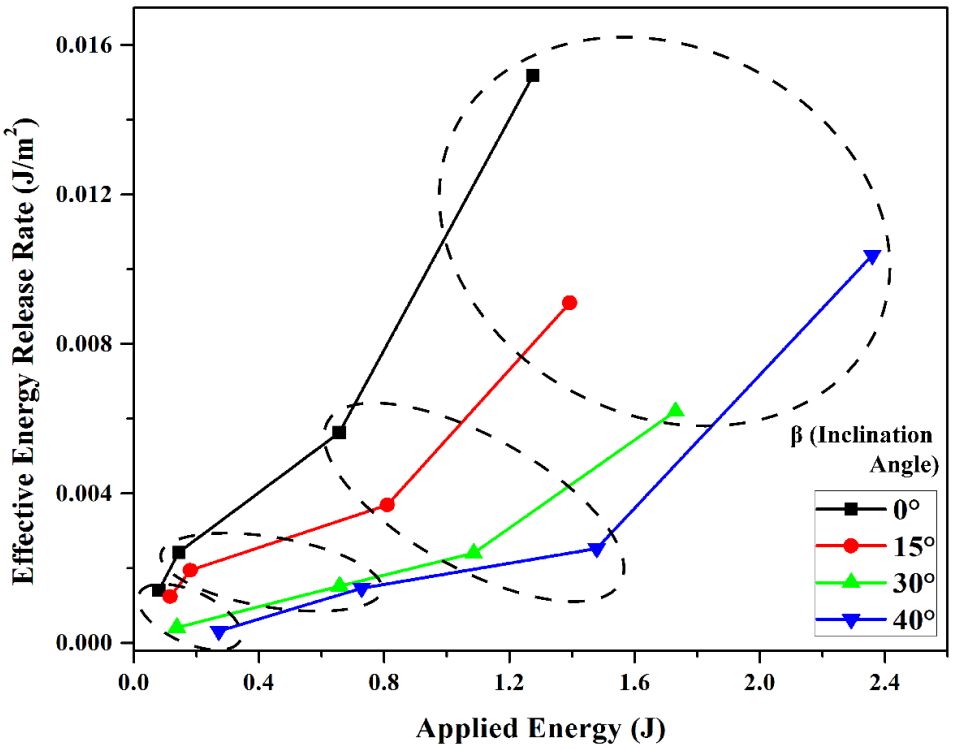

Figure 6.21 *A comparison between the applied energy and the energy-release rates for different modes, including mode I, mixed mode (I/II) and mode II. S1, S2, S3 and S4 represent the strain rates at which those specimens were loaded*

From the experimental results shown in **Figure 6.21**, it can be seen that energy absorption or the applied energy and the energy-release rate (G) gradually increase with increasing strain rates. This is in accordance with certain earlier findings (Liang et al., 2015). From **Figure 6.21** it can be inferred that, at all strain rates, a lower amount of energy is required for the onset of crack growth in case of mode I, when compared to the mixed mode and the mode II. Mode II requires the maximum energy for the onset of fracture. This is so because mode I failure involves only tensile opening, which is the easiest mode of failure because it requires a lower amount of applied load when compared to other modes such as the shear mode and the compression mode. The mixed mode involves some shear and tensile opening, whereas mode II involves only shear opening. Therefore, mode II will require the maximum amount of energy for the onset of cracks. The values of the energy that is required for the mixed-mode failure will lie in between the range of energy required for mode I and mode II. Similarly, the energy-release rate will be the maximum for mode I, intermediate for the mixed mode and minimum for mode II. The exact magnitude will depend on the fracture area that is formed after failure.

6.3 Influence of strain rate on the fracture toughness and tensile strength of sandstone using flattened Brazilian disc

6.3.1 Overview

Brazilian splitting test with arc loading condition may result in a reduction of the stress concentration in the disc and the crack initiation from the central position of the Brazilian disc cannot be guaranteed, because of the non-uniformity of stress loading arcs. In order to achieve the theoretical foundation of the Brazilian-splitting test, flattened Brazilian disc (FBD) specimen can be used as an alternative that prevents local crack initiation. FBD specimen can be used for the estimation of different geomechanical properties of rock such as σ_t, and K_{IC}, because of the ease for the sample preparation and loading geometry. For the validation of indirect tensile test using complete Brazilian disc, the crack must be initiated from the central region of the specimen and the loading angle corresponding to the arc of the disc must be greater than 19.5°. In the current study, an attempt has been made to investigate the strain rate sensitivity to various geo-mechanical properties (σ_t, and K_{IC}) of a homogenous fine grain sandstone using FBD specimens. The strain rates were varied between low and intermediate rates in the range of 10^{-5} to 10^{-2} s^{-1}. Two sets of specimens were tested with loading angle $2\alpha = 20°$ and $2\alpha = 30°$ for the better experimental observation of the strain rate sensitivity to various geo-mechanical properties. The test results illustrate that with increasing strain rates the fracture toughness and tensile strength gradually increase. Fracture toughness corresponds to loading angle of 20° overestimates the fracture toughness of the rock.

6.3.2 Background knowledge

For various aspects associated with the field of rock mechanics such as design, construction and geotechnical engineering analysis, rock properties like uniaxial compressive strength, tensile strength, Young's modulus, Poisson's ratio and fracture toughness carry a very vital role. Since the advent of Brazilian disc method by the Brazilian and Japanese in the 1940s, it has been extensively used for the indirect measurement of tensile strength of rocks and concrete; and subsequently, in 1978 for the first time, Brazilian tensile test was proposed by ISRM for the determination of tensile strength of rock materials (ISRM, 1981). In the following time, many researchers have concentrated their work on the Brazilian disc method resulting in the widening of its applications (Hudson, 1969; Mellor and Hawkes, 1971; Mighani et al., 2016).

For the first time, Fairhurst (1964) discussed the validity of the Brazilian tensile test. According to his findings, failure in a disc sample away from the central area might be due to the small contact area of loading. Furthermore, Mellor and Hawkes studied the contact stresses under the applied loads and subsequently designed a test jig with curved platens also known as jaws (Mellor and Hawkes, 1971). However, the manufacture of the curved jaws is quite a difficult job, and rock specimen of varied curvatures cannot be tested with the same set of the jaw; thus reducing the ease of application. The force that is applied during a Brazilian tensile test should be a line load, but the contact surface between the jaws and the specimen, need not necessarily ensure in achieving pre-requisite of line load. Hudson et al. (1972) inferred from their experimental analysis that the failure was always initiated directly under the loading points when loaded diametrically with flat steel plates which invalidated the Brazilian tensile test. Despite the extensive study of this Brazilian test method both experimentally and analytically; rarely does it gain attention on the validity of such test. Still, questions like the assurance of central crack initiation during a Brazilian tensile test are unsolved. In addition to this, experimentally it was observed that tensile strengths measured directly and indirectly are rarely equivalent. The direct tensile strength test estimates the true tensile strength of the rock. However, the Brazilian tensile test overestimates the tensile strength of rock because of its biaxial stress distribution instead of tension in a single direction. Furthermore, it has been reported by many researchers that the stress concentration as a result of the compressive loading near the loading platen has a significant influence on the results of Brazilian tests (Li and Wong, 2013; Perras and Diederichs, 2014).

To overcome such types of unavoidable instances, FBD was introduced for the measurement of tensile strength of rock that assures the central crack initiation during the test. Flattened Brazilian disc consists of two flat surfaces diametrically opposite to each other over which the compressive loading is applied. Additionally, it validates the equal stress distribution over the surface during the testing. As a whole, the loading associated with FBD specimen is far better than the line loading condition in case of Brazilian tensile test. In FBD test, local cracking or breakage, initiation of secondary cracking away from the central region and yielding around the loading point due to the stress concentration can be avoided (Wang and Xing, 1999; Wang et al., 2004).

Guo et al. (1993) proposed a new method to determine the mode I fracture toughness of rock without the introduction of any crack or notch and with progressive time, Wang and Xing (1999), brought some modification to Guo's method to determine the mode I fracture toughness

of rock. Since then many researchers have focused their research on this method for the measurement the of mode I fracture toughness and tensile strength of rocks (Keles and Tutluoglu, 2011; Lin et al., 2015a, 2015b, Wang and Cao, 2016, 2015; Wang and Xing, 1999; Wang et al., 2004).

FBD specimen can be used for the estimation of different geomechanical parameters of rock like σ_t, and K_{IC}, because of the ease for the sample preparation and loading geometry. For the validation of indirect tensile test using Flattened Brazilian disc, the crack must be initiated from the central region of the specimen and the loading angle must be greater than 19.5°.

In this study, an attempt has been made to investigate the effect of strain rates on properties such as mode I fracture toughness and tensile strength of rock measured using the flattened Brazilian disc. The whole experiment was conducted in static to quasi-static strain rate conditions ranging from $10^{-5}s^{-1}$ to $10^{-2}s^{-1}$. As the loading angle must be greater than 19.5° for the validation of FBD test, in this study, two angles i.e. 20° and 30° have been preferred for the observation of the strain effects.

6.3.3 Methodology

For the analysis, 50 mm disc specimens were used. After the preparation of specimens of required dimensions, diametral opposite flat surfaces are introduced depending upon the requirement of the loading angles. Flat surface of length of 8.68 mm and 12.94 mm was introduced to the specimen for 20° and 30° loading angle, respectively. A total number of 42 samples were tested for the observation of the experimental detail. During the preparation of the FBD specimens, special care was taken for the proper geometrical configuration and to avoid any irregularities that may affect the results of the test.

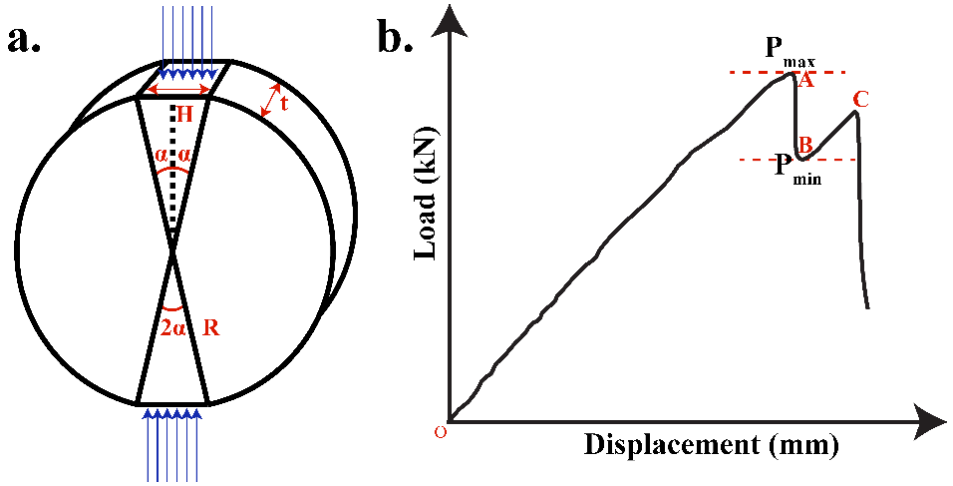

Figure 6.22 *Schematic diagram of the FBD specimens (left) and load-displacement curve (right)*

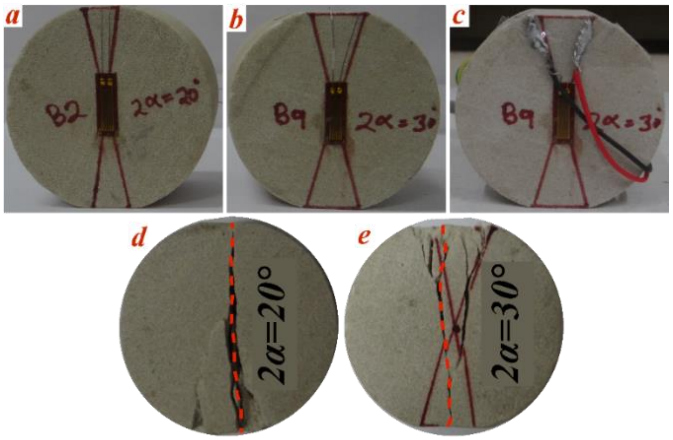

Figure 6.23 *FBD specimens with required loading angles (a, b, c) and failed specimens (d, e)*

Figure 6.22a represents the schematic diagram of the FBD specimen. **Figure 6.23** represents some of the specimens with required loading angles (a, b, c) and some experimentally failed specimens with centrally initiated cracks (d, e). Mode I fracture toughness and the tensile strength of the rock using FBD method can be evaluated with the following formulae:

$$K_{IC} = \frac{P_{min}}{\sqrt{R}t}\varphi_{max}$$

$$\sigma_t = K^* \frac{2P_{max}}{\pi D t}$$

Where,

P_{min} : Local minimum load (kN)

Pmax : Maximum load before failure (kN)

R : Radius of the specimen (mm),

t : Thickness of the specimen (mm)

K* : Correction coefficient for FBD

D : Diameter of the FBD specimen (mm)

φ : Dimensionless SIF

φ_{max} : Maximum dimensionless SIF

In case of FBD, when 2α > 19.5°, the crack initiation can be expected from the centre of the specimen, followed by its extension along the loading diameter of the disc specimen. The point 'A' in **Figure 6.22b** represents the point from which the crack initiates and starts to propagate and at the same time, φ will be zero, which gradually increases and reaches its maximum value (φ_{max}) at point 'B'. After point 'B', it monotonically decreases until final breakage of the specimen. In region 'AB', it undergoes unstable crack growth as in this stage crack will propagates even if the load is held constant and φ increases with relative increase of the crack length. After reaching, point 'B', φ decreases with increase in the non-dimensional crack length

and in region ‘BC’, it undergoes stable crack propagation, as the crack will stop to propagate if the load is not increased. The transit point between the unstable crack propagation and the stable crack propagation at point ‘B’ corresponds to the local minimum load immediately succeeding the peak load in the load-displacement graph (Wang and Xing, 1999; Wang et al., 2004). With the knowledge of current load and crack length at any point during the crack propagation, the fracture toughness of brittle material like a rock can be estimated. Point ‘B’ is considered as the critical point because of the convenience for the measurement of the critical load that is the local minimum load occurring soon after the peak load. The unstable crack growth followed by its arrest at the critical point, after which the subsequent crack growth is stable in nature. That is why this critical point is considered for the measurement of mode I fracture toughness of rock-like materials.

6.3.3.1 Results and discussion

Table 6.6 represents the experimentally found peak load before failure and the local minimum load with different strain rates that shows that with an increase of the strain rates from static to quasi-static level, the maximum applied load required for the failure of the rock as well as the local minimum load gradually increase. The fracture toughness of any material is directly proportional to the applied load. As with increasing strain rates the strength of the material increases, which in turn increases the fracture toughness of the material, as both are directly proportional to each other (**Figure 6.23a**).

Under low strain rate, intergranular (IG-I) fracturing played the dominant role in forming the fracture surface of a specimen. Under such conditions of loading, the fracture surfaces were rougher, when compared to that of the specimens failed at high strain rates. This is because of the dominance of intergranular fractures, which get enough time to allow propagation along the grain boundaries resulting into a rough fracture surface. With the increase in strain rate, the transgranular fractures become dominant and as a result, the fracture path becomes straighter, and possesses a less rough surface, compared to that at low strain rates. Under static compression test, the strain rate is slow and as a result, the plastic strain gets enough time to develop completely before the next incremental load is applied. In such cases, the stress field near the crack tip has sufficient time for its redistribution to other parts of the grains and as a result, there may be more damage along the weaker parts near the crack tip i.e. along the grain boundary. The overall resultant dominant mode of fracture is therefore intergranular. At higher strain rates, the loading is fast and the plastic strain component may not get enough time to develop fully until when the next incremental load is applied and in such cases, the stress does

not get enough time for its redistribution and the stress does not spread far away from the crack tip. This causes the material near to the crack tip to fail suddenly giving rise to the less rough or straight fracture surfaces involving transgranular fractures. Consequently, it appears that the material has stiffened because of the incomplete development of the plastic strain due to insufficient time. With increasing strain rates, the fracture mechanism in the rocks changes from intergranular to transgranular, which leads to more fragmentation of rock in case of high strain rates. In between the intergranular and the transgranular fractures, the transgranular fractures are quite difficult to form, as they require high-energy input. During compression, certain locations of the rock materials may be subjected to tension that gives rise to the nucleation and growth of microcracks. With increasing strain rate, the applied stress gradually increases which is responsible for the activation of more numbers of microcracks. The number of activated microcracks is directly proportional to the applied stress and therefore at slow strain rates, few relatively large microcracks are activated, leading to few large broken pieces of the specimen, whereas, in high strain rate, more and relatively small microcracks are activated resulting smaller broken pieces of the specimen. Also in high strain rates, the crack is forced to pass through the grains, in this case, quartz; a higher fracture toughness value results.

Table 6.6 *Maximum load (*P_{max}*) and local minimum load (*P_{min}*) with different strain rates*

Strain Rate	20°		30°	
	P_{max}	P_{min}	P_{max}	P_{min}
3.00E-05	6.29±0.15	4.46±0.34	7.10±0.18	5.10±0.18
1.00E-04	7.01±0.16	4.80±0.37	7.97±0.10	6.00±0.11
8.00E-04	8.03±0.24	6.24±0.26	9.44±0.14	6.45±0.17
1.00E-03	10.59±0.18	6.42±0.24	11.07±0.22	6.92±0.19
0.008	12.57±0.12	6.97±0.32	11.85±0.20	8.13±0.23

For both the cases i.e. 20° and 30°, fracture toughness increases with increasing strain rates. For the static strain rates, the mode I fracture toughness of the rock measured through SCB specimen is 0.72 MPa $m^{1/2}$ (Mahanta et al., 2016). When the fracture toughness was measured through both the SCB and FBD tests, it can be well inferred that the fracture toughness measured at 30° loading angle in FBD test is quite comparable with the SCB method whereas, the fracture toughness measured at 20° loading angle overestimates the fracture toughness of the rock, which may be due to low area involvement in case of 20° loading angle. In case of 20° loading angle, the distance from the centre to the surface of loading (H in **Figure 6.22a**) is higher compared to the 30° loading angle which causes a relative higher fracture toughness as

a result of the reduction in the process zone size relative to the specimen dimensions and higher distance to the load application area. Crack is forced to follow the targeted path towards applied compressional principal stress path (Keles and Tutluoglu, 2011). Therefore, 30° loading angle is more preferable for the estimation of fracture toughness of rock using FBD specimens. A comparison between the tensile strength measured using Brazilian disc test and flattened Brazilian disc test has been done (**Figure 6.24b**). Tensile strengths for FBD case were calculated according to the formula proposed by Wang et al. (Wang and Xing, 1999; Wang et al., 2004), Wang and Cao (Wang and Cao, 2016, 2015) and Lin et al. (Lin et al., 2015a, 2015b). From the comparison, it can be well established that Brazilian test always overestimates the tensile strengths compared to that measured through FBD test. Earlier, similar findings have been reported by Li and Wang (2013) and Perras and Diederichs (2014). Therefore, it can be concluded that FBD test is more reliable as compared to the Brazilian disc specimen for the determination of tensile strength of the rock.

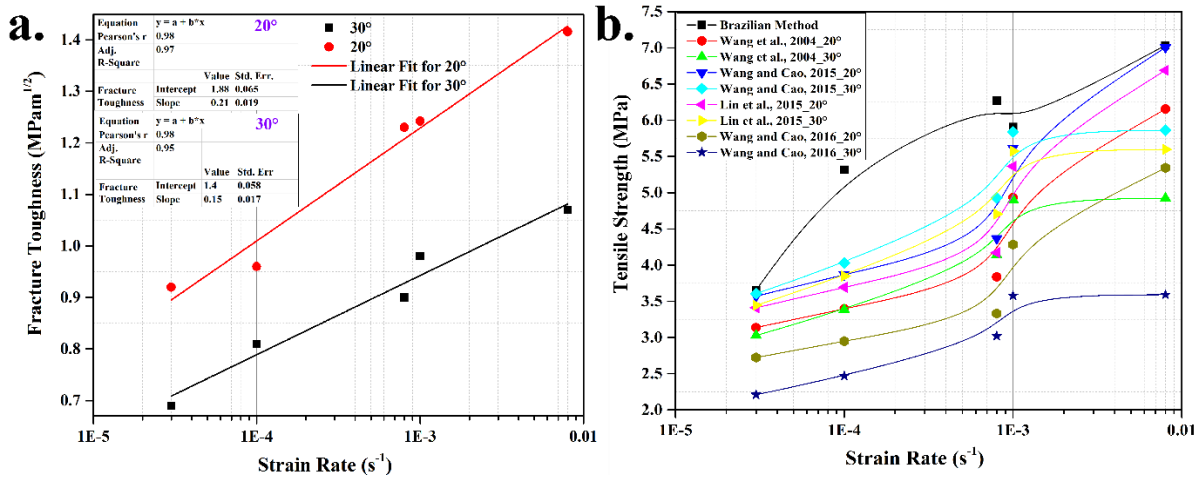

Figure 6.24 *A correlation between mode I fracture toughness and strain rates (left). Comparison between the tensile strength measured through complete Brazilian disc specimens and flattened Brazilian disc specimens*

Chapter 7 Experimental investigation of the mechanical behaviour of sandstone under high-temperature and high-pressure conditions

Experimental investigations that have been carried out thus far are restricted to unconfined conditions. However, deep inside the earth, rocks experiences confinement from the surround. In addition, deep-seated rocks experience high-temperature and high-pressure conditions. Hence, to simulate the fracturing characteristics of the specimens deep inside the earth, high-temperature and high-pressure triaxial tests were performed.

7.1 Sample preparation

For the high-temperature and high-pressure triaxial tests, a cylindrical specimen of the sandstone that was 22.5 mm diameter and 45 mm in length was prepared (**Figure 7.1**). In order to avoid surface irregularities, both the end faces were ground with a surface grinder for equilibrium in the load application throughout the face of the specimen.

Figure 7.1 *Cylindrical specimens that are 22.5 mm in diameter and 45 mm in height*

7.2 Experimental methodology

7.2.1 Experimental setup

For the experimental investigation, the high-temperature and high-pressure triaxial test apparatus at the Deep Earth Energy Laboratory in Monash University was used. This triaxial apparatus is capable of applying a confining pressure of up to 140 MPa, a maximum temperature of up to 300 °C, and a maximum injection pressure of 137 MPa. Essentially, the triaxial apparatus comprises four systems: the loading system, heating unit, confinement line, and injection line. In order to perform high-temperature testing, silicon oil was used as the

confining media. The target temperatures were achieved by using an electric band heating that was placed around the confinement chamber, and the precise temperature inside the confinement chamber was measured by using the thermocouples inside the confinement chamber and connected to the barrel of the band heater (**Figure 7.2**). The thermocouple that was installed inside the pressure cell was used to monitor the temperatures of the specimen and the confining media; whereas, the thermocouple that was present outside the chamber was connected to the heating-band and its heating was controlled. The heating of the band was controlled using a controller. In order to avoid any thermal shock to the specimen, the heating rate was kept at 2.5 °C/min. The band heater would heat the pressure cell, which in turn would heat the sandstone specimen that was placed inside. An insulating jacket was placed outside the band heater to avoid heat loss during the experiment. A hydraulic pump was used to apply the axial load to the sample, and the axial load was directly recorded with the help of a data acquisition system. During the experiments, hydraulic pumps were used to apply both the confining pressure and the load. Pressure transducers that had an accuracy of 0.25 per cent of the maximum pressure were used to monitor the injection and the confining pressure. Inside the confining cell, a copper sleeve was used as a membrane to avoid contact between the confining media and the rock specimen.

Prior to the measurement of the permeability of the specimens, all the lines were drained to ensure that air bubbles were not present. Loading tests were started after the temperature and the pressure of the cell achieved equilibrium. The experimental investigation included the testing of the sandstone at four different temperatures such as room temperature, 100 °C, 200 °C and 300 °C; and two different confinement pressures—30 MPa and 60 MPa. Based on the availability of resources and by considering the experimental constraints, these sets of temperature and pressure conditions were chosen to simulate the conditions deep underground and to establish a better understanding of the failure criteria under such conditions.

In order to avoid contact between the specimen and the confining media, a cylindrical copper sleeve was used. Prior to the testing of the specimen, the copper sleeve was annealed so that it would not offer additional resistance to applied load. The sandstone specimen was placed inside the copper sleeve and both were placed inside the cell.

All mechanical tests were performed when the system achieved steady-state equilibrium in temperature and pressure across the sample. Equilibrium was achieved by observing the confinement pump volume and the thermocouple placed inside the pressure cell close to the

specimen. For loading, a constant pump flow rate of 1 ml/min was maintained, and upon conversion to displacement, the rate was 0.05 mm/min. The application of the load was accompanied by the measurement of axial strain by means of the linear variable differential transducers (LVDTs) that were attached to the ram of the load cell.

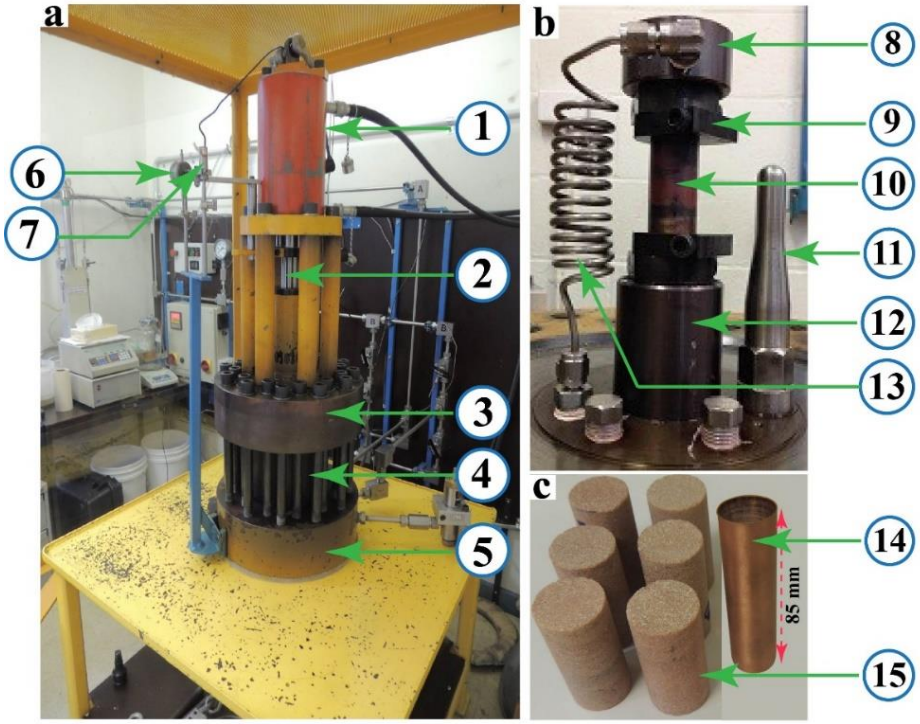

1: Load cell
2: Loading shaft
3: Cell top
4: Band Heater
5: Cell pedestal
6: Dial gauge
7: LVDT
8: Top Plate
9: Steel clamp
10: Specimen with annealed copper sleeve
11: Thermocouple (inside)
12: Bottom plate
13: Fluid pipe
14: Copper sleeve
15: Sandstone specimen

Figure 7.2 *Experimental setup indicating different components of the high-temperature and high-pressure loading system*

7.3 Results and discussion

7.3.1 Failure characteristics of the specimens

Under triaxial compressive stress, failure of rocks is possible in two different ways: (1) under low confining conditions, which occur predominantly due to dilatancy and strain softening; (2) under high confining condition, failure is predominantly due to strain hardening. However, in some scenarios, a transitional regime is observed under intermediate confining pressure (Klein et al., 2001; Kumari et al., 2017b).

Based on the visual inspection of the experimentally tested specimens, it can be observed that, in all the cases of tested temperatures, the specimens that were tested at 30 MPa of confinement showed a single localised shear band. However, in the specimens that were tested at 60 MPa

of confinement in all temperature cases, multiple localised shear bands or wider single localised shear bands were observed (**Figure 7.3**). While considering the angle that these shear bands/planes make with the minor principal stress, a slight decrease in the angle was observed with increasing confinements, which indicated a possible reduction in the friction angle of the specimens. The reduction in the friction angle can be due to the greater quasi-brittle behaviour of the rocks under high confinement conditions (Wong et al., 2001).

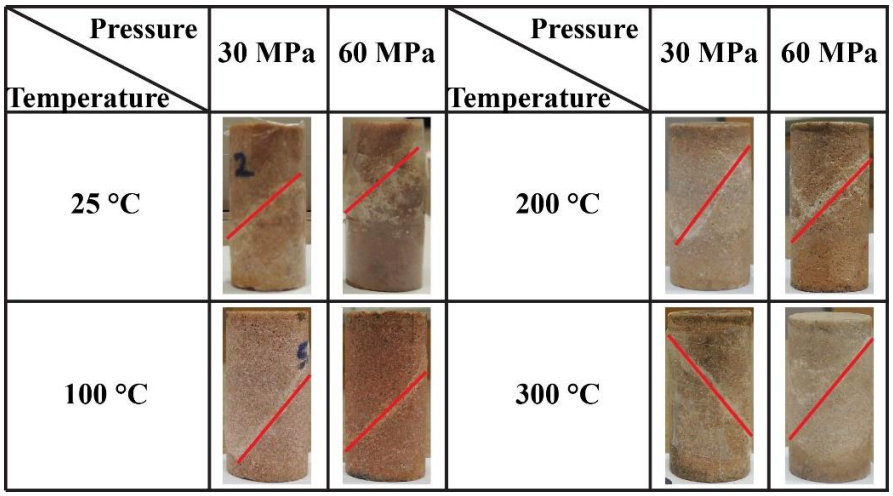

Figure 7.3 *Experimentally failed sandstone specimens, indicating the developed shear bands*

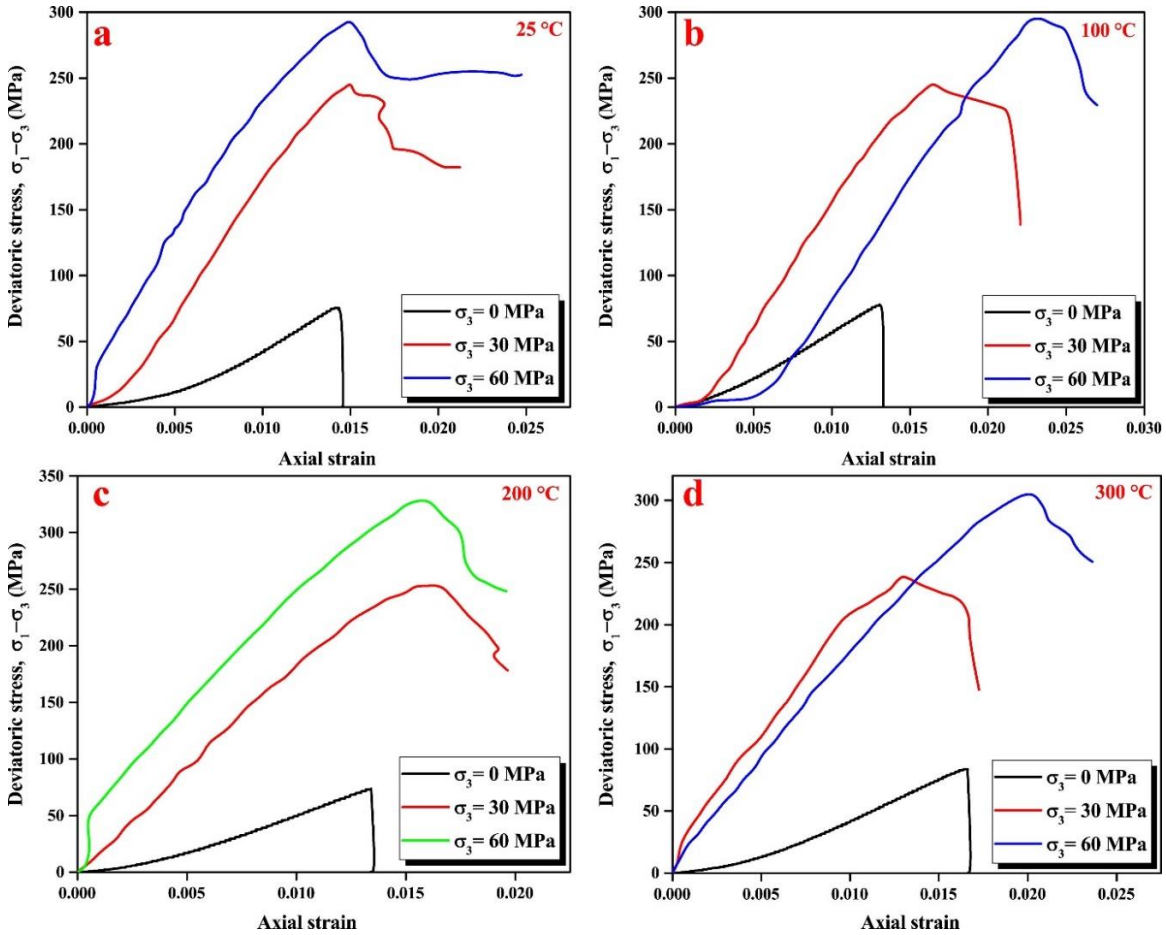

Figure 7.4 *Stress-strain curves of sandstone at different temperatures*

7.3.2 Stress-strain behaviour at different temperatures and confinements

The various stress-strain curves at different temperatures for both the confining condition and the unconfined conditions are represented in **Figure 7.4**. When we compare the stress-strain curves of the sandstone in all the confined cases and the unconfined case, it can be observed that the specimens that were tested under confinements display some sort of strain softening after the peak load, which is not marked in the case of the unconfined condition. An increase in the peak stress is observed with increasing confining pressure (**Figure 7.5**).

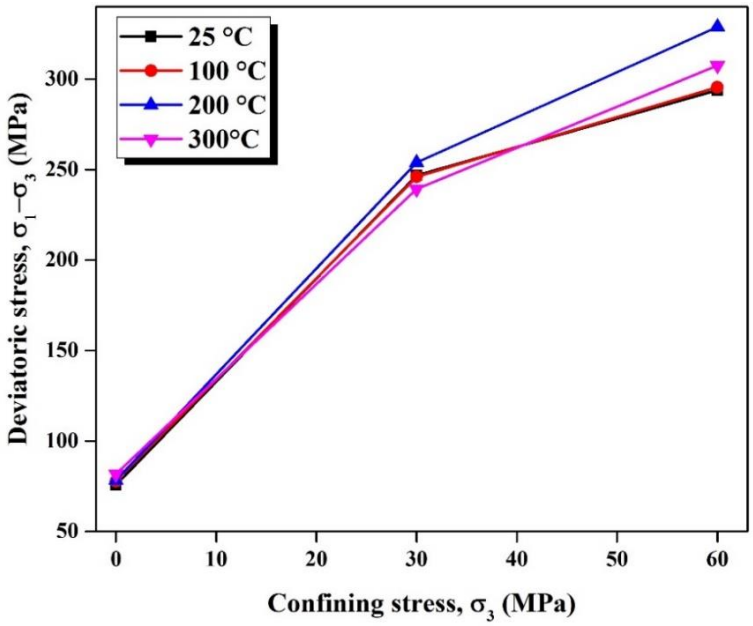

Figure 7.5 *Variation in the deviatoric stress of sandstone at different temperatures and different confinements*

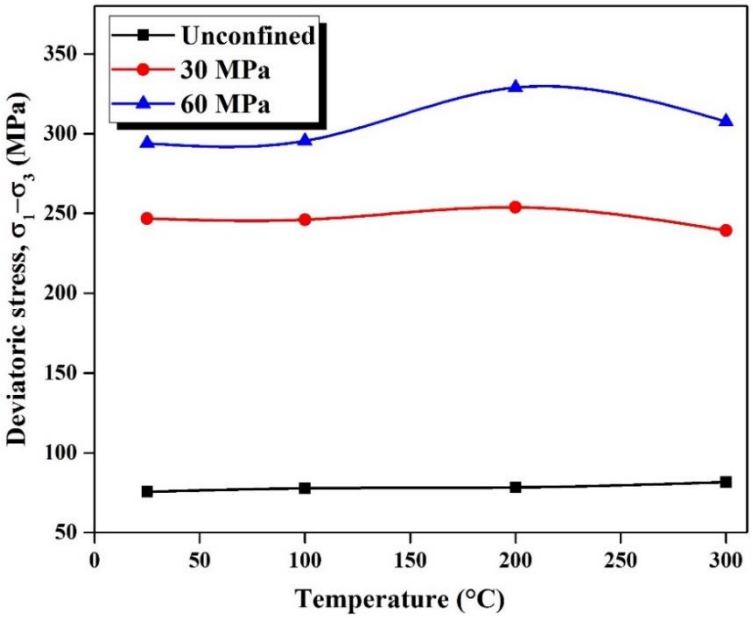

Figure 7.6 *Variation in the deviatoric stress of sandstone at different confinements and different temperatures*

7.3.3 Effect of temperature and pressure on the mechanical strength parameters of sandstone

In the current experimental investigation, two confining conditions, 30 MPa and 60 MPa; and four temperatures, 25 °C, 100 °C, 200 °C and 300 °C were observed. When temperature and confinement are compared, the latter has a more significant influence on the strength behaviour of the sandstone than on the temperature range.

In the studied range, the temperature has a very marginal effect on the strength of the sandstone. In the unconfined condition, the peak strength of the sandstone is found to be in an increasing order that increases along with the increase in the temperature. However, the increment is quite marginal (**Figure 7.6**). For both the 30 MPa and 60 MPa confining conditions, the peak strength of the sandstone increases from room temperature up to 200 °C, due to which the deviatoric stress curves follow a slight decreasing trend up to 300 °C (**Figure 7.6**).

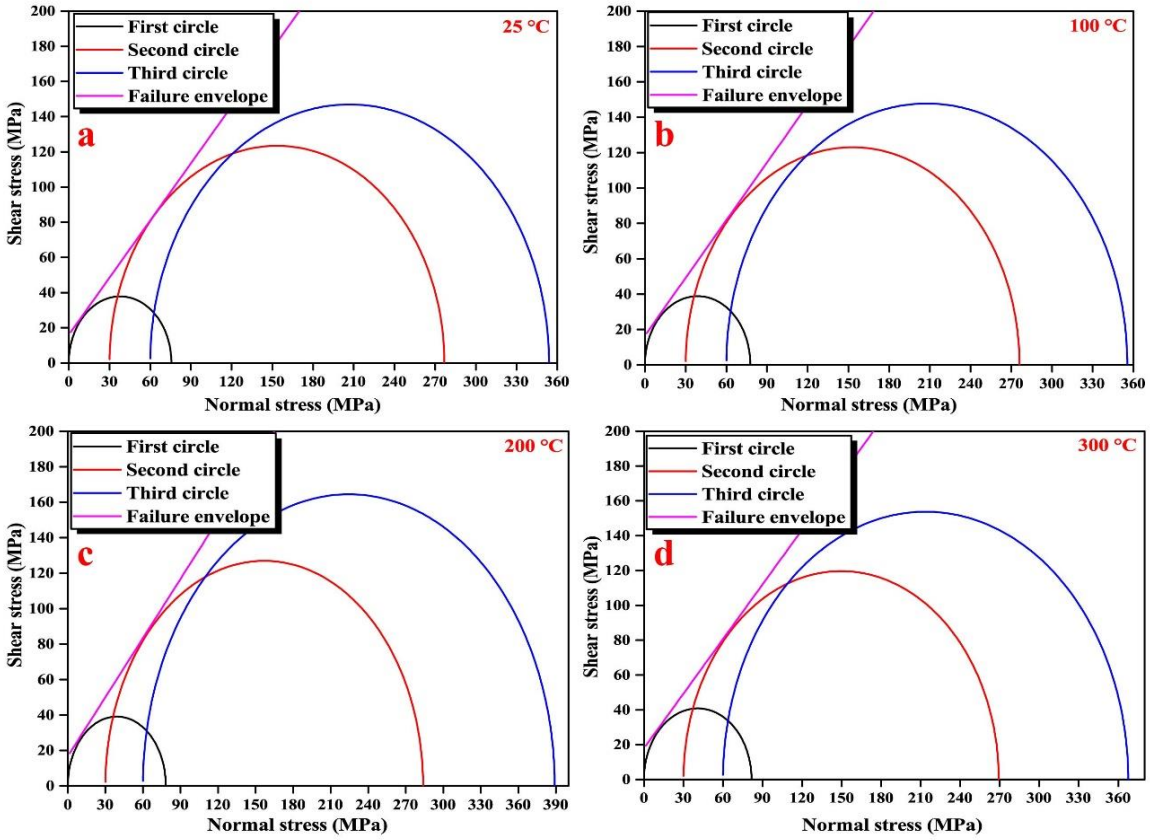

***Figure 7.7** Mohr–Coulumb failure envelope of the sandstone at different temperatures*

Mohr circles for different peak stresses and their corresponding strain have been plotted for different temperatures, in **Figure 7.7**. With a progressive increase in the confining pressure, an increasing trend of peak stress was observed for all the studied temperatures. Low confining pressure conditions are always associated with higher potential for dilation, which results in an

easy opening of microcracks. However, in the high confining condition, no such dilation potential and ease of microcracks opening are observed. The higher confinements compress the preexisting microcracks, which does not facilitate the easy development of microcracks; hence, the rock failure shifts from brittle to predominantly ductile (Kumari et al., 2017b). The Mohr–Coulomb envelope does not follow linearity at higher confinements and its slope gradually decreases with increasing confinements; at a certain critical value of the confining stress, the Mohr–Coulomb failure envelopes attain a zero gradient (Barton, 1976; Hoek, 1983).

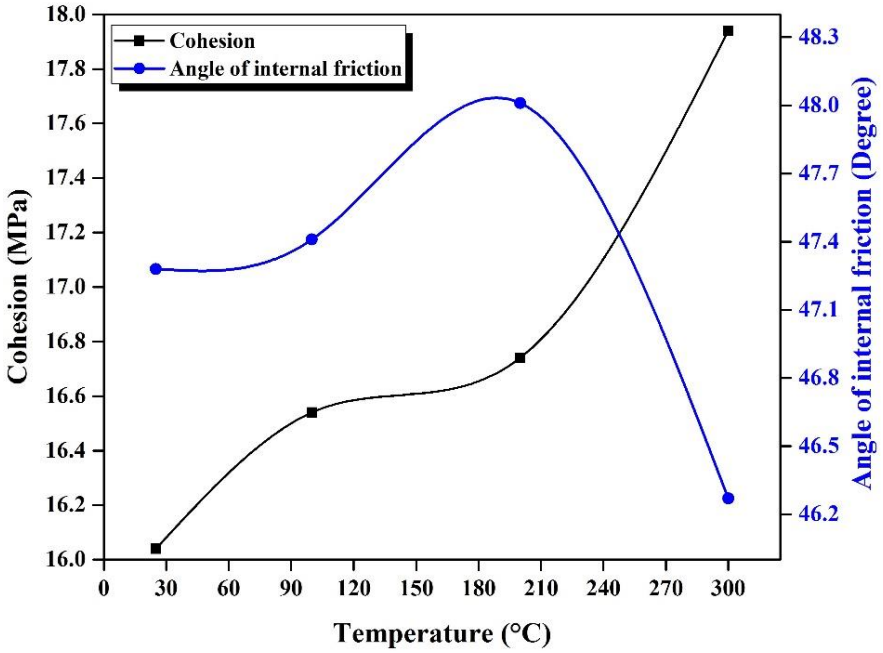

Figure 7.8 *Variation of cohesion and friction angles of the sandstone at different temperatures*

With a progressive increase in temperatures, from room temperature to 300 °C, the cohesion of the sandstone increased. The values of the friction angle increased from room temperature up to 200 °C, which resulted in a decreased of up to 300 °C. However, the variation of both the cohesion and the friction angles over the studied temperature range is not significant (**Figure 7.8**).

7.4 Insight into the post-failure microstructure

7.4.1 Methodology of micro-CT-based investigation

Flow behaviour and transport properties of rocks are substantially influenced by the deformation process and by the evolution of strain geometry, grain structure and pore spaces in aspects of volume connectivity, shape and tortuosity (Sulem and Ouffroukh, 2006). In brittle rocks, shear bands are the weak zones when compared to the surrounding rocks that undergo

intense localised damage upon application of load. During application of load, depending on the stress level and the initial porosity, rocks display contraction (strain hardening) or dilation (strain softening).

When rocks are close to the peak stress localised shear bands are formed due to the orientation and coalescence of microcracks. As has been discussed previously, the stress-strain curve of the rocks can be classified into different regions based on the nature of the curve. The inelastic deformations of the rocks are always associated with significant grain crushing and pore collapse. An in-depth observation of the shear bands that form due to applied stress provides an understanding of the behaviour of rocks at higher stress levels at which the collapsing of the pore collapse and grain crushing are important.

Researchers, El Bied et al. (2002), have investigated the evolution of shear zones in Fontainebleau sandstone that has 21 per cent porosity, which was tested under triaxial compression. At a low confining, pressure (seven MPa); they reported a nine per cent increment in the porosity inside the shear band, which gradually decreased away from the shear band. They interpreted it as the dilating of the shear band under low confinement. However, at a higher confining pressure (28 MPa), a compaction band with high grain crushing and lower porosity was observed in the centre of the shear band that was surrounded by a dilating band that had grain cracking and higher porosity.

However, in the current investigation, the characteristics of the shear band that forms at different temperatures and pressure conditions are analysed using micro-CT techniques. The detailed working principle and the mechanism of micro-CT techniques are explained in chapter 8.

Figure 7.9 *Visible shear bands on the surface of the specimen (30 MPa, 100 °C)*

Axis-symmetric triaxial tests for the sandstone at different temperatures (25 °C, 100 °C, 200 °C, and 300 °C) and at different confinements (30 MPa and 60 MPa) were performed.

Soon after the maximum load and the failure of the specimens, tests were stopped in order to keep the specimens in a state that enabled the observation of the shear bands as much as possible by using micro-CT techniques. One or more shear bands formed at the end of the test of the specimens, which enabled a better observation of the characteristics of the shear band. However, the presence of any material discontinuity would prevent the observation. Specimens that are under a triaxial loading configuration fail upon formation of one or multiple shear bands. In general, specimens that are tested under low confining pressures tend to fail along unique shear bands, however, specimens that are tested under high confining pressures tend to fail along several bands (Sulem and Ouffroukh, 2006).

With increasing confining pressures, the maximum effective stress increases. The maximum effective stress at different confinements can be fitted to the Mohr–Coulomb criterion, which provides information regarding the cohesion and the angle of internal friction of the specimens. For the current investigation, cohesion and the angle of internal friction were obtained for all the temperatures that were used in the investigation. The shear bands that are produced at the end of the test are white and are clearly visible on the surface of the specimen (**Figure 7.9**). This white colour is due to the crushing of quartz grains, which allows for precise evaluation of the orientation and the thickness of the shear bands.

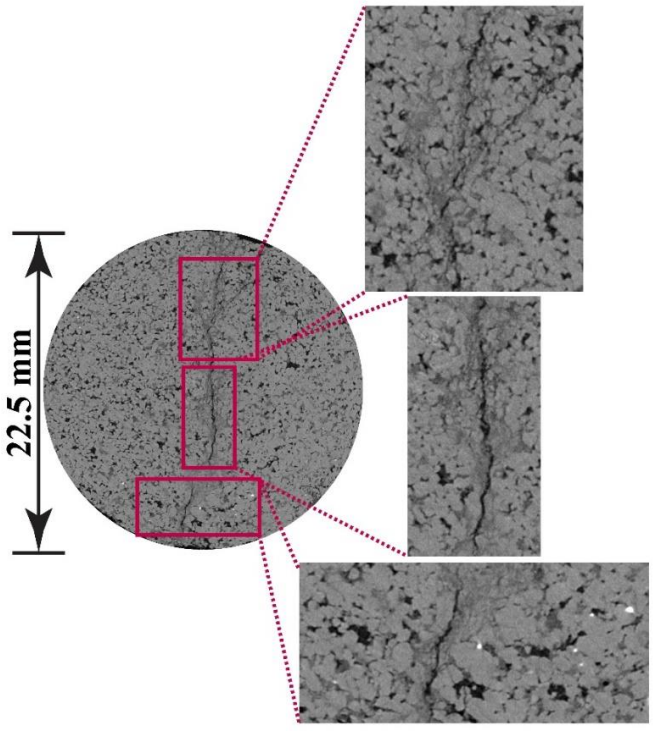

Figure 7.10 *Developed shear bands in the micro-CT images of the sandstone (30 MPa and 100 °C)*

Previous researchers have reported a decrease in the orientation of the shear band upon an increase in the confinement. The variation in the orientation of the shear band in response to different confinements can be explained in terms of the sensitivity of granular rocks to pressure (Bésuelle et al., 2000; El Bied et al., 2002; Sulem and Ouffroukh, 2006).

Currently, the microstructural investigation of rocks by using micro-CT techniques is popular among researchers of various domains in the fields of earth sciences, due to the ease of the working of these techniques and the accuracy of interpretation that they afford. Micro-CT based techniques is an image-based analysis that requires good resolution input images that have a good tone of contracts and grey-level thresholds, which facilitates discrimination between the solids and the void spaces, and provides reliable results. **Figure 7.10** represents the micro-CT based approach for the investigation of the experimentally failed specimen.

7.4.2 Results and discussion

7.4.2.1 Grain-size-based investigation

Specimens that are tested under 30 MPa confining pressure possess a single shear band predominantly, whereas specimens that are tested under 60 MPa confining pressure possess multiple shear bands and display intense grain crushing and pulverisation (**Figure 7.3** and **Figure 7.11**). The grain-size analysis of the inside shear band and the outside shear band of the studied sections indicate a major variation in the grain size distribution in both the cases.

In all the tested temperature and pressure cases, the inside shear bands possess finer grains in comparison to respective outside shear bands of all the temperature and pressure cases (**Figure 7.12**). Due to crushing under both the confining conditions, very small particles, which appear white and powdery to the naked eye and are in the order of micrometres, are formed. Similar observations for Fontainebleau sandstone were reported by El Bied et al. (2002) and Sulem and Ouffroukh (2006). The porosity of the sandstone was measured at various places, both inside and outside the shear bands. Additionally, grain-size analysis of both the inside and outside shear zones was performed by using image analysis techniques. The minimum size of the sections of the image that was used to estimate the porosity and the grain size was greater than 3000 μm, which can be considered a representative part of the specimen. All the sections of the image at different temperatures and pressures, which were used to estimate the porosity, are represented in **Figure 7.11**.

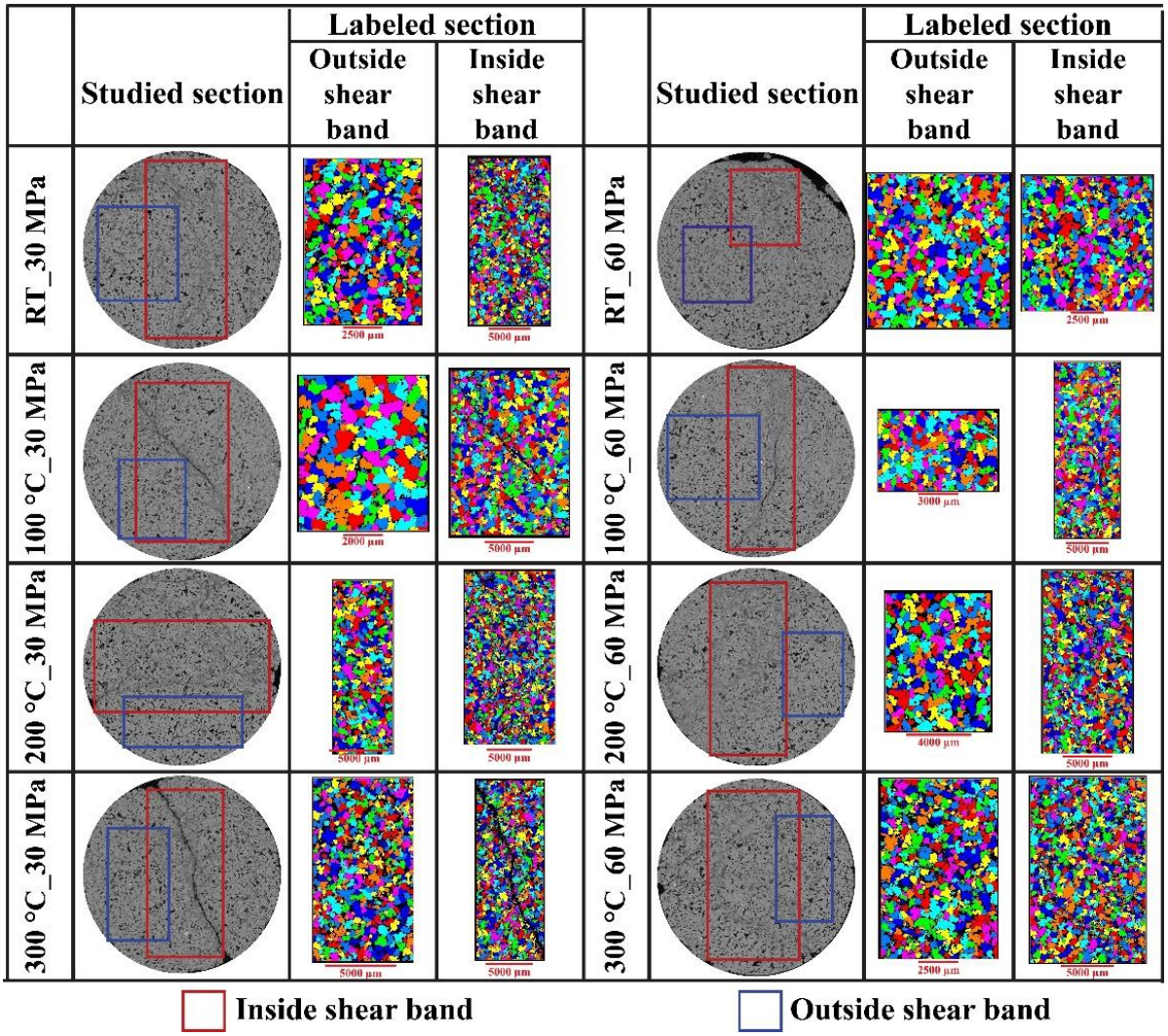

Figure 7.11 *Greyscale micro-CT images and processed images of the inside shear zone and the outside shear zone of specimens tested at different confinements and temperatures*

While investigating the grains sizes between both the zones of the sandstone, it was found that the grains of the inside shear zone are smaller than the grain sizes of the outside shear zone. This clearly indicates crushing and grain-size reduction of the shear bands. Similar interpretations were inferred for all the studied temperatures and confinement conditions. In all the cases, the inside shear zones are found to have higher porosity than the outside shear zone, which can be due to the possible reduction of grain sizes inside the shear zone.

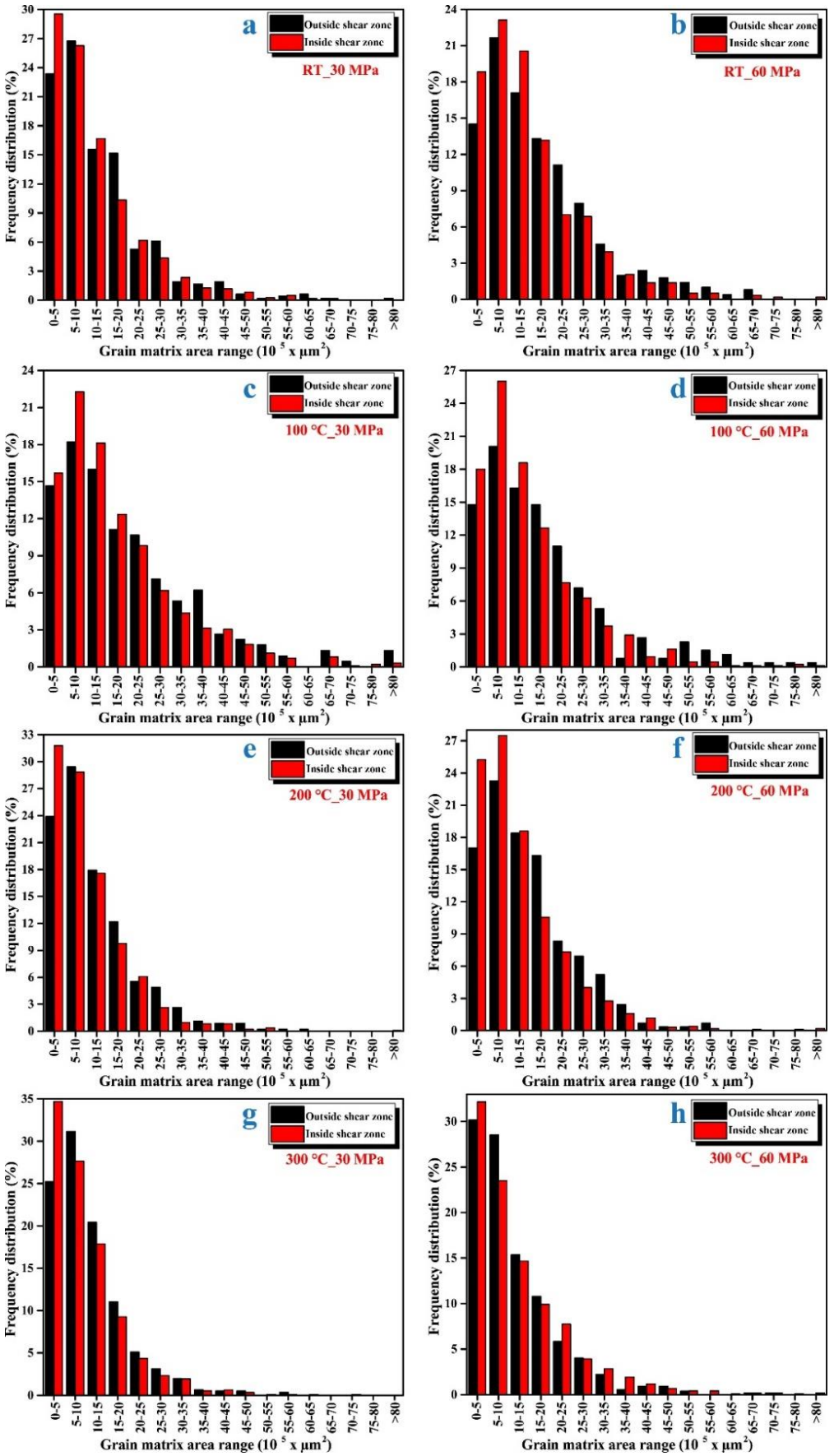

Figure 7.12 *Frequency distribution of grain matrix at different confinements and temperatures*

7.4.2.2 Porosity-based investigation

The porosities of both the zones for all temperatures and pressures are shown in **Figure 7.13a**. The figure suggests that for both the confinements, when temperatures were increased, the porosities decreased up to 100 °C, which resulted in an increasing trend up to 300 °C. Similarly, the difference in the porosities of both the zones has been shown in **Figure 7.13b**. The figure indicates that the differences between the porosities of both the zones are marginal at room temperature. However, a considerable amount of differences in the porosity was observed for the other temperatures that were used for the investigations (100 °C, 200 °C, and 300 °C).

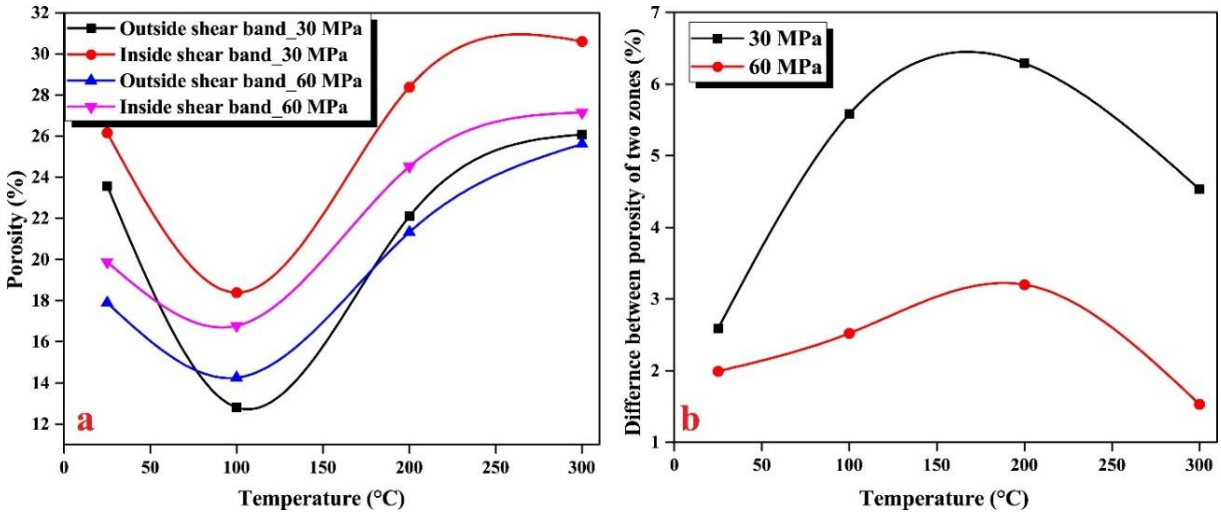

Figure 7.13 *Comparison of the porosities inside the shear zone and outside the shear zone at different temperatures (a), difference between the porosities of the two zones (b)*

Chapter 8 Micro-CT based microstructural investigation of sandstones

8.1 Microstructural insight into progressive deformation of sandstone after heat treatment

8.1.1 Overview

The physico-morphological and the mechanical behaviour of rocks under or post high-temperature conditions is quite significant in the successful implementation of various engineering projects such as underground coal gasification, radioactive nuclear waste disposal in geological formations, geothermal energy extractions and enhanced oil recovery. The microstructural behaviour of rocks is quite important in the macroscopic behaviour and in the successful implementation of these engineering projects. The foremost microscopic attributes of rocks are pore volume, pore radius, the pore coordination number, the throat radius and the throat channel length. This paper extensively reviews the various reasons for the microstructural modification of rocks upon exposure to high temperatures. Additionally, the authors' experiential understanding of the characterisation of various microscopic attributes of the structure of pores, which the use of the micro-CT technique afforded, has also been reviewed. An attempt has been made to investigate the microstructural response of three Indian sandstones (Dholpur sandstone, Jodhpur sandstone and Gondwana sandstone) to elevated temperatures (200 °C, 400 °C, 600 °C and 800 °C) using the high-resolution micro-CT techniques. The investigation includes microstructural modifications, the evolution of pores spaces and pore-network modelling (PNM) of the three sandstones as a function of elevated temperatures. The overall trend of porosity in Dholpur and Gondwana sandstones was found to have an escalating pattern as a function of temperature. However, in case of Jodhpur sandstone, the maximum porosity is achieved at 600 °C and thereby a decreasing trend up to 800 °C possibly due to the formation of a cementing material. Of the three sandstones, Gondwana sandstone was found to be the most vulnerable to elevated temperatures when compared to Dholpur and Jodhpur sandstones. Based on the current investigation, it can be concluded that 370 °C– 680 °C is the common temperature window at which the three sandstones undergo major structural damage.

8.1.2 Background knowledge

Modern-day energy requirements have been fulfilled by various engineering applications such as nuclear engineering, underground coal gasification, enhanced oil recovery, and geothermal

energy extractions, all of which involve direct or indirect heating of the underground rock strata. At elevated temperatures, thermal stress alters the physical (volume, density, mass, ultrasonic wave velocity, porosity, and thermal expansion); mechanical (strength parameters, Elastic modulus) and flow behaviour (permeability) of rocks. Most of the physical, mechanical, and hydraulic behaviour of rocks and building stones are strongly dependent on the presence of microcracks. The stability of various geo-materials that are used in civil engineering structures is critically dependent on the distributions of microcracks and their evolution to different factors such as temperature, pressure, loading rate and chemical environment (Delle Piane et al., 2015; Mahanta et al., 2017b, 2017a, 2016; P. G. Ranjith et al., 2012; N Sirdesai et al., 2017; N N Sirdesai et al., 2016; Vishal et al., 2011). The thermal properties of rocks at high temperatures or after being exposed to high temperatures yield information that is valuable in different fields of science and development and in solutions to engineering problems. On the basis of the mechanism and the microstructure of rocks, microcracks can be classified into three categories: intergranular (within the single grain), transgranular (across two or more grains) and intergranular or circumgranular (along the grain boundary) (Blenkinsop, 2000). As a result of exposure to high temperatures, the stress conditions of rocks are modified due to additional thermal stress, which produces microcracks (intragranular, intergranular and transgranular) within the rock, thereby damaging the micro-structures of the rocks (Hajpal and Torok, 2004; Sun et al., 2017, 2015, Tian et al., 2017, 2016). Thermal damages, which occur as a result of elevated temperatures, are considered to be the consequences of microcracks that are generated due to internal stresses. These stresses occur because of the mismatch between the thermal expansions of the different mineral phases that are present in the rocks; the anisotropic thermal expansion within individual minerals; the thermal gradient; and the chemical alteration of the associated minerals. The degree of thermal expansion in the minerals within a rock depends upon the temperature to which the minerals are exposed (Fredrich and Wong, 1986; Somerton, 1992; Yavuz et al., 2010).

The thermal property of rocks is not only dependent on the in situ temperature and pressure but also on the mineralogical composition, the shape and size of the grain, the structure and geometry of the pore, and the shape and the density of the cracks (Sun et al., 2016a). In general, sandstone possesses a very complex pore geometry and pore-throat structure; it also contains a wide range of pore-throat sizes that range from the nanoscale to the micro-scale. In most of the cases, the fluid flow or gas flow behaviour in sandstones is governed by the microscopic pore-throat structure (Lai et al., 2017). The quantitative characterisation of the microscopic pore

structure includes the characterisation of pore geometry, size distribution, and pore connectivity. However, the complex and irregular microscopic pore-throat structure makes their characterisation quite difficult (Desbois et al., 2011). The porosity and the permeability of rocks are predominantly governed by the morphology and connectivity of pores and the characterisation of the pore structure. A quantitative evaluation of the pores structure is necessary for the successful quantification of the relationships among the porosity, storage, transport and reservoir properties (Anovitz and Cole, 2015). Similarly, the compaction of sandstone and its texture, such as the sorting, shape, and grain size determine the intergranular pore space (Ajdukiewicz and Larese, 2012). Poorly sorted sandstones result in lower intergranular pore volume, and different degrees of sorting results in furthermore variation in pore spaces (Mozley et al., 2016). Additionally, the mineralogy, especially of the clay minerals of sedimentary rocks is responsible largely for effective reservoir properties such as the porosity and permeability. Mechanical and chemical compaction, authigenic clay (pore-filling kaolinite, pore-lining and -filling chlorite, pore-lining and -bridging illite and mixed-layer illite/smectite, and swelling smectite) content and cementation are the controlling factors in the primary pore volume, whereas the grain of the framework, the dissolution of cement and fracture are the key parameters for pore volume enhancement (Bjørlykke et al., 1989; Nabawy and Géraud, 2016). Burial depth is quite significant and influential in the porosity of sedimentary rocks because of the overburden pressure and the temperature, which promotes the compaction and cementation. The porosity of sandstone has an exponential inverse relationship with the burial depth (Ehrenberg et al., 2009; Lai et al., 2017). The microscopic pore structure plays an important role in many geological processes such as the retention and migration of the hydrocarbons, gases and water during various engineering applications such as enhanced coalbed methane, enhanced oil recovery, geothermal energy extraction, and underground coal gasification (Anovitz et al., 2013). A better understanding of the microscopic structure of the pore-throat network will be helpful in accurate predictions during this engineering applications.

Since the past couple of decades, Digital Rock Physics (DRP) has generated a lot of interest as an alternative method for the determination of image-based rock properties. It has emerged as a potential and vital source of valuable rock properties due to its high-resolution insight into the complexity of pore geometry and rock structure through the application of micro-CT techniques. The basic principle of DRP is the imaging and digitising of pore spaces and grain-matrices of various rocks, which enables the implementing of various physical processes

numerically in these digital objects in order to obtain various imperative rock properties such as porosity, permeability, electrical conductivity, and elastic modulus. The analysis of the DRP includes image acquisition; image processing, which in turn includes modules such as noise reduction, smoothing and segmentation; and the setting up of numerical experiments by means of field equations and their solution (Andrä et al., 2013; Devarapalli et al., 2017). Due to the implementation of very fine 3D resolution for imaging as well as the availability of powerful software and hardware for post-processing, DRP has become quite important in the field of rock mechanics and its related fields. The image-based DRP technique has been extensively used in industries such as reservoir engineering and hydrogeology for enhanced oil recovery and flow analysis. In recent times, on the basis of micro-CT techniques, many researchers have focused their research on a wide range of rocks such as sandstone (Al-Kharusi and Blunt, 2007; Dong et al., 2008; Mohammadmoradi et al., 2017; Sharqawy, 2016), shale (Goral et al., 2015), limestone (Mohammadmoradi et al., 2017) and carbonates (Al-Kharusi and Blunt, 2007; Dong et al., 2008; Rabbani et al., 2017). In addition, many of DRP studies that involve the 3D simulation of micro-CT images for the estimation of various rock properties such as porosity, permeability and elastic moduli of rocks have been carried out (Andrä et al., 2013; Arns et al., 2004, 2002; Devarapalli et al., 2017; Fusseis et al., 2014; Madonna et al., 2012). The advantages that are associated with DRP analysis are its ability to afford much deeper insight into the microstructure of the rocks, by which it complements laboratory experimental results; additionally, it provides a platform for multiple studies with the same set of images. On the contrary, in some instances, experimental results are found to be different from the results of DRP simulation, turning it into one of the major disadvantages that are associated with this type of study. However, these discrepancies are attributed to the complex pore geometries and the rock structure. During DRP simulations sometimes, the pores are not captured because of their smaller size in comparison to the size of the voxel, which provides mismatched information when compared to experimentally observed data (Devarapalli et al., 2017).

The thermal behaviour of rocks is mostly controlled by two sets of parameters: external parameters such as fluid saturation, pressure and temperatures; and internal parameters such as the mineralogical composition, pore volume and pore structure of the rock (McKenna et al., 1996; Nabawy and Géraud, 2016). Sandstone is composed of diverse minerals that have different coefficients of thermal expansions and other thermal properties. Upon heating, these minerals undergo inhomogeneous thermal expansion and thermal reaction and, sometimes, phase transition, thereby generating internal stress and microcracks (Sun et al., 2016a). Porosity

pore volume and pore structure) is a digenetic property of sedimentary rocks, due to which it (controls different physical properties (Jones and Meredith, 1998; Nabawy and Géraud, 2016). Since sandstone is a reservoir rock, its high-temperature behaviour is quite crucial in the appropriate optimisation of engineering activities. Researchers such as Gautam et al. (2015), Kompaníková et al. (2014), Kong et al. (2016), Tian et al. (2012) have focused on the aspects of the modification of the microstructure, the mechanical properties and the physico-morphological properties of sandstones as a function of temperatures.

There is still a gap in the knowledge of the evolution of microscopic pore structures in rocks that are exposed to high temperatures. A detailed microscopic investigation of the structural changes of the sandstone and its characterisation has not yet been carried out. In order to close the gap in knowledge, a micro-nano-scale investigation of the structural change of three different types of sandstone has been made with the support of micro-CT techniques in this paper. The in-depth investigation includes the observation of microstructural responses, pore space evolution and pore-network models as a function of temperatures. As discussed earlier, burial depth, pore geometry and size distribution, pore connectivity, sorting, grain size and mineralogical composition directly control the behaviour (physical, mechanical and hydrological) of rocks. Hence, for this study, three sandstones from two different stratigraphic formations with diverse mineralogical compositions were chosen to investigate the effect of temperature on their pore structure.

8.1.3 Specimen preparation and methodology

8.1.3.1 Specimen preparation

The experimental investigations, which are associated with temperatures, are largely influenced by the heating rate, cooling rate and the constant time of interval. In general, fast heating or cooling processes induce additional thermal stress, which creates additional thermal damage in the rock structure (Tian et al., 2016). Cylindrical samples were placed in a furnace with the required temperature and a heating rate of 5 °C/min. Previous experimental observations suggest that, at a particular required temperature, the sample should be kept for at least 20 minutes for equilibrium in heating all around the sample (Tian et al., 2016). Once the required temperature was achieved, the temperatures were maintained for three hrs for equilibrium in heating throughout the sample. After the process of the thermal treatment, the samples were allowed to cool (air-cooled) to room temperature. The current investigation involves analysis of samples at room temperature (25 °C) and thermally treated at 200 °C, 400 °C, 600 °C, and 800 °C.

8.1.3.2 Methodology

The methodology includes the investigation of various structural and morphological changes in three different types of sandstones as a function of elevated temperatures by using the micro-CT technique. A micro-CT image of a rock is a set of arrays of three-dimensional cubic atoms that are known as voxels, of which each voxel is assigned a non-zero value in case of pore space and zero for the matrix. The micro-CT image is an integration of factors such as absorption, reflection, attenuation and diffraction patterns of electromagnetic waves (Silin and Patzek, 2006). The study of DRP involves three steps: digital imaging or image acquisition (high-resolution micro-CT scan); image processing, which involves smoothing and denoising, sharpening and segmentation; and computational simulation of rock properties (Andrä et al., 2013; Dvorkin et al., 2011).

8.1.3.3 Image acquisition

The micro-CT instrument that is used in the current study is Xradia Versa 520 (manufactured by Zeiss), which is capable of proving a true spatial resolution of 0.7 µm with a minimum achievable voxel size of 70 nm. The rotating stage on which the specimen is placed is positioned along a guide rail that can be rotated with a high precision in the order of milli-degrees (Devarapalli et al., 2017; Zeiss ^{TM}, 2013). The imaging process consists of the targeting of multi-directional X-rays at an object/specimen, followed by the measuring of the decrease in its intensity along a series of linear paths, which is characterised by Beer's Law.; The law describes the reduction in the intensity as a function of path length, X-ray energy and the material's linear attenuation coefficient, which, in turn, is a function of X-ray energy, density and composition of the material.

Table 8.1 *Parameters used for micro-CT scanning*

Parameters used for the micro-CT scanning	**Specifications**
Imaging Mode	Tomography
Camera Binning	2
Sample size	1 mm x 1 mm x 1 mm
Source Filter	Air
Voxel size	0.7 µm
Source-RS Distance	-10 mm
Det-RA Distance	9 mm
Optical Magnification	20X

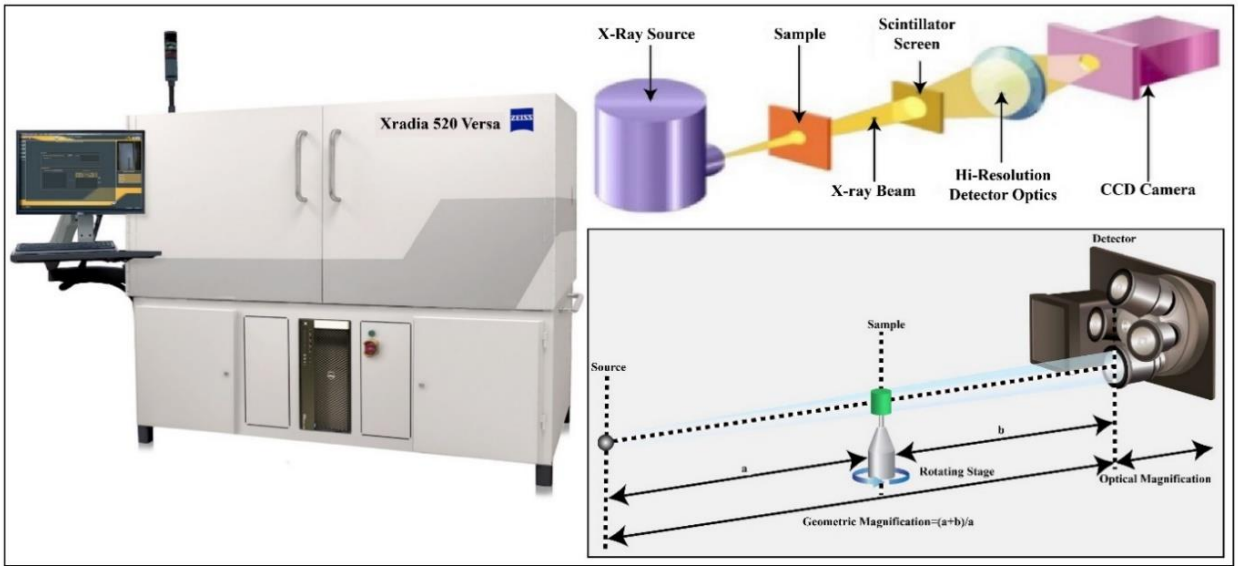

Figure 8.1 *The Xradia Versa 520 instrument used for image acquisition, and its principle (modified after Zeiss TM 2013)*

After passing through the sample, these X-ray images are imaged on a scintillator in which they are converted to visible light; thus, the images are magnified by an optical objective before reaching the detector. After X-ray scanning, the exposure of the X-ray attenuation distribution in the volume to X-rays is reconstructed in the form of grey levels by applying certain specialised algorithms. These grey levels in every slice of the image corresponding to the X-ray attenuations. These X-ray attenuations replicate the amount of X-rays being scattered or absorbed by the voxel as the X-rays pass through the material. The detailed mechanism of the working principle of the imaging procedure by using micro-CT techniques is represented in **Figure 8.1**, and further details can be found in Zeiss ™ (2013). **Table 8.1** represents the scanning parameters that are used to obtain the micro-CT images.

8.1.3.4 Image Processing

After image acquisition, the images are processed by using several algorithms in order to derive various kinds of information from the image set. In the current study, the micro-CT images were analysed using AVIZO 9.0 software, which was developed by FEI Visualization Sciences Group. The image processing comprises steps such as smoothing and denoising, sharping, and segmentation. During the stages of image processing, such as smoothing, denoising and sharpening, various filters are applied to the micro-CT image, which improves the visualisation of the image by emphasising its particular features (Buades et al., 2005).

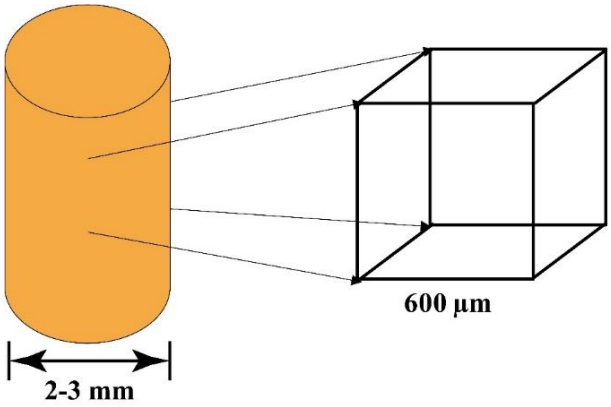

Figure 8.2 *Schematic diagram of the volume used in the current study*

Before image processing, of the acquired 3D constructed volume, a cubical volume of 600 X 600 X 600 μm^3 was chosen (**Figure 8.2**). This selection was done in order to remove the edge artefacts that appear in the corner of the image and to ensure that the computational process was better. **Figure 8.3** represents the schematic diagram of the workflow that was used for the analysis.

8.1.3.4.1 Smoothening and denoising

This process comprises the processing of the acquired CT images through certain filters that are used to denoise scalar volume data. In the current study, the anisotropic diffusing filter was used for smoothing and denoising. The advantage of this filter over other filters is its ability to preserve strong edges and to enhance the contrast of the edges. The algorithm that was used for this compares the value of the current voxel with the value of its adjacent neighbouring six voxels. If the difference in the voxel values does not surpass the diffusion stop criterion, then there is diffusion (Bernard et al., 2011).

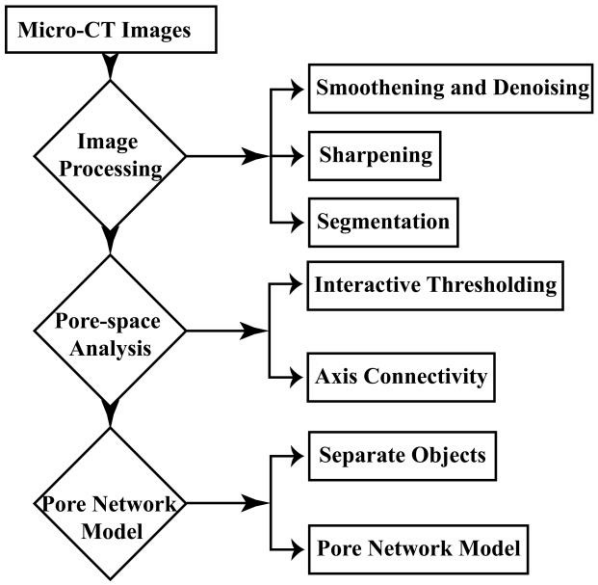

Figure 8.3 *Schematic diagram illustrating the workflow used for the analysis*

8.1.3.4.2 Sharpening

This module results in the sharpening of the edges of the elements without further increase in the noise. During this module, in the first place, a Gaussian filter is first applied to a copy of the original image, which is followed by its blending with the original image. Due to this, a mask is used to sharpen the desired regions. In the current study, for sharpening, the unsharp masking filter was used.

8.1.3.4.3 Segmentation

Segmentation is a prerequisite and crucial stage in the generation of the various surface models and accurate quantification of various volume measurements. Improper segmentation leads to the misinterpretation of pore space and mineral phases, thereby introducing error into the measured rock properties. During the segmentation stage, a label is assigned to each pixel of the image, which is stored in a separate data object termed as a Label Field describing to which it belongs to such as pores, or grain-matrix. Segmentation module refers to the delineation and labelling of pores and the mineral phases that are present in the 3D reconstructed volume after image acquisition. Due to the large volume data set, manual segmentation is not quite feasible; therefore, various algorithms are required for the process to perform automatically. The various common 3D segmentation tools that are used for the segmentation are spatial filtering, denoising and the removal of artefacts and thresholding, followed by the morphological operations and cluster analysis (Andrä et al., 2013).

In general, during segmentation, it is quite difficult to label the interface areas correctly by thresholding; hence, to avoid such issues, a three-stage process is implemented for better and accurate results. The first stage involves the computation of the gradient magnitude of the image, which identifies all the boundaries by means of thresholding. As a result of the first stage, these boundary voxels are not further considered for the segmentation process. During the second stage, the pore space (dark pixels) and the minerals (bright pixels) were thresholded. However, in our study, no classification of different minerals has been attempted. The pixels near the boundary were excluded during the second stage; however, they are captured in the third stage by means of the watershed expansion technique. The two selections, after the second stage, are then used as markers for a watershed algorithm, and the gradient magnitude image was used as the landscape input to the algorithm (Andrä et al., 2013; Beucher and Meyer, 1993).

An accurate segmentation depends on the selection of the filtering parameter, segmentation algorithms and the greyscale threshold (Andrä et al., 2013). However, the accuracy of the

computation of various rock properties from these digital data sets depends on the resolution of the image.

8.1.3.5 Computationally simulated rock properties

This section involves the extraction of pore-data and the modelling of the pore network from the segmented volume of the pore spaces within the rock.

8.1.3.5.1 Pore-data extraction

This section involves the extraction of different types of pore spaces with the 3D constructed volume of the rock. Information related to parameters such as the total pore volume, connected pore volume and non-connected pore volume were collected in this module.

8.1.3.5.1.1 Interactive Thresholding

The interactive thresholding module allows thresholds to be selected interactively for a particular label of the specimens, such as the pore spaces or the grain-matrix or minerals. Out of the 3D-constructed rock volume, different labels such as pore spaces and matrix volume are separated by using this module.

8.1.3.5.1.2 Axis Connectivity

Axis connectivity is the module that is applied to the total pore-volume label field to acquire the connected pore volume in a certain direction. The axis connectivity module, which contains a set of two planes and an image, results in an image that possesses all the paths that connect the two planes.

8.1.3.5.2 Pore-network modelling

In the pore-network modelling (PNM) view, the branching or the endpoints of the network are considered pores and the connecting lines of these pores are considered throats. The pore-network modelling section represents the pore and throat configurations of the studied 3D volume.

8.1.3.5.2.1 Separate objects

This module is a high-level combination of the watershed, distance transform, and numerical reconstruction algorithms, in which all the adjacent pores are represented by a separate colour. This module is a prerequisite for the generation of the pore-network model.

8.1.3.5.2.2 Pore-network model generation

In recent times, with the advantages afforded by modern technology and computational facilities, precise PNM enables a fundamental understanding of multiphase flow behaviour and

fluid transport properties in porous media such as rocks (Silin and Patzek, 2006). A detailed review of the PNM of porous media are presented in Blunt (2001) and Xiong et al. (2016).

Since the last decade, various attempts at the extraction of pore networks from 3D images have been made, out of which the algorithms of the medial axis-based method and the maximum ball method are important. The details of the working principle and algorithms of these methods can be found in Al-Kharusi and Blunt (2007), Baldwin et al. (1996), Dong and Blunt (2009), Lindquist et al. (1996) and Silin and Patzek (2006). The earlier investigation of PNM was based on the concepts of the skeleton and the medial axis and have played a pivotal role in subsequent investigations (Silin and Patzek, 2006). However, most of the skeletonisation algorithms are based on thinning methods that remove redundant elements in the image and preserve the topological properties of the pore space (Lindquist and Venkatarangan, 2000, 1999; Silin and Patzek, 2006). Previous studies that are based on the thinning algorithms of micro-CT images suggest a refinement of the resolution, which can cause results that are low in accuracy (Silin and Patzek, 2006). To avoid issues associated with the PNM, the concept of the maximal ball was developed. The maximum ball algorithm accounts for the largest of the inscribed spheres that are centred on each voxel of the image that touches either the grain or the boundary. The other included spheres are considered inclusions and are removed. After the removal of the inclusions, the remaining spheres are referred to as the maximal balls, which describe the pore space without redundancy. The larger balls are identified to be pores and the smallest balls between the pores are considered to be throats (Al-Kharusi and Blunt, 2007; Dong and Blunt, 2009; Silin and Patzek, 2006). The maximal ball algorithm accounts for the biggest of the inscribed spheres at each voxel in the pore space. In the current investigation, the maximal ball algorithm was implemented for the extraction of the pore-network model.

8.1.4 Results and discussion

The results and discussion section is divided into three for ease of explanation of the processes that are a result of thermal treatment. The sections are microstructural modifications, the evolution of pore spaces and PNM as a function of elevated temperatures. The microstructural analysis represents the structural variations or the morphological changes that are induced in sandstone as a result of being exposed to high temperatures. The section on pore-space evolution demonstrates the variations in pore spaces, namely, total, connected, and non-connected pores in sandstones at different temperatures. The concluding portion of results and discussion highlights the PNM of these sandstones at different temperatures.

8.1.4.1 Microstructural modification as a function of temperatures

The mechanical strength and the flow behaviour of rocks are strongly influenced by the presence of cracks. Progressive increase of temperature either induces new microcracks into the structure of the rocks or enlarges the pre-existing microcracks. The distribution of crack damage in rocks may be isotropic or anisotropic, which is predominantly dependent on the structure and the mineralogy of the rocks.

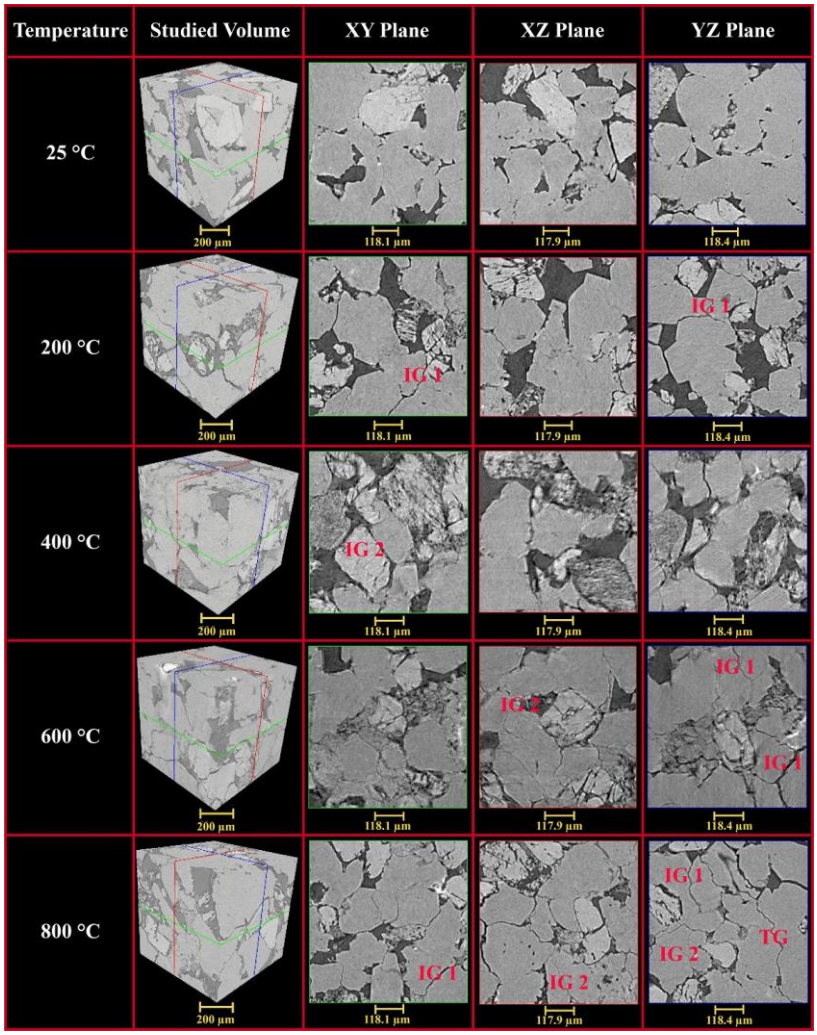

Figure 8.4 *A comparison of microstructural modification in Dholpur sandstone at an ambient condition (25 °C) and after being exposed to elevated temperatures (200 °C, 400 °C, 600 °C and 800 °C)*

In response to elevated temperatures, minerals have different rates of thermal expansion along the crystallographic axes (refer **Table 4.1**), which results in the dissimilarity of thermal stress in different crystallographic axes and induces new microcracks. Rocks that have quartz, feldspar, mica and certain clay minerals as the major minerals tend to display a remarkable

change in response to high temperatures (Mahanta et al., 2016; Siegesmund et al., 2008; Tian et al., 2012).

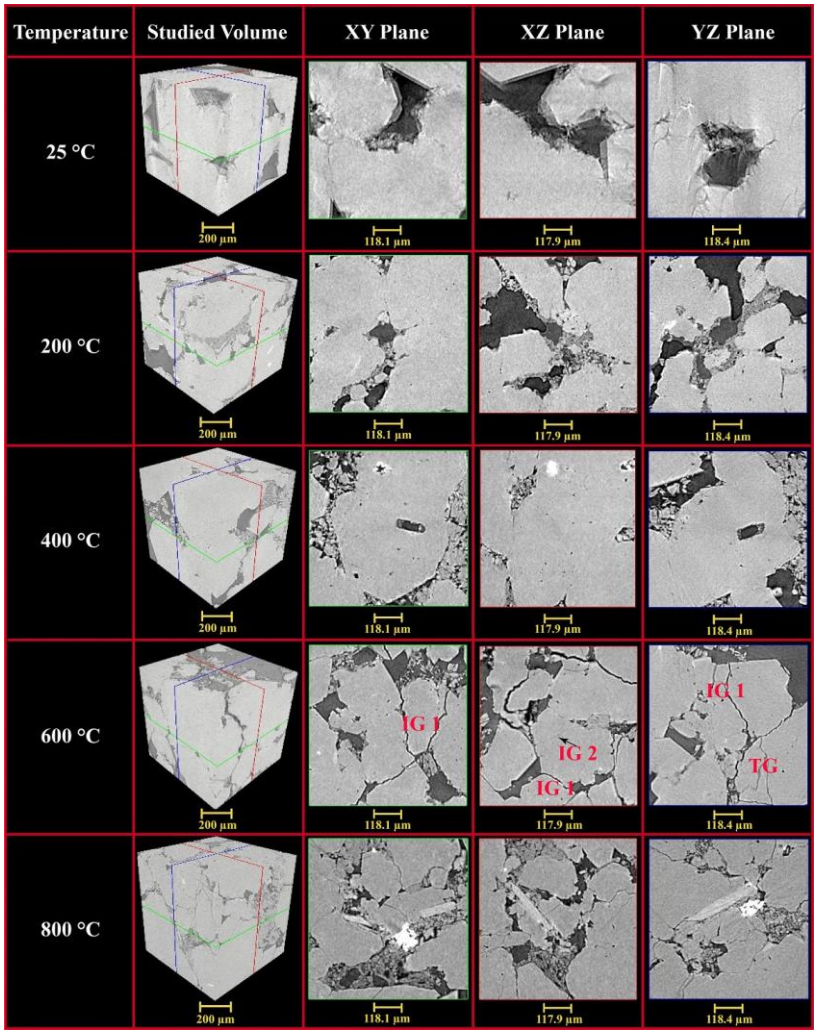

Figure 8.5 *A comparison of microstructural modification in Jodhpur sandstone at an ambient condition (25 °C) and after being exposed to elevated temperatures (200 °C, 400 °C, 600 °C and 800 °C)*

As a result of elevated temperature, minerals undergo differential thermal expansion. Quartz experiences the maximum amount of expansion that is perpendicular to its crystallographic c-axis, and minimum along the c-axis. Additionally, the percentage of expansion increases with the increase in temperatures. Similarly, calcite experiences expansion that is perpendicular to its crystallographic c-axis. However, at the same time, it experiences contraction along the c-axis (**Table 4.2)**. With the progressive increase in temperatures, differential expansion of the constituent minerals leads to the formation of different types of microcracks, such as intergranular (IG-1), intragranular (IG-2), and transgranular (TG-I) cracks, which are induced in the rocks on the basis of their mineral assemblages.

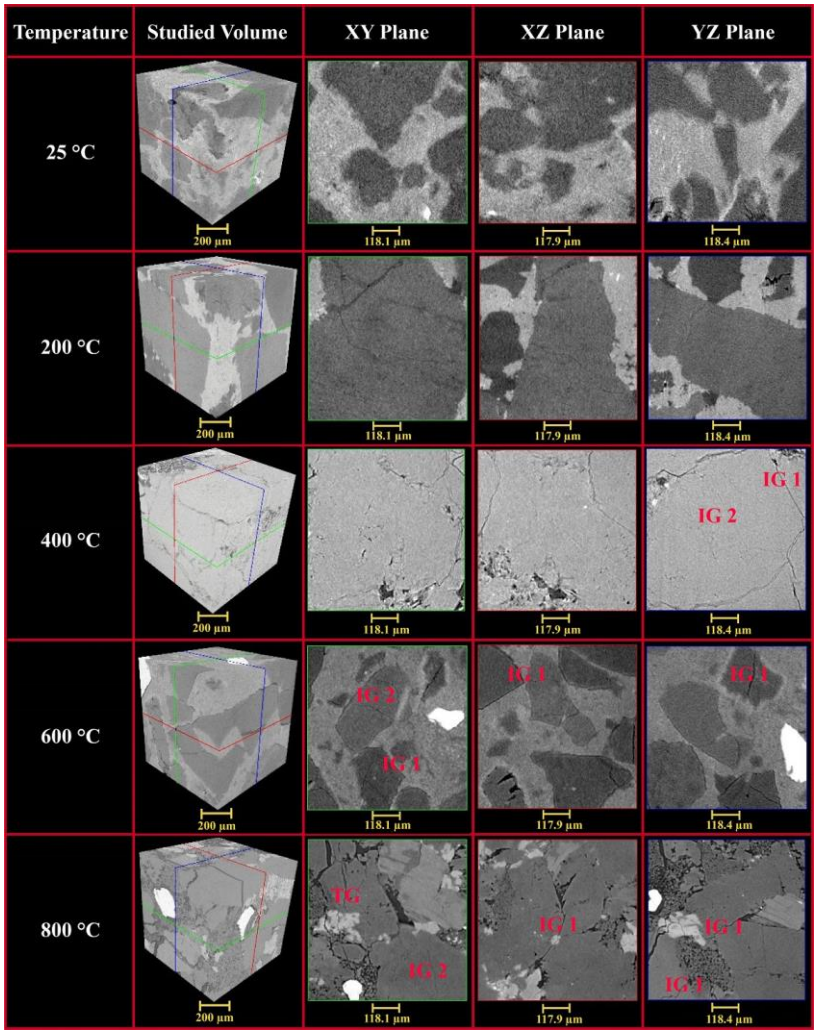

Figure 8.6 *A comparison of microstructural modification in Gondwana sandstone at an ambient condition (25 °C) and after being exposed to elevated temperatures (200 °C, 400 °C, 600 °C and 800 °C)*

Figure 8.4, **Figure 8.5**, and **Figure 8.6** represent the greyscale micro-CT images of Dholpur sandstone, Jodhpur sandstone and Gondwana sandstone, respectively. When the greyscale micro-CT images of the three sandstones at an ambient condition are compared with the cases of elevated temperatures, the appearance of new microcracks can be observed at the elevated temperatures. Except for Jodhpur sandstones, the other two types of sandstones have the highest density of microcracks at 800 °C when compared to other temperature conditions. In both the sandstones, with a progressive increase in temperature, a higher number of widened cracks can be observed as a result of the thermal stress of the exposed temperatures. However, in the case of Jodhpur sandstone, the highest density of microcracks is observed at 600 °C rather than at 800 °C. This is possibly due to the formation of new cementing material in the

form of Portlandite, which results in microcracks that have low density in the case of 800 °C (explained in the following section).

8.1.4.2 Evolution of pore spaces as a function of temperatures

The physico-morphological changes that appear within the structure of rocks are either due to the induced microcracks or as a result of the chemical alteration of constituent minerals such as the decomposition, dehydroxylation, volatilisation, and oxidation of minerals within the rock, which induces additional pore spaces into the structure of the rock.

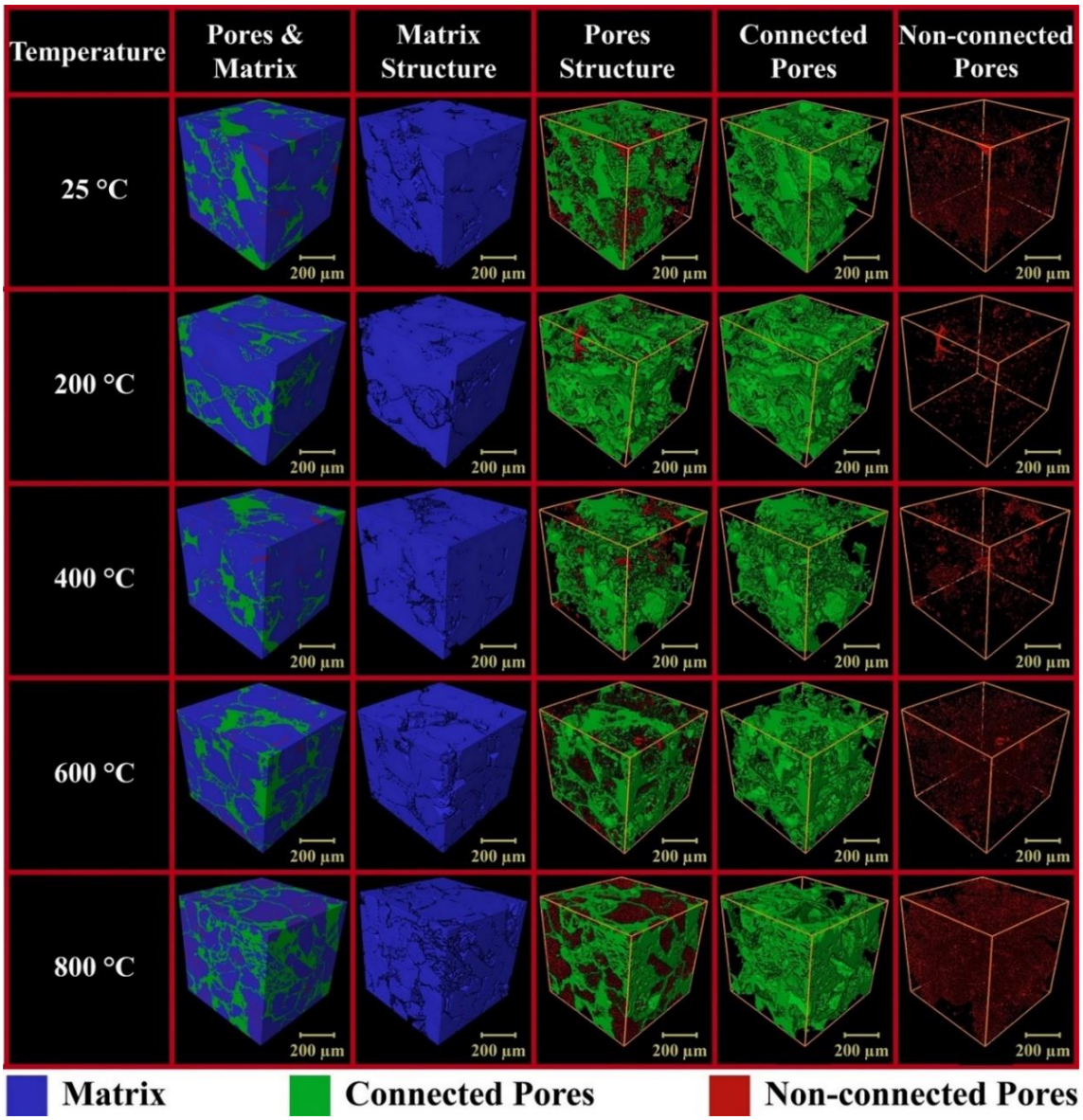

Figure 8.7 *A comparison of pore-space evolution in Dholpur sandstone at room temperature (25 °C) and after the thermal treatment (200 °C, 400 °C, 600 °C and 800 °C)*

In the first phase (from 25 °C–200 °C), the free**,** adhered and combined water that is present in the sandstone are lost and the mineral grains in sandstone undergo expansion, which causes a reduction in the porosity. Between 200 °C and 400 °C, the crystal water and the structural water

are removed, causing a slight increase in the porosity of the sandstone (Sun et al., 2016a). Below 400 °C, the change in porosity is marginal. Between 400 °C and 600 °C, an increment in porosity can be marked due to various thermal reactions in sandstone (Sun et al., 2016a). The porosity changes drastically because most of the mineral grains are micro-cracked at approximately 600 °C, which can be explained in terms of thermal expansion and the altered microcracks network driven by the structural damage (Sun et al., 2016a; Tian et al., 2012).

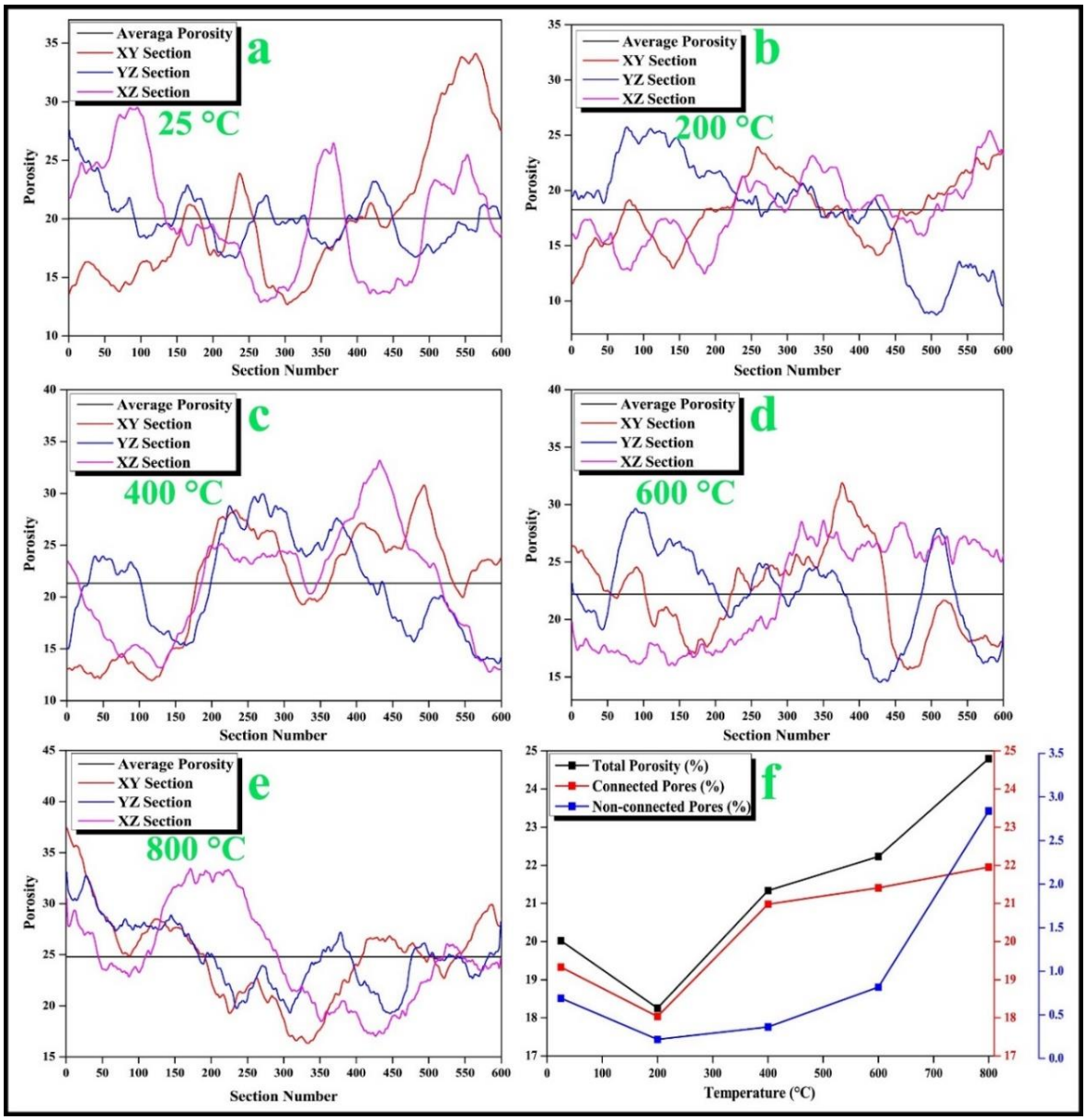

Figure 8.8 *Average porosity and porosity profiles of the three coordinate directions for Dholpur sandstone. Plate a, plate b, plate c, plate d and plate e represent 25 °C, 200 °C, 400 °C, 600 °C and 800 °C, respectively. Plate f represents the comparison of the total porosity, connected pore spaces, and non-connected pore spaces of Dholpur sandstone at different temperatures*

Figure 8.7, **Figure 8.10**, and **Figure 8.12** represent the progressive evolution of pore spaces in response to increasing temperatures in Dholpur sandstone, Jodhpur sandstone, and Gondwana sandstone, respectively.

Figure 8.8, **Figure 8.11**, and **Figure 8.13** represent the porosity profiles and the average measured porosity (total porosity, connected porosity and non-connected porosity) in three sandstones as a function of temperatures. Plates a, b, c, d and e represent the porosity profile in three coordinate directions (XY, YZ, XZ) and the average porosity at 25 °C, 200 °C, 400 °C, 600 °C and 800 °C, respectively. However, plate f, in each figure, represents the comparison of total porosity, connected porosity and non-connected porosity of the respective sandstone at different temperatures. At an ambient condition, Dholpur sandstone, Jodhpur sandstone and Gondwana sandstone have a porosity value of 20 per cent, 14.37 per cent, and 13.99 per cent, respectively. For all the three sandstones, up to 200 °C, the porosity either decreases or remains almost the same in comparison to the ambient condition. With the increase in temperature from the ambient condition to 200 °C, a reduction of eight per cent and one per cent in the porosity of Dholpur sandstone and Gondwana sandstone, respectively, was observed, whereas, a three per cent increment in the porosity of Jodhpur sandstone was observed in the same temperature range.

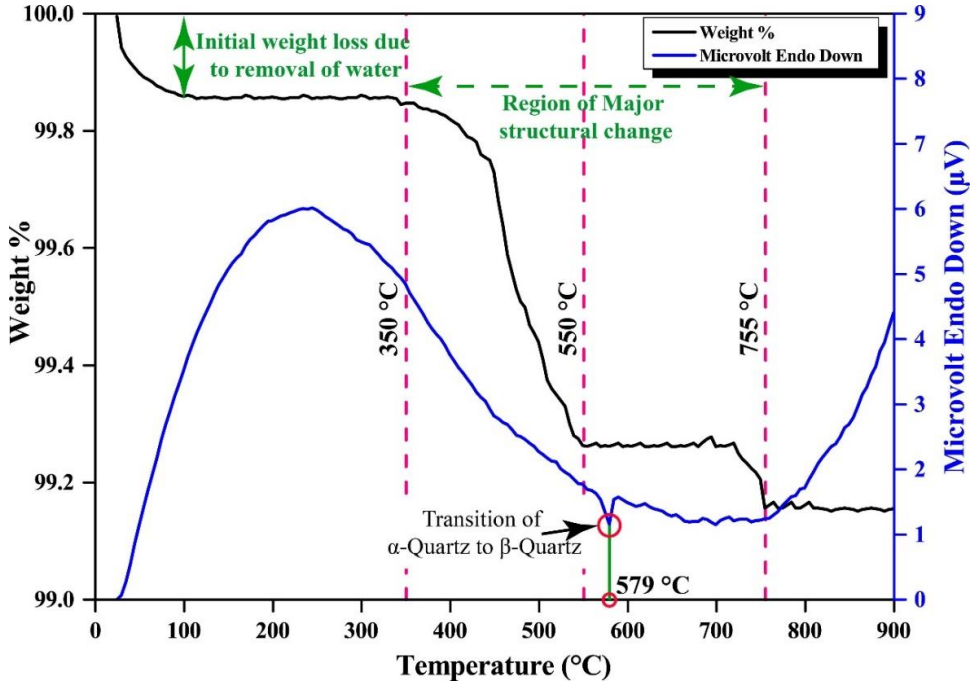

Figure 8.9 *TG-DTA curve for Dholpur sandstone*

Figure 8.9 represents the TG-DTA curve for Dholpur sandstone. The TG curve represents an initial weight loss below 350 °C, which can be due to the removal of adhered water, crystal

water and structural water, as explained by Sun et al. (2016). From the TG-DTA curve, it can be interpreted that a majority of the structural changes take place in the range of 350 °C to 755 °C, which can be explained in terms of the thermal cracking of the minerals that are present in the rock, and the α-β quartz inversion, which can be observed at 579 °C for Dholpur sandstone.

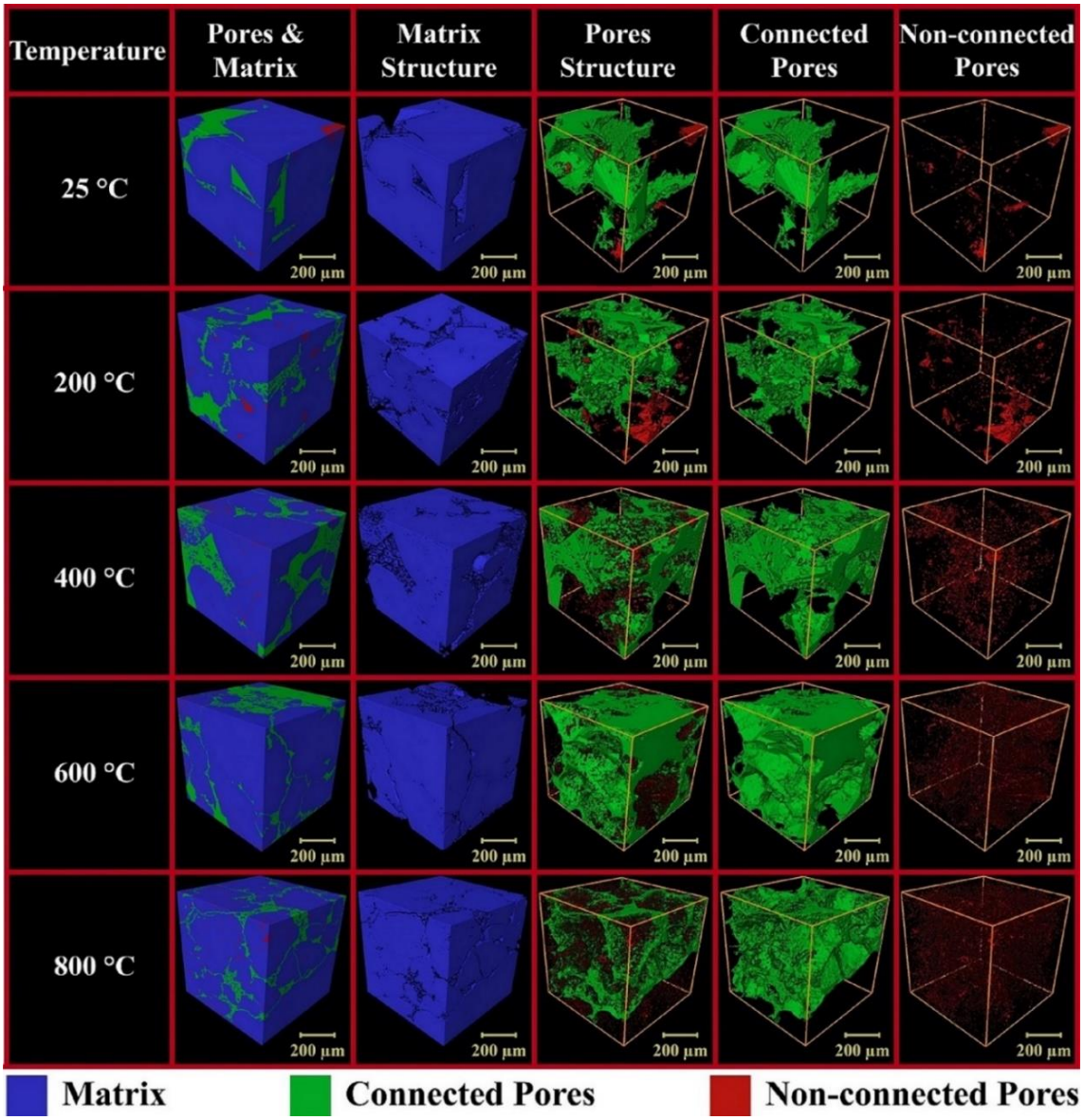

Figure 8.10 *A comparison of pore-space evolution in Jodhpur sandstone at room temperature (25 °C) and after the thermal treatment (200 °C, 400 °C, 600 °C and 800 °C)*

In the range of 400 °C to 600 °C, most of the physical and chemical features of sandstone change (Sun et al., 2016a). At 573 °C, quartz undergoes a phase transition from α-quartz to β-quartz. Although some of the reaction in this phase transition (such as the α-β quartz inversion) are reversible and the heat absorbed is returned to the system upon heating, many of the major

reactions are irreversible (Somerton, 1992; Somerton and Boozer, 1960; Sun et al., 2016a). In this temperature range (500 °C and 600 °C), this phase transition is marked by a two per cent increment in the volume, which is due to the difference in the densities of α-quartz and β (Schacht, 2004; N Sirdesai et al., 2017). In the range of 500 °C to 600 °C, minerals such as kaolinite, ankerite, illite, dolomite, siderite, magnetite, pyrrhotite and pyrite undergo various chemical alterations such as decomposition, Dehydroxylation, volatilisation and oxidation (Just and Kontny, 2012; Sun et al., 2016a, 2015).

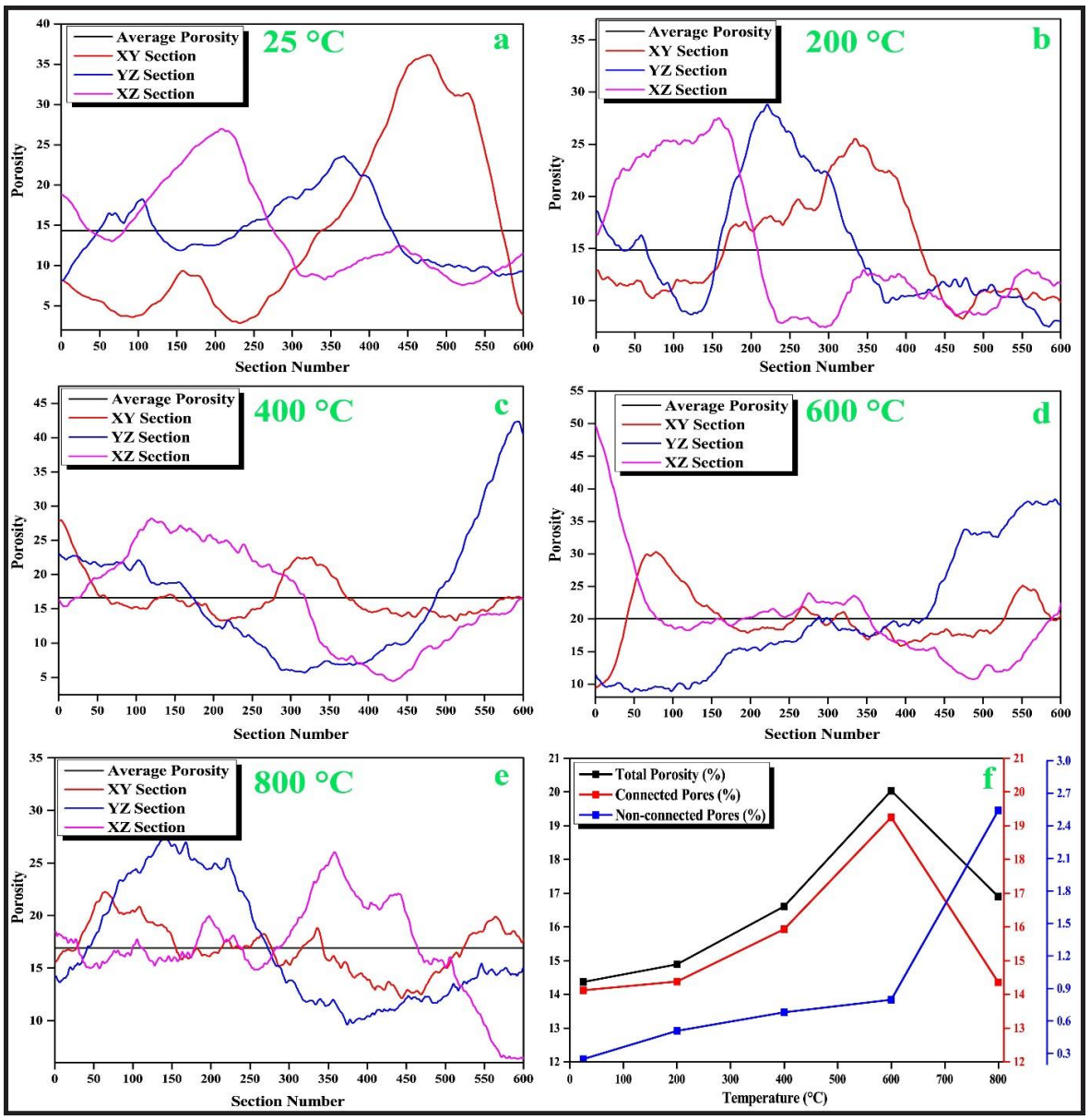

Figure 8.11 *Average porosity and porosity profile of the three coordinate directions for Jodhpur sandstone. Plate a, plate b, plate c, plate d and plate e represent 25 °C, 200 °C, 400 °C, 600 °C and 800 °C, respectively. Plate f represents the comparison of total porosity, connected pore spaces, and non-connected pore spaces of Jodhpur sandstone at different temperatures*

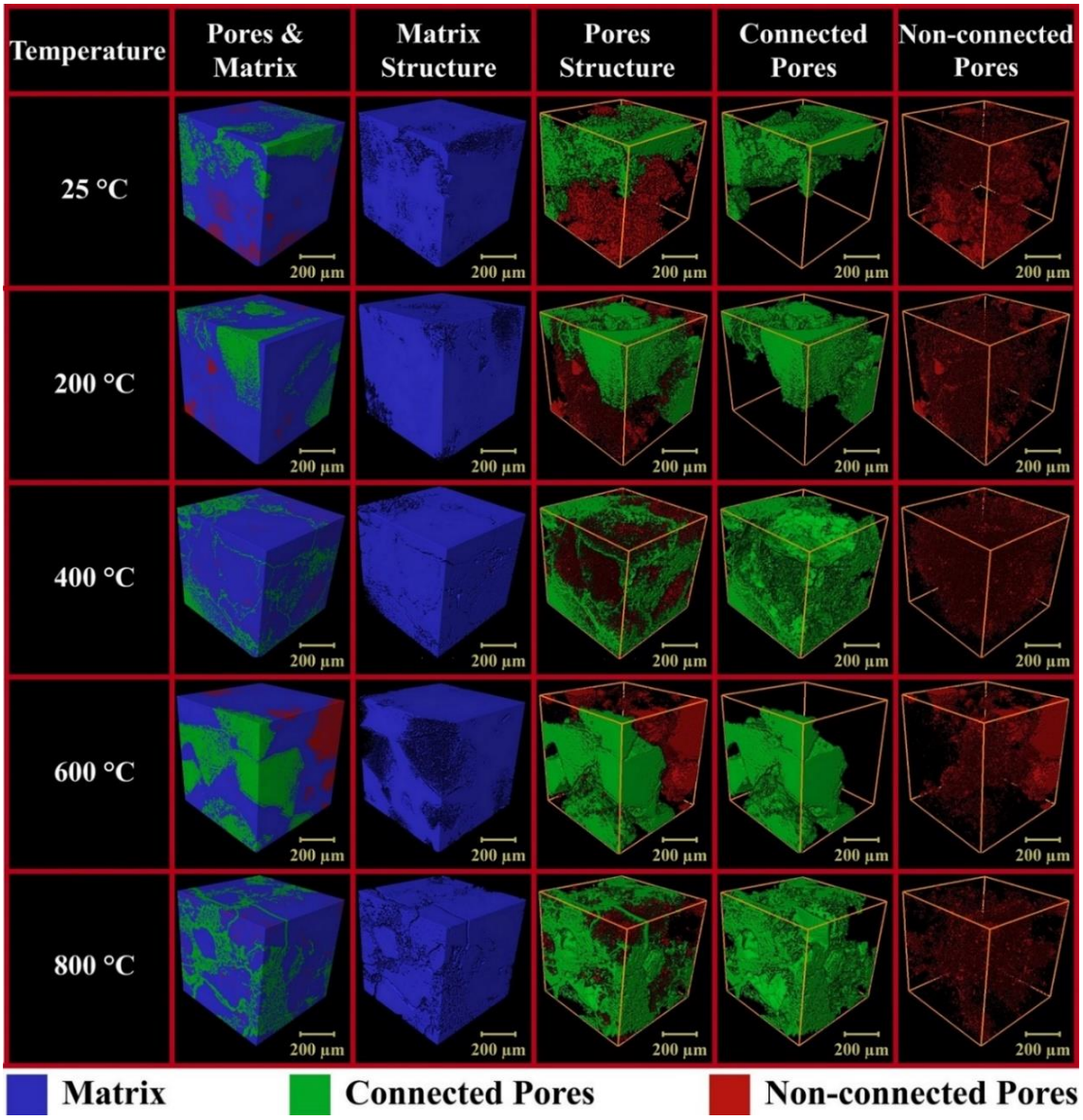

Figure 8.12 *A comparison of pore-space evolution in Gondwana sandstone at room temperature (25 °C) and after thermal treatment (200 °C, 400 °C, 600 °C and 800 °C)*

With further increase in temperature, the porosity of all the three-sandstones increases further. 24.79 per cent of porosity was measured for Dholpur sandstone at 800 °C with an increment of 23 per cent when compared to the ambient condition. Similarly, in Gondwana sandstone, the maximum porosity was observed at 600 °C, achieving a value of 23.47 per cent with an increment of 71 per cent when compared to the room-temperature condition. However, Jodhpur sandstone did not possess the same trend of pore-space evolution with an increase in temperature. For Jodhpur sandstone, the maximum porosity was observed at 600 °C with a value of 20 per cent; thereby, a reduction of 35 per cent of porosity was observed up to 800 °C. The complete evolution of pore spaces in these sandstones as a function of temperature has been summarised in **Table 8.2**.

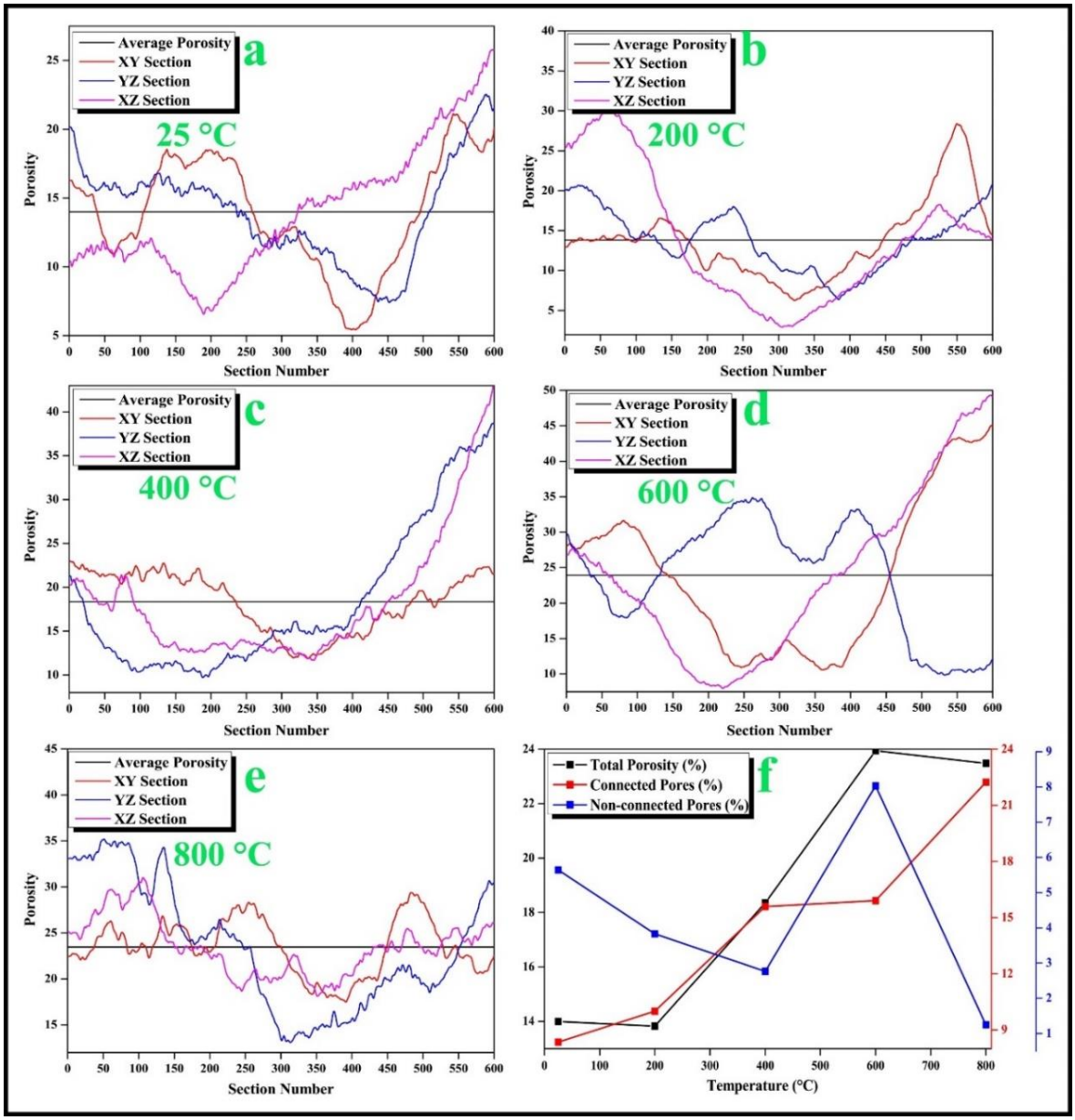

Figure 8.13 *Average porosity and porosity profiles of the three coordinate directions for Gondwana sandstone. Plate a, plate b, plate c, plate d and plate e represent 25 °C, 200 °C, 400 °C, 600 °C and 800 °C, respectively. Plate f represents the comparison of total porosity, connected pore spaces, and non-connected pore spaces of Gondwana sandstone at different temperatures*

Table 8.2 *Summary of pore spaces and their evolution with the elevated temperatures for the three sandstones*

Temperature	**Total Porosity**			**% of increment compared to the ambient condition**		
°C	Dholpur Sandstone	Jodhpur sandstone	Gondwana sandstone	Dholpur Sandstone	Jodhpur sandstone	Gondwana sandstone
25	20.02	14.37	13.99	-	-	-

200	18.25	14.88	13.82	-8.8	3.61	-1.19
400	21.33	16.61	18.35	6.58	15.59	31.16
600	22.22	20.03	23.94	11.02	39.44	71.09
800	24.79	16.89	23.47	23.84	17.58	67.79

The possible cause for the reduction in porosity in the case of Jodhpur sandstone may be the formation of a new cementing material, portlandite ($Ca(OH)_2$) (Hajpal and Torok, 2004), which may be a by-product of the dehydroxylation of dickite ($Al_2Si_2O_5(OH)_4$) at 680 °C and decomposition of calcite ($Ca(CO)_3$) at approximately 700 °C. In this study, no experimental observation has been documented to support the assumption that the new cementing material is Portlandite. However, the formation of a new cementing material is supported by the TG/DTA analysis, which demonstrates a segment of weight gain in the TG curve after 680 °C, soon after the dehydroxylation of dickite (**Figure 4.12**). The TG/DTA analysis of Jodhpur sandstone suggest a temperature range of 400 °C–680 °C in which the TG curve experiences a drastic loss of weight. This is the temperature window at which the majority of the structural variations are observed in Jodhpur sandstone. This is possibly due to the decomposition and dehydroxylation of the clay minerals (dickite and kaolinite) and the inversion of α-quartz to β-quartz at 573 °C (**Figure 4.12** and **Table 4.2**). In this range, the porosity of Jodhpur sandstone increased from 16.61 per cent at 400 °C to 20.03 per cent at 600 °C. Similarly, for Gondwana sandstone, a region of major structural change is observed from 370 °C to 670 °C, which suggests a drastic weight loss in that region (**Figure 8.15**). This may be due to the decomposition of clay minerals such as siderite, illite and kaolinite, which are present in the rock (**Table 4.2**)(Somerton, 1992). Between 400 °C and 600 °C, the porosity of Gondwana sandstone increases from 18.35 per cent to 23.94 per cent.

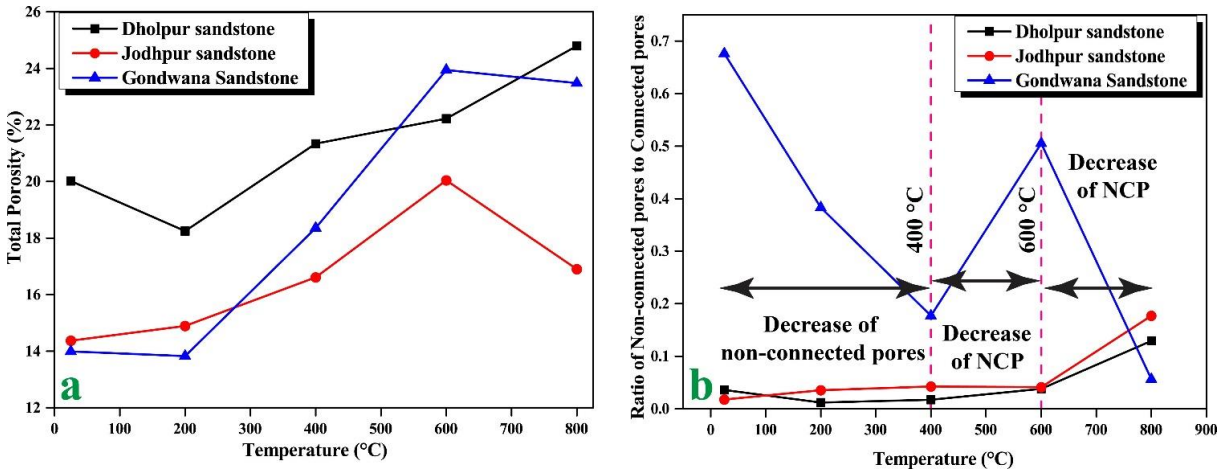

Figure 8.14 *A comparison of porosity (a) and the ratio of non-connected pores to connected pores (b) in three sandstones after thermal treatment*

Finally, a comparison between the evolution of the pore space and the ratio of non-connected pores to connected pores of the three sandstones has been made (**Figure 8.14** and **Table 8.2**). Among the three rocks, Dholpur sandstone is the most porous in comparison to the other two types of sandstones. The evolution of total porosity has been explained in the earlier section. With progressive heating, the porosity of Dholpur sandstone and Gondwana sandstone follows an overall increasing trend, whereas, Jodhpur sandstone has maximum porosity at 600 °C and follows a decreasing trend up to 800 °C. The presence of a larger amount of clay minerals controls most of the thermal behaviour of Gondwana sandstone.

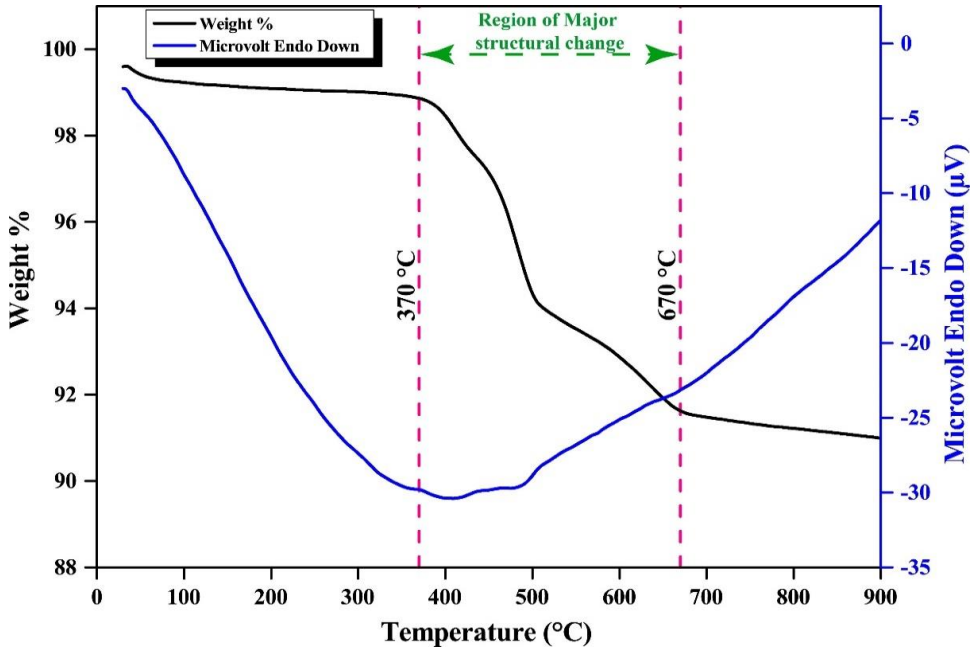

Figure 8.15 *TG-DTA curve for Gondwana sandstone*

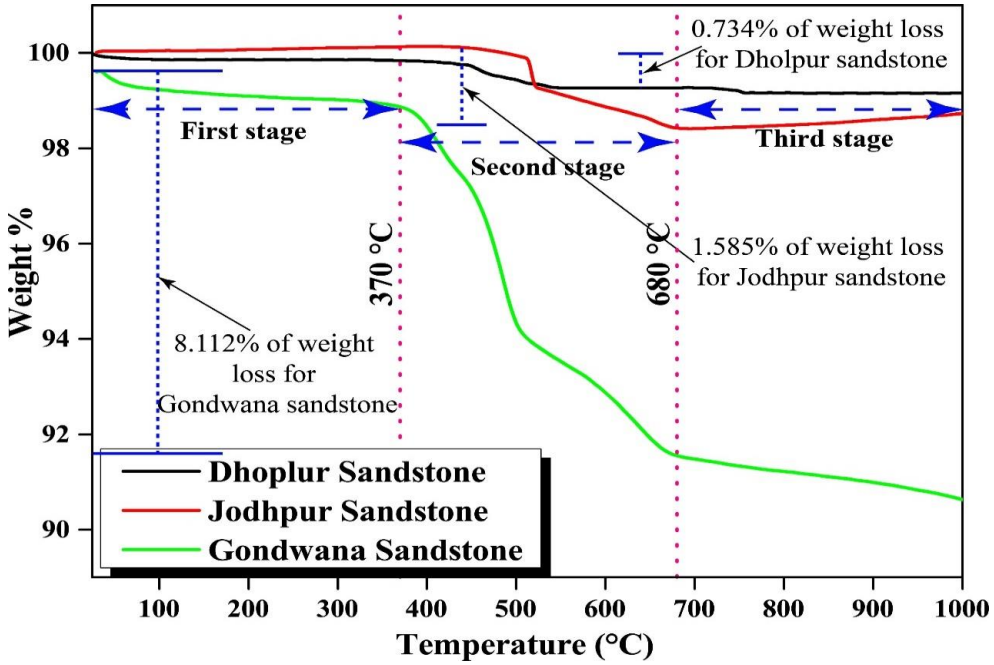

Figure 8.16 *A comparison of the Thermogravimetric analyses of the three sandstones*

As discussed earlier, Gondwana sandstone is the most clay-rich sandstone among the three studied sandstones, containing nearly 30 per cent of clay minerals (**Table 3.4**). In general, clay, pores are non-connected. As Dholpur and Jodhpur sandstones contain a lower amount of clay minerals, the ratio of non-connected pores to connected pores is quite low when compared to Gondwana sandstone.

At room temperature, out of the total porosity, Gondwana sandstone contains nearly 40 per cent of non-connected pores. With a gradual increase in temperature from room temperature to 400 °C, the non-connected pore volume decreases and reaches nearly 15 per cent of the total porosity. This decrease can be attributed to the formation of new pore space as a result of the induction of new microcracks in the structure of the rock in response to the increasing temperature. However, in the range from 400 °C to 600 °C, the volume of non-connected pores followed an increasing trend, which can be due to the chemical alteration of the clay minerals in that temperature range.

Similarly, a comparison has been made between the Thermogravimetric (TG) analyses of the three sandstones (**Figure 8.16**). The comparison demonstrates that 370 °C–680 °C is the temperature window at which all the three sandstones experience a major structural change. Up to a temperature of 680 °C, 0.734 per cent, 1.585 per cent and 8.112 per cent of weight loss are observed in the case of Dholpur sandstone, Jodhpur sandstone and Gondwana sandstone, respectively, which shows that Gondwana sandstone is the most vulnerable to high temperatures among the three sandstones. The greater vulnerability of Gondwana sandstone to temperature is because it is clay-rich.

8.1.4.3 PNM as a function of temperatures

The pore-network modelling section represents the pore and throat configuration of the studied sandstones and their progressive evolution with the increased temperatures. Very important information that is associated with pore connectivity, such as the pore radius, pore coordination number, throat radius and throat channel length can be extracted from these PNM. These parameters provide very significant microstructural information about rocks.

In recent times, pore-scale modelling has been proven to be a vital tool to study the multiphase flow behaviour in rocks in fields such as petroleum engineering, hydrology and environmental engineering (Al-Kharusi and Blunt, 2007; Blunt et al., 2002; Dong and Blunt, 2009). The pore spaces within a rock are represented by a network of pores (larger void space) and throat (narrow opening connecting the pores) (Dong and Blunt, 2009). In general, the three-

dimensional pore space within a rock can be represented by three methods, namely, the micro-X-ray computed tomography method; the statistical method that synthesises the 3D structure, which possesses the properties of the 2D thin section; and the simulation of the packing of grains for the formation of sedimentary structures by following geological processes such as sedimentation, compaction and diagenesis (Dong and Blunt, 2009).

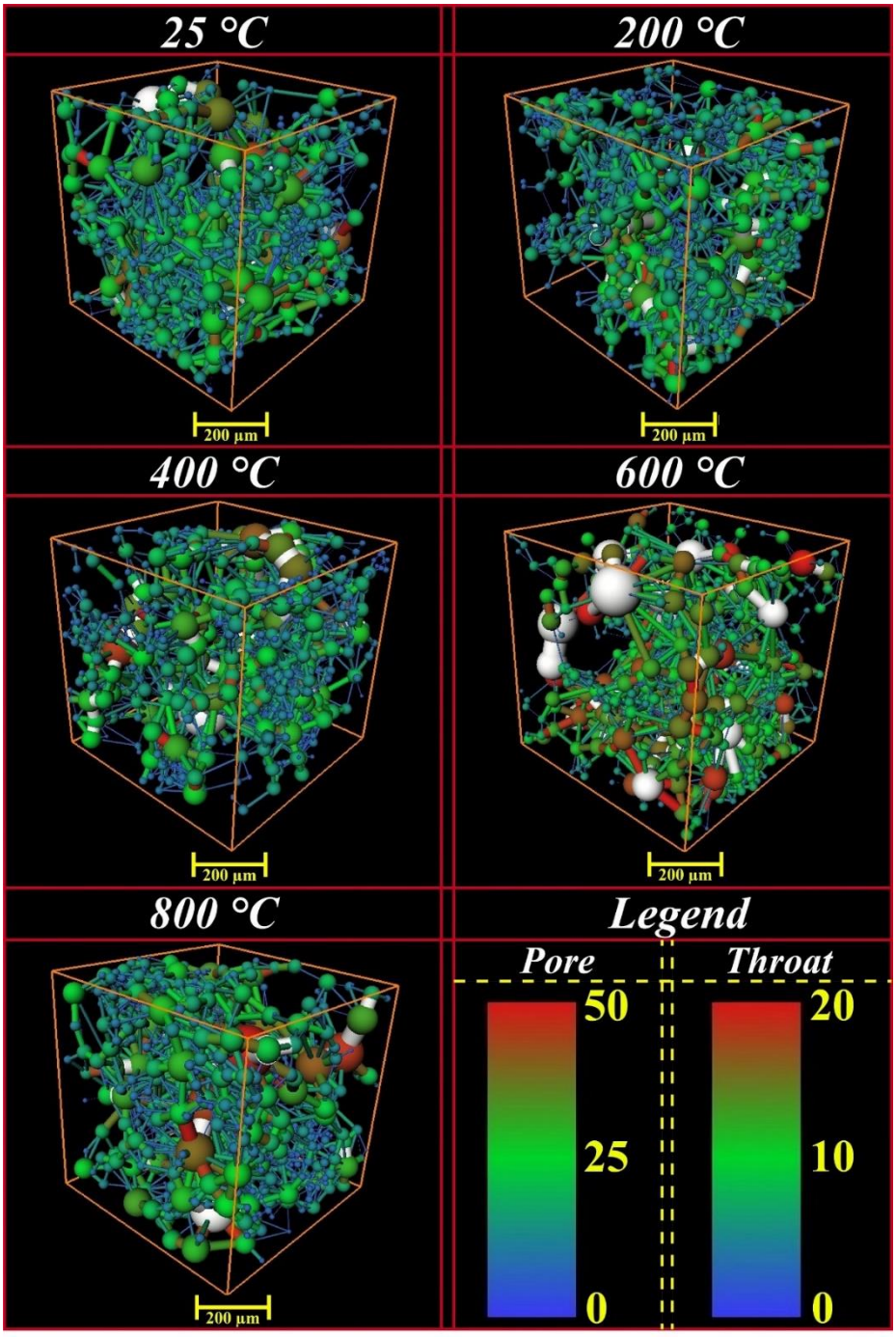

Figure 8.17 *Comparison of the PNM of Dholpur sandstone at 25 °C, 200 °C, 400 °C, 600 °C and 800 °C (white represents the value beyond the values used for the legend)*

Prediction of capillary-controlled multiphase flow is quite easy when the pore-network models in which the pore spaces within the rocks are replaced by a network of equivalent pores and throats are used (Dong and Blunt, 2009; Øren and Bakke, 2002). The pore-network model computes the location and sizes of pores and throats in a rock and a three-dimensional (3D) image that is topologically equivalent of the void space by using the concepts of certain pore-network algorithms such as the concept of medial axis (Lindquist et al., 1996; Lindquist and Venkatarangan, 1999) and the concept of maximal ball (Al-Kharusi and Blunt, 2007; Dong and Blunt, 2009; Silin and Patzek, 2006).

In the current study, pore-network models were regenerated by considering all connected pores. After the pore volume was determined, the same pore volume is represented by a sphere that has the same amount of calculated volume. In the case of the throat, the determined throat volume is represented by a cylindrical volume that represents the computed volume of the throat, and the length of the cylinder is determined on the basis of the maximum distance calculated between any two spheres or pores (Al-Kharusi and Blunt, 2007).

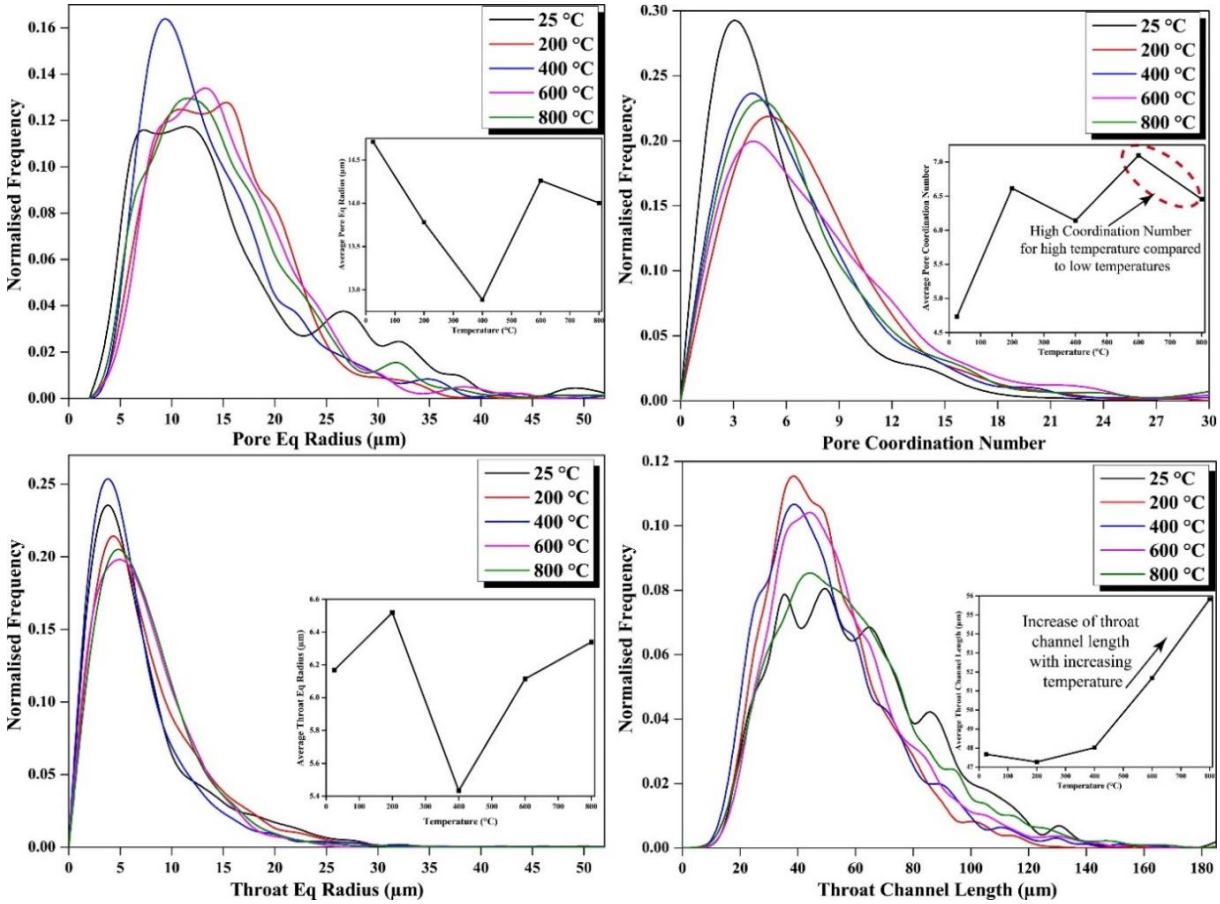

Figure 8.18 *Comparison of pore-network attributes of Dholpur sandstone at different temperatures*

Figure 8.17, **Figure 8.19**, and **Figure 8.21**, represent the comparison of pore-network models at different temperatures for Dholpur, Jodhpur, and Gondwana sandstones, respectively. **Figure 8.18**, **Figure 8.20**, and **Figure 8.22** represent the various pore-network attributes such as the pore equivalent radius, coordination number, throat equivalent radius, and throat channel length for Dholpur, Jodhpur, and Gondwana sandstones, respectively. In addition, these images include the average value of the various pore-network attributes, which are further summarised in **Table 8.3**.

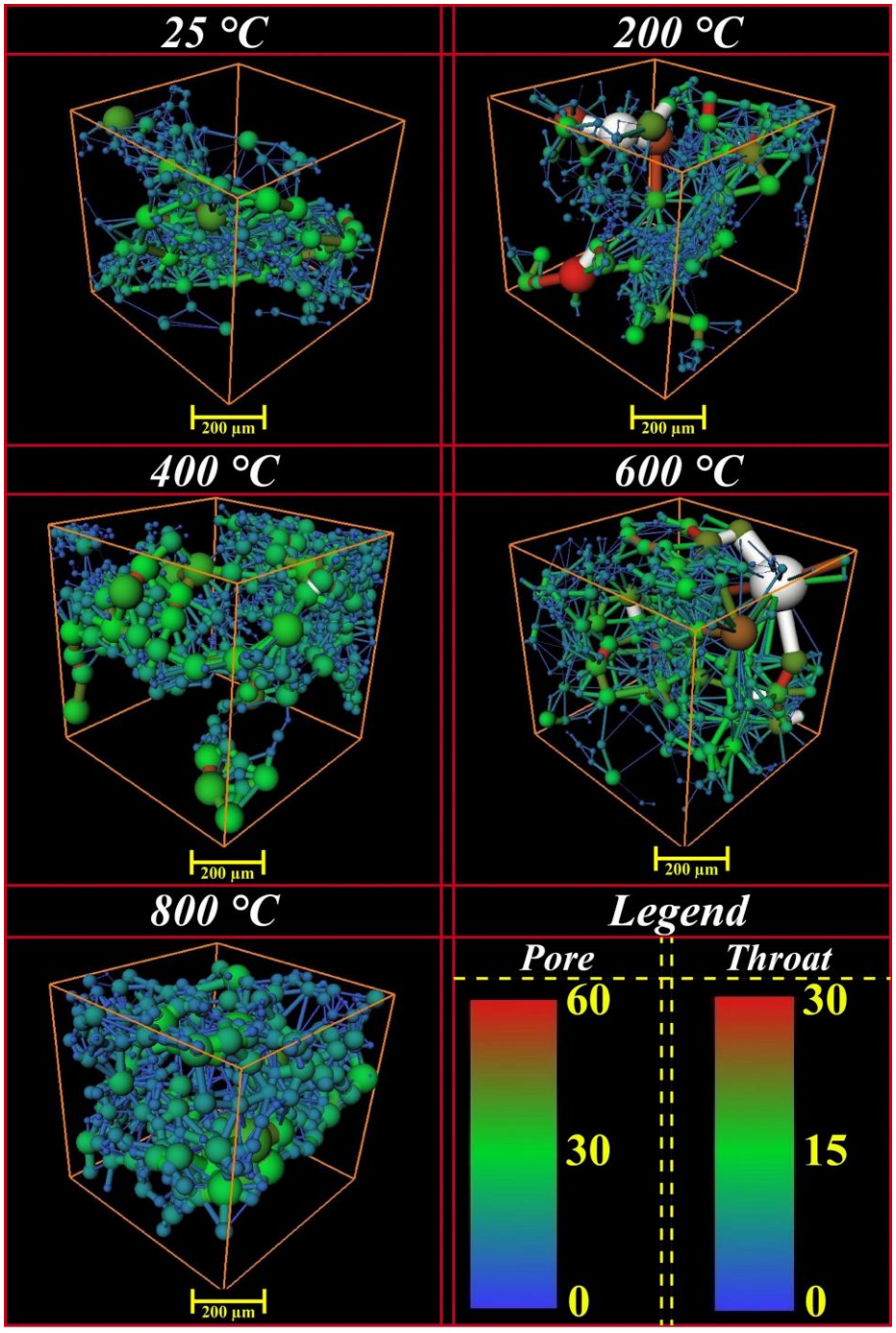

Figure 8.19 *Comparison of the PNM of Jodhpur sandstone at 25 °C, 200 °C, 400 °C, 600 °C and 800 °C (white represents the value beyond the values used for the legend)*

Fredrich and Wong (1986) reported a significant increment in the intergranular crack density above 250 °C. Géraud (1994) conducted experiments using mercury porosimetry for the evaluation of porosity and crack aperture distributions in granite up to 700 °C; he modelled the effect of the heating of the permeability of the granite by using a mixed structure of transgranular cracks and an intergranular tube structure.

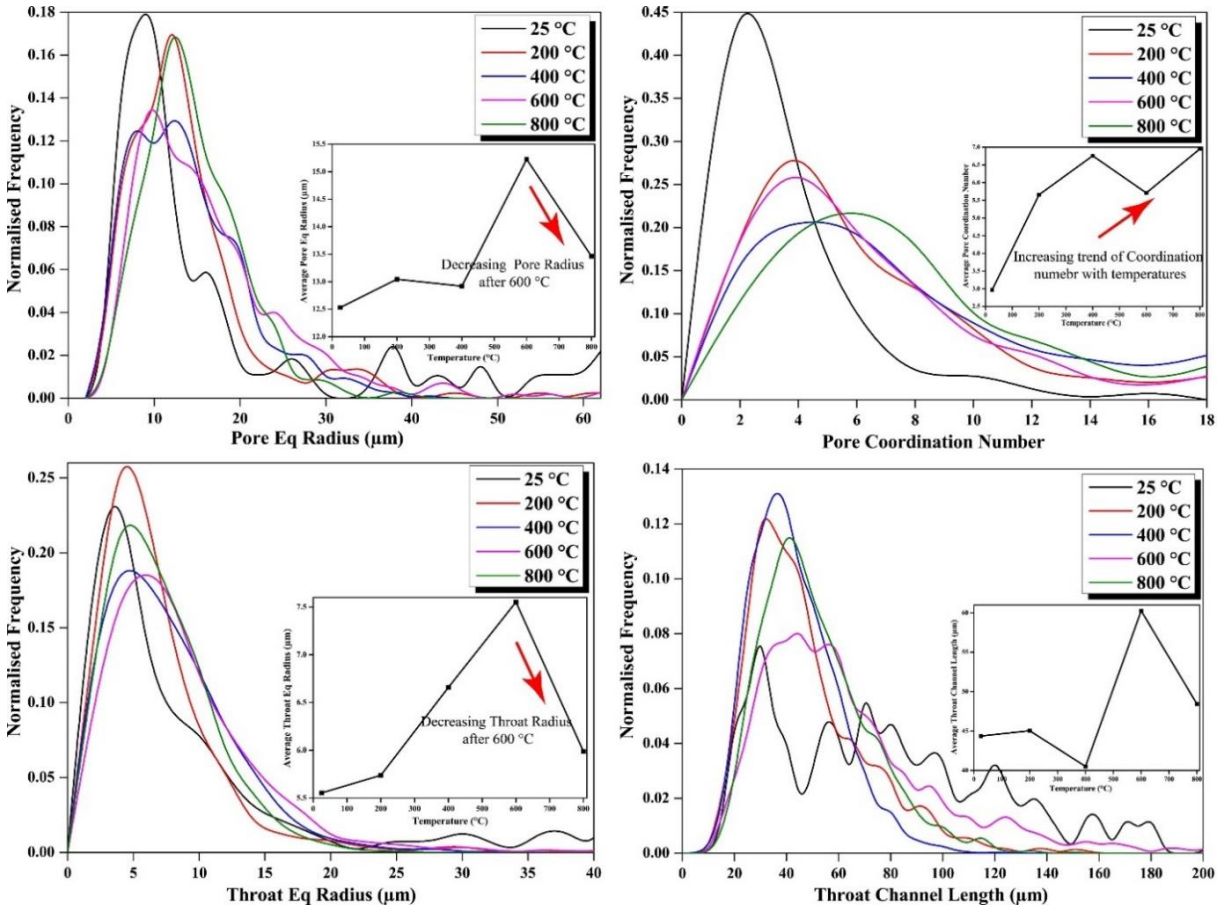

Figure 8.20 *Comparison of pore-network attributes of Jodhpur sandstone at different temperatures*

In the current study, Dholpur sandstone shows increasing temperature along with an average coordination number and throat channel length. The average coordination number achieved its maximum value at 600 °C with a trend of a slight decrease up to 800 °C. However, the average channel length is found to be the maximum at 800 °C (**Figure 8.18** and **Table 8.3)**. For Jodhpur sandstone, the maximum average coordination number is observed at 800 °C, however, a decrease in its average pore radius and throat radius is observed after 600 °C up to 800 °C. This decrease in the pore radius and the throat radius could be the result of the formation of the new cementing material. As discussed earlier, in the current study, only the connected pore volume has been used for the generation of PNM, and Gondwana sandstone contains a considerable amount of non-connected pores at different temperatures (**Figure 8.12**, **Figure 8.13**, Figure

8.14). Hence, no conclusive remarks can be made for Gondwana sandstone based on the data from the pore-network model; further investigation is required for results that are more conclusive.

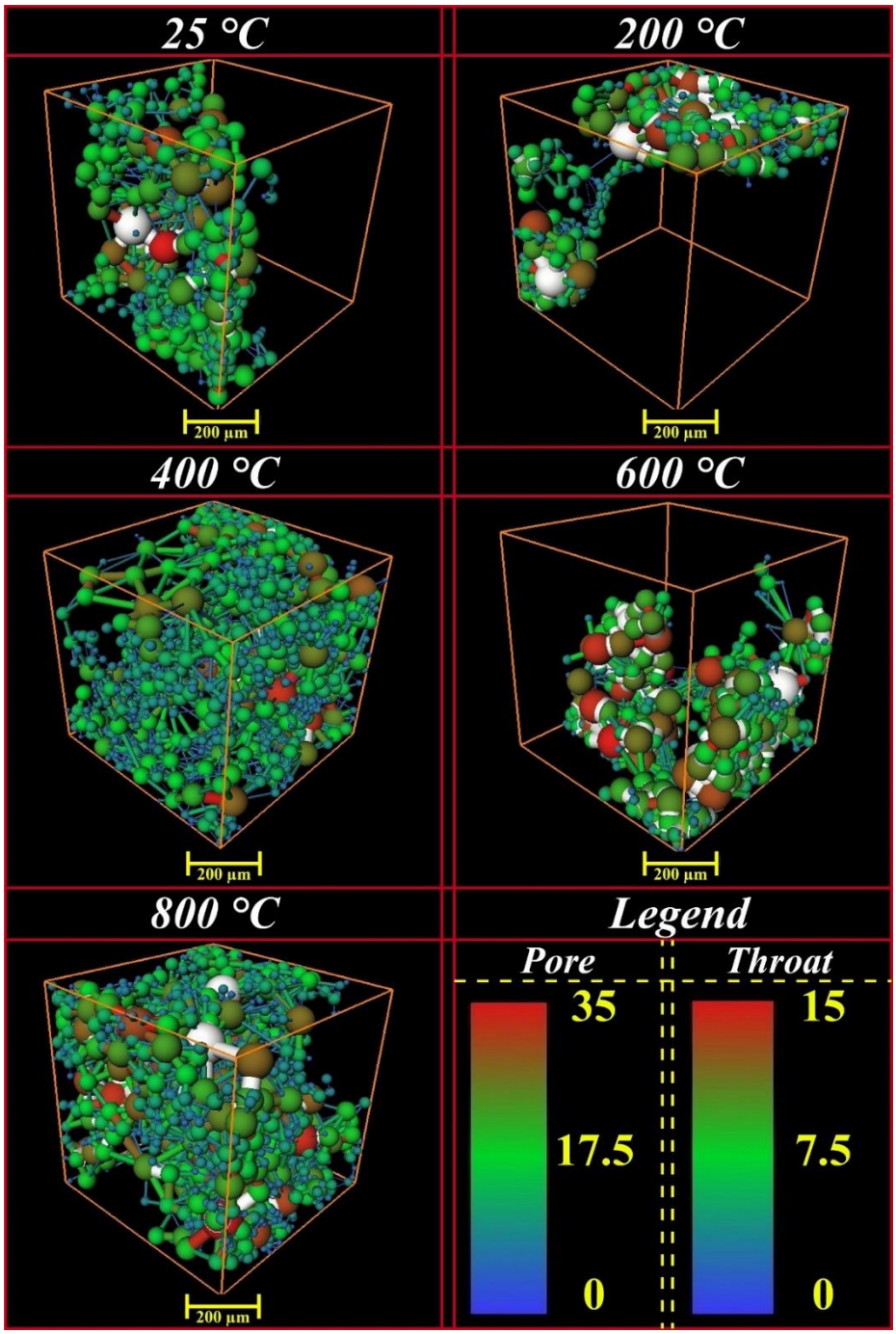

Figure 8.21 *Comparison of the PNM of Gondwana sandstone at 25 °C, 200 °C, 400 °C, 600 °C and 800 °C (white represents the value beyond the values used for the legend)*

Glover et al. (1995) measured the acoustic emission during the process of thermal cracking. According to their findings, a strong peak of microcracking was observed at the phase transition temperature of quartz (573 °C). The effect of thermal cracking is explained by the successful

measurement of the crack surface area, porosity, pore-fluid permeability, and surface conductivity. However, the measurement of these parameters revealed a drastic increase of cracking in the range of 500 °C–600 °C (Glover et al., 1995; Reuschlé et al., 2006). Distinctive microcracks can be formed as a result of the strain that is associated with solid-state phase transformation. For example, the transformation of coesite to quartz involves an increment of the volume of 11 per cent. The measurement of the fracture surface energy reveals the possible formation of microfractures during the phase transformation of α-quartz to β-quartz and other minerals that undergo similar transformations (Blenkinsop, 2000; Wang et al., 1989).

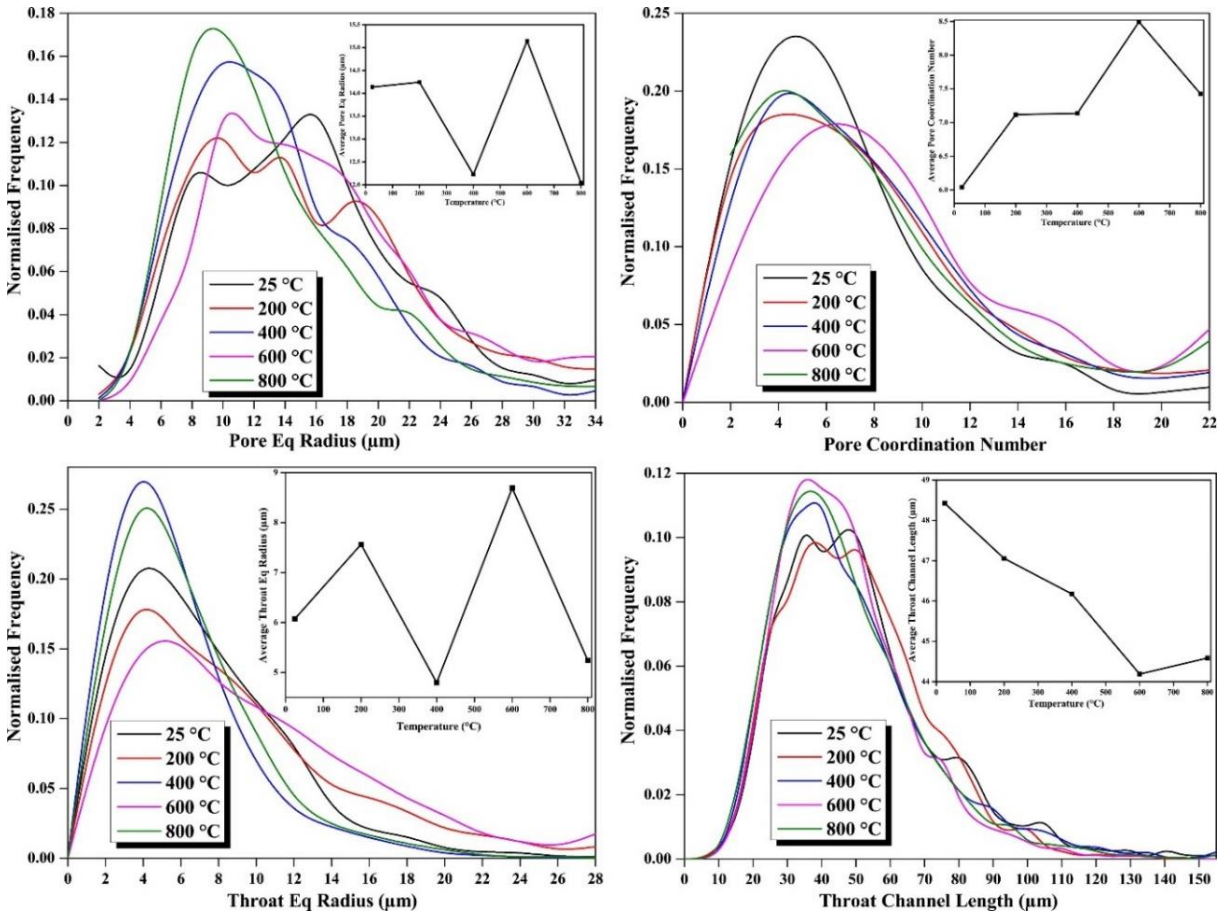

Figure 8.22 *Comparison of pore-network attributes of Gondwana sandstone at different temperatures*

The transformation of Aragonite when replaced by the calcite inclusions results in a volume increase of 8.5 per cent, which brings radial microcracks around calcite inclusions (Wang and Liou, 1991). Intergranular microcracks are distinctive features that are associated with phase transformation (Blenkinsop, 2000). From the previous literature, it is clear that most of the major changes in the rock structure take place in the range of 500 °C to 600 °C. A similar conclusive remark can be made from the average pore-network model data of the current study. At around 600 °C, all the three sandstones experience major structural damages due to the

mineralogical phase transformation and the chemical alteration of the constituent minerals in the range of 500 °C to 600 °C.

Table 8.3 *Various Pore-network attributes as a function of temperatures in three sandstones*

Rock Type	Temperature (°C)	Average pore Eq. Radius (µm)	Average Pore Coordination Number	Average Throat Eq. Radius (µm)	Average Throat Channel Length (µm)
Dholpur sandstone	25	14.711	4.733	6.168	47.673
	200	13.780	6.615	6.518	47.271
	400	12.885	6.141	5.433	48.021
	600	14.264	7.097	6.114	51.673
	800	14.004	6.457	6.339	55.832
Jodhpur Sandstone	25	12.531	2.967	5.555	44.359
	200	13.045	5.659	5.738	45.036
	400	12.919	6.758	6.659	40.507
	600	15.228	5.708	7.552	60.250
	800	13.466	6.953	5.988	48.436
Gondwana Sandstone	25	14.136	6.039	6.074	48.424
	200	14.244	7.118	7.566	47.057
	400	12.227	7.137	4.795	46.176
	600	15.147	8.495	8.691	44.188
	800	12.043	7.425	5.243	44.583

8.2 Microstructural insight into progressive deformation of sandstone at different stress levels

Various underground rock structures are formed in stressed brittle rocks. Over the course of time, under high-stress conditions, stress redistribution results in an imbalance in the energy in the rock mass. Depending upon the stages of applied stress, microcracks are formed, propagated, and coalesced, which alters the mechanical properties of the surrounding associated rocks; this affects the stability of the rock structures. Hence, the progressive deformation of rocks and fundamental studies in order to assess the failure and damage mechanism of rocks at different stress levels is of great importance (Chang and Lee, 2004; He et al., 2018).

Previously, different authors have tried to investigate the mechanical behaviour of rocks by means of various numerical tools (Hazzard et al., 2000; Zhu and Tang, 2004; Lan et al., 2010; Mahabadi et al., 2014). Using the rock failure process analysis code (RFPA), Zhu and Tang (2004) studied the mesoscopic deformational and failure processes of heterogeneous rocks.

Using the Y-Geo code, Mahabadi et al. (2014) studied the mechanical responses of different crystalline rocks and their failure behaviours. Hazzard et al. (2000) used particle flow code (PFC) to assess the nucleation and propagation of cracks in brittle rocks during the energy release during failure, whereas, Lan et al. (2010) used grain-based universal distinct element code (UDEC) to investigate the influence of microheterogeneity on the micromechanical and macroscopic responses in rocks.

8.2.1 Sample preparation and methodology

In the current analysis, the failure behaviour of sandstone at different stress levels was observed by using micro-CT techniques. For this analysis, a specimen of Jodhpur sandstone that had a dimension of 10 mm x 10 mm x 8 mm was used (**Figure 8.23**). The samples were loaded to a certain percentage of the peak load, and at the loaded condition, computed tomographic X-ray images were acquired; this was followed by their analysis in AVIZO software.

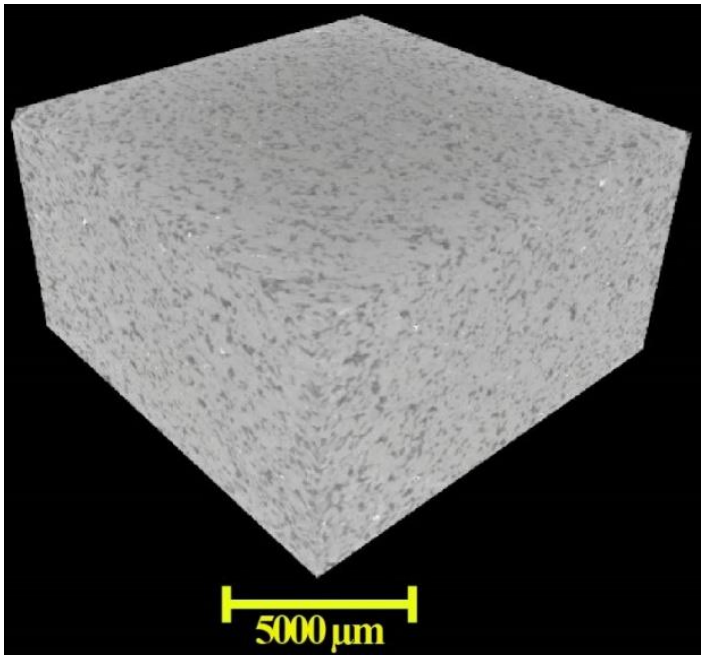

Figure 8.23 *Studied volume for the analysis of progressive deformation of sandstone*

Analyses were performed at without loading, 25 per cent, 50 per cent, 75 per cent and at failure condition. At the end, all the stages were compared to enable a better perception of the progressive deformational behaviour of sandstone. Pore-space evolution and PNM evolutions were investigated at different stress levels. Based on the results of PNM, the frequency distribution of various pore and throat attributes (pore volume, pore area, pore equivalent radius, pore coordination number, throat area, throat equivalent radius and throat channel length) were evaluated.

Details of the mechanism of micro-CT X-ray image acquisition and the techniques that are used to enhance and process this mechanism have been included in the previous section of this chapter.

8.2.2 Results and discussion

8.2.2.1 Evolution of pore spaces at different stress levels

The stress-strain curve of brittle materials such as rocks can be divided into five regions: crack-closure, elastic region, stable crack growth, and unstable crack growth that are followed by the complete failure of the specimens. The initial region belongs to the crack-closure zone, where preexisting cracks are closed under the influence of the applied load.

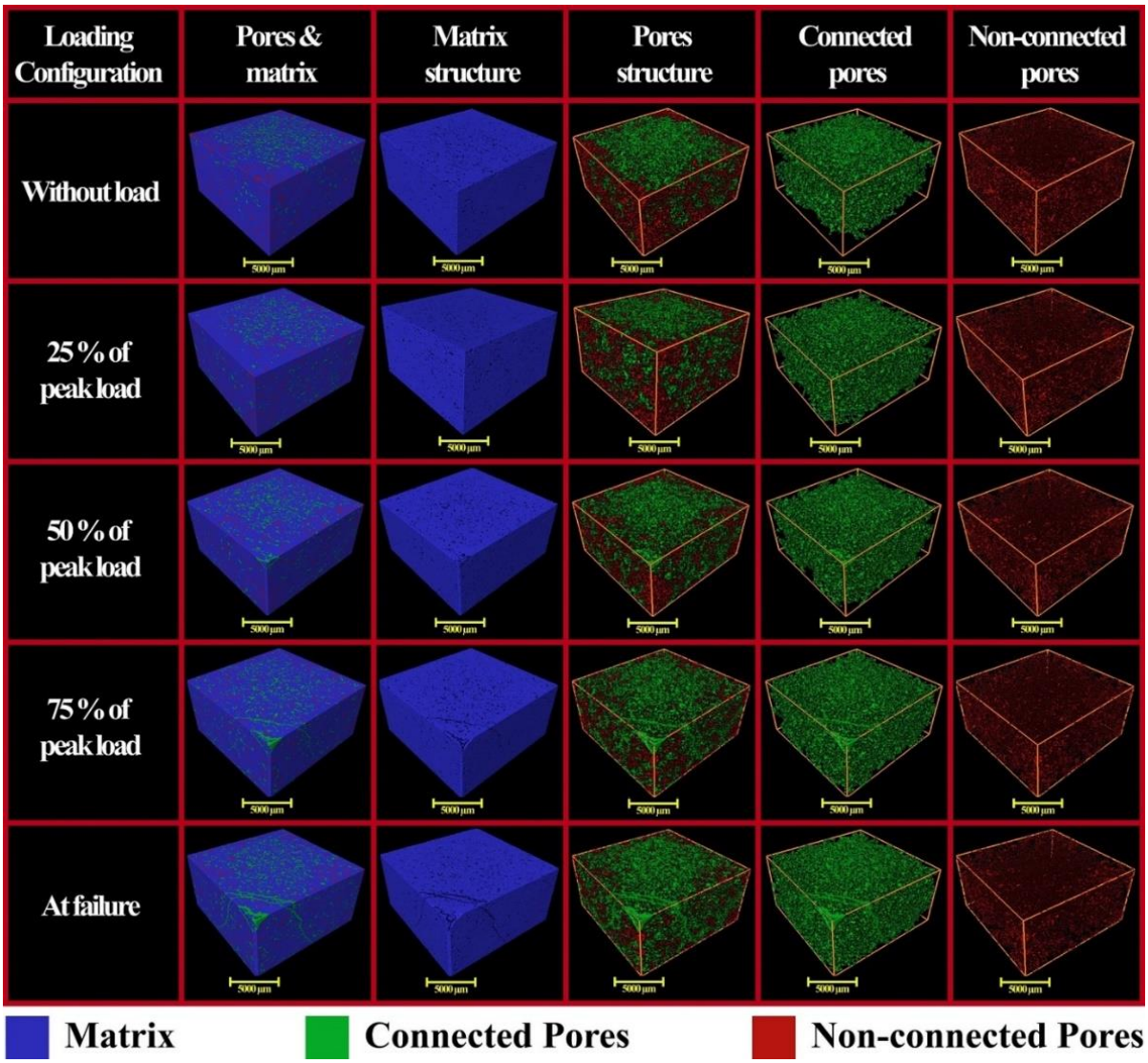

Figure 8.24 *A comparison of pore-space evolution at different stress levels*

However, the existence of the crack closure region in the stress-strain curve of a brittle material is dependent on the initial density and the geometry of the crack. Once the preexisting cracks

are closed, the stress-strain curve maintains a linear path. The zone of linear correlation with the applied stress and strain is known as the elastic region. After the termination of the elastic zone, the region of stable crack growth starts. This is the region where new cracks initiate, which is known as the crack-initiation point. Stable crack growth continues up to the crack coalescence point at which unstable crack growth starts. Furthermore, with an additional applied load, the rock reaches its ultimate strength point at which it undergoes failure.

A progressive increase in the load results in fracture planes due to the coalescence of the microcracks. **Figure 8.24** shows a comparison of the pore-space evolution at different stages of the peak load. In the case of 25 per cent of the peak load, no fracture plane is observed, because the associated load is not adequate for the formation of new cracks. However, progressive stages such as that at 50 per cent of the peak load are observed along with the formation of certain small crack planes, which clearly indicates the crack-initiation stress level for the sandstone at between 25 per cent and 50 per cent of the peak load. Furthermore, 75 per cent of the peak load stage and the failure stage are observed in certain well-developed fracture planes.

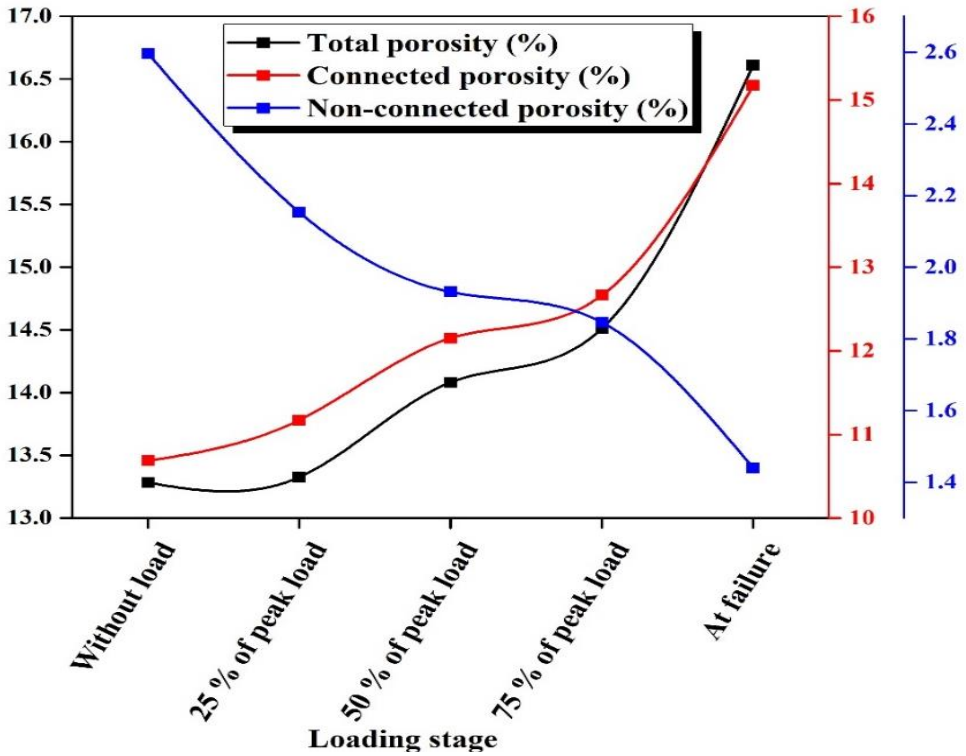

Figure 8.25 *A comparison of total porosity, connected pore spaces, and non-connected pore spaces at different stress levels*

When we compare the porosity of the specimen at all the stages of loading, it can be inferred that with progressive loading, the total porosity and the connected porosity gradually increase,

which indicates the formation of new pore spaces with progressive stages. However, non-connected pores are found in a decreasing trend along with the stages of increasing loads. As the load level increases from stage to stage, new microcracks are created and, often, the existing cracks or pore spaces (connected or non-connected) are connected; this could be due to the gradual decrease of non-connected pores along with increase of stress levels (**Figure 8.25**).

8.2.2.2 PNM at different stress levels

When it comes to the PNM of the sandstone at different stress levels, the induced fractures are well captured in the PNM. Various pore-network attributes such as the pore equivalent radius, pore coordination number, throat equivalent radius and throat channel lengths were extracted from the pore network models (**Figure 8.26**), and their frequency distributions have been shown in **Figure 8.27**. When we compare the frequency distributions for all the stress levels, the pore-network attributes that correspond to the stage at the failure of the specimens display the maximum frequencies in comparison to other stress levels. With a gradual increase in the stress levels, the frequencies of different pore-network attributes gradually increase, indicating the formation of a new pore volume in terms of new pores and throats.

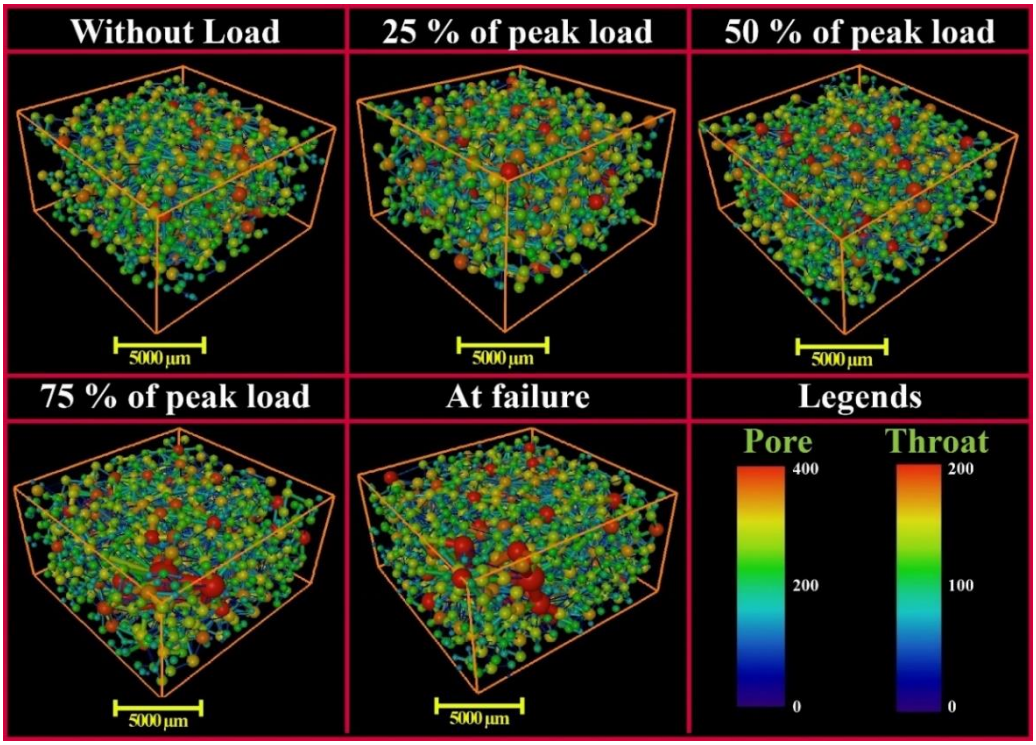

Figure 8.26 *Comparison of the PNM at different stress levels*

The statistical distribution of the pore-network attributes has been shown in **Table 8.4**, and the maximum values of the pore attributes and the throat attributes have been plotted in **Figure 8.28** and **Figure 8.29**, respectively. Both the pore attributes and the throat attributes gradually increase along with the increase in stress levels. The increment in pores and throats is quite

marginal up to 50 per cent of the peak load thereby a significant increment was observed up to the failure stage. This clearly indicates that the majority of pores are induced in the specimen after 50 percent of the peak load.

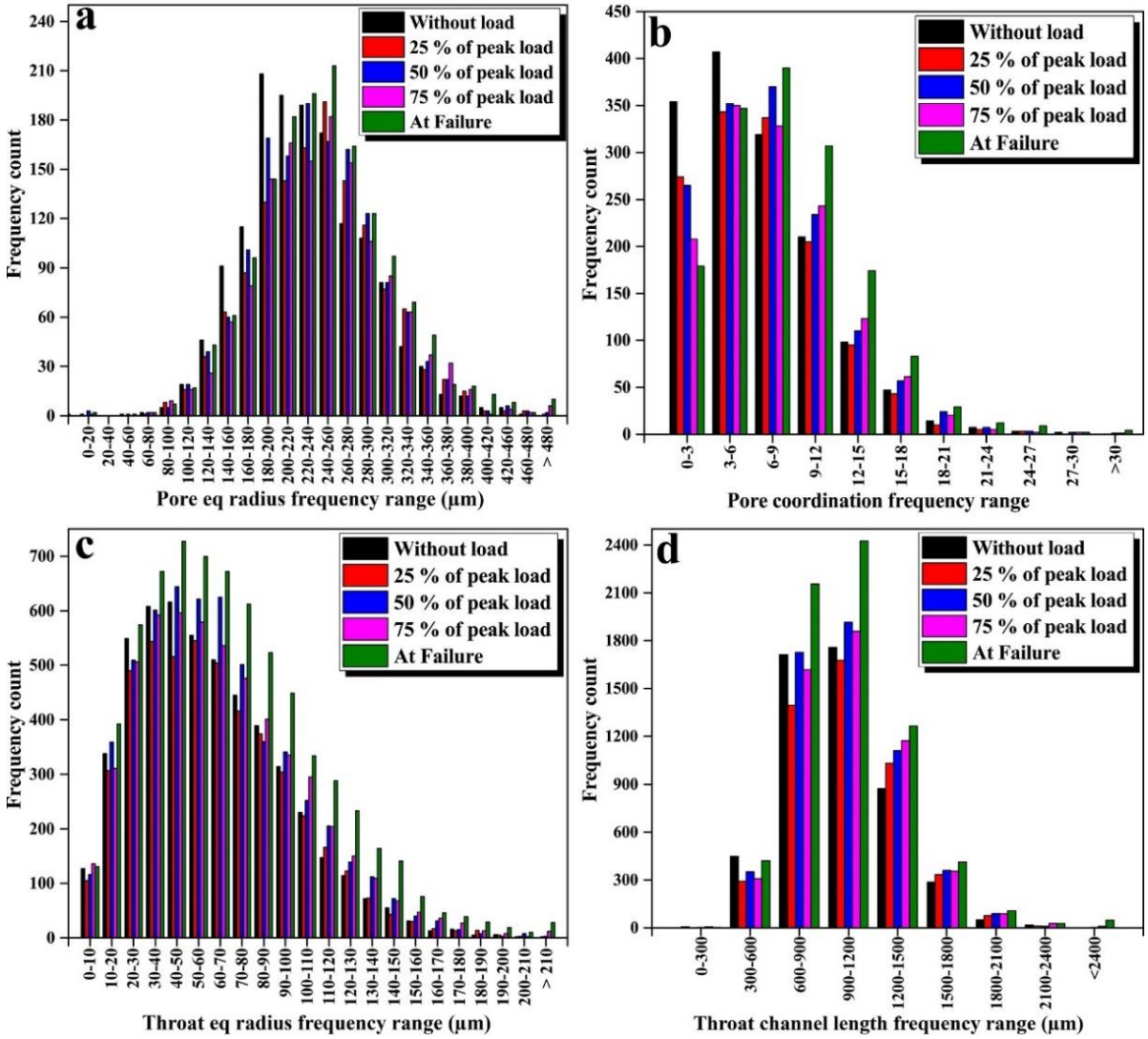

Figure 8.27 *Comparison of pore-network attributes at different stress levels*

Table 8.4 *Statistical distribution of pore-network attributes at different stress levels*

Pore attributes		Maximum	Minimum	Mean	Median
Pore volume (μm^3)	Without load	4.36E+08	6.23E+03	7.73E+07	6.21E+07
	25 % of peak load	4.87E+08	6.23E+03	8.73E+07	7.44E+07
	50 % of peak load	5.45E+08	3.11E+04	8.62E+07	7.09E+07
	75 % of peak load	1.85E+09	3.74E+04	9.25E+07	7.47E+07
	At failure	4.51E+09	4.98E+04	9.60E+07	7.53E+07
	Without load	2.18E+07	1.02E+03	3.69E+06	2.93E+06

Pore area (μm^2)	25 % of peak load	2.40E+07	1.02E+03	4.29E+06	3.68E+06
	50 % of peak load	2.47E+07	4.31E+03	4.23E+06	3.50E+06
	75 % of peak load	7.62E+07	5.07E+03	4.51E+06	3.66E+06
	At failure	1.54E+08	5.97E+03	4.57E+06	3.65E+06
Pore eq radius (µm)	Without load	4.70E+02	1.14E+01	2.50E+02	2.46E+02
	25 % of peak load	4.88E+02	1.14E+01	2.61E+02	2.61E+02
	50 % of peak load	5.07E+02	1.95E+01	2.59E+02	2.57E+02
	75 % of peak load	7.61E+02	2.07E+01	2.65E+02	2.61E+02
	At failure	1.02E+03	2.28E+01	2.65E+02	2.62E+02
Pore coordination number	Without load	3.00E+01	1.00E+00	7.04E+00	6.00E+00
	25 % of peak load	2.70E+01	1.00E+00	7.33E+00	7.00E+00
	50 % of peak load	3.30E+01	1.00E+00	7.81E+00	7.00E+00
	75 % of peak load	3.90E+01	1.00E+00	8.10E+00	7.00E+00
	At failure	8.30E+01	1.00E+00	8.93E+00	8.00E+00
Throat area (μm^2)	Without load	1.30E+05	7.52E+01	1.54E+04	9.78E+03
	25 % of peak load	1.84E+05	6.22E+01	1.63E+04	1.07E+04
	50 % of peak load	1.70E+05	6.22E+01	1.69E+04	1.08E+04
	75 % of peak load	3.23E+05	6.22E+01	1.80E+04	1.13E+04
	At failure	6.31E+05	6.22E+01	2.03E+04	1.28E+04
Throat eq. radius (µm)	Without load	2.03E+02	4.89E+00	6.10E+01	5.58E+01
	25 % of peak load	2.42E+02	4.45E+00	6.29E+01	5.84E+01
	50 % of peak load	2.33E+02	4.45E+00	6.40E+01	5.88E+01
	75 % of peak load	3.21E+02	4.45E+00	6.56E+01	6.00E+01
	At failure	4.48E+02	4.45E+00	6.95E+01	6.38E+01
Throat channel length (µm)	Without load	2.35E+03	2.28E+02	9.94E+02	9.60E+02
	25 % of peak load	2.43E+03	2.78E+02	1.05E+03	1.02E+03
	50 % of peak load	2.60E+03	2.50E+02	1.03E+03	1.00E+03
	75 % of peak load	2.84E+03	2.08E+02	1.05E+03	1.02E+03
	At failure	3.95E+03	2.13E+02	1.04E+03	9.99E+02

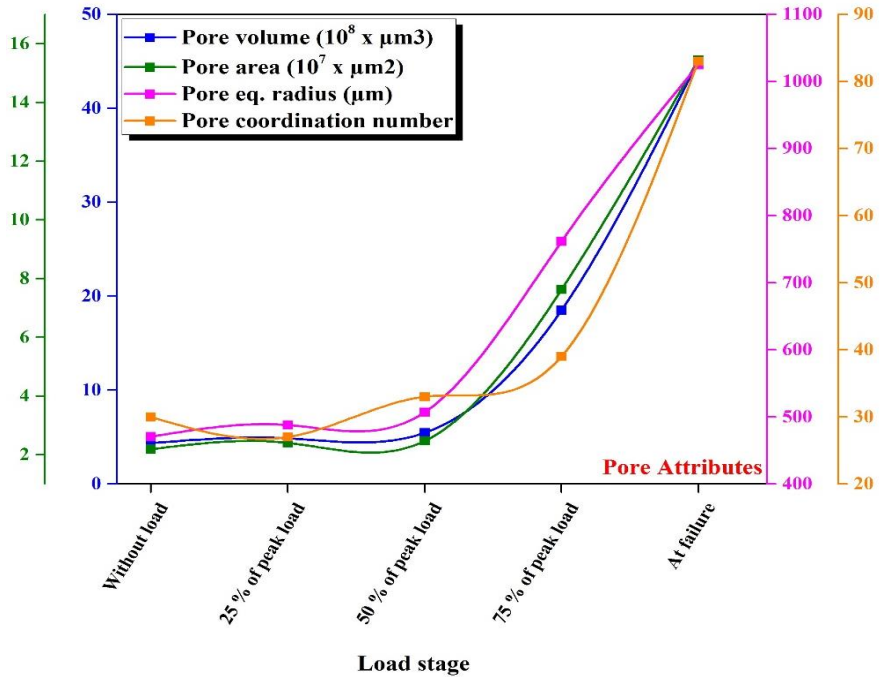

Figure 8.28 *Maximum values of various pore attributes at different stages of loading*

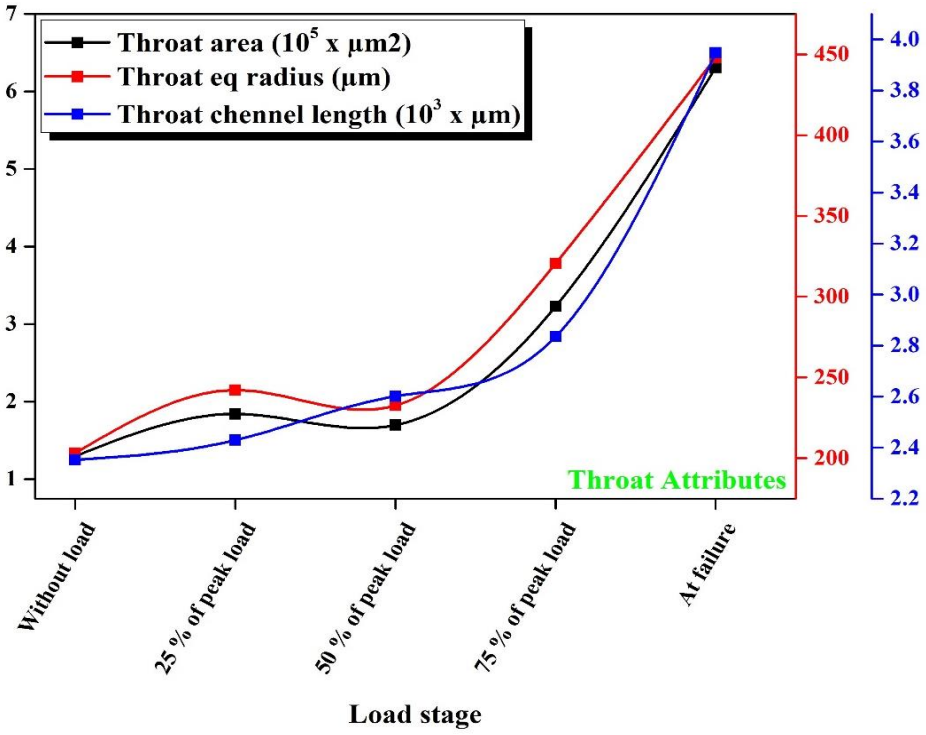

Figure 8.29 *Maximum values of various throat attributes at different stages of loading*

Chapter 9 Conclusions and future work

9.1 Conclusions

9.1.1 Summary and conclusions from the physico-morphological investigation

All the physical changes and chemical reactions as a result of being exposure to temperatures bring changes into the structure of the rock in the form of porosity increment, mineral transformation, minerals decomposition and dihydroxylation, reduction in the adhesive force between the minerals, development of microcracks and their accumulation that results in macrocracks. Based on the physico-morphological analysis the following conclusions can be drawn.

- The P-wave velocity graph for both thermally treated and rapid cooled sandstone specimens represented an overall decreasing trend from 100 °C to 900 °C. However, from 100 °C to 400 °C, the reduction in the P-wave velocity for both the cases was not that much significant as compared to the temperature range 400 °C to 600 °C. There was a little decrease in the P-wave velocity up to 400 °C and thereafter a significant reduction in the P-wave velocity of the sandstone is observed. In the temperature range 25 °C – 400 °C, on the one hand, the free water that is present in the rock turns into steam and escapes from the open pore spaces, which increases the pore volume. On the other hand, the process of heating results in the expansion of the mineral grains, which fills certain pore spaces. Due to the combination of both these effects, the pore volume of the rock decreases at certain times and increases at others. In the temperature range 400 °C – 900 °C, the induced structural damages within the structure of the sandstone provide major contribution for the reduction of the P-wave velocity.
- SEM, petrographic analysis of thermally treated and rapid cooled sandstone display induction of major structural damage for 600 °C and 800 °C cases. The extent of structural damage is correlated to the thermal expansion of minerals and the formation of microcracks such as intergranular, intragranular and transgranular cracks and their network.

9.1.2 Summary and conclusions from mechanical testing

9.1.2.1 Investigation in the unconfined condition

This section investigated the high-temperature mechanical alteration of Indian sandstone in unconfined condition by coupling various techniques such as AE and DIC by using ARAMIS. Various mechanical properties of the thermally treated and rapid cooled sandstone were

measured after they were exposed to different temperatures. A summary of the important conclusions that are drawn from the current investigation are listed below:

- The tested sandstone underwent major structural damage in the temperature window of 400 °C to 680 °C. It was found that the formation of new microcracks, chemical alteration of clay and carbonate minerals (kaolinite, dickite and calcite, respectively) and the phase transition of quartz mineral at 573 °C led to these structural damages. At room temperature, Young's modulus of sandstone is found to be 34.87 GPa, whereas Young's modulus of the sandstone thermally treated at 600 °C, was 15.62 GPa.
- An overall reduction in the strength of the tested samples upon heating was observed. However, a marginal increase in the UCS and the tensile strength of the sandstone was observed after 700 °C. This is possibly due to the formation of a new cementing mineral, Portlandite which may be the by-product of the dihydroxylation of dickite ($Al_2 SI_2 O_5 (OH)_4$) at 680 °C and the decomposition of calcite ($CaCO_3$) at approximately 700 °C.
- Stress thresholds were delineated by using cumulative AE counts along with the progressive deformation of the rock. In samples that were treated at high temperatures (600 °C–900 °C), it was found that the CIST and the CDST occurred at an earlier stage of deformation when compared to the samples that were treated at low temperatures (25 °C–500 °C). At room temperature, the crack initiation and the crack damage stage start at around 41 per cent and 91 per cent of the failure strength, respectively. However, the crack initiation and the crack damage stage start at nearly 17 per cent and 62 per cent of the failure strength in the specimens at 700 °C, which suggests a possible reduction in the linear-elastic region and the stable crack propagation region in thermally treated specimens.

9.1.2.2 Investigation in the confined condition

Triaxial setup simulates the actual in situ temperature and pressure conditions deep inside the earth and thereby provides the platform to acquire information about the in situ high temperature and high-pressure rock behaviour. In situ rock tests are performed up to 300 °C and 60 MPa from normal temperature and pressure (NTP) condition. In addition to the mechanical strength investigation, the characteristics of shear bands formed as a result of the mechanical tests were explained.

- Based on the experimental results, it can be stated that pressure does have significant influence on the strength parameter of the sandstone, as compared to temperatures. With progressive increase of confining pressure, the strength gradually increased. From room

temperature to 200 °C, strength of the sandstone got increased and thereby a slight reduction up to 300 °C was observed. However the variation of strength due to temperature is insignificant.

- In the existing literature, it has been observed that cohesion and internal friction of rocks are drastically influenced under the influence of temperature and pressure. However, for Jodhpur sandstone, neither temperature not pressure have significant effect on the cohesion and internal friction.
- Observation of mechanically formed shear bands revealed the higher porous nature of the inside shear band as compared to the outside shear zone. For all the combination of investigated temperatures and pressures, the inside shear bands were observed with having finer grains compared to the outside shear band.

9.1.3 Summary and conclusions from the cyclic loading-unloading and strain rate tests

- Based on the cyclic loading-unloading analysis it can be concluded that at room temperature condition the phenomena of Kaiser effect is quite satisfactory and significant AE counts produced once the stress level in the current cycle exceeds the maximum stress level of the previous cycle.
- However, for higher temperature condition Kaiser effect is insignificant as compared to the room temperature condition for both case two and case three (chapter 5). For high temperature cases, significant amount of AE counts are observed well before the previous maximum stress. In such situation the accuracy of Kaiser effect or the stress memory effect of the sandstone can be explained in terms of Felicity ratio.
- Based on the strain rate study, it was found that the geomechanical properties such as UCS, tensile strength, Young's modulus, failure strain, mode I and mode II fracture toughness, and the brittleness index of rock were significantly affected due to variations in the strain rates. At 7.9 x 10^{-5} s^{-1} strain rate, the UCS, the tensile strength, and the mode I fracture toughness and mode II fracture toughness of the rock were found to be 25.45 MPa, 7.71 MPa, 0.171 MPa $m^{1/2}$, 0.083 MPa $m^{1/2}$, respectively, which increased up to 50.57 MPa, 13.06 MPa, 0.565 MPa $m^{1/2}$, 0.467 MPa $m^{1/2}$, respectively, at 1.7 x 10^{-2} s^{-1} strain rate.
- All these properties except for failure strain were found to increase with the increase in the strain rate. At high strain rates, predominantly the rock possesses shear mode of failure. Crack branching is a common phenomenon under high strain rate conditions. This indicates

that there is some energy consumption, which is used for the branching or bifurcation of cracks, and that contributes to the increment in strength properties at high strain rates.

9.1.4 Summary and conclusions from fracture mechanical investigations

9.1.4.1 With varying temperatures

In this section, an attempt were made to establish a relation between mode I static fracture toughness and elevated temperatures up to 600 °C, using CSTSCB specimens of two type of sandstones. The following important conclusions were drawn:

- The fracture toughness of these rocks increases up to a temperature range of 100 °C, possibly due to the closure of pre-existing cracks and the desorption of the water that is present in these rocks.
- A gradual fall in the fracture toughness value up to 600 °C was observed. This might be due to the induced micro-cracks within these rocks, which are induced by gradual treatment at elevated temperatures. These results were interpreted with the support of microscopic observations of the microstructures within these rocks along with the help of SEM and petrographic thin-section analyses.
- Thermally induced micro-cracks within these rocks, which are primarily responsible for the decrease in fracture toughness, are clearly visible when the temperature exceeds 200 °C.
- However, the fracture toughness value for Manoharpur sandstone shows a sharp decrease in the temperature range between 550 °C to 600 °C, which may be due to the thermal decomposition of the clay materials present within it. At 600°C, the fracture toughness value for Manoharpur sandstone and Dholpur sandstone decreased by 59 per cent and 30 per cent, respectively, when compared to their fracture toughness at room temperature.

9.1.4.2 With varying strain rates

In this section, attempts were made to observe the effects of different strain rates on the fracture toughness and energy-release rate of rock in mode I, mixed mode (I/II), and mode II loading conditions, using semicircular bending specimens. The following conclusions were drawn from the study:

- The fracture toughness gradually increases with increasing strain rates. At high strain rates, the strength or stiffness of rock increases; this, in turn, increases the fracture toughness of the shale.

- It was found that the total energy-release rate also increased with increasing strain rates in all three modes of loading applied in the experiments. Among all the cases, the energy-release rate of mode I is maximum when compared to the other two modes because it involves the least amount of the fracture area. For all the strain rates, the loading condition in mode I requires the least amount of applied energy, while the loading condition in mode II requires the maximum amount of energy for the onset of crack growth.
- Among all cases, mode I had the highest amount of strain-energy-release rate. At lower strain rates, the fracture toughness and the strain-energy-release rates for all the modes are comparable but vary significantly at higher strain rates.
- Based on the strain rate analysis using the FBD specimens, it can be concluded that the specimens with 20° loading angle overestimates the fracture toughness of the rock when compared to the specimens with 30° loading angle. With increasing strain rates, both peak load and the fracture toughness increase gradually. With increasing strain rates, the probability of achieving centrally initiated fracture reduces.

9.1.5 Summary and conclusions from the microstructural investigation

In the current study, an attempt has been made to investigate the microstructural response of three Indian sandstones to elevated temperatures. The sandstones, Dholpur sandstone, Jodhpur sandstone, and Gondwana sandstone, which were investigated in this study, are of diverse natures. They were selected from two different stratigraphic formations with different mineralogy. Out of the three sandstones, Gondwana sandstone was the most clay-rich in comparison to the other two. Dholpur sandstone was devoid of any significant clay minerals, whereas, Jodhpur sandstone was intermediate in terms of the clay content when compared to Dholpur sandstone and Gondwana sandstone. High-resolution micro-CT technique was used for the microstructural investigation of the studied rocks/sandstones. The sandstone samples were thermally treated at 200 °C, 400 °C, 600 °C, and 800 °C and were compared with the sample that was at ambient conditions. The result of the investigation can be summarised as follows.

- Based on the current investigation, it can be concluded that 370 °C–680 °C is the common temperature window at which all the three sandstones undergo major structural damage.
- These structural damages can be explained in terms of the formation of new microcracks within the structure of the rocks, decomposition, dehydroxylation, volatilisation, and

oxidation of the constituent minerals within the rock and the phase transition of quartz minerals at 573 °C (for Jodhpur sandstone) and 579 °C (Dholpur sandstone).

- Among the three studied sandstones, Gondwana sandstone was more vulnerable to elevated temperatures when compared to Dholpur sandstone and Jodhpur sandstone, which can be explained in terms of the high amount of clay minerals in Gondwana sandstone that is about 30 per cent in the form of siderite, illite and kaolinite.
- An overall trend of increase in the porosity of Dholpur and Gondwana sandstones when there was an increase in temperature was observed. Jodhpur sandstone, however, possessed its maximum porosity at 600 °C and, thereby, a decreasing trend up to 800 °C, which can be due to the formation of a new cementing material in between 600 °C and 800 °C.
- Based on the micro-CT study performed at different stress level of the peak load reveals the appearance of macrofractures at 50 per cent of the peak load. In addition, it suggests, with increasing the load level total porosity of the sandstone gradually increases whereas, the volume of non-connected pores gradually decreases that indicates the coalescence of non-connected microfractures to form microfractures that results in the increase of total pores of the sandstone.

9.2 Recommendations for future work

As it has already been mentioned earlier, UCG is an unexplored technique in India and it needs a lot of research work in terms of both experimental investigation and numerical analysis prior to its development in the Indian context.

Based on the existing literature study, it was found that majority of the thermomechanical behaviours of sandstone have been assessed from the mechanical and physical point of view where various mechanical properties such as uniaxial compressive strength, tensile strength, elastic modulus, Poisson's ratio, damage factors, fracture toughness, triaxial compressive strength, cohesion and internal friction; and physical properties such as the ultrasonic wave velocities, mass, density, porosity and thermal expansions were evaluated by many researchers. However, the existing literature still lacks the microstructural characterisation and flow behaviour of sandstone in response to the different degree of heating. Out of the two knowledge gaps, in the current research work, various attempts were made to investigate the microstructural variation at different temperature levels. However, knowledge about the permeability or the fluid flow aspects of sandstone at different temperature levels is still missing in the literature and that can be the possible future work or the extension of the current research work.

A rock is composed of various rock-forming minerals and various microscopic features such as microcracks, mineral cavities, and microcavities. Even if in the macroscopic observation rocks are seemed to be quite homogeneous, at the microstructural level they are far more inhomogeneous. The macroscopic mechanical behaviour of rocks is predominantly depended on the behaviour of these microscopic features, grain boundaries and their interactions with each other. During the time of exposure to external stress or any environmental conditions such as high-temperature and high-pressures, a lot of interactions takes place inside the rock in the micro and nanoscale. In the current research work, various attempts have been made to investigate the behaviour of rocks in the macroscopic and microscopic level when they are exposed to conditions like high temperatures, high pressures, and loading rate. However, an investigation needs to be made in furthermore smaller scale i.e. in the atomic/nanoscale, where the development of microcracks, their propagation as macrocracks and structural irregularities in the micro and nanoscale can be precisely observed. Such problems can be answered with the help of molecular dynamics (MD) simulation that observes the precise atomic motion. Molecular and atomic trajectories are calculated based on their interactions.

Appendix

Appendix 1 The theoretical background for the strain-rate effect on the rock properties

To explain the strain rate effect on the various mechanical properties of the rock, a model has been described in this section.

Standard nonlinear solid model

The standard nonlinear solid model is used to describe the behaviour of a viscoelastic material such as a rock with the help of a spring and a dashpot in series with each other, both of which are in parallel with another spring (**Figure I**). Chong et al. (1980); Chong and Boresi (1990); and Wasantha et al. (2015) have employed this model to describe the strain-rate dependency of the oil shale and sandstone.

Microscopically, every particle is considered as a minute standard nonlinear solid.

Let

η_p : viscosity of the particle;

e_1 : spring constant in series with η_p;

e_2 : spring constant parallel to η_p and e_1;

v : volume of the test sample;

t : time variable;

s : space variable; and

x : longitudinal distance (along with load direction)

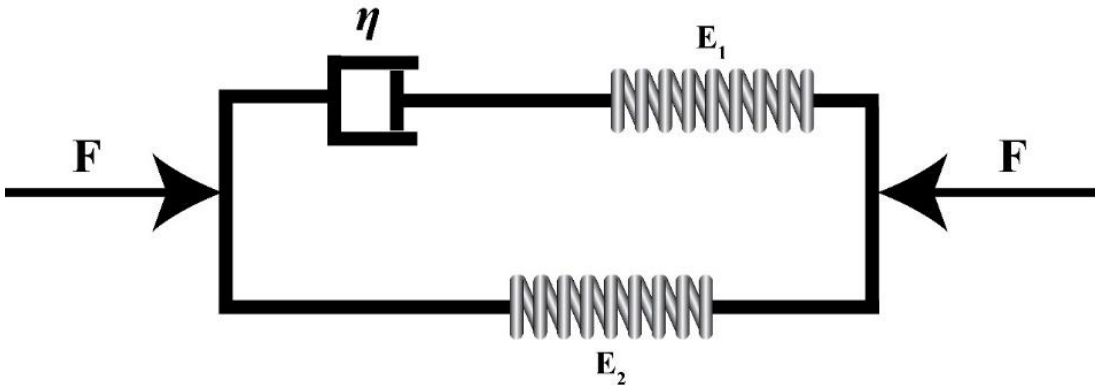

Figure I *Standard nonlinear solid model (modified after Chong et al. (1980))*

The input energy can be evaluated by the following relation:

$$W_{IN} = F \iint \dot{\varepsilon}\, dx\, dt \qquad \text{Eq. 1}$$

Similarly, the strain energy can be given as

$$W_S = \frac{1}{2}\int k(e_1 + e_2)\,(\iint \dot{\varepsilon}\, ds\, dt)^2 dV \qquad \text{Eq. 2}$$

where,

k : orientation constant.

The dissipative energy can be evaluated as

$$W_D = \iiint k\, \eta_p \dot{\varepsilon}^2\, ds\, dt\, dV \qquad \text{Eq. 3}$$

From the energy balance point of view,

$$W_{IN} = W_S + W_D \qquad \text{Eq. 4}$$

For a low strain rate condition: $\dot{\varepsilon}^2 \rightarrow 0$; as a result of this, the relaxation of the dashpot, spring e_1, does not act.

$$F \iint \dot{\varepsilon}\, dx\, dt = \frac{1}{2}\int k(e_2)\,(\iint \dot{\varepsilon}\, ds\, dt)^2 dV \qquad \text{Eq. 5}$$

At a condition of ultimate load and strain,
F= F_u, $e_2 = e_{2u}$ and $\sigma_u = F_u/A$.

In higher strain rate conditions, W_D does not approach zero. In such a situation, both spring e_1 and e_2 act simultaneously along with the dashpot, and the observed strain remains constant. In such cases, a higher ultimate load (F_u) is required to induce a fracture in the rock. Thus, σ_u is also much higher in the case of a high strain rate.

Viscosity in rock is primarily due to the intermolecular forces prior to nucleation of microcracks, and frictional forces throughout the crack propagation stage. With low strain rates, the dashpot relaxes gradually, allowing the spring E_2 to hold the total applied load in the form of strain energy, which gradually leads to the failure of the rock material. However, in a high strain rate condition, the dashpot stiffens, and both the spring E_1 and E_2 act simultaneously. In such cases, there will be a dissipation of some input energy through the dashpot and a higher force will be required for the failure of the rock specimen. Ultimately, the higher strain rate condition will lead to a much higher strength and elastic modulus of the rock (Chong et al., 1980; Chong and Boresi, 1990; Wasantha et al., 2015).

Appendix 2 Energy-release rate

As proposed by Griffith, the strain-energy-release rate is a measure of the energy that is dissipated per unit increase in an area during crack growth and is represented by *G* (Griffith, 1921).

According to Westergaard's approach (Westergaard, 1939), the displacement field in the vicinity of the crack tip for plane stress condition in the direction of maximum tension can be obtained using Eq. 6:

$$u_2 = \frac{K_I}{\mu}\sqrt{\left(\frac{r}{2\pi}\right)}\, sin\frac{\theta}{2}\left(\frac{2}{(1+\nu)} - cos^2\frac{\theta}{2}\right) \qquad \text{Eq. 6}$$

where *r, θ* are the polar coordinates of the point.

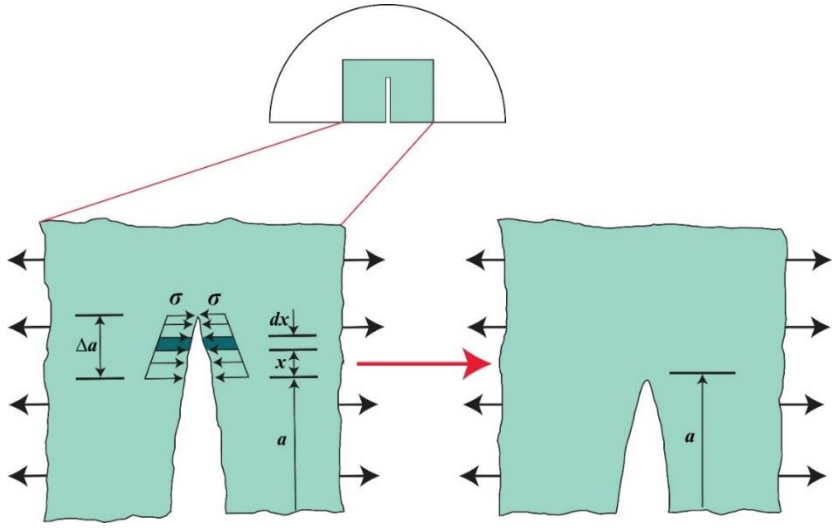

Figure II *Closure of the crack to find the relation between G_I and K_I (modified after Kumar (2009))*

Considering a crack of initial length *a*, with the application of load the crack starts to propagate and the initial crack length is extended by an incremental length of Δ*a* (**Figure**). The new crack length is *a'* = *a*+Δ*a* and the stress intensity factor for the new crack length is *K'*. At distance *x*, from the previous crack tip, that is at a distance Δ*a*-*x* from the extended crack tip, the displacement of a crack face in the direction of the maximum tension for θ=180° is:

$$u_2(x) = \frac{K_I'}{\mu}\sqrt{\left(\frac{\Delta a - x}{2\pi}\right)}\frac{2}{1+\nu} \qquad \text{Eq. 7}$$

Each crack face in the portion of Δ*a* has moved a distance of $u_2(x)$ due to the influence of the normal stress, σ_{22} equal to:

$$\sigma_{22}(x) = \frac{K_I}{\sqrt{2\pi x}} \quad \text{Eq. 8}$$

According to Irwin, the total elastic work required by σ_{22} to close the crack is equal to the energy released (Irwin, 1957).

$$G_I B\,\Delta a = 2\int_0^{\Delta a} \frac{B\sigma_{22}u_2}{2} dx \quad \text{Eq. 9}$$

where B is the thickness of the specimen. Putting Eq.7 and Eq.8 in Eq.9 and taking the limit $\Delta a \rightarrow 0$:

$$G_I = \lim_{\Delta\to 0} \frac{2}{(1+\nu)\,\mu\,\Delta a}\int_0^{\Delta a} \frac{K_I}{\sqrt{2\pi x}} \frac{K_I'\sqrt{(\Delta a - x)}}{\sqrt{2\pi}} dx \quad \text{Eq. 10}$$

$$K_I' = K_I + \Delta K_I \quad \text{Eq. 11}$$

Δa can be very small, such that $\Delta K'$ can be made small enough in comparison to K_I, and as a result of which $\Delta K'$ can be neglected.

$$G_I = \lim_{\Delta\to 0} \frac{K_I^2}{(1+\nu)\,\pi\,\mu\,\Delta a}\int_0^{\Delta a} \sqrt{\frac{\Delta a - x}{x}} dx \quad \text{Eq. 12}$$

In order to solve the integral equation, putting $x = \Delta a\, Sin^2\alpha$

When $x = 0$ and $\alpha = 0$, and when $x = \Delta a$, $\alpha = \pi/2$ and $dx = \Delta a$ 2Sinα Cosα dα

$$G_I = \lim_{\Delta\to 0} \frac{K_I^2}{(1+\nu)\,\pi\,\mu\,\Delta a}\int_0^{\frac{\pi}{2}} \sqrt{\frac{(\Delta a - \Delta a\, Sin^2\alpha)}{\Delta a\, Sin^2\alpha}}\,\Delta a\, 2Sin\alpha\, Cos\alpha\, d\alpha$$

$$G_I = \frac{K_I^2\,\Delta a}{(1+\nu)\,\pi\,\mu\,\Delta a}\int_0^{\frac{\pi}{2}} 2Cos^2\alpha\, d\alpha$$

$$G_I = \frac{K_I^2}{(1+\nu)\,\pi\,\mu}\int_0^{\frac{\pi}{2}} 2Cos^2\alpha\, d\alpha$$

$$G_I = \frac{K_I^2}{(1+\nu)\,\pi\,\mu}\,\frac{\pi}{2} \quad \text{Eq. 13}$$

Replacing μ by E/2(1+ν)

$$G_I = \frac{K_I^2\,2\,(1+\nu)}{(1+\nu)\,\pi\,E}\,\frac{\pi}{2}$$

$$G_I = \frac{K_I^2}{E} \quad \text{Eq. 14}$$

Similarly, for mode II and mode III, G_{II} and G_{III} can be derived as:

$$G_{II} = \frac{K_{II}^2}{E}$$

$$G_{III} = (1+\nu)\frac{K_{III}^2}{E} = \frac{K_{III}^2}{2\mu}$$

The total energy-release rate of each mode can be summed and evaluated as $G_{TOT} = G_I + G_{II} + G_{III}$.

Appendix 3 Number of specimens used for various mechanical testing

Rock type	**Location**	**Investigation (Measured properties/analysis)**	**Number of specimen used**
Jodhpur sandstone	Jodhpur, Rajasthan, India	Uniaxial compressive strength (NTP, TT, HT, RC, CL)	104 (5+27+27+27+18)
		Young's modulus (NTP, TT, HT, RC)	
		Poisson's ratio (NTP, TT, RC)	
		Tensile strength (NTP, TT, HT, RC)	60 (6+18+18+18)
		Triaxial compressive strength (NTP, HTP)	8
		Young's modulus (NTP, HTP)	
		Cohesion (NTP, HTP)	
		Internal friction (NTP, HTP)	
Dholpur sandstone	Dholpur, Rajasthan, India	Uniaxial compressive strength	5
		Young's modulus	
		Tensile strength	5
		Fracture toughness	15
Gondwana Sandstone	Benhardhi, Jharkhand, India	Uniaxial compressive strength	5
		Young's modulus	
		Tensile strength	6
Monaharpur sandstone	Sundergarh, Odisha, India	Uniaxial compressive strength	5
		Young's modulus	
		Tensile strength	5
		Fracture toughness	15
Jhiri Shale	Jhiri, Madhya Pradesh, India	Uniaxial compressive strength	16
		Young's modulus	
		Tensile strength	16
		Fracture toughness	16
		Energy release rate	

NTP: Normal temperature and pressure; TT: Thermally treated; HT: High temperature; RC: Rapid cooled; HTTP: High temperature and pressure, CL: Cyclic loading

References

AAPG Energy Minerals Division, 2015. Unconventional energy resources: 2015 review. Nat. Resour. Res. 24, 443–508. https://doi.org/10.1007/s11053-015-9288-6

Ajdukiewicz, J.M., Larese, R.E., 2012. How clay grain coats inhibit quartz cement and preserve porosity in deeply buried sandstones: Observations and experiments. Am. Assoc. Pet. Geol. Bull. 96, 2091–2119. https://doi.org/10.1306/02211211075

Akanksha, Singh, A.K., Mohantya, D., Jena, H.M., 2017. Characterization of lignite for underground coal gasification in India. Energy Sources, Part A Recover. Util. Environ. Eff. 39, 1762–1770. https://doi.org/10.1080/15567036.2017.1352630

Al-Kharusi, A.S., Blunt, M.J., 2007. Network extraction from sandstone and carbonate pore space images. J. Pet. Sci. Eng. 56, 219–231. https://doi.org/10.1016/j.petrol.2006.09.003

Al-Shayea, N.A., Khan, K., Abduljauwad, S.N., 2000. Effects of confining pressure and temperature on mixed-mode (I-II) fracture toughness of a limestone rock. Int. J. Rock Mech. Min. Sci. 37, 629–643. https://doi.org/10.1016/S1365-1609(00)00003-4

Aliha, M.R.M., Ashtari, R., Ayatollahi, M.R., 2006. Mode I and Mode II Fracture Toughness Testing for a Coarse Grain Marble. Appl. Mech. Mater. 5–6, 181–188. https://doi.org/10.4028/www.scientific.net/AMM.5-6.181

Aliha, M.R.M., Sistaninia, M., Smith, D.J., Pavier, M.J., Ayatollahi, M.R., 2012. Geometry effects and statistical analysis of mode I fracture in guiting limestone. Int. J. Rock Mech. Min. Sci. 51, 128–135. https://doi.org/10.1016/j.ijrmms.2012.01.017

Altindag, R., 2002. The evaluation of rock brittleness concept on rotary blast hole drills. J. South African Inst. Min. Metall. 102, 61–66.

Altindag, R., Guney, A., 2010. Predicting the relationships between brittleness and mechanical properties (UCS, TS and SH) of rocks. Sci. Res. Essays 5, 2107–2118.

Andrä, H., Combaret, N., Dvorkin, J., Glatt, E., Han, J., Kabel, M., Keehm, Y., Krzikalla, F., Lee, M., Madonna, C., Marsh, M., Mukerji, T., Saenger, E.H., Sain, R., Saxena, N., Ricker, S., Wiegmann, A., Zhan, X., 2013. Digital rock physics benchmarks-Part I: Imaging and segmentation. Comput. Geosci. 50, 25–32. https://doi.org/10.1016/j.cageo.2012.09.005

Anovitz, L.M., Cole, D.R., 2015. Characterization and Analysis of Porosity and Pore Structures. Rev. Mineral. Geochemistry 80, 61–164. https://doi.org/10.2138/rmg.2015.80.04

Anovitz, L.M., Cole, D.R., Rother, G., Allard, L.F., Jackson, A.J., Littrell, K.C., 2013.

Diagenetic changes in macro- to nano-scale porosity in the St. Peter Sandstone: An (ultra) small angle neutron scattering and backscattered electron imaging analysis. Geochim. Cosmochim. Acta 102, 280–305. https://doi.org/10.1016/J.GCA.2012.07.035

Araújo, R.G.S., Sousa, J.L.A.O., Bloch, M., 1997. Experimental investigation on the influence of temperature on the mechanical properties of reservoir rocks. Int. J. Rock Mech. Min. Sci. 34, 298. https://doi.org/10.1016/S1365-1609(97)00065-8

Arias-Buitrago, J.A., 2015. Efecto de la Temperatura en las Propiedades Mecánicas y Petrofísicas de Formaciones de Crudo Pesado. (Ph.D. Thesis). Universidad Nacional de Colombia Facultad, Medellín, Colombia.

Arns, C.H., Bauget, F., Limaye, A., Sakellariou, A., Senden, T.J., Sheppard, A.P., Sok, R.M., Pinczewski, W. V, Bakke, S., Berge, L.I., Øren, P., 2004. Pore Scale Characterisation of Carbonates using X-ray microtomography. SPE Annu. Tech. Conf. Exhib. https://doi.org/10.2118/90368-MS

Arns, C.H., Knackstedt, M.A., Pinczewski, W.V., Garboczi, E.J., 2002. Computation of linear elastic properties from microtomographic images: Methodology and agreement between theory and experiment. Geophysics 67, 1396–1405. https://doi.org/10.1190/1.1512785

Arora, V., Cai, Y., 2014. U.S. natural gas exports and their global impacts. Appl. Energy 120, 95–103. https://doi.org/10.1016/j.apenergy.2014.01.054

Asadi, S., Javan, M.M., Bohloli, B., Mutabashiani, S., 2013. Experimental, numerical and analytical investigation the initiation and propagation of hydraulic fracturing (case study: Sarvak lime stone). World Appl. Sci. J. 22, 637–646. https://doi.org/10.5829/idosi.wasj.2013.22.05.1696

ASTM D2845-08, 2008. Standard Test Method for Laboratory Determination of Pulse Velocities and Ultrasonic Elastic Constants of Rock. ASTM International, West Conshohocken, United States. https://doi.org/10.1520/D2845-08.2

ASTM D3967-08, 2008. Standard Test Method for Splitting Tensile Strength of Intact Rock Core Specimens. ASTM Int. West Conshohocken, PA, 20–23. https://doi.org/10.1520/D3967-08.2

ASTM D4543, 2008. Standard Practices for Preparing Rock Core as Cylindrical Test Specimens and verifying Conformance to Dimensional and Shape Tolerances. Astm 1–9. https://doi.org/10.1520/D4543-08.

ASTM D7012-13, 2013. Standard Test Methods for Compressive Strength and Elastic moduli of Intact Rocks and Core Specimens under varying States of Stress and Temperatures. ASTM International, West Conshohocken, United States. https://doi.org/10.1520/D7012-

13.1

ASTM D7012-14, 2004. Compressive Strength and Elastic Moduli of Intact Rock Core Specimens under Varying States of Stress and Temperatures 1. ASTM 4–11. https://doi.org/10.1520/D7012-14.1.5.1.1

Atkinson, C., Smelser, R.E., Sanchez, J., 1982a. Combined mode fracture via the cracked Brazilian disk. Int. J. Fract. 18, 279–291.

Atkinson, C., Smelser, R.E., Sanchez, J., 1982b. Combined mode fracture via the cracked Brazilian disc test. Int. J. Fract. 18, 279–291.

Awasthi, A.K., Parkash, B., 1981. Depositional environments of unfossiliferous sediments of the Jodhpur group, Western India. Sediment. Geol. 30, 15–42. https://doi.org/10.1016/0037-0738(81)90012-9

Ayatollahi, M.R., 2015. Stress Intensity Factors of Semi - Circular Bend Specimens with Straight - Through and Chevron Notches. Rock Mech. Rock Eng. 1–12. https://doi.org/10.1007/s00603-015-0830-y

Ayatollahi, M.R., Alborzi, M.J., 2013. Rock fracture toughness testing using SCB specimen. 13the Int. Conf. Fract. 1–7.

Ayatollahi, M.R., Aliha, M.R.M., 2007. Fracture toughness study for a brittle rock subjected to mixed mode I/II loading. Int. J. Rock Mech. Min. Sci. 44, 617–624. https://doi.org/10.1016/j.ijrmms.2006.10.001

Ayatollahi, M.R., Aliha, M.R.M., 2006. On determination of mode II fracture toughness using semi-circular bend specimen. Int. J. Solids Struct. 43, 5217–5227. https://doi.org/10.1016/j.ijsolstr.2005.07.049

Ayatollahi, M.R., Mahdavi, E., Alborzi, M.J., Obara, Y., 2015. Stress Intensity Factors of Semi - Circular Bend Specimens with Straight - Through and Chevron Notches. Rock Mech. Rock Eng. 1–12.

Azad, A., Chalaturnyk, R.J., 2011. Numerical Study of SAGD: Geomechanical-Flow Coupling for Athabasca Oil Sands Reservoirs, in: 45th US Rock Mechanics and Geomechanics Symposium. pp. 1–14.

Baldwin, C.A., Sederman, A.J., Mantle, M.D., Alexander, P., Gladden, L.F., 1996. Determination and Characterization of the Structure of a Pore Space from 3D Volume Images. J. Colloid Interface Sci. 181, 79–92. https://doi.org/10.1006/JCIS.1996.0358

Balme, M.., Rocchi, V., Jones, C., Sammonds, P.., Meredith, P.., Boon, S., 2004. Fracture toughness measurements on igneous rocks using a high-pressure, high-temperature rock fracture mechanics cell. J. Volcanol. Geotherm. Res. 132, 159–172.

https://doi.org/10.1016/S0377-0273(03)00343-3

Banks-Sills, L., Bortman, Y., 1986. A mixed mode fracture specimen; analysis and testing. Int. J. Fract. 30, 181–201.

Barshad, I., 1972. Temperature and heat of reaction calibration of the differential thermal apparatus. Am. Mineral. 37, 667–694.

Barton, N., 1976. The shear strength of rock and rock joints. Int. J. Rock Mech. Min. Sci. 13, 255–279. https://doi.org/10.1016/0148-9062(76)90003-6

Bazant, Z.P., Prat, P.C., 1988. Effect of Temperature and Humidity on Fracture Energy of Concrete. ACI Mater. J. 85, 262–271.

Bernard, D., Guillon, O., Combaret, N., Plougonven, E., 2011. Constrained sintering of glass films: Microstructure evolution assessed through synchrotron computed microtomography. Acta Mater. 59, 6228–6238. https://doi.org/10.1016/j.actamat.2011.06.022

Bertani, R., 2015. Geothermal Power Generation in the World 2010 – 2014 Update Report, in: Proceedings World Geothermal Congress. pp. 1–19. https://doi.org/10.1016/j.geothermics.2011.10.001

Bésuelle, P., Desrues, J., Raynaud, S., 2000. Experimental characterisation of the localisation phenomenon inside a Vosges sandstone in a triaxial cell. Int. J. Rock Mech. Min. Sci. 37, 1223–1237. https://doi.org/10.1016/S1365-1609(00)00057-5

Beucher, S., Meyer, F., 1993. The morphological approach to segmentation: The watershed transformation, in: Dougherty, E.. (Ed.), Mathematical Morphology in Image Processing. pp. 433–481.

Bhutto, A.W., Bazmi, A.A., Zahedi, G., 2013. Underground coal gasification: From fundamentals to applications. Prog. Energy Combust. Sci. 39, 189–214. https://doi.org/10.1016/j.pecs.2012.09.004

Bieniawski, Z.T., 1970. Time-dependent behaviour of fractured rock. Rock Mech. Rock Eng. 2, 123–137. https://doi.org/10.1007/BF01239744

Bieniawski, Z.T., 1967. Mechanism of brittle fracture of rock Part-I. Int. J. Rock Mech. Min. Sci. 4, 395–406.

Bjørlykke, K., Ramm, M., Saigal, G.C., 1989. Sandstone diagenesis and porosity modification during basin evolution. Geol. Rundschau 78, 243–268. https://doi.org/10.1007/BF01988363

Blanton, T.L., 1981. Effect of strain rates from 10-2 to 10 sec-1 in triaxial compression tests on three rocks. Int. J. Rock Mech. Min. Sci. 18, 47–62. https://doi.org/10.1016/0148-

9062(81)90265-5

Blenkinsop, T., 2000. Cataclasis, in: Deformation Microstructures and Mechanisms in Minerals and Rocks. Kluwer Academic Publishers, pp. 7–23.

Blinderman, M.S., Klimenko, A.Y., 2018. Introduction to underground coal gasification and combustion, in: Underground Coal Gasification and Combustion. pp. 1–8.

Blunt, M.J., 2001. Flow in porous media - Pore-network models and multiphase flow. Curr. Opin. Colloid Interface Sci. 6, 197–207. https://doi.org/10.1016/S1359-0294(01)00084-X

Blunt, M.J., Jackson, M.D., Piri, M., Valvatne, P.H., 2002. Detailed physics, predictive capabilities and macroscopic consequences for pore-network models of multiphase flow. Adv. Water Resour. 25, 1069–1089. https://doi.org/10.1016/S0309-1708(02)00049-0

Bose, P.R., 2011. Essar Oil, Lanco, Adani bid for Coal India's underground gasification projects., in: Business Line. https://www.thehindubusinessline.com/companies/essar-oil-lanco-adani-bid-for-coal-indias-underground-gasification-projects/article23049526.ece.

Brace, W.F., 1964. Brittle fracture of rocks, in: Judd, W.. (Ed.), State of Stress in the Earth's Crust. American Elsevier Publishing Co, New York, USA, pp. 111–180.

Brede, M., 1993. Brittle-to-ductile transition in silicon. Acta Metall. Mater. 41, 211–228.

Brotóns, V., Tomás, R., Ivorra, S., Alarcón, J.C., 2013. Temperature influence on the physical and mechanical properties of a porous rock: San Julian's calcarenite. Eng. Geol. 167, 117–127. https://doi.org/10.1016/j.enggeo.2013.10.012

Buades, A., Coll, B., Morel, J.M., 2005. A Non-Local Algorithm for Image Denoising, in: EEE Computer Society Conference on Computer Vision and Pattern Recognition (CVPR'05). IEEE, pp. 60–65. https://doi.org/10.1109/CVPR.2005.38

Cadoni, E., 2010. Dynamic characterization of orthogneiss rock subjected to intermediate and high strain rates in tension. Rock Mech. Rock Eng. 43, 667–676. https://doi.org/10.1007/s00603-010-0101-x

Chaki, S., Takarli, M., Agbodjan, W.P., 2008. Influence of thermal damage on physical properties of a granite rock: Porosity, permeability and ultrasonic wave evolutions. Constr. Build. Mater. 22, 1456–1461. https://doi.org/10.1016/j.conbuildmat.2007.04.002

Chang, S.H., Lee, C.I., 2004. Estimation of cracking and damage mechanisms in rock under triaxial compression by moment tensor analysis of acoustic emission. Int. J. Rock Mech. Min. Sci. 41, 1069–1086. https://doi.org/10.1016/j.ijrmms.2004.04.006

Chang, S.H., Lee, C.I., Jeon, S., 2002. Measurement of rock fracture toughness under modes I and II and mixed-mode conditions by using disc-type specimens. Eng. Geol. 66, 79–97.

https://doi.org/10.1016/S0013-7952(02)00033-9

Chauhan, D.S., Ram, B., Ram, N., 2004. Jodhpur Sandstone: a gift of ancient beaches to western Rajasthan. J. Geol. Soc. India 64.

Chen, T., Xu, J., Liu, S., Zhi, L., 2013. Experimental study on ultrasonic and mechanical properties of sandstone influenced by water-saturation and high temperatures. Chinese J. Undergr. Sp. Eng. 9, 1236–1241.

Cho, S.H., Ogata, Y., Kaneko, K., 2003. Strain-rate dependency of the dynamic tensile strength of rock. Int. J. Rock Mech. Min. Sci. 40, 763–777. https://doi.org/10.1016/S1365-1609(03)00072-8

Chong, K., Kuruppu, M.D., 1984. New specimen for fracture toughness determination for rock and other materials. Int. J. Fract. 26, R59–R62. https://doi.org/10.1007/BF01157555

Chong, K.P., Boresi, A.P., 1990. Strain rate dependent mechanical properties of new albany reference shale. Int. J. Rock Mech. Min. Sci. 27, 199–205. https://doi.org/10.1016/0148-9062(90)94328-Q

Chong, K.P., Hoyt, P.M., Smith, J.W., Paulsen, B.Y., 1980. Effects of Strain Rate on Oil Shale Fracturing. Int. J. Rock Mech. Min. Sci. Geomech. Abstr. 17, 35–43. https://doi.org/10.1016/0148-9062(80)90004-2

Chong, K.P., Kuruppu, M.D., Kuszmaul, J.S., 1987. Fracture toughness determination of layered materials. Eng. Fract. Mech. 28, 43–54. https://doi.org/10.1016/0013-7944(87)90118-4

Cleja-Tigoiu, S., 1991. Elasto-viscoplastic constitutive equations for rock-type materials (finite deformation). Int. J. Eng. Sci. 29, 1531–1544.

Dai, F., Xia, K., 2013. Laboratory measurements of the rate dependence of the fracture toughness anisotropy of Barren granite. Int. J. Rock Mech. Min. Sci. 60, 57–65. https://doi.org/10.1016/j.ijrmms.2013.08.011

Dai, F., Xia, K., Zheng, H., Wang, Y.X., 2011. Determination of dynamic rock Mode-I fracture parameters using cracked chevron notched semi-circular bend specimen. Eng. Fract. Mech. 78, 2633–2644. https://doi.org/10.1016/j.engfracmech.2011.06.022

Darot, M., Gueguen, Y., Benchemam, Z., Gaboriaud, R., 1985. Ductile-brittle transition investigated by micro-indentation : results for quartz and olivine. Phys. Earth Planet. Inter. 40, 180–186.

David, C., Wong, T.F., Zhu, W., Zhang, J., 1994. Laboratory measurement of compaction-induced permeability change in porous rocks: Implications for the generation and maintenance of pore pressure excess in the crust, Pure and Applied Geophysics

PAGEOPH. https://doi.org/10.1007/BF00874337

Delle Piane, C., Arena, A., Sarout, J., Esteban, L., Cazes, E., 2015. Micro-crack enhanced permeability in tight rocks: An experimental and microstructural study. Tectonophysics 665, 149–156. https://doi.org/10.1016/j.tecto.2015.10.001

Demirbas, A., 2016. Waste energy for life cycle assessment, Waste Energy for life Cycle Assessment. Springer International Publishing, Switzerland. https://doi.org/10.1007/978-3-319-40551-3_2

Den'gina, N.I., Kazak, V.N., Pristash, V. V., 1993. Changes in rocks at high temperatures. J. Min. Sci. 29, 472–477. https://doi.org/10.1007/BF00733026

Deng, X.B., 2007. The thermal-drag exploitation study from UCG Trial, Sciencepaper Online. S. 1-8 (in Chinese). http://www.paper.edu.cn/index.php/default/releasepaper/content/200707-374.

Desbois, G., Urai, J.L., Kukla, P.A., Konstanty, J., Baerle, C., 2011. High-resolution 3D fabric and porosity model in a tight gas sandstone reservoir:A new approach to investigate microstructures from mm- to nm-scale combining argon beam cross-sectioning and SEM imaging. J. Pet. Sci. Eng. 78, 243–257. https://doi.org/10.1016/J.PETROL.2011.06.004

Devarapalli, R.S., Islam, A., Faisal, T.F., Sassi, M., Jouiad, M., 2017. Micro-CT and FIB–SEM imaging and pore structure characterization of dolomite rock at multiple scales. Arab. J. Geosci. 10. https://doi.org/10.1007/s12517-017-3120-z

Domanski, M., Webb, J., 2007. A review of heat treatment research. Lithic Technol. 32, 153–194.

Donath, F.A., Fruth, L.S., 1971. Dependence of Strain-Rate Effects on Deformation Mechanism and Rock Type. J. Geol. 79, 347–371. https://doi.org/10.1086/627630

Dong, H., Blunt, M.J., 2009. Pore-network extraction from micro-computerized-tomography images. Phys. Rev. E - Stat. Nonlinear, Soft Matter Phys. 80, 1–11. https://doi.org/10.1103/PhysRevE.80.036307

Dong, H., Fjeldstad, S., Roth, S., Bakke, S., Øren, P., 2008. Pore Network Modelling on Carbonate: A comparative Study of Different Micro-CT Network Extraction Methods, in: Proc. International Symp. Society of Core Analysts. pp. 2008–2031.

Dragon, A., Mroz, Z., 1979. A continuum model for plastic-brittle behaviour of rock and concrete. Int. J. Eng. Sci. 17, 121–137.

Duda, M., Renner, J., 2013. The weakening effect of water on the brittle failure strength of sandstone. Geophys. J. Int. 192, 1091–1108. https://doi.org/10.1093/gji/ggs090

Dvorkin, J., Derzhi, N., Diaz, E., Fang, Q., 2011. Relevance of computational rock physics.

GEOPHYSICS 76, E141–E153. https://doi.org/10.1190/geo2010-0352.1

Dwivedi, R.D., Goel, R.K., Prasad, V.V.R., Sinha, A., 2008. Thermomechanical properties of Indian and other granites. Int. J. Rock Mech. Min. Sci. 45, 303–315.

Eberhardt, E., Stead, D., Stimpson, B., Read, R.S., 1998. Identifying crack initiation and propagation thresholds in brittle rock. Can. Geotech. J. 35, 222–233. https://doi.org/10.1139/t97-091

Ehrenberg, S.N., Nadeau, P.H., Steen, Ø., 2009. Petroleum reservoir porosity versus depth: Influence of geological age. Am. Assoc. Pet. Geol. Bull. 93, 1281–1296. https://doi.org/10.1306/06120908163

El Bied, A., Sulem, J., Martineau, F., 2002. Microstructure of shear zones in Fontainebleau sand stone. Int. J. Rock Mech. Min. Sci. 39, 917–932.

Elahi, S.M., 2016. Geomechanical Modeling of Underground Coal Gasification.

Ergo Exergy-GAIL, 1999. Ergo Exergy-GAIL UCG in India. http://www.ergoexergy.com/about_us_ourb_projects_gail.htm.

Ergo Exergy, 2015. Ergo Exergy – Abhijeet Group – UCG in India. http://www.ergoexergy.com/about_us_ourb_projects_ae.html.

Escalera, E., Antti, M.L., Odén, M., 2012. Thermal treatment and phase formation in kaolinite and illite based clays from tropical regions of Bolivia, in: 6th EEIGM International Conference on Advanced Materials Research. IOP Conference Series: Materials Science and EngineeringIOP Conference Series: Materials Science and Engineering. pp. 1–8. https://doi.org/10.1088/1757-899X/31/1/012017

Fairhurst, C., 1964. On the validity of the 'Brazilian' test for brittle materials. Int. J. Rock Mech. Min. Sci. Geomech. Abstr. 1, 535–546. https://doi.org/10.1016/0148-9062(64)90060-9

Fourmeau, M., Gomon, D., Vacher, R., Hokka, M., Kane, A., Kuokkala, V.-T., 2014. Application of DIC technique for studies of Kuru granite rock under static and dynamic loading. Procedia Mater. Sci. 3, 691–697.

Fowell, R.J., 1995. Suggested method for determining mode I fracture toughness using cracked chevron notched Brazilian disc (CCNBD) specimens. Int J Rock Mech Min Sci Geomech Abstr 32, 57–64.

Fredrich, J.T., Evans, B., Wong, T.-F., 1990. Effect of grain size on brittle and semibrittle strength: Implications for micromechanical modelling of failure in compression. J. Geophys. Res. 95, 10907–10920. https://doi.org/10.1029/JB095iB07p10907

Fredrich, J.T., Wong, T., 1986. Micromechanics of Thermally Induced Cracking in Threee

Crustal Rocks. J. Geophys. Res. 91, 743–764. https://doi.org/10.1029/JB091iB12p12743

Fu, X., Xie, Q., Liang, L., 2015. Comparison of the Kaiser effect in marble under tensile stresses between the Brazilian and bending tests. Bull. Eng. Geol. Environ. 74, 535–543. https://doi.org/10.1007/s10064-014-0707-4

Fuenkajorn, K., Kenkhunthod, N., 2010. Influence of Loading Rate on Deformability and Compressive Strength of Three Thai Sandstones. Geotech. Geol. Eng. 28, 707–715. https://doi.org/10.1007/s10706-010-9331-7

Fukui, K., Okubo, S., Ogawa, A., 2004. Some aspects of loading-rate dependency of Sanjome andesite strengths. Int. J. Rock Mech. Min. Sci. 41, 1215–1219. https://doi.org/10.1016/j.ijrmms.2004.06.001

Funatsu, T., Kuruppu, M., Matsui, K., 2014a. Effects of temperature and confining pressure on mixed-mode (I–II) and mode II fracture toughness of Kimachi sandstone. Int. J. Rock Mech. Min. Sci. 67, 1–8. https://doi.org/10.1016/j.ijrmms.2013.12.009

Funatsu, T., Kuruppu, M., Matsui, K., 2014b. Effects of temperature and confining pressure on mixed-mode (I-II) and mode II fracture toughness of Kimachi sandstone. Int. J. Rock Mech. Min. Sci. 67, 1–8. https://doi.org/10.1016/j.ijrmms.2013.12.009

Funatsu, T., Seto, M., Shimada, H., Matsui, K., Kuruppu, M., 2004. Combined effects of increasing temperature and confining pressure on the fracture toughness of clay bearing rocks. Int. J. Rock Mech. Min. Sci. 41, 927–938. https://doi.org/10.1016/j.ijrmms.2004.02.008

Fusseis, F., Xiao, X., Schrank, C., De Carlo, F., 2014. A brief guide to synchrotron radiation-based microtomography in (structural) geology and rock mechanics. J. Struct. Geol. 65, 1–16. https://doi.org/10.1016/j.jsg.2014.02.005

Gale, J., Reed, R., Holder, J., 2007. Natural fractures in the Barnett Shale and their importance for hydraulic fracture treatments. Am. Assoc. Pet. Geol. Bull. 91, 603–622.

Gao, G., Yao, W., Xia, K., Li, Z., 2015. Investigation of the rate dependence of fracture propagation in rocks using digital image correlation (DIC) method. Eng. Fract. Mech. 138, 146–155. https://doi.org/10.1016/j.engfracmech.2015.02.021

Gautam, P.K., Verma, A.K., Jha, M.K., Sarkar, K., Singh, T.N., Bajpai, R.K., 2016. Study of Strain Rate and Thermal Damage of Dholpur Sandstone at Elevated Temperature. Rock Mech. Rock Eng. 49, 3805–3815. https://doi.org/10.1007/s00603-016-0965-5

Gautam, P.K., Verma, A.K., Maheshwar, S., Singh, T.N., 2015. Thermomechanical Analysis of Different Types of Sandstone at Elevated Temperature. Rock Mech. Rock Eng. https://doi.org/10.1007/s00603-015-0797-8

Géraud, Y., 1994. Variations of connected porosity and inferred permeability in a thermally cracked granite. Geophys. Res. Lett. 21, 979–982. https://doi.org/10.1029/94GL00642

Germanovich, L.N., Salganik, R.L., Dyskin, A. V, Lee, K.K., 1994. Mechanisms of brittle fracture of rock with pre-existing cracks in compression. Pure Appl. Gephysics 143, 117–149.

Glover, P.W.J., Baud, P., Darot, M., Meredith, P.G., Boon, S.A., LeRavalec, M., Zoussi, S., Reuschlé, T., 1995. α/β phase transition in quartz monitored using acoustic emissions. Geophys. J. Int. 120, 775–782. https://doi.org/10.1111/j.1365-246X.1995.tb01852.x

Goodman, R.E., 1963. Subaudible noise during compression of rocks. Bull. Geol. Soc. Am. 74, 487–490. https://doi.org/10.1130/0016-7606(1963)74[487:SNDCOR]2.0.CO;2

Goral, J., Miskovic, I., Gelb, J., Kasahara, J., 2015. Pore Network Investigation in Marcellus Shale Rock Matrix, in: Society of Petroleum Engineers. pp. 9–11. https://doi.org/10.1017/CBO9781107415324.004

Griffith, A.A., 1921. The Phenomena of Rupture and Flow in Solids. Philos. Trans. R. Soc. A Math. Phys. Eng. Sci. 221, 163–198. https://doi.org/10.1098/rsta.1921.0006

Gunsallus, K.L., Kulhawy, F.H., 1984. A comparative evaluation of rock strength measures. Int. J. Rock Mech. Min. Sci. Geomech. Abstr. 21, 233–248.

Guo, H., Aziz, N.I., Schmidt, L.C., 1993. Rock fracture-toughness determination by the Brazilian test. Eng. Geol. 33, 177–188. https://doi.org/10.1016/0013-7952(93)90056-I

Guo, X., Zou, G., Wang, Y., Wang, Y., Gao, T., 2017. Investigation of the temperature effect on rock permeability sensitivity. J. Pet. Sci. Eng. 156, 616–622. https://doi.org/10.1016/j.petrol.2017.06.045

Gupta, A., Civan, F., 1994. Temperature Sensitivity of Formation Damage in Petroleum Reservoirs, in: Society of Petroleum Engineers. pp. 1–14. https://doi.org/SPE-27368-MS

Haberfield, C., Johnston, I., 1989. Relationship between fracture toughness and tensile strength for geomaterials, in: 12th International Conference on Soil Mechanics and Foundation Engineering. Rio de Jeneiro, Brazil, pp. 47–52.

Hajpál, M., 2002. Changes in sandstones of historical monuments exposed to fire or high temperature. Fire Technol. 38, 373–382. https://doi.org/10.1023/A:1020174500861

Hajpal, M., Torok, A., 2004. Mineralogical and colour changes of quartz sandstones by heat. Environ. Geol. 46, 311–322. https://doi.org/10.1007/s00254-004-1034-z

Hajpál, M., Török, Á., 1998. Petrophysical and mineralogical studies of burnt sandstones, in: 2nd International PhD Symposium in Civil Engineering. Budapest, Hungary, pp. 1–9.

Hamawand, I., Yusaf, T., Hamawand, S.G., 2013. Coal seam gas and associated water: A

review paper. Renew. Sustain. Energy Rev. 22, 550–560. https://doi.org/10.1016/j.rser.2013.02.030

Hammond, G.P., O'Grady, Á., 2016. Indicative energy technology assessment of UK shale gas extraction. Appl. Energy In Press. https://doi.org/http://dx.doi.org/10.1016/j.apenergy.2016.02.024

Hardy, H.R.J., 1977. Emergence of acoustic emission/microseismic activity as a tool in geomechanics, in: Hardy, H.R., Leighton, L.W. (Eds.), Proceedings of the 1st Conference on Acoustic Emission/Microseismic Activity in Geologic Structures and Materials. Trans Tech Publications, Clausthal, Germany, pp. 3–31.

Hassanzadegan, A., 2013. Thermomechanical and poromechanical behavior of Flechtinger sandstone. (Ph.D. thesis). Technischen Universit, Berlin.

Hassanzadegan, A., Blöcher, G., Milsch, H., Urpi, L., Zimmermann, G., 2014. The effects of temperature and pressure on the porosity evolution of flechtinger sandstone. Rock Mech. Rock Eng. 47, 421–434. https://doi.org/10.1007/s00603-013-0401-z

Hazzard, J.F., Young, R.P., Maxwell, S.C., 2000. Micromechanical modeling of cracking and failure in brittle rocks. J. Geophys. Res. Solid Earth 105, 16683–16697. https://doi.org/10.1029/2000JB900085

He, M.Y., Cao, H.C., Evans, A.G., 1990. Mixed-mode fracture: the four point shear specimen. Acta Metall. Mater. 38, 839–846.

He, T.-M., Zhao, Q., Ha, J., Xia, K., Grasselli, G., 2018. Understanding progressive rock failure and associated seismicity using ultrasonic tomography and numerical simulation. Tunn. Undergr. Sp. Technol. 81, 26–34. https://doi.org/10.1016/j.tust.2018.06.022

Heap, M.J., Baud, P., Meredith, P.G., Bell, A.F., Main, I.G., 2009. Time-dependent brittle creep in darley dale sandstone. J. Geophys. Res. Solid Earth 114, 1–22. https://doi.org/10.1029/2008JB006212

Heuze, F.E., 1983. High-Temperature Mechanical, Physical and Thermal-Properties of Granitic-Rocks—a Review. Int. J. Rock Mech. Min. Sci. 20, 3–10.

Hoek, E., 1983. Strength of jointed rock masses. Géotechnique 23, 187–223. https://doi.org/10.1680/geot.1983.33.3.187

Hogan, J.D., Rogers, R.J., Spray, J.G., Boonsue, S., 2012. Dynamic fragmentation of granite for impact energies of 6-28J. Eng. Fract. Mech. 79, 103–125. https://doi.org/10.1016/j.engfracmech.2011.10.006

Hokka, M., Black, J., Tkalich, D., Fourmeau, M., Kane, A., Hoang, N.H., Li, C.C., Chen, W.W., Kuokkala, V.T., 2016. Effects of strain rate and confining pressure on the

compressive behavior of Kuru granite. Int. J. Impact Eng. 91, 183–193. https://doi.org/10.1016/j.ijimpeng.2016.01.010

Holmes, R., Rupp, E.C., Vishal, V., Wilcox, J., 2015. Characterization and Adsorption Investigations of the Nanostructure of Gas Shales. Offshore Technology Conference, Rio de Janeiro, Brazil. https://doi.org/10.4043/26192-MS

Holt, R.M., Fjær, E., Stenebråten, J.F., Nes, O.-M., 2015. Brittleness of shales: Relevance to borehole collapse and hydraulic fracturing. J. Pet. Sci. Eng. 131, 200–209. https://doi.org/10.1016/j.petrol.2015.04.006

Homand-Etienne, F., Houpert, R., 1989. Thermally induced microcracking in granites: characterization and analysis. Int. J. Rock Mech. Min. Sci. Geomech. Abstr. 26, 125–134. https://doi.org/10.1016/0148-9062(89)90001-6

Hou, Z., Luo, X., 2012. Investigation of thermal effect on stability of deep wellbores in low and high permeable formations, in: Harmonising Rock Engineering and the Environment - Proceedings of the 12th ISRM International Congress on Rock Mechanics. pp. 1315–1319.

Hu, Q., Yang, X., Cai, Q., Huang, C., 2015. Application of ARAMIS Digital Speckle In Clay Interlayer Deformation Measurement. Electron. J. Geotech. Eng. 20, 287–300.

Huang, J., Wang, S., 1985. An experimental investigation concerning the comprehensive fracture toughness of some brittle rocks. Int. J. Rock Mech. Min. Sci. Geomech. Abstr. 22, 99–104.

Hucka, V., Das, B., 1974. Brittleness determination of rocks by different methods. Int. J. Rock Mech. Min. Sci. 11, 389–392. https://doi.org/10.1016/0148-9062(74)91109-7

Hudson, J.A., 1969. Tensile strength and the ring test. Int. J. Rock Mech. Min. Sci. Geomech. Abstr. 6, 91–97. https://doi.org/10.1016/0148-9062(69)90029-1

Hudson, J.A., Brown, E.T., Rummel, F., 1972. The controlled failure of rock discs and rings loaded in diametral compression. Int. J. Rock Mech. Min. Sci. 9, 241–248. https://doi.org/10.1016/0148-9062(72)90025-3

Indian Bureau of Mines, 2018. Coal & Lignite, in: Indian Minerals Yearbook 2017 (Part-III: Mineral Reviews).

Irwin, G.., 1957. Analysis of Stresses and Strains Near the End of a Crack Traversing a Plate. J. Appl. Mech. 24, 361–364.

ISRM, 2007. The complete ISRM suggested methods for rock characterisation, testing and monitoring: 1974–2006. ISRM and Turkish National Group of ISRM, Ankara.

ISRM, 1981. The ISRM Suggested Methods for Rock Characterization, Testing and

Monitoring. Pergamon Press.

Jaeger, J., Cook, N., 1976. Fundamentals of rock mechanics. Chapman and Hall, London.

Jain, P.K., 2017. Underground Coal Gasification-Experience of ONGC, in: Earth and Environmental Science. pp. 1–60.

Jian-an, H., Sijing, W., 1985. An Experimental Investigation Concerning the Comprehensive Fracture Toughness of Some Brittle Rocks. Int. J. Rock Mech. Min. Sci. Geomech. Abstr. 22, 99–104.

Jian-ping, Z., He-ping, X., Hong-wei, Z., Su-ping, P., 2010. SEM in situ investigation on thermal cracking behaviour of Pingdingshan sandstone at elevated temperatures. Geophys. J. Int. 181, 593–603. https://doi.org/10.1111/j.1365-246X.2010.04532.x

Jones, C., Meredith, P., 1998. An Experimental Study of Elastic Wave Propagation an Isotropy and Permeability an Isotropy In an Illitic Shale., in: SPE/ISRM Rock Mechanics in Petroleum Engineering. Society of Petroleum Engineers. https://doi.org/10.2118/47369-MS

Just, J., Kontny, A., 2012. Thermally induced alterations of minerals during measurements of the temperature dependence of magnetic susceptibility: a case study from the hydrothermally altered Soultz-sous-Forêts granite, France. Int. J. Earth Sci. 101, 819–839. https://doi.org/10.1007/s00531-011-0668-9

Kahraman, S., Altindag, R., 2004. A brittleness index to estimate fracture toughness. Int. J. Rock Mech. Min. Sci. 41, 343–348. https://doi.org/10.1016/j.ijrmms.2003.07.010

Kanninen, M.F., Popelar, C.H., 1985. Advanced Fracture Mechanics, Oxford Eng. ed. Oxford University Press, New York.

Kataoka, M., Kang, H., Cho, S., Obara, Y., 2014. Influence of Loading Rate on Fracture Toughness of Rock by Semi-Circular Bend (SCB) Test, in: 8th Asian Rock Mechanics Symposium. pp. 257–262.

Keles, C., Tutluoglu, L., 2011. Investigation of proper specimen geometry for mode i fracture toughness testing with flattened Brazilian disc method. Int. J. Fract. 169, 61–75. https://doi.org/10.1007/s10704-011-9584-z

Kempka, T., Nakaten, N., Schlüter, N., Azzam, R., 2009. Economic viability of in-situ coal gasification with downstream CO_2 storage. Glückauf Min. Report. 1, 43–50.

Kerr, R.A., 2010. Natural Gas From Shale Bursts Onto the Scene. Science (80-.). 328, 1624–1626.

Khadse, A., Qayyumi, M., Mahajani, S., Aghalayam, P., 2007. Underground coal gasification: A new clean coal utilization technique for India. Energy 32, 2061–2071.

https://doi.org/10.1016/j.energy.2007.04.012

Khan, E.A., Sogani, P.C., 1973. Stratigraphy and sedimentation of Trans-Aravalli Vindhyans of Western Rajasthan, in: Seminar on Recent Advances in the Geology of Rajasthan and Gujarat. Jaipur, Rajasthan, India, pp. 13–14.

Khan, K., Al-Shayea, N.A., 2000. Effect of Specimen Geometry and Testing Method on Mixed Mode I-II Fracture Toughness of a Limestone Rock from Saudi Arabia. Rock Mech. Rock Eng. 33, 179–206. https://doi.org/10.1007/s006030070006

Khandelwal, M., Ranjith, P.G., Pan, Z., Sanjayan, J.G., 2013. Effect of strain rate on strength properties of low-calcium fly-ash-based geopolymer mortar under dry condition. Arab. J. Geosci. 6, 2383–2389. https://doi.org/10.1007/s12517-011-0507-0

Klein, E., Baud, P., Reuschlé, T., Wong, T.F., 2001. Mechanical behaviour and failure mode of Bentheim sandstone under triaxial compression. Phys. Chem. Earth, Part A Solid Earth Geod. 26, 21–25. https://doi.org/10.1016/S1464-1895(01)00017-5

Kompaníková, Z., Gomez-Heras, M., Michňová, J., Durmeková, T., Vlčko, J., 2014. Sandstone alterations triggered by fire-related temperatures. Environ. Earth Sci. 72, 2569–2581. https://doi.org/10.1007/s12665-014-3164-2

Kong, B., Wang, E., Li, Z., Wang, X., Liu, J., Li, N., 2016. Fracture mechanical behavior of sandstone subjected to high-temperature treatment and its acoustic emission characteristics under uniaxial compression conditions. Rock Mech. Rock Eng. 49, 2641–2653.

Kranz, R.L., 1983. Microcracks in rocks: A review. Tectonophysics 100, 449–480. https://doi.org/10.1016/0040-1951(83)90198-1

Kumar, A., 1968. The effect of stress rate and temperature on the strength of basalt and granite. Geophysics 33, 501–510.

Kumar, A., Jain, P.K., Sharma, R.K., 2010. ONGC strive for underground coal gasification in India – past, present and future., in: Petrotech. pp. 1–5.

Kumar, P., 2009. Elements of Fracture Mechanics, 1st ed. Tata McGraw Hill Education private limited, New Delhi, India.

Kumari, W.G.P., Ranjith, P.G., Perera, M.S.A., Chen, B.K., Abdulagatov, I.M., 2017. Temperature-dependent mechanical behaviour of Australian Strathbogie granite with different cooling treatments. Eng. Geol. 229, 31–44. https://doi.org/10.1016/j.enggeo.2017.09.012

Kumari, W.G.P., Ranjith, P.G., Perera, M.S.A., Shao, S., Chen, B.K., Lashin, A., Arifi, N.A., Rathnaweera, T.D., 2017. Mechanical behaviour of Australian Strathbogie granite under

in-situ stress and temperature conditions: An application to geothermal energy extraction. Geothermics 65, 44–59. https://doi.org/10.1016/J.GEOTHERMICS.2016.07.002

Kuruppu, M.D., 2000. Fracture Toughness Testing of Geomaterials using Semicircular Specimens. Int. Conf. Geotech. Geol. Eng. Paper No. Gcc 0806.

Kuruppu, M.D., 1998. Stress intensity factors of chevron notched semi-circular Specimen, in: Proceeding of 3rd APCOM, Australian Institute of Mining and Metallurgy. pp. 111–112.

Kuruppu, M.D., 1997. Fracture toughness measurement using chevron notched semicircular bend specimen. Int J Fract 86, 33–38.

Kuruppu, M.D., Chong, K.P., 2012. Fracture toughness testing of brittle materials using semi-circular bend (SCB) specimen. Eng. Fract. Mech. 91, 133–150. https://doi.org/10.1016/j.engfracmech.2012.01.013

Kuruppu, M.D., Obara, Y., Ayatollahi, M.R., Chong, K.P., Funatsu, T., 2014. ISRM-Suggested Method for Determining the Mode I Static Fracture Toughness Using Semi-Circular Bend Specimen. Rock Mech. Rock Eng. 47, 267–274. https://doi.org/10.1007/s00603-013-0422-7

Lai, J., Wang, G., Wang, Z., Chen, J., Pang, X., Wang, S., Zhou, Z., He, Z., Qin, Z., Fan, X., 2017. A review on pore structure characterization in tight sandstones. Earth-Science Rev. https://doi.org/10.1016/j.earscirev.2017.12.003

Lajtai, E.Z., Duncan, E.J.S., Carter, B.J., 1991. The effect of strain rate on rock strength. Rock Mech. Rock Eng. 24, 99–109. https://doi.org/10.1007/BF01032501

Lan, H., Martin, C.D., Hu, B., 2010. Effect of heterogeneity of brittle rock on micromechanical extensile behavior during compression loading. J. Geophys. Res. 115, B01202. https://doi.org/10.1029/2009JB006496

Lankford, J.J., 1976. Dynamic strength of oil shale. Soc. Pet. Eng. 16, 17–22.

Lavrov, A., 2003. The Kaiser effect in rocks: Principles and stress estimation techniques. Int. J. Rock Mech. Min. Sci. 40, 151–171. https://doi.org/10.1016/S1365-1609(02)00138-7

Lawrence Livermore National Laboratory, 2012. LLNL to work with Interior Department on underground coal gasification [WWW Document]. URL https://www.llnl.gov/news/llnl-work-interior-department-underground-coal-gasification

Li, C., Nordlund, E., 1993. Assessment of damage in rock using the Kaiser effect of acoustic emission. Int. J. Rock Mech. Min. Sci. 30, 943–946. https://doi.org/10.1016/0148-9062(93)90049-J

Li, D., Wong, L.N.Y., 2013. The brazilian disc test for rock mechanics applications: Review and new insights. Rock Mech. Rock Eng. 46, 269–287. https://doi.org/10.1007/s00603-

012-0257-7

Li, H.B., Zhao, J., Li, T.J., 2000. Triaxial compression tests on a granite at different strain rates and confining pressures. Int. J. Rock Mech. Min. Sci. 36, 1057–1063.

Li, Y., Xia, C., 2000. Time-dependent tests on intact rocks in uniaxial compression. Int. J. Rock Mech. Min. Sci. 37, 467–475. https://doi.org/10.1016/S1365-1609(99)00073-8

Li, Z., Wang, Q., 2006. Experimental research on effect of loading rate for dynamic fracture toughness of rock. Chinese J. Geotech. Eng. 28, 2116–2120.

Liang, C., Wu, S., Li, X., Xin, P., 2015. Effects of strain rate on fracture characteristics and mesoscopic failure mechanisms of granite. Int. J. Rock Mech. Min. Sci. 76, 146–154. https://doi.org/10.1016/j.ijrmms.2015.03.010

Liang, W.G., Zhao, Y.S., Xu, S.G., Dusseault, M.B., 2011. Effect of strain rate on the mechanical properties of salt rock. Int. J. Rock Mech. Min. Sci. 48, 161–167. https://doi.org/10.1016/j.ijrmms.2010.06.012

Lim, I.L., Johnston, I.W., Choi, S.K., 1993. Stress intensity factors for semi-circular specimens under three-point bending. Eng. Fract. Mech. 44, 363–382. https://doi.org/10.1016/0013-7944(93)90030-V

Lim, I.L., Johnston, I.W., Choi, S.K., Boland, J.N., 1994a. Fracture testing of a soft rock with semi-circular specimens under three-point bending . Part 2--mixed-mode. Int. J. Rock Mech. Min. Sci. Geomech. Abstr. 31, 199–212. https://doi.org/http://dx.doi.org/10.1016/0148-9062(94)90464-2

Lim, I.L., Johnston, I.W., Choi, S.K., Boland, J.N., 1994b. Fracture testing of a soft rock with semi-circular specimens under three-point bending. Part 1-mode I. Int. J. Rock Mech. Min. Sci. 31, 185–197. https://doi.org/10.1016/0148-9062(94)90463-4

Lin, H., Xiong, W., Xiong, Z., Gong, F., 2015a. Three-dimensional effects in a flattened Brazilian disk test. Int. J. Rock Mech. Min. Sci. 74, 10–14. https://doi.org/10.1016/j.ijrmms.2014.11.006

Lin, H., Xiong, W., Yan, Q., 2015b. Modified Formula for the Tensile Strength as Obtained by the Flattened Brazilian Disk Test. Rock Mech. Rock Eng. 49, 1579–1586. https://doi.org/10.1007/s00603-015-0785-z

Lindquist, W.B., Lee, S.-M., Coker, D.A., Jones, K.W., Spanne, P., 1996. Medial axis analysis of void structure in three-dimensional tomographic images of porous media. J. Geophys. Res. Solid Earth 101, 8297–8310. https://doi.org/10.1029/95JB03039

Lindquist, W.B., Venkatarangan, A., 2000. Pore and throat size distributions measured from synchrotron X-ray tomographic images. J. Geop 105, 21509–21527.

Lindquist, W.B., Venkatarangan, A., 1999. Investigating 3D geometry of porous media from high resolution images. Phys. Chem. Earth, Part A Solid Earth Geod. 24, 593–599. https://doi.org/10.1016/S1464-1895(99)00085-X

Liu, H.., 1983. On the fundamental basis of fracture mechanics. Eng. Fract. Mech. 17, 425–438. https://doi.org/10.1016/0013-7944(83)90039-5

Liu, S., Xu, J., 2015. Effect of strain rate on the dynamic compressive mechanical behaviors of rock materials subjected to high temperatures. Mech. Mater. 82, 28–38.

Liu, X., Zhang, C., Yuan, S., Fityus, S., Sloan, S.W., Buzzi, O., 2016. Effect of High Temperature on Mineralogy, Microstructure, Shear Stiffness and Tensile Strength of Two Australian Mudstones. Rock Mech. Rock Eng. 49, 3513–3524. https://doi.org/10.1007/s00603-016-1024-y

Lockner, D., 1993. The role of acoustic emission in the study of rock fracture. Int. J. Rock Mech. Min. Sci. Geomech. Abstr. 30, 883–899. https://doi.org/10.1016/0148-9062(93)90041-b

Lü, C., Sun, Q., Zhang, W., Geng, J., Qi, Y., Lu, L., 2017. The effect of high temperature on tensile strength of sandstone. Appl. Therm. Eng. 111, 573–579. https://doi.org/10.1016/j.applthermaleng.2016.09.151

Luo, Y.H., Zhu, D.Q., Pan, J., Zhou, X.L., 2016. Thermal decomposition behaviour and kinetics of Xinjiang siderite ore. Miner. Process. Extr. Metall. Institutions Min. Metall. Sect. C 125, 17–25. https://doi.org/10.1080/03719553.2015.1118213

Maccagno, T.M., Knott, J.F., 1989. The fracture behaviour of PMMA in mixed modes I and II. Eng. Fract. Mech. 34, 65–86.

Madonna, C., Almqvist, B.S.G., Saenger, E.H., 2012. Digital rock physics: Numerical prediction of pressure-dependent ultrasonic velocities using micro-CT imaging. Geophys. J. Int. 189, 1475–1482. https://doi.org/10.1111/j.1365-246X.2012.05437.x

Mahabadi, O.K., Tatone, B.S.A., Grasselli, G., 2014. Journal of Geophysical Research : Solid Earth Influence of microscale heterogeneity and microstructure on the tensile behavior of crystalline rocks. J. Geophys. Res. Solid Earth 119, 5324–5341. https://doi.org/10.1002/2014JB011064.1.

Mahajan, R. V, Ravi-Chandar, K., 1989. An experimental investigation of mixed-mode fracture. Int. J. Fract. 41, 235–252.

Mahanta, B., Singh, T.N., Ranjith, P.G., 2016. Influence of thermal treatment on mode I fracture toughness of certain Indian rocks. Eng. Geol. 210, 103–114. https://doi.org/10.1016/j.enggeo.2016.06.008

Mahanta, B., Singh, T.N., Ranjith, P.G., Vishal, V., 2018. Experimental investigation of the influence of strain rate on strength; failure attributes and mechanism of Jhiri shale. J. Nat. Gas Sci. Eng. 58, 178–188. https://doi.org/10.1016/j.jngse.2018.08.001

Mahanta, B., Sirdesai, N., Singh, T.N., Ranjith, P.G., 2017a. Experimental Study of Strain Rate Sensitivity to Fracture Toughness of Rock using Flattened Brazilian Disc, in: Procedia Engineering. pp. 256–262. https://doi.org/10.1016/j.proeng.2017.05.179

Mahanta, B., Tripathy, A., Vishal, V., Singh, T.N., Ranjith, P.G., 2017b. Effects of strain rate on fracture toughness and energy release rate of gas shales. Eng. Geol. 218, 39–49. https://doi.org/10.1016/j.enggeo.2016.12.008

Mahmutoglu, Y., 2006. The effects of strain rate and saturation on a micro-cracked marble. Eng. Geol. 82, 137–144. https://doi.org/10.1016/j.enggeo.2005.09.001

Masuda, K., Mizutani, H., Yamada, I., 1987. Experimental study of strain-rate dependence and pressure dependence of failure properties of Granite. J. Phys. Earth 35, 37–66.

Matsuki, K., Hasibuan, S.S., Takahashi, H., 1991. Specimen Size Requirements for Determining the Inherent Fracture Toughness of Rocks According to the ISRM Suggested Methods. Int J. Rock. Mech. Sci. 28, 365–374.

McCabe, S., Smith, B.J., Warke, P.A., 2010. Exploitation of inherited weakness in fire-damaged building sandstone: The “fatiguing” of “shocked” stone. Eng. Geol. 115, 217–225. https://doi.org/10.1016/j.enggeo.2009.06.003

McKenna, T.E., Sharp, J.M., Lynch, F.L., 1996. Thermal conductivity of Wilcox and Frio sandstones in South Texas (Gulf of Mexico Basin) 80, 1203–1215.

Mecholsky, J.J., Mackin, T.J., 1988. Fractal analysis of fracture in Ocala chert. J. Mater. Sci. Lett. 7, 1145–1147.

Mellor, M., Hawkes, I., 1971. Measurement of tensile strength by diametral compression of discs and annuli. Eng. Geol. 5, 173–225. https://doi.org/10.1016/0013-7952(71)90001-9

Meng, Q., Zhang, M., Han, L., Pu, H., Chen, Y., 2018. Acoustic Emission Characteristics of Red Sandstone Specimens Under Uniaxial Cyclic Loading and Unloading Compression. Rock Mech. Rock Eng. 51, 969–988. https://doi.org/10.1007/s00603-017-1389-6

Meredith, P.G., 1983. A fracture mechanics study of experimentally deformed crystal rocks. University of London.

Meredith, P.G., Atkinson, B.K., 1985. Fracture toughness and subcritical crack growth during high-temperature tensile deformation of Westerly granite and Black gabbro. Phys. Earth Planet. Inter. 39, 33–51. https://doi.org/10.1016/0031-9201(85)90113-X

Middleton, R.S., Carey, J.W., Currier, R.P., Hyman, J.D., Kang, Q., Karra, S., Jiménez-

Martínez, J., Porter, M.L., Viswanathan, H.S., 2015. Shale gas and non-aqueous fracturing fluids: Opportunities and challenges for supercritical CO2. Appl. Energy 147, 500–509. https://doi.org/10.1016/j.apenergy.2015.03.023

Mighani, S., Sondergeld, C.H., Rai, C.S., 2016. Observations of Tensile Fracturing of Anisotropic Rocks. Soc. Pet. Eng. Preprint.

Ministry of Coal, 2015. Steps for Development of Underground Coal Gasification Technology, in: PIB News Bulletin. http://pib.nic.in/newsite/PrintRelease.aspx?relid=132935.

Mohammadmoradi, P., Bashtani, F., Goudarzi, B., Taheri, S., Kantzas, A., 2017. Pore Network and Morphological Characterization of Pore-Level Structures Pore Network Modeling, in: Society of Petroleum Engineers.

Mohanty, D., 2017. An overview of the geological controls in underground coal gasification. IOP Conf. Ser. Earth Environ. Sci. 76, 1–8. https://doi.org/10.1088/1755-1315/76/1/012010

Mozley, P.S., Heath, J.E., Dewers, T.A., Bauer, S.J., 2016. Origin and heterogeneity of pore sizes in the Mount Simon Sandstone and Eau Claire Formation: Implications for multiphase fluid flow. Geosphere 12, 1341–1361. https://doi.org/10.1130/GES01245.1

Nabawy, B.S., Géraud, Y., 2016. Impacts of pore- and petro-fabrics, mineral composition and diagenetic history on the bulk thermal conductivity of sandstones. J. African Earth Sci. 115, 48–62. https://doi.org/10.1016/J.JAFREARSCI.2015.11.025

Nasseri, M.H.., Mohanty, B., 2008. Fracture toughness anisotropy in granitic rocks. Int. J. Rock Mech. Min. Sci. 45, 167–193.

Nasseri, M.H.B., Tatone, B.S.A., Grasselli, G., Young, R.P., 2009. Fracture toughness and fracture roughness interrelationship in thermally treated Westerly granite. Pure Appl. Geophys. 166, 801–822. https://doi.org/10.1007/s00024-009-0476-3

Nikolaevsky, V.N., 1990. Mechanics of porous and fractured media. World Scientific, Singapore.

Noori, A., Rais, S., 2014. Geochemistry and Detrital Modes of Sandstone From Barakar Formation in Mand Valley Basin, Chhattisgarh, India: Implications for Provenance, Tectonic Setting and Paleoweathering. Int. J. Basic Appl. Sci. 3, 124–133. https://doi.org/10.14419/ijbas.v3i2.2353

Okubo, S., Hashiba, K., Fukui, K., 2013. Loading rate dependency of the strengths of some Japanese rocks. Int. J. Rock Mech. Min. Sci. 58, 180–185. https://doi.org/10.1016/j.ijrmms.2012.09.003

Øren, P.E., Bakke, S., 2002. Process Based Reconstruction of Sandstones and Prediction of

Transport Properties. Transp. Porous Media 46, 311–343. https://doi.org/10.1023/A:1015031122338

Ouchterlony, F., 1990. Fracture toughness testing of rock with coore base specimens. Eng. Fract. Mech. 7, 351–366.

Ouchterlony, F., 1988. ISRM suggested methods for determining fracture toughness of rocks. Int J Rock Mech Min Sci Geomech Abstr 25, 71–96.

Özfirat, M.K., Yenice, H., Şimşir, F., Yaralı, O., 2016. A new approach to rock brittleness and its usability at prediction of drillability. J. African Earth Sci. 119, 94–101. https://doi.org/10.1016/j.jafrearsci.2016.03.017

Ozguven, A., Ozcelik, Y., 2014. Effects of high temperature on physico-mechanical properties of Turkish natural building stones. Eng. Geol. 183, 127–136. https://doi.org/10.1016/j.enggeo.2014.10.006

Palciauskas, V., Domenico, P.A., 1982. Characterizatioonf Draineda nd Undrained Response of Thermally Loaded Repository Rocks. Water Resour. Res. 18, 281–290.

Papanastasiou, P., 1999. The effective fracture toughness in hydraulic fracturing. Int. J. Fract. 96, 127–147. https://doi.org/10.1023/a:1018676212444

Pareek, H.S., 1984. Pre-Quaternary Geology and mineral resources of northwestern Rajasthan. Mem. Geol. Surv. India 115, 1–95.

Perras, M.A., Diederichs, M.S., 2014. A Review of the Tensile Strength of Rock: Concepts and Testing. Geotech. Geol. Eng. 32, 525–546. https://doi.org/10.1007/s10706-014-9732-0

Prabu, V., Mallick, N., 2015. Coalbed methane with CO_2 sequestration: An emerging clean coal technology in India. Renew. Sustain. Energy Rev. 50, 229–244. https://doi.org/10.1016/j.rser.2015.05.010

Prasad, B.R., Rao, V. V, 2006. Deep seismic reflection study over the Vindhyans of Rajasthan: implications for geophysical setting of the basin. J. Earth Syst. Sci. 115, 135–147.

Rabbani, A., Assadi, A., Kharrat, R., Dashti, N., Ayatollahi, S., 2017. Estimation of carbonates permeability using pore network parameters extracted from thin section images and comparison with experimental data. J. Nat. Gas Sci. Eng. 42, 85–98. https://doi.org/10.1016/j.jngse.2017.02.045

Ramachandran, V.S., Kacker, K.P., 1964. The thermal decomposition of dye-clay mineral complexes. J. Appl. Chem. 14, 455–460.

Ranjith, P.G., Viete, D.R., Chen, B.J., Perera, M.S.A., 2012. Transformation plasticity and the effect of temperature on the mechanical behaviour of Hawkesbury sandstone at atmospheric pressure. Eng. Geol. 151, 120–127.

https://doi.org/10.1016/j.enggeo.2012.09.007

Ranjith, P.G., Viete, D.R., Chen, B.J., Perera, M.S.A., 2012. Transformation plasticity and the effect of temperature on the mechanical behaviour of Hawkesbury sandstone at atmospheric pressure. Eng. Geol. 151, 120–127. https://doi.org/10.1016/j.enggeo.2012.09.007

Rao, M.V.M.S., Ramana, Y. V., 1992. A study of progressive failure of rock under cyclic loading by ultrasonic and AE monitoring techniques. Rock Mech. Rock Eng. 25, 237–251. https://doi.org/10.1007/BF01041806

Rao, Q., Wang, Z., Xie, H., Xie, Q., 2007. Experimental study of properties of sandstone at high temperature. J. Cent. South Univ. Technol. 14, 478–483.

Rao, Q., Wang, Z., Xie, H., Xie, Q., 2007. Experimental study of mechanical properties of sandstone at high temperature. J. Cent. South Univ. Technol. 14, 478–483. https://doi.org/10.1007/s11771

Ray, S.., Sarkar, M., Singh, T.., 1999. Effect of cyclic loading and strain rate on the mechanical behaviour of sandstone. Int. J. Rock Mech. Min. Sci. 36, 543–549. https://doi.org/10.1016/S0148-9062(99)00016-9

Reinhardt, H., Weerheijm, J., 1991. Tensile fracture of concrete at high loading rates taking account of inerta and crack velocity effects. Int. J. Fract. 51, 31–42.

Reuschlé, T., Gbaguidi Haore, S., Darot, M., 2006. The effect of heating on the microstructural evolution of La Peyratte granite deduced from acoustic velocity measurements. Earth Planet. Sci. Lett. 243, 692–700. https://doi.org/10.1016/j.epsl.2006.01.038

Roddy, D.J., Younger, P.L., 2010. Underground coal gasification with CCS: a pathway to decarbonising industry. Energy Environ. Sci. 3, 400–407.

Rosenbrand, E., Haugwitz, C., Jacobsen, P.S.M., Kjøller, C., Fabricius, I.L., 2014. The effect of hot water injection on sandstone permeability. Geothermics 50, 155–166. https://doi.org/10.1016/j.geothermics.2013.09.006

Rummel, F., Winter, R.B., 1982. Application of laboratory fracture mechanics data to hydraulic fracturing field tests, in: 1st Japan- USA Symp. on Fracture Mechanics Approach, Hydraulic Fracture and Geothermal Energy. Sendai, Japan, pp. 495–501.

Rutqvist, J., Wu, Y.S., Tsang, C.F., Bodvarsson, G., 2002. A modeling approach for analysis of coupled multiphase fluid flow, heat transfer, and deformation in fractured porous rock. Int. J. Rock Mech. Min. Sci. 39, 429–442.

Rybacki, E., Meier, T., Dresen, G., 2016. What controls the mechanical properties of shale rocks? - Part II: Brittleness. J. Pet. Sci. Eng. 144, 39–58.

https://doi.org/10.1016/j.petrol.2016.02.022

Sabri, M., Ghazvinian, A., Nejati, H.R., 2016. Effect of particle size heterogeneity on fracture toughness and failure mechanism of rocks. Int. J. Rock Mech. Min. Sci. 81, 79–85. https://doi.org/10.1016/j.ijrmms.2015.11.002

Sam Boggs, J., 2006. Principle of Sedimentology and stratigraphy, 4th Editio. ed, Journal of Chemical Information and Modeling. Pearson Prentice Hall, Upper Saddle River, New Jersey, New Jersey, USA. https://doi.org/10.1017/CBO9781107415324.004

Sano, O., Ito, I., Terada, M., 1981. Influence of strain rate on dilatancy and strength of Oshima granite under uniaxial compression. J. Geophys. Res. 86, 9299–9311. https://doi.org/10.1029/JB086iB10p09299

Scavia, C., 1990. Fracture mechanics approach to stability analysis of rock slopes. Eng. Fract. Mech. 35, 899–910.

Schacht, C., 2004. Refractories handbook. CRC Press.

Scott, J., Proskin, S., Adhikary, D., 1994. Volume And Permeability Changes Associated With Steam Stimulation In an Oil Sands Reservoir. J. Can. Pet. Technol. 33, 44–52. https://doi.org/10.2118/94-07-06

Sharqawy, M.H., 2016. Construction of pore network models for Berea and Fontainebleau sandstones using non-linear programing and optimization techniques. Adv. Water Resour. 98, 198–210. https://doi.org/10.1016/j.advwatres.2016.10.023

Shetty, D.K., Rosenfield, A.R., Duckworth, W.H., 1987. Mixed-mode fracture in biaxial stress state: application of the diametral-compression (Brazilian disk) test. Eng. Fract. Mech. 26, 825–840.

Siegesmund, S., S, M., Scheffzu, k. C., Nikolayev, D.., 2008. The bowing potential of granitic rocks: rock fabrics, thermal properties and residual strain. Environ. Geol. 55, 1437–1448.

Siegesmund, S., Ullemeyer, K., Weiss, T., Tschegg, E.K., 2000. Physical weathering of marbles caused by anisotropic thermal expansion. Int. J. Earth Sci. 89, 170–182.

Silin, D., Patzek, T., 2006. Pore space morphology analysis using maximal inscribed spheres. Phys. A Stat. Mech. its Appl. 371, 336–360. https://doi.org/10.1016/j.physa.2006.04.048

Singan, A., Ranade, V. V., 2017. Deployment of underground coal gasification in India. Curr. Sci. 113, 218–227. https://doi.org/10.18520/cs/v113/i02/218-227

Singh, T.N., Naidu, A.S., 2000. Influence of strain rate and cyclic compression on physico-mechanical behaviour of rock. Indian J. Eng. Mater. Sci. 8, 8–12.

Sirdesai, N., Mahanta, B., Ranjith, P.G., Singh, T.N., 2017. Effects of thermal treatment on physico-morphological properties of Indian fine-grained sandstone. Bull. Eng. Geol.

Environ. https://doi.org/10.1007/s10064-017-1149-6

Sirdesai, N., Singh, R., Sing, T.N., Ranjith, P.G., 2015. Numerical and experimental study of strata behavior and land subsidence in an underground coal gasification project, in: International Association of Hydrological Sciences. pp. 455–462. https://doi.org/10.5194/piahs-92-1-2015

Sirdesai, N., Singh, T.N., Pathegama Gamage, R., 2017. Thermal alterations in the poro-mechanical characteristic of an Indian sandstone – A comparative study. Eng. Geol. 226, 208–220. https://doi.org/10.1016/j.enggeo.2017.06.010

Sirdesai, N.N., Mahanta, B., Singh, T.N., Ranjith, P.G., 2016. Elastic modulus of thermally treated fine grained sandstone using non-contact laser extensometer, in: Recent Advances in Rock Engineering (RARE 2016). Bangalore, India, pp. 105–109.

Sirdesai, N.N., Singh, T.N., Ranjith, P.G., Singh, R., 2016. Effect of Varied Durations of Thermal Treatment on the Tensile Strength of Red Sandstone. Rock Mech. Rock Eng. https://doi.org/10.1007/s00603-016-1047-4

Skinner, B.J., 1966. Thermal expansion, in: Clark, J.S.P. (Ed.), Handbook of Physical Constants. Geological Society of America, pp. 75–96.

Somerton, W.H., 1992. Thermal properties and temperature-related behavior of rock/fluid systems. Elsevier Science Publishers, Amsterdam, The Netherlands.

Somerton, W.H., Boozer, G.D., 1960. Thermal Characteristics of Porous Rocks At Elevated Temperatures. J. Pet. Technol. 12, 77–81. https://doi.org/10.2118/1372-G

Somerton, W.H., Mathur, A.. K., 1976. Effects of temperature and stress on fluid flow and storage capacity of porous rocks, in: American Rock Mechanics Association. p. ARMA-76-0097.

Srivastava, P., 2012. Treptichnus pedum: An Ichnofossil representing Ediacaran - Cambrian boundary in the Nagaur Group, the Marwar Supergroup, Rajasthan, India. Proc. Indian Natl. Sci. Acad. 78, 161–169.

Stephens, G., Voight, B., 1982. Hydraulic fracturing theory for conditions of thermal stress. Int. J. Rock Mech. Min. Sci. Geomech. Abstr. 19, 279–284. https://doi.org/10.1016/0148-9062(82)91364-X

Stoch, L., Wacławska, I., 1981. Dehydroxylation of kaolinite group minerals. J. Therm. Anal. 20, 305–310. https://doi.org/10.1007/BF01912878

SU, C., Guo, W., Li, X., 2008. Experimental research on mechanical properties of sandstone after high temperatures. Chinese J. Rock Mech. Eng. 27, 1162–1170.

Sulem, J., Ouffroukh, H., 2006. Shear banding in drained and undrained triaxial tests on a

saturated sandstone: Porosity and permeability evolution. Int. J. Rock Mech. Min. Sci. 43, 292–310. https://doi.org/10.1016/j.ijrmms.2005.07.001

Sun, H., Sun, Q., Deng, W., Zhang, W., Lü, C., 2017. Temperature effect on microstructure and P-wave propagation in Linyi sandstone. Appl. Therm. Eng. 115, 913–922. https://doi.org/10.1016/j.applthermaleng.2017.01.026

Sun, Q., Lü, C., Cao, L., Li, W., Geng, J., Zhang, W., 2016a. Thermal properties of sandstone after treatment at high temperature. Int. J. Rock Mech. Min. Sci. 85, 60–66. https://doi.org/10.1016/j.ijrmms.2016.03.006

Sun, Q., Zhang, W., Su, T., Zhu, S., 2016b. Variation of wave velocity and porosity of sandstone after high temperature heating. Acta Geophys. 64, 633–648. https://doi.org/10.1515/acgeo-2016-0021

Sun, Q., Zhang, W., Xue, L., Zhang, Z., Su, T., 2015. Thermal damage pattern and thresholds of granite. Environ. Earth Sci. 74, 2341–2349. https://doi.org/10.1007/s12665-015-4234-9

Sundberg, J., Back, P.E., Christiansson, R., Hokmark, M., Landell, M., Wrafter, J., 2009. Modelling of thermal rock mass properties at the potential sites of a Swedish nuclear waste repository. Int. J. Rock Mech. Min. Sci. 46, 1042–1054.

Thallak, S., Holder, J., Gray, K.E., 1993. The pressure dependence of apparent hydro- fracture toughness. Int. J. Rock Mech. Min. Sci. Geomech. Abstr. 30, 831–835.

Tian, H., 2013. Development of a thermo-mechanical model for rocks exposed to high temperatures during underground coal gasification. (Ph.D Thesis). RWTH Aachen University, Germany.

Tian, H., Kempka, T., Xu, N.-X., Ziegler, M., 2012. Physical Properties of Sandstones After High Temperature Treatment. Rock Mech. Rock Eng. 45, 1113–1117. https://doi.org/10.1007/s00603-012-0228-z

Tian, H., Kempka, T., Yu, S., Ziegler, M., 2016. Mechanical Properties of Sandstones Exposed to High Temperature. Rock Mech. Rock Eng. 49, 321–327. https://doi.org/10.1007/s00603-015-0724-z

Tian, H., Mei, G., Jiang, G.S., Qin, Y., 2017. High-Temperature Influence on Mechanical Properties of Diorite. Rock Mech. Rock Eng. 50, 1661–1666. https://doi.org/10.1007/s00603-017-1185-3

Udell, K.S., Lofy, J.D., 1989. Permeability Reduction of Unconsolidated Media Caused by Stress-Induced Silica Dissolution, in: SPE Formation Evaluation. p. 56–62. https://doi.org/10.2118/13655-PA

Uribe-Patino, J.A., Alzate-Espinosa, G.A., Arbelaex-Londono, A., 2017. Geomechanical aspects of reservoir thermal alteration: A literature review. J. Pet. Sci. Eng. 152, 250–266. https://doi.org/10.1016/j.petrol.2017.03.012

Valdiya, K.S., 2016. The Making of India: Geodynamic Evolution, Second Edi. ed. Springer International Publishing, Switzerland. https://doi.org/10.1007/978-3-319-25029-8

Valente, S., Fidelibus, C., Loew, S., Cravero, M., Iabichino, G., Barpi, F., 2012. Analysis of fracture mechanics tests on opalinus clay. Rock Mech. Rock Eng. 45, 767–779. https://doi.org/10.1007/s00603-012-0225-2

Vavro, L., Souček, K., 2013. Study of the effect of moisture content and bending rate on the fracture toughness of rocks. Acta Geodyn. Geomater. 10, 247–253.

Vishal, V., Jain, N., Singh, T.N., 2015. Three dimensional modelling of propagation of hydraulic fractures in shale at different injection pressures. Sustain. Environ. Res. 25, 217–225.

Vishal, V., Pradhan, S.P., Singh, T.N., 2011. Tensile Strength of Rock Under Elevated Temperatures. Geotech. Geol. Eng. 29, 1127–1133. https://doi.org/10.1007/s10706-011-9440-y

Wang, M., Cao, P., 2016. Numerical Analysis of Flattened Brazilian Disc Test Based on the Cusp Catastrophe Theory. Math. Probl. Eng. 2016, 1–9.

Wang, M., Cao, P., 2015. Numerical Study on Flattened Brazilian Test and Its Empirical Formula. Electron. J. Geotech. Eng. 20, 12211–12224.

Wang, M.C., Benway, J.M., Arayssi, A.M., 1990. The Effect of Heating on Engineering Properties of Clays, in: Physico-Chemical Aspects of Soil and Related Materials. pp. 1139–1158.

Wang, Q.-Z., Xing, L., 1999. Determination of fracture toughness KIC by using the flattened Brazilian disk specimen for rocks. Eng. Fract. Mech. 64, 193–201. https://doi.org/10.1016/S0013-7944(99)00065-X

Wang, Q.., Jia, X.., Kou, S.., Zhang, Z.., Lindqvist, P.-A., 2004. The flattened Brazilian disc specimen used for testing elastic modulus, tensile strength and fracture toughness of brittle rocks: analytical and numerical results. Int. J. Rock Mech. Min. Sci. 41, 245–253. https://doi.org/10.1016/S1365-1609(03)00093-5

Wang, X., Liou, J.G., 1991. Regional ultrahigh-pressure coesite-bearing eclogitic terrane in central China: Evidence from country rocks, gneiss, marble, and metapelite. Geology 19, 933. https://doi.org/10.1130/0091-7613(1991)019<0933:RUPCBE>2.3.CO;2

Wang, X., Liou, J.G., Mao, H.K., 1989. Coesite-bearing eclogite from the Dabie Mountains in

central China. Geology 17, 1085. https://doi.org/10.1130/0091-7613(1989)017<1085:CBEFTD>2.3.CO;2

Wang, Y., Dusseault, M.B., 2003. A coupled conductive-convective thermo-poroelastic solution and implications for wellbore stability. J. Pet. Sci. Eng. 38, 187–198. https://doi.org/10.1016/S0920-4105(03)00032-9

Wang, Y., Papamichos, E., 1994. Conductive heat flow and thermally induced fluid flow around a well bore in a poroelastic medium. Water Resour. Res. 30, 3375–3384.

Wasantha, P.L.P., Ranjith, P.G., Zhao, J., Shao, S.S., Permata, G., 2015. Strain Rate Effect on the Mechanical Behaviour of Sandstones with Different Grain Sizes. Rock Mech. Rock Eng. 48, 1883–1895. https://doi.org/10.1007/s00603-014-0688-4

Weijermars, R., 2014. US shale gas production outlook based on well roll-out rate scenarios. Appl. Energy 124, 283–297. https://doi.org/10.1016/j.apenergy.2014.02.058

Westergaard, H.., 1939. Bearing Pressures and Cracks. J. Appl. Mech. 6, A49-53.

Whittaker, B.N., Singh, R.N., Sun, G., 1992. Rock fracture mechanics: principles, design and applications, developments in geotechnical engineering. Elsevier Publisher, Amsterdam, The Netherlands.

Wong, T., Baud, P., Klein, E., 2001. Localised failure modes in a compactant porous rock. Geophys. Res. Lett. 28, 2521–2524.

Working Group on Underground Coal, 2007. Status Report on Underground Coal Gasification. Office of the Principal Scientific Advisor to the Government of India.

WU, G., Wang, D., Zhai, S., 2012. Acoustic emission characteristics of sandstone after high temperature under uniaxial compression. Rock Soil Mech. 33, 3237–3242.

Wu, G., Wang, Y., Swift, G., Chen, J., 2013. Laboratory Investigation of the Effects of Temperature on the Mechanical Properties of Sandstone. Geotech. Geol. Eng. 31, 809–816. https://doi.org/10.1007/s10706-013-9614-x

Wu, G., Xing, A., Zhang, L., 2007. Mechanical characteristics of sandstone after high temperatures. Chinese J. Rock Mech. Eng. 26, 2010–2116.

Xia, K., Nasseri, M., Mohanty, B., Lu, F., Chen, R., Luo, S., 2008. Effects of microstructures on dynamic compression of Barre granite. Int. J. Rock Mech. Min. Sci. 45, 879–887.

Xiong, Q., Baychev, T.G., Jivkov, A.P., 2016. Review of pore network modelling of porous media: Experimental characterisations, network constructions and applications to reactive transport. J. Contam. Hydrol. 192, 101–117. https://doi.org/10.1016/j.jconhyd.2016.07.002

Yang, S., Zeng, S., Wang, H., 2005. Experimental analysis on mechanical effects of loading

rates on limestone. Chinese J. Geotech. Eng. 27, 786–788.

Yang, S.Q., Jing, H.W., 2013. Evaluation on strength and deformation behavior of red sandstone under simple and complex loading paths. Eng. Geol. 164, 1–17. https://doi.org/10.1016/j.enggeo.2013.06.010

Yavuz, H., Demirdag, S., Caran, S., 2010. Thermal effect on the physical properties of carbonate rocks. Int. J. Rock Mech. Min. Sci. 47, 94–103. https://doi.org/10.1016/j.ijrmms.2009.09.014

Yilmaz, G., 2011. The effects of temperature on the characteristics of kaolinite and bentonite. Sci. Res. Essays 6, 1928–1939. https://doi.org/10.5897/SRE10.727

Yilmaz, G., 2003. Temperature Effects and Shrinkage Properties on Clays. J. Am. Soc. Cer. Bull 82, 9601–9605.

Yin, T., Li, X., Cao, W., Xia, K., 2015. Effects of Thermal Treatment on Tensile Strength of Laurentian Granite Using Brazilian Test. Rock Mech. Rock Eng. 48, 2213–2223. https://doi.org/10.1007/s00603-015-0712-3

Yin, T., Li, X., Xia, K., Huang, S., 2012. Effect of thermal treatment on the dynamic fracture toughness of laurentian granite. Rock Mech. Rock Eng. 45, 1087–1094. https://doi.org/10.1007/s00603-012-0240-3

Yu, J., Chen, S., Chen, X., Zhang, Y., Cai, Y., 2015. Experimental investigation on mechanical properties and permeability evolution of red sandstone after heat treatments. J. Zhejiang Univ. A 16, 749–759. https://doi.org/10.1631/jzus.A1400362

Zeiss ™, 2013. ZEISS Xradia 520 Versa submicron X-ray imaging : extending the limits of exploration.

Zhan, F., Cai, M., 2007. Influence of high temperature on anchoring system of cable bolts at stope hangingwall. J. Liaoning Tech. Univ. 26, 524–526.

Zhang, D., Ranjith, P.G., Perera, M.S.A., 2016. The brittleness indices used in rock mechanics and their application in shale hydraulic fracturing: A review. J. Pet. Sci. Eng. 143, 158–170. https://doi.org/10.1016/j.petrol.2016.02.011

Zhang, L., Mao, X., Lu, A., 2009. Experimental study on the mechanical properties of rocks at high temperature. Sci. China, Ser. E Technol. Sci. 52, 641–646. https://doi.org/10.1007/s11431-009-0063-y

Zhang, Q.B., Zhao, J., 2014. A review of dynamic experimental techniques and mechanical behaviour of rock materials. Rock Mech. Rock Eng. 47, 1411–1478. https://doi.org/10.1007/s00603-013-0463-y

Zhang, Q.B., Zhao, J., 2013. Effect of loading rate on fracture toughness and failure

micromechanisms in marble. Eng. Fract. Mech. 102, 288–309. https://doi.org/10.1016/j.engfracmech.2013.02.009

Zhang, Y., Sun, Q., He, H., Cao, L., Zhang, W., Wang, B., 2017. Pore characteristics and mechanical properties of sandstone under the influence of temperature. Appl. Therm. Eng. 113, 537–543. https://doi.org/10.1016/j.applthermaleng.2016.11.061

Zhang, Y.Q., Hao, H., Lu, Y., 2003. Anisotropic dynamic damage and fragmentation of rock materials under explosive loading. Int. J. Eng. Sci. 41, 917–929. https://doi.org/10.1016/S0020-7225(02)00378-6

Zhang, Y.T., Qi, D.X., Gao, J., Huang, T., 2008. Analysis of kinking in elastoplastic materials with strain-softening behavior. Int. J. Eng. Sci. 46, 1077–1086. https://doi.org/10.1016/j.ijengsci.2008.04.008

Zhang, Z.X., 2002. An empirical relation between mode I fracture toughness and the tensile strength of rock. Int. J. Rock Mech. Min. Sci. 39, 401–406.

Zhang, Z.X., Kou, S.Q., Jiang, L.G., Lindqvist, P.A., 2000. Effects of loading rate on rock fracture characteristics and energy partitioning. Int. J. Rock Mech. Min. Sci. 37, 745–762.

Zhang, Z.X., Yu, J., Kou, S.Q., Lindqvist, P.-A., 2001. Effects of high temperatures on dynamic rock fracture. Int. J. Rock Mech. Min. Sci. 38, 211–225. https://doi.org/10.1016/S1365-1609(00)00071-X

Zhao, J., Li, H.., Wu, M.., Li, T.., 1999. Dynamic uniaxial compression tests on a granite. Int. J. Rock Mech. Min. Sci. 36, 273–277. https://doi.org/10.1016/S0148-9062(99)00008-X

Zhao, Y.S., 2000. Rock mechanics problems in geothermal exploitation of hot dry rocks, in: The 6th Academy Conference of Chinese Rock Mechanics and Engineering. Wuhan Science & Technology Press, pp. 361–364.

Zhou, X., Qian, Q., Yang, H., 2010. Effect of loading rate on fracture characteristics of rock. J. Cent. South Univ. Technol. 17, 150–155. https://doi.org/10.1007/s11771

Zhu, W.C., Tang, C.A., 2004. Micromechanical Model for Simulating the Fracture Process of Rock. Rock Mech. Rock Eng. 37, 25–56. https://doi.org/10.1007/s00603-003-0014-z

Zoback, M.D., Byerlee, J.D., 1976. Effect of High-Pressure Deformation on Permeability of Ottawa Sand. Am. Assoc. Pet. Geol. Bull. 60, 1531–1542.

Publications out of the research work

- ***Journal Article***

Published

1. **Mahanta, B.,** Tripathy, A., Vishal, V., Singh, T.N., Ranjith, P.G., 2017. Effects of strain rate on fracture toughness and energy release rate of gas shales. **Engineering Geology**. 218, 39–49.
2. **Mahanta, B.**, Singh, T.N., Ranjith, P.G., 2016. Influence of thermal treatment on mode I fracture toughness of certain Indian rocks. **Engineering Geology**. 210, 103–114.
3. **Mahanta, B.**, Singh, T.N., Ranjith, P.G., Vishal, V. Experimental investigation of the influence of strain rate on strength; failure attributes and mechanism of Jhiri shale. **Journal of Natural Gas Science and Engineering**.

Submitted/Under Preparation

1. **Mahanta, B.**, Ranjith, P.G., Sirdesai, N., Singh, T.N., Vishal, V. Practical implications of high-resolution X-ray computed tomography in thermal engineering: An investigation of pore-structure and pore network modelling of post high-temperature sandstones.
2. **Mahanta, B.**, Ranjith, P.G., Vishal, V., Singh, T.N. Temperature-induced deformational behaviour and microstructural alteration of sandstone: an application to underground coal gasification.
3. **Mahanta, B.**, Vishal, V., Singh, T. N., Ranjith, P. G. Microstructural insight into progressive deformation of sandstone at different stress levels.
4. **Mahanta, B.**, Ranjith, P. G., Badulla A., Kumari W.G.P., Vishal, V., Singh, T. N., Experimental Investigation of the Mechanical behaviour of sandstone under high temperature and pressure conditions: An Insight into the grain-boundary crushing.

- ***Conference Article***

1. **Mahanta, B.**, Ranjith, P. G., Singh, T. N., Vishal, V., Duan, W., Sazid, M., 2018. Digital rock physics and application of high-resolution micro-CT techniques for geomaterials. International Conference on Geo-Mechanics, Geo-Energy and Geo-Resources (IC3G) 2018, Chengdu, China.
2. **Mahanta, B.**, Sirdesai, N.N., Singh, T.N., Ranjith, P.G., 2017. Experimental Study of Strain Rate Sensitivity to Fracture Toughness of Rock using Flattened Brazilian Disc. **Procedia Engineering,** in**: EUROCK 2017**, Ostrava, Czech Republic.

3. **Mahanta, B.**, Vishal, V., Singh, T., Ranjith, P.G., 2016. Strain Rate Dependency of Fracture Toughness, Energy Release Rate and Geomechanical Attributes of Select Indian Shales, in: **AGU Fall Meeting 2016**, San Fransisco, USA.

Declaration regarding the publication of various parts of the thesis in different journals and conferences

1. Section 5.2 of Chapter 5 has been published in **Journal of Natural Gas Science and Engineering** (Mahanta et al., 2018).
2. Section 6.1 of Chapter 6 has been published in **Engineering Geology** (Mahanta et al., 2016).
3. Section 6.2 of Chapter 6 has been published in **Engineering Geology** ((Mahanta et al., 2017b)
4. Section 6.3 of Chapter 6 has been published in **Procedia Engineering** after its presentation in EUROCK 2017 conference at Ostrava, Czech Republic. (Mahanta et al., 2017a)
5. Content of Section 8.1 of Chapter 8 has been submitted for its publication.
6. In addition to already published portion of the thesis, contents of Chapter 4, Chapter 7 Section 8.2 of Chapter 8 are under preparation for their publication in various journals in the near future.

Other publications during the course of the research work

1. Vishal, V., **Mahanta, B.**, Pradhan, S.P., Singh, T.N., Ranjith, P.G., 2018. Geologic sequestration of anthropogenic CO_2 for enhanced coalbed methane recovery in Jharia coalfields, India. **Energy**. (Journal Article)
2. **Mahanta, B.**, Singh, H.O., Singh, P.K., Kainthola, A., Singh, T.N., 2016a. Stability analysis of potential failure zones along NH-305, India. **Natural Hazards**. 83, 1341–1357. (Journal Article)
3. Kundu, J., **Mahanta, B.**, Sarkar, K., Singh, T.N., 2018. The Effect of Lineation on Anisotropy in Dry and Saturated Himalayan Schistose Rock Under Brazilian Test Conditions. **Rock Mechanics and Rock Engineering**. 51, 5–21. (Journal Article)
4. Madhubabu, N., Singh, P.K., Kainthola, A., **Mahanta, B.**, Tripathy, A., Singh, T.N., 2016. Prediction of compressive strength and elastic modulus of carbonate rocks. **Measurement.** 88, 202–213. (Journal Article)
5. Singh, P.K., Tripathy, A., Kainthola, A., **Mahanta, B.**, Singh, V., Singh, T.N., 2016. Indirect estimation of compressive and shear strength from simple index tests. **Engineering with Computers.** 33, 1–11. (Journal Article)
6. Sirdesai, N.N., **Mahanta, B.**, Ranjith, P.G., Singh, T.N., 2017. Effects of thermal treatment on physico-morphological properties of Indian fine-grained sandstone. **Bulletin of Engineering Geology and Environment**. (Journal Article)
7. Wanniarachchi, W.A.M., Ranjith, P.G., Perera, M.S.A., Rathnaweera, T.D., Lyu, Q., **Mahanta, B**., 2017. Assessment of dynamic material properties of intact rocks using seismic wave attenuation: An experimental study. **Royal Society Open Science**, 4, 170896. (Journal Article)
8. Kundu, J., **Mahanta, B**., Tripathy, A., Sarkar, K., Singh, T.N., 2016. Stability Evaluation of Jointed Rock Slope with Curved Face, in: **INDOROCK 2016**. Mumbai, India, pp. 971–978. (Conference Article)
9. Sirdesai, N.N., **Mahanta, B**., Singh, T.N., Ranjith, P.G., 2016. Elastic modulus of thermally treated fine grained sandstone using non-contact laser extensometer, in: **Recent Advances in Rock Engineering (RARE 2016)**. Bangalore, India, pp. 105–109. (Conference Article)
10. Tripathy, A., **Mahanta, B**., Singh, T.N., 2016. Deformational behaviour of coal measure rocks, in: **International Conference on Earth Sciences and Engineering**. Coimbatore, Tamil Nadu, pp. 305–309. (Conference Article)

Acknowledgement

I would like to acknowledge the roles of several individuals who have been continuously involved with the journey of the research work. The journey of the research work would not have been possible without the guidance and support of these people.

First and foremost, I would like to express my utmost gratitude and appreciation to my PhD supervisors, Prof. T N Singh (IIT Bombay, India) and Prof. P G Ranjith (Monash University, Australia) for providing me with the opportunity to commence my research work and then for their continuous guidance, support and encouragement during the entire span of the research work. The research atmosphere that they provided me during my stay at IIT Bombay, India and Monash University, Australia is highly appreciated, which enabled me to have an effective and efficient research work during the course of the time.

Secondly, I am deeply grateful to my co-supervisor Assistant Prof. Vikram Vishal for mentoring and guiding me with my research work. I think myself to be fortunate enough to work with him for around two and half years. The valuable suggestions and he provided at various stages of the research work is highly appreciated. I would also like to acknowledge the effort from Prof. WenHui Duan (Monash University) for his continuous association with the research work.

I am very much thankful to IITB-Monash research academy, IIT Bombay, India for my selection into the academy and the constant support from the academic staff in simplifying various jobs at various stages during the course of the research work. I would like to thank Mrs Laya Vijayan, Mrs Jayasree T S, Mrs Nancy Sowho, Mrs Kuheli Banarjee, Mrs Beena Pillai, and Mr Kiran More for the same. I would also like to acknowledge the effort made by Mrs Sheba Sanjay and Mr Krishna Warrier of IITB-Monash research academy and, Mrs Jane Moodie of Monash University for their valuable discussion and suggestion regarding the writing of thesis. In addition, Mrs Sheba Sanjay is greatly acknowledged for her assistance with proofreading this thesis.

I am grateful to the respective Head, Departments of Earth Sciences, IIT Bombay, India, and Department of Civil Engineering, Monash University, Australia for their immense support and cooperation throughput the tenure of my PhD work. I am grateful to all the staff members of Department of Earth Sciences, IIT Bombay and Department of Civil Engineering, Monash University for their committed support in achieving the way towards the goals of my research work. A special thanks to Mr Saravan Mani, Mr Michael Leach, Mr Zoltan Csaki, Mr Mark

Taylor, Mr Philip Warnes, Mr Andres Cortes, and Mr Jeffrey Doddrell of Department of Civil Engineering, Monash University for their assistance in conducting my experiments in a safe and efficient way.

My colleagues and friends at both institutes have been pillars during the entire period and beyond, and deserve due acknowledgement. I thank Ratan Das, Mr Manas Ranjan Panda and Assistant Prof. Nikhil Sirdesai, VNIT Nagpur, India for their help during laboratory experiments at IIT Bombay. I thank Avanthi Badulla Liyanage and W.G.P. Kumari for their help during laboratory experiments at Monash University. I would also like to thank Guanglei Zhang for his help in understanding Avizo software.

I have been blessed with a friendly and cheerful group of seniors, labmates, fellow students, and friends during the candidature of my research work. I am thankful to Assistant Prof. Prakash Kumar Singh, Allahbad University, India; Assistant Prof. Asutosh Kainthola, Banaras Hindu University, India; Assistant Prof. Rajesh Singh, Lucknow University for their valuable advice during the initial period of my research work. I am thankful for the great company of Kartick Dey, Hari Om Singh, Jagadish Kundu, Shashibhushan Biliangadi, Vinod Vijay Kumar, Dr Tushar Gupta, Dr Debanjan Guha Roy, Dr Lakshmikant Sharma, Dr Vinoth Srinivasan, Tariq Anwar Ansari, Ashutosh Tripathy, and Mrityunjay Shrama. Their companionship truly made a relaxing friendly environment for me to work in during my candidature. I am thankful to all of them for this.

Last, but not the least, my deepest appreciation goes to my beloved parents and my sister for their continuous support.